



University  
of Glasgow

Younis, Usman (2010) *Monolithic integration for nonlinear optical frequency conversion in semiconductor waveguides*. PhD thesis.  
<http://theses.gla.ac.uk/2178/>

Copyright and moral rights for this thesis are retained by the author

A copy can be downloaded for personal non-commercial research or study, without prior permission or charge

This thesis cannot be reproduced or quoted extensively from without first obtaining permission in writing from the Author

The content must not be changed in any way or sold commercially in any format or medium without the formal permission of the Author

When referring to this work, full bibliographic details including the author, title, awarding institution and date of the thesis must be given.

MONOLITHIC INTEGRATION FOR  
NONLINEAR OPTICAL FREQUENCY  
CONVERSION IN SEMICONDUCTOR  
WAVEGUIDES

A THESIS SUBMITTED TO  
THE DEPARTMENT OF ELECTRONICS AND ELECTRICAL ENGINEERING  
UNIVERSITY OF GLASGOW  
IN FULFILMENT OF THE REQUIREMENTS  
FOR THE DEGREE OF  
DOCTOR OF PHILOSOPHY

By  
Usman Younis  
May 2010

© Usman Younis  
All Rights Reserved



# Abstract

This thesis presents an investigation into the feasibility of tunable, monolithically integrated, nonlinear optical frequency conversion sources which work under the principles of an optical parametric oscillator (OPO). The room-temperature continuous wave (CW) operation of these devices produces narrow line-width, near- and mid-infrared wavelengths, primarily used in chemical sensing applications. The devices detailed here, based on the GaAs–AlGaAs superlattice material system, benefit from post growth, ion implantation induced, quantum well intermixing, to achieve 1<sup>st</sup> order phase matching. The experiments, which have been performed to optimize the second-order nonlinear processes in our GaAs–AlGaAs superlattice waveguides, have demonstrated improved conversion efficiencies when compared to the performance achieved previously in similar superlattice nonlinear waveguides. We have achieved pulsed type-I phase matched second harmonic generation (SHG) with powers up to 3.65  $\mu\text{W}$  (average pulse power), CW type-I phase matched SHG up to 1.6  $\mu\text{W}$  for the first time, and pulsed type-II phase matched SHG up to 2  $\mu\text{W}$  (average pulse power), again for the first time. Moreover, we have been able to achieve both CW type-I and CW type-II phase matched difference frequency generation, which converts C-band wavelengths into L- and U-band wavelengths, over at least a 20 nm conversion bandwidth. These results have been made possible through the systematic optimization of processes developed to fabricate nonlinear optical waveguides. Fabrication processes have also been developed to facilitate the incorporation of on-chip lasers and optical routing components, required to achieve a fully integrated OPO and nonlinear optical frequency converter. The optical routing in these devices has been demonstrated using a frequency selective multi-mode interference (MMI) coupler. The superlattice laser material has been designed by optimizing the material structure and employing different growth technologies. Room-temperature CW laser action has been achieved in 100 nm thick, superlattice core, half-ring lasers. The laser excitation is measured at 801 nm, and the internal power of the on-chip pump is estimated to be in excess of 200 mW in a full-ring, after accounting for optical routing, linear, bending and nonlinear losses. We have been able to conclude that our designed OPO and frequency converter is just feasible with the performance achieved in different components.

# Acknowledgements

Firstly, I would like to thank my supervisors, Prof. David C. Hutchings and Dr. Barry M. Holmes, for their help and experience, which were essential in the completion of this work. I pay my gratitude to Prof. Hutchings, for his guidance which started even before I came to this country, and his support when it was required the most. I am personally thankful to Dr. Holmes for his continual encouragement (almost every day), and his incredible assistance, at work, and more importantly, at the social level. Similarly, I would like to thank Dr. Corrie D. Farmer for his expert advice in some portions of this work.

I would like to thank Prof. J. Stewart Aitchison, Prof. Amr S. Helmy, and Sean J. Wagner at the University of Toronto, for collaborating on this work, and providing us with the nonlinear optical measurements.

I would like to thank all my colleagues and fellow postgraduate students, for each and every bit of their help. Many thanks to Masoud, Gabor, Steven, Antonio, Piotr, Michael, Carla, Giuseppe, Yasir, Jehan, Shahid, Azhar, Kamran, Lianping, Ali Khokhar, Rafal, Basudev, Cheng, and Moss. I wish good luck to all of you.

I am thankful to the technical assistance of Mr. William Ward and Mr. Thomas Reilly, for arranging the necessary tools and equipments, and making the experimental labs available to me all the time. I am thankful to all the technical support staff of the James Watt Nanofabrication Centre. Especially, the dry-etch team, Mark, Ronnie, Dougie, and Eve, for expediting my work most of the times.

Being an international student could be challenging sometimes; however, I would like to pay my sincere regards to some good friends I made in these years. I would like to thank Dr. Nadeem Javid, for being a great companion and a true friend.

I am hugely indebted to the love of my family. It is the emotional support and the affection of my parents which brings me this achievement, and I pray for this affection to remain as a life long guidance.

I am thankful to the National University of Sciences and Technology, Islamabad, Pakistan, for funding my Ph.D. studies. I should also acknowledge the partial assistance which I received from the University of Glasgow.

Above all, I am thankful to God, who gave me health and strength to accomplish another milestone in my life.

# Contents

Abstract .....	i
Acknowledgements .....	ii
Contents .....	iv
List of Figures .....	vii
List of Tables .....	xiii
Abbreviations .....	xiv
List of Publications .....	xvi
<i>Chapter 1</i> Introduction .....	1
1.1 Mid-Infrared Technologies .....	1
1.1.1 Lead-salt Lasers .....	1
1.1.2 Quantum Cascade Lasers .....	2
1.1.3 Nonlinear Optical Frequency Conversion.....	3
1.1.4 Applications .....	4
1.2 Optical Parametric Oscillator     (principle of operation) .....	7
1.3 Objectives and Motivation .....	8
1.4 Device Overview.....	10
1.5 Thesis Outline .....	12
<i>Chapter 2</i> Literature Review and Theoretical Background .....	15
2.1 Optical Nonlinearity.....	15
2.1.1 Induced Polarization .....	16
2.1.2 Induced Electric Field .....	18
2.1.3 Phase Matching .....	19
2.1.4 Parametric Oscillation.....	21
2.2 Multimode Interference.....	22
2.2.1 General Interference.....	23
2.2.2 Restricted interference .....	27
2.3 Semiconductor Laser.....	27
2.3.1 Double Heterostructure (The birth of modern semiconductor lasers) .....	28
2.3.2 Quantum Well .....	30

2.3.3 Multiple Quantum Well .....	32
2.3.4 Superlattice Heterostructure.....	33
<i>Chapter 3</i> Quasi Phase Matching Waveguides.....	35
3.1 Material .....	35
3.1.1 Superlattice Heterostructure.....	35
3.1.2 Passive Wafers .....	37
3.2 Quantum Well Intermixing (QWI) .....	38
3.2.1 Sputtered Silica Tests.....	40
3.2.2 Ion Implantation Tests .....	42
3.3 Second Harmonic Generation (SHG) .....	49
3.3.1 QPM Period.....	50
3.3.2 Ion Implantation Mask.....	51
3.3.3 Protective Dielectric Cap .....	54
3.3.4 Device Design .....	55
3.4 Sample Fabrication .....	57
3.5 Characterization .....	58
3.5.1 Type-I SHG.....	58
3.5.2 Type-II SHG .....	63
3.5.3 Difference Frequency Generation (DFG) .....	66
3.6 Fabrication Process Optimization .....	68
3.6.1 Improved Gold Electroplating .....	72
3.6.2 Resist Contamination Removal.....	73
3.6.3 Ti Layer Contamination Removal.....	74
<i>Chapter 4</i> Di-chroic Multimode Interference Coupler .....	79
4.1 Coupler Design .....	79
4.2 Dry Etch Optimization .....	82
4.2.1 RIE with Laser Reflectometry .....	83
4.2.2 RIE Lag .....	84
4.3 Simulations and Tests near Band-gap.....	85
4.4 Simulations and Tests near Half-Band-gap .....	89
4.5 Tapered Coupler.....	91
<i>Chapter 5</i> Superlattice Lasers .....	94
5.1 Materials.....	94

5.2 Material Tests.....	103
5.2.1 Transmission Line Measurement (TLM).....	104
5.2.2 Broad Area Lasers (BAL).....	108
5.3 Ridge Waveguide Lasers .....	112
5.3.1 Device Design .....	113
5.3.2 Fabrication Process .....	114
5.3.3 Basic Device Characterization (Annealed semiconductor chip).....	121
5.3.4 Material Parameters .....	125
5.3.5 Gain Calculation .....	127
5.3.6 Spectrum Analysis .....	130
5.3.7 As-grown Semiconductor Chip.....	132
5.4 Resonant Tunneling in Superlattices.....	133
5.4.1 Energy Band Calculation .....	134
5.4.2 Experiments .....	137
<i>Chapter 6 Monolithically Integrated Devices</i> .....	139
6.1 Ring Design.....	139
6.2 Coupler Simulations Revisited.....	145
6.3 Integrated OPO Design .....	146
6.4 Integrated Frequency Converter Design .....	147
6.5 Integrated Chip.....	148
6.6 Monolithic Integration Demonstrated.....	150
<i>Chapter 7 Conclusions &amp; Future Recommendations</i> .....	153
APPENDIX I.....	I
APPENDIX II .....	II
APPENDIX III.....	VIII
REFERENCES.....	XIII

# List of Figures

Figure 1-1 [15] – Intra-cavity singly-resonant OPO for mid-infrared wavelengths generation.....	7
Figure 1-2 [34] – Simplified schematic of an OPO demonstrated using OPG-GaAs.....	9
Figure 1-3 [22] – The designed optical parametric oscillator.....	11
Figure 2-1 – Linear and nonlinear response of a medium. ....	16
Figure 2-2 [43] – Dipoles which result in the induced polarizations in a medium.....	16
Figure 2-3 [44] – Quasi phase matching. ....	20
Figure 2-4 – Phase matched second order nonlinear processes. ....	20
Figure 2-5 [54] – Field propagation in a multimode cavity. ....	24
Figure 2-6 – Simulated length of a directional coupler for the cross operation (775 nm wavelength), the inset shows the device geometry. ....	25
Figure 2-7 [56] – Design of a MMI coupler with length $L = M/N (3L_{\pi}/a)$ . ....	26
Figure 2-8 [64] – Double heterostructure laser under applied bias.....	28
Figure 2-9 [76] – Absorption spectra for quantum wells of different thicknesses, measured at 2 K (Permission to reproduce this figure has been granted by The American Physical Society).....	31
Figure 2-10 [80] – GRIN-SCH energy level schematic.....	31
Figure 2-11 [86] – MQW structure which achieved 2.4 mA threshold current at the room-temperature.....	32
Figure 2-12 [93] – Sequential resonant tunneling: (a) from the ground state into the first excited state, and (b) from the ground state into the second excited state. ....	34
Figure 3-1 – Schematic conduction band diagram of a six period 14 ML GaAs / 14ML $\text{Al}_{0.85}\text{Ga}_{0.15}\text{As}$ superlattice with moduli-squared wave-function for the lower edge of $E_0$ mini-band (the diagram is only for the illustration purpose and none of the energies are up to the scale). ....	36
Figure 3-2 – Cross-sectional scanning electron microscope image of the material.....	39
Figure 3-3 – Photoluminescence measurements setup. ....	41
Figure 3-4 – Photoluminescence measurements of sputtered silica induced QWI at different annealing temperatures – annealing time is 60 s (solid lines are a smoothed fit to the data).....	41

Figure 3-5 – Ion implantation induced QWI, (a) Disorder cluster created in the result of high energy ion collisions, (b) The inter-diffusion of group III atoms increase the band-gap of intermixed material. ....	43
Figure 3-6 – Photoluminescence measurements of ion implantation induced QWI at different annealing temperatures – annealing time is 60 s (solid lines are a smoothed fit to the data).....	44
Figure 3-7 – linear loss measurements for different implantation doses, samples were annealed at 775 °C for 60 s. ....	45
Figure 3-8 – (a) Top view of the periodic electroplated gold (designed as: 60% masked / 40% exposed), (b) Cross-sectional SEM micrograph of the same duty cycle after ion implantation. ....	47
Figure 3-9 – Simulated penetration of As <sup>2+</sup> ions in gold. ....	52
Figure 3-10 – Cross-sectional view of the developed photolithography. ....	53
Figure 3-11 – Cross-sectional view of a dose test performed using 15%15% PMMA. .	55
Figure 3-12 – Designed E-beam mask for QPM samples.....	56
Figure 3-13 - Mode profile of the designed waveguide at 1550 nm.....	56
Figure 3-14 – SEM image of the periodic gold mask created over a test sample.....	57
Figure 3-15 – Cross-sectional view of the final sample – dark shaded HSQ resist is visible.....	58
Figure 3-16 – SHG phase matching polarization configurations.....	59
Figure 3-17 – Schematic diagram of the type-I SHG measurements setup. ....	60
Figure 3-18 [130] – Pulse spectrum of the phase matched type-I SHG – the curve resembles Sinc <sup>2</sup> -function which is consistent with the phase-matched process. ....	61
Figure 3-19 [131] – Tuning curve for CW SHG.....	62
Figure 3-20 [131] – Filtered tuning curves for CW SHG with increasing input powers. ....	63
Figure 3-21 – Schematic diagram of the type-II SHG measurements setup.....	64
Figure 3-22 [133] – Tuning curve for type-II SHG. ....	65
Figure 3-23 – Mode solution for TE polarized band-gap excitation.....	66
Figure 3-24 [135] – The output spectra of measured DFG – the signal wavelengths are between 1535-1555 nm, and the arrows indicate the generated idler wavelengths.....	68
Figure 3-25 – The fabrication process flow chart for a monolithically integrated device. The left section provides the process if one wishes to achieve only the passive nonlinear	

waveguides; however, the right section continues with the fabrication to achieve the on-chip lasers in the case of an active device.....	70
Figure 3-26 – SEM image of a test sample – no GaAs cap removal etch.....	71
Figure 3-27 – SEM image of a partially gold etched sample.....	74
Figure 3-28 – SEM image of a gold etched sample – masked region and exposed region are visible. ....	75
Figure 3-29 – Edge-on view of the sample partially exposed to Ti wet-etch. ....	76
Figure 3-30 – Top view of a sample exposed to non-HF-based Ti wet-etch. ....	77
Figure 4-1 – Required design: (a) cross coupler near the band-gap (775 nm), (b) bar coupler near the half-band-gap (1550 nm).....	80
Figure 4-2 – (a) Mode solutions of the designed waveguide structure for the band-gap and the half-band-gap-wavelengths, (b) the designed access waveguide structure. ....	81
Figure 4-3 –Recorded plot of a real time RIE signal (the oscillations in the signal are seen as the etch depth increases with time).....	83
Figure 4-4 – The measured RIE etch depth against the number of oscillations recorded. ....	84
Figure 4-5 – Cross-sectional SEM micrographs of the small gaps depicting RIE lag....	85
Figure 4-6 – Simulated cross operation at the excitation wavelength of 780 nm (MMI cavity dimensions: 6.5 $\mu\text{m}$ wide, 220 $\mu\text{m}$ long, and 1.35 $\mu\text{m}$ deep etched). ....	86
Figure 4-7 – SEM image of a test sample with various coupler lengths. ....	87
Figure 4-8 – Measurement setup for the near band-gap wavelengths. ....	87
Figure 4-9 – Measurements for 797 nm wavelength, and simulations for 780 nm wavelength (quasi-TE polarized light in both cases). Solid lines are a smoothed fit to the data. Solid circles represent the measured data, and the empty circles are the simulated data. ....	88
Figure 4-10 –Cross + bar state power. ....	89
Figure 4-11 – Simulated bar operation at the excitation wavelength of 1560 nm. ....	90
Figure 4-12 – Measured and simulated performance of the coupler for 1560 nm wavelength (quasi-TE polarized light). Solid lines are a smoothed fit to the data. Solid circles and squares represent the measured data, and the empty circles are the simulated data. ....	91
Figure 4-13 – Tapered couplers, (a) tapers have been introduced in the inner side of the access waveguides, (b) SEM images of the fabricated couplers.....	92

Figure 4-14 – Measured performance of the tapered coupler for the half-band-gap wavelength (quasi-TE polarized light). Solid line is a smoothed fit to the data, solid circles and squares represent the measured data. ....	93
Figure 5-1 – PL map of the wafer BMH4. ....	97
Figure 5-2 – The real time growth information for BMH6. ....	99
Figure 5-3 – Left a) A mesa etch section with 5 contact pads having multiple gaps in between them; Right b) RTA profile of the annealing treatment provided to the samples after mesa definition. ....	104
Figure 5-4 – Schematic of the four-probe station measurement. The bias voltage is applied across VF & VM, and the current flow is measured from IF to IM. ....	105
Figure 5-5 – The measured resistances’ scatter, plotted against their respective pads separation. ....	107
Figure 5-6 – V-I curves for the measured BAL. ....	109
Figure 5-7 – TLM, current flow measurement (BMH4). ....	109
Figure 5-8 – L-I-V curves for the BAL (BMH9). ....	110
Figure 5-9 – L-I-V curves for the BAL (BMH9 annealed at 775 °C). ....	111
Figure 5-10 – V-I curves for the BAL, fabricated with as-grown and annealed (775 °C) BMH9_REV. ....	111
Figure 5-11 – Left a) Effective refractive index calculations with varying the waveguide width (the upper cladding has been etched completely). Right b) The proceeded ridge structure (also highlighted by the green markers in (a)). ....	113
Figure 5-12 – Mode profile for 3 μm wide waveguide, etched down to the core. ....	114
Figure 5-13 – Optical micrograph of an exposed and developed E-beam registration job. ....	117
Figure 5-14 – The edge-on SEM image of an etched ring (HSQ mask is visible on the waveguide). ....	118
Figure 5-15 – Cross-sectional SEM image of a 3 μm wide ridge waveguide laser. ....	121
Figure 5-16 – Optical micrograph of a fabricated chip, using the annealed material. ...	122
Figure 5-17 – L-I curves for various cavity length ridge waveguide lasers (3 μm wide ridges). ....	123
Figure 5-18 – L-I curves for different ridge widths (500 μm long FP cavities). ....	124
Figure 5-19 – Room-temperature CW threshold current density for various FP cavity lengths (solid lines are a smoothed fit to the data). ....	124

Figure 5-20 – The external differential quantum efficiency plotted against the cavity length.....	127
Figure 5-21 – Gain at threshold is plotted against the $J_{nom}$ .....	128
Figure 5-22 – a) The calculated gain for an un-doped GaAs [158] (Permission to reproduce this figure has been granted by IEEE), b) Gain calculated for BMH9 using the experimentally obtained parameters. ....	129
Figure 5-23 – Excitation wavelength of 801 nm for a 500 $\mu\text{m}$ long annealed FP ridge. ....	130
Figure 5-24 – Measured excitation wavelength using pulsed injection for: (a) As-grown BAL, (b) Annealed BAL.....	132
Figure 5-25 – V-I curves for the as-grown diodes in comparison with the annealed diode.....	133
Figure 5-26 – Schematic representation of BMH9/BMH9_REV.....	135
Figure 5-27 – Schematic representation of the calculated conduction band under the application of an electric field in BMH9. ....	136
Figure 5-28 – I-V curves for the resonant tunneling measurements in BMH9_REV which has 150 nm thick superlattice core. ....	137
Figure 6-1 – The designed E-beam pattern for the half ring lasers.....	140
Figure 6-2 – The bending losses calculated using the simulations. Solid lines are a smoothed fit to the data. The solid circles and squares are the values calculated using measurements from the half ring lasers, and the empty circles represent the simulated data. ....	142
Figure 6-3 – L-I curves of the half ring lasers with different ring radii (all rings had the same etch depth of $1.3 \pm 0.07$ ). ....	142
Figure 6-4 – Losses of the ring cavity.....	143
Figure 6-5 – The internal power estimates of the rings before the saturation effects become significant. All the rings are biased at same current density of $6.6 \text{ kA/cm}^2$ ....	144
Figure 6-6 – Cross coupler for the 801 nm laser excitation (MMI cavity dimensions: 6.5 $\mu\text{m}$ wide, 220 $\mu\text{m}$ long, and 1.35 $\mu\text{m}$ deep etched). ....	145
Figure 6-7 – The designed integrated OPO. ....	146
Figure 6-8 – Simulated directional coupler for the longer wavelengths, (a) cross-sectional view of the structure, (b) 350 $\mu\text{m}$ long coupler is estimated to couple out 20% of the power. ....	147

Figure 6-9 – The designed nonlinear optical frequency converter for 1.5 $\mu\text{m}$ telecommunication band. ....	148
Figure 6-10 – The designed semiconductor chip which includes monolithically integrated devices.....	149
Figure 6-11 – The SEM image of the gold mask for the integrated DFG. ....	150
Figure 6-12 – The SEM image of the deep etched waveguide. ....	151
Figure 6-13 – The IR image of an integrated DFG being tested.....	151

## List of Tables

Table 1-1 – Resource distribution map. ....	14
Table 3-1 – Intermixing process selection criteria.....	48
Table 3-2 – Gold electroplating tests. ....	73
Table 5-1 – Designed active wafer BMH3. ....	95
Table 5-2 – Designed active wafer BMH4. ....	96
Table 5-3 – Designed active wafers BMH5 & BMH6.....	98
Table 5-4 – Designed active wafer BMH7. ....	101
Table 5-5 – Designed active wafer BMH8 (a/b).....	102
Table 5-6 – Designed active wafer BMH9. ....	103
Table 5-7 – Measured specific contact resistances of the different active materials. ....	107
Table 6-1 – Bending losses for various rings.....	141
Table 6-2 – The ring parameters used for the internal power calculation. ....	144

# Abbreviations

BAL	Broad Area Laser
CW	Continuous Wave
DD-QPM	Domain Disordered Quasi Phase Matching
DFG	Difference Frequency Generation
DFB	Distributed Feedback
ECA	Energy levels Calculation in GaAs–AlGaAs
EDFA	Erbium Doped Fiber Amplifier
EDTA	Ethylenediaminetetraacetic Acid
EL	Electroluminescence
EPSRC	Engineering and Physical Sciences Research Council
FP	Fabry-Pérot
FSR	Free Spectral Range
FWHM	Full Width at Half Maximum
GRIN-SCH	Graded Index Separate Confinement Heterostructure
HF	Hydrofluoric
HSQ	Hydrogen Silsesquioxane
ICP	Inductive Coupled Plasma
IFVD	Impurity Free Vacancy Disordering
IID	Impurity Induced Disordering
IPA	Isopropyl Alcohol
I-V	Current-Voltage
JWNC	James Watt Nano Fabrication Centre
KI	Potassium Iodide
L-I	Light-Current
L-I-V	Light-Current-Voltage
MBE	Molecular Beam Epitaxy
MIBK	Methyl Isobutyl Ketone
ML	Monolayer
MMI	Multimode Interference
MOCVD	Metalorganic Chemical Vapour Deposition

MOVPE	Metalorganic Vapour Phase Epitaxy
MPA	Modal Propagation Analysis
MQW	Multiple Quantum Well
NDR	Negative Differential Resistance
OPG	Orientation Patterned Growth
OPO	Optical Parametric Oscillator
OSA	Optical Spectrum Analyzer
PECVD	Plasma Enhanced Chemical Vapour Deposition
PL	Photoluminescence
PMMA	Poly Methyl Methacrylate
PTFE	Polytetrafluoroethylene
QPM	Quasi Phase Matching
QWI	Quantum Well Intermixing
RIE	Reactive Ion Etching
RPM	Revolutions per minute
RO	Reverse Osmosis
RT	Resonant Tunneling
RTA	Rapid Thermal Annealing
SEM	Scanning Electron Microscope
SHG	Second Harmonic Generation
TE	Transverse Electric
TLM	Transmission Line Measurement
TM	Transverse Magnetic
TMAH	Tetramethylammonium Hydroxide
TMI	Two Mode Interference
TRIM	Transport of Ions in Matter
V-I	Voltage-Current
WDM	Wavelength Division Multiplexing

# List of Publications

Journal:

**Usman Younis**, Barry M. Holmes, David C. Hutchings and John S. Roberts, “Towards Monolithic Integration of Nonlinear Optical Frequency Conversion,” IEEE Photonics Technology Letters, vol. 22, pp. 1358-1360, Sep. 15 2010.

A. S. Helmy, P. Abolghasem, J. S. Aitchison, Bhavin J. Bijlani, Junbo Han, B. M. Holmes, D. C. Hutchings, **U. Younis**, and S. J. Wagner, “Recent Advances in Phase-Matching Second Order Nonlinearities in Monolithic Semiconductor Waveguides,” Laser & Photonics Reviews, DOI: 10.1002/lpor.201000008, Sep. 17 2010.

David C. Hutchings, Sean J. Wagner, Barry M. Holmes, **Usman Younis**, Amr S. Helmy, and J. Stewart Aitchison, “Type-II quasi phase matching in periodically intermixed semiconductor superlattice waveguides,” Optics Letters, vol. 35, pp. 1299-1301, Apr. 15 2010.

Sean J. Wagner, Barry M. Holmes, **Usman Younis**, Amr S. Helmy, J. Stewart Aitchison, and David C. Hutchings, “Continuous wave second-harmonic generation using domain-disordered quasi-phase matching waveguides”, Applied Physics Letters, vol. 94, pp. 151107, Apr. 14 2009.

Sean J. Wagner, Barry M. Holmes, **Usman Younis**, Amr S. Helmy, David C. Hutchings, and J. Stewart Aitchison, “Controlling Third-Order Nonlinearities by Ion-Implantation Quantum-Well Intermixing,” IEEE Photonics Technology Letters, vol. 21, pp. 85-87, Jan. 15 2009.

## Conferences:

S. J. Wagner, S. Chaitanya Kumar, O. Kokabee, B. M. Holmes, **U. Younis**, M. Ebrahim-Zadeh, D. C. Hutchings, A. S. Helmy, and J. S. Aitchison, "Performance and Limitations of Quasi-Phase Matching Semiconductor Waveguides with Picosecond Pulses," Photonics North, Niagara, Canada, Jun. 2010.

David C. Hutchings, **Usman Younis**, Barry M. Holmes, Sean J. Wagner, Amr S. Helmy and J. Stewart Aitchison, "Developing Integrated Optical Frequency Convertors and Generators on a Semiconductor Chip (Invited)," Photonics North, Niagara, Canada, Jun. 2010.

S. J. Wagner, I. Sigal, A. S. Helmy, J. S. Aitchison, **U. Younis**, B. Holmes, and D. C. Hutchings, "Difference Frequency Generation in Domain-Disordered Quasi-Phase-Matched Semiconductor Waveguides," Conference on Lasers and Electro-optics (CLEO), San Jose, CA, May 2010.

**Usman Younis**, Barry M. Holmes, David C. Hutchings and John S. Roberts, "Towards Monolithic Integration of Nonlinear Optical Frequency Conversion," 15<sup>th</sup> European Conference on Integrated Optics (ECIO), Cambridge, UK, Apr. 2010.

**Usman Younis**, Barry M. Holmes, David C. Hutchings, Sean J. Wagner, Amr S. Helmy and J. Stewart Aitchison, "Optical Frequency Generation and Conversion in Domain-Disordered Quasi-Phase-Matched Semiconductor Waveguides," Nonlinear Photonics in Micro- and Nanostructure, Institute of Physics, London, UK, Dec. 2009.

B.M. Holmes, **U. Younis**, D. C. Hutchings, S. J. Wagner, A. S. Helmy, and J. S. Aitchison, "Type-II Quasi-Phase-Matched Second Harmonic Generation in Domain-Disordered Semiconductor Waveguides," Conference on Lasers and Electro-Optics (CLEO), Baltimore, MD, Jun. 2009.

**Usman Younis**, Barry Holmes and David C. Hutchings, “Experiments toward the Integrated OPO through Periodic  $\chi^{(2)}$  Modulation,” Mini-symposium on Periodically-Modulated and Artificially Hetero-Structured Devices (Rank Prize Funds), Grasmere, UK, May 2009.

J. S. Aitchison, S. J. Wagner, A. S. Helmy, B. M. Holmes, **U. Younis**, and D. C. Hutchings, “Nonlinear Superlattice Waveguides,” Photonics North, Quebec City, Canada, May 2009.

S. J. Wagner, B. M. Holmes, **U. Younis**, A. S. Helmy, D. C. Hutchings, and J. S. Aitchison, “Quasi-phase matched continuous wave second harmonic generation in periodically intermixed GaAs/AlGaAs superlattice waveguides,” IEEE Lasers and Electro Optic Society (LEOS) meeting, Newport Beach, CA, Nov. 2008.

S. J. Wagner, A. S. Helmy, J. S. Aitchison, **U. Younis**, B. M. Holmes and D. C. Hutchings, “Control of the Third-Order Nonlinearities in a GaAs/AlGaAs Superlattice by Ion Implantation Quantum Well Intermixing,” Conference on Lasers and Electro-Optics (CLEO), San Jose, CA, May 2008.

# *Chapter 1*

## Introduction

There is an increasing demand to develop tunable coherent sources for sensing applications in the 2-20  $\mu\text{m}$  region of the electromagnetic spectrum, in which most molecules find their vibrational resonances [1]. This effort has been complemented by the industrial need to trace gases which are hazardous for the working environment [2-3]. The applications for such mid-IR sources extend further into tracing pollutants in the environment [4], and are finding increasing demand in air quality control in closed environments, e.g. hospitals and large buildings. Other applications which can be generally placed in this category are security, forensics, clinical analysis, and food monitoring.

### 1.1 Mid-Infrared Technologies

The state of the art tunable laser based sources suitable for the above given applications have been realized in the form of diode lasers, i.e., lead-salt lasers, quantum cascade lasers, and others. In addition to this, state of the art nonlinear optical frequency conversion sources developed for mid-IR generation include optical parametric oscillators and difference frequency generators.

#### 1.1.1 Lead-salt Lasers

Lead-salt lasers are based on IV-VI semiconductor materials which can cover a wide range of emission wavelengths between 3-30  $\mu\text{m}$ . These lasers have been successfully employed for numerous sensing applications; however, the laser action in these devices

is limited to operation at cryogenic temperatures which makes them expensive to use. The power levels are limited up to several hundred microwatts and the emission suffers from multimode behavior. Moreover, lead-salt lasers are limited by the much higher threshold current densities required for continuous wave operation, which has been so far achieved only at low temperatures [5]. Their beam quality and the spectral reproducibility have also been reported as non ideal [3]. Therefore, pulsed operation of these devices has been used for applications which do not require high spectral resolution [5].

### 1.1.2 Quantum Cascade Lasers

The basic idea of quantum cascade lasers (QCL) originated as early as 1971; however, the first demonstration was achieved later in 1994 [6]. These lasers are not dependent upon the band-gap transitions as in the case of conventional semiconductor lasers. The photon emission is achieved by inter sub-band transitions which can be engineered to any desired energy in conduction band of these uni-polar devices. The cascade of equal energies allows the generation of multiple photons from a single electron which results in an increased optical power. Additional benefit includes the mature fabrication and material technologies developed for III-V semiconductors which are used in QCL.

Quantum cascade lasers have an advantage to circumvent the problems which lead-salt lasers face, and they provide considerable output powers while maintaining single-longitudinal-mode operation. The research in QCL has seen a massive ascend after the achievement of room-temperature continuous wave (CW) operation in a buried heterostructure [7]. This demonstration opened new opportunities for QCL based semiconductor lasers to cover the mid-IR region, e.g., room-temperature CW emission in single-mode at 4.8  $\mu\text{m}$  is reported in [8], and CW emission above 400 K at 8.38  $\mu\text{m}$  is reported in [9]. High power room-temperature CW emission (4.6  $\mu\text{m}$ ) with powers up to few W's has also been achieved in InP based QCL [10-11].

Recent demonstrations have reported wide tunability for QCL, e.g., a grating coupled external cavity high power QCL with  $166\text{ cm}^{-1}$  tuning bandwidth centered at  $4.6\text{ }\mu\text{m}$  is reported in [12], and external cavity QCLs with  $155\text{ cm}^{-1}$  and  $182\text{ cm}^{-1}$  tuning bandwidths centered at  $5.3\text{ }\mu\text{m}$  and  $8.4\text{ }\mu\text{m}$ , respectively, are reported in [13]. In addition to this, a more compact tunable device is demonstrated in an array of distributed feedback (DFB) buried heterostructure QCL lasers, each with a different period, to provide tunability in  $8.7\text{-}9.4\text{ }\mu\text{m}$  for spectroscopic applications [14].

These demonstrations show that quantum cascade lasers are highly sophisticated for mid-IR generation in contrast to lead-salt lasers. However, one must recognize that the emission is limited by the inter-sub-band splitting which is defined at the wafer growth stage.

### 1.1.3 Nonlinear Optical Frequency Conversion

Another approach to realize tunable long wavelength sources used in chemical sensing is through nonlinear optical frequency conversion. The principle advantage in this technique is the flexibility to select a desired band of wavelengths, which depends upon the phase matching period, and subsequent tuning is achieved with a tunable pump source. Initially, nonlinear frequency conversion was achieved by exciting a nonlinear material with a high power, optically-pumped source, which resulted in systems with a large footprint [15]. However, contemporary sources employ a high power diode lasers to excite the nonlinear crystals, and hence they achieve a more compact form [2, 16-17].

The second-order nonlinear optical frequency conversion process can be achieved either by placing the nonlinear material in a cavity, i.e., optical parametric oscillator (OPO) [16, 18], or it can be achieved by pumping the nonlinear material by two sources, i.e., difference frequency generation (DFG) [1, 19] [20] [4] [21]. The bulk crystals (e.g., KTP, LiNbO<sub>3</sub>, KTA, etc.) which are employed for these nonlinear interactions have a second order nonlinear coefficient of a few  $\text{pmV}^{-1}$ ; therefore, much higher pump

powers up to few W's are required to generate sufficient powers at the longer wavelengths in the case of an OPO. However, similar three-wave-mixing can be achieved in DFG using two different pump sources with powers in the hundreds of mW range, at the cost of added complexity in managing two input pumps. Nevertheless, both DFG and OPO have been successfully employed for the spectroscopic detection of trace gases; especially, the gas imaging OPO based devices used for industrial use in methane detection [2]. As much as there is an industrial demand for these mid-IR sources, they typically retail at hundreds of thousands of GB pounds [22].

In the recent past, OPO technology has also been used to generate the THz emission at room-temperature which is in great demand for THz imaging applications (e.g., to detect concealed weapons) [23-24]. The benefit of employing OPO over QCL in THz generation is the room-temperature operation which has not been achieved in the latter by 2009 [25].

#### 1.1.4 Applications

A significant number of demonstrations have been reported over the last few decades in the development of mid-IR technologies which have benefited numerous environmental and industrial needs. Some examples from the literature are presented in order to identify these achievements, and establish the importance of a continual requirement for such sophisticated and highly sensitive systems.

Lead-salt lasers have been used in numerous sensing systems, and one of such systems is reported in [26]. This mid-IR (7.8  $\mu\text{m}$ ) high-frequency modulation spectrometer has been developed to detect methane ( $\text{CH}_4$ ) concentrations in ambient atmosphere.

Quantum cascade lasers are more promising in high sensitivity and broad-band spectroscopic applications when compared to lead-salt lasers. A few examples of the systems which have employed QCL are given next:

- 1) A wavelength modulation spectrometer to detect N<sub>2</sub>O and CH<sub>4</sub> is given in [27]. The system performs absorption spectroscopy in the chemical fingerprint wavelengths near 8 μm using a DFB QCL.
- 2) Absorption spectroscopy of the ambient air has been performed to detect CH<sub>4</sub> and N<sub>2</sub>O using a near room-temperature pulsed DFB QCL which emits ~8 μm wavelengths [28].
- 3) A cryogenically cooled tunable QCL (8 μm emission wavelength) has been used measure CH<sub>4</sub> and N<sub>2</sub>O up to 20 km in the stratosphere [29].
- 4) A high resolution broadband absorption spectroscopy of Ethanol, NO and N<sub>2</sub>O has been performed in [13]. The system employs an external cavity tunable QCL with tuning bandwidths in excess of 150 cm<sup>-1</sup>.

As identified in the previous section, nonlinear optical frequency converters are highly promising in the generation of mid-IR wavelengths. A few examples of these converters are given next:

- 1) A compact tunable difference frequency generation source has been reported in [20], which produces wavelengths near 5 μm. The output powers up to 0.2 μW have been used for the absorption spectroscopy of carbon-monoxide (CO).
- 2) The detection of formaldehyde (H<sub>2</sub>CO), which is a well known pollutant, has been performed using DFG [4]. The output powers up to 4.7 μW have been produced in this case with ~3.5 μm emission wavelengths.
- 3) Mid-IR spectroscopy has been performed for the trace gases using DFG in [19]. Tunable radiations between 3.33-3.73 μm and 2.65-2.90 μm wavelength ranges have been produced to detect methane and water vapors.
- 4) An interesting experiment of guided-wave difference frequency generation in periodically poled lithium-niobate (PPLN) waveguides is reported in [21]. The idler wavelengths produced between 3.43-3.73 μm have been used to perform high resolution spectroscopy of methane.
- 5) The long-wave IR (8-15 μm) is considered to be more useful than the mid-wave IR (3-5 μm), because of its lower absorption in the atmospheric water vapor window. The nonlinear optical frequency converters which employ conventional ferroelectrics are limited by their material absorption to generate long-wave IR.

GaAs has gained much attention due to its wide transparency range which extends up to 17  $\mu\text{m}$ , and its higher second order nonlinearity. In these lines, a tunable long-wave IR source has been demonstrated in [3], which produces wavelengths between 7.95-8.6  $\mu\text{m}$  using diode-pumped DFG in orientation patterned grown GaAs.

- 6) Gas imaging systems are a very effective tool for monitoring industrial leaks, and they can also be used in oil & gas explorations. One such system is reported in [2], which has been developed using a pump enhanced OPO. Output powers up to 50 mW are able to scan an area of 4  $\text{m}^2$  at a distance of 3 m. The broad spectral coverage (3.18-3.50  $\mu\text{m}$ ) is useful in the spectroscopic detection of methane and other gases.
- 7) A backscatter-absorption, portable gas-imaging system has been presented in [3]. In this system a continuous wave diode-pumped Nd:YAG laser has been used as a pump source to excite a PPLN crystal, which creates a singly resonant, continuous wave OPO. The PPLN crystal has phase matching periods in the range of 29.3-30.1  $\mu\text{m}$ , and the adjustment of its position produces idler tuning between 3.18-3.53  $\mu\text{m}$ . The image detection optics creates images at the rate of 30 frames per second. A shoulder-borne version of this system has also been developed using a fiber amplified, continuous wave, diode-pumped Nd:YAG laser.
- 8) Probably one of the most important applications of OPO based system has been reported in [30]. The tunable source produces wavelengths between 6-8  $\mu\text{m}$ , and it has been used to detect a variety of explosives which include: TNT, TATP, RDX, PETN, and Tetryl.

The applications of nonlinear optical frequency conversion are equally important in near-IR as in the case of mid-IR. For example, short wavelengths are required in the detection of  $\text{CO}_2$  (which is a greenhouse gas) and monitoring air quality and carbon sequestration storage sites. Modern wavelength division multiplexing (WDM) telecommunication networks require all-optical wavelength switching in the backbone, and nonlinear optical frequency conversion is one way to achieve this switching. The feasibility of a fully integrated optical frequency conversion source for 1.5  $\mu\text{m}$  telecommunication band is recently reported by us in [31].

## 1.2 Optical Parametric Oscillator (principle of operation)

In order to understand the principle of operation, consider the case of an intra-cavity continuous wave (CW) singly-resonant OPO [15], in which the oscillations cavity is created within the pump laser cavity using the conventional optics, figure 1-1 [15]. Singly-resonant means that the OPO cavity is formed only for signal oscillations. The tunable Ti:Sapphire laser acts as a pump source for the OPO, in which the pump near 800 nm wavelength produces the singly-resonant signal in 1.14-1.27  $\mu\text{m}$  range, and the idler is produced in the range of 2.23-2.73  $\mu\text{m}$ , using the periodically poled KTiOPO<sub>4</sub> (PPKTP). In an interesting experiment, using the same setup and placing a unidirectional device in the pump cavity, the OPO operation has been achieved in a ring configuration. A similar setup has been used to report the singly-resonant OPO operation using PPLN [32], and the nonlinear material KTiOAsO<sub>4</sub> (KTA) [18]. In each of these devices, the signal and the idler are produced with hundreds of milli-watts of output powers, and the mid-infrared wavelengths enable these devices to set a bench mark.

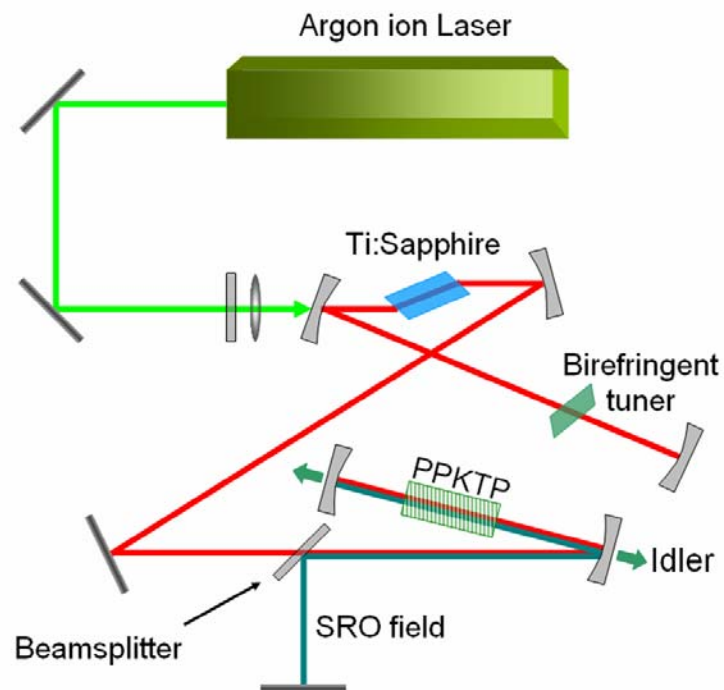


Figure 1-1 [15] – Intra-cavity singly-resonant OPO for mid-infrared wavelengths generation.

Using a similar approach to an intra-cavity OPO, in which a 1-W diode-pumped-Nd:YVO<sub>4</sub> source has been used to pump the PPLN, the idler wavelengths in 3.16-4.02  $\mu\text{m}$  have been produced [16]. A considerable reduction in the footprint was achieved in this case.

### 1.3 Objectives and Motivation

The objective of this investigation is to develop monolithically integrated mid-IR sources using the same technique of OPO, but employing III-V semiconductor as the nonlinear material. These semiconductors benefit from their large second order susceptibilities, e.g., the nonlinear coefficient ( $d_{14}$ ) for GaAs is about 5 times of the largest coefficient ( $d_{33}$ ) in LiNbO<sub>3</sub> at  $\lambda = 4.1 \mu\text{m}$  [33]. Further benefits of GaAs include: a very broad transparency range (0.9-17  $\mu\text{m}$ ), low absorption, very mature material/fabrication technologies, and most importantly, GaAs is a very attractive light generating source. It has been identified in the literature that the nonlinear interaction is improved in a waveguide, as compared to that of bulk crystals, because much higher irradiance is available over a sizeable interaction length [19, 21] [22]. All these benefits complement the realization of such sources with estimated out put powers up to few mW for the longer wavelengths, if the nonlinear material is placed inside the laser cavity. Therefore, the monolithic integration of the nonlinear waveguide and an on-chip pump source is an attractive route to achieve such powers.

The single chip OPO design which has been investigated in thesis can potentially benefit the mid-IR source market by considerably reducing the size and lowering the cost and power consumption currently required. Additionally, due to its small scale, many devices (each with a modest tunability) can be placed on the same semiconductor chip offering multiple frequencies and arraying of powers.

The motivation for selecting GaAs as a nonlinear material in our research arises from its successful use in OPO demonstrations. It should be mentioned at this point that the

nonlinear frequency conversion requires a necessary phase matching of different phase velocities (more on this has been presented in the next chapter), and the quasi phase matching (QPM) technique is usually employed in GaAs based systems. One such example, in which QPM has been achieved in orientation patterned growth (OPG) GaAs, is reported by K. L. Vodopyanov to demonstrate an OPO [34]. This domain reversed GaAs has a QPM period of  $61.2 \mu\text{m}$ , and with the pump wavelength near  $2 \mu\text{m}$ , the signal and the idler have been produced in  $2.28\text{-}3.08 \mu\text{m}$  and  $5.78\text{-}9.14 \mu\text{m}$  wavelength ranges, respectively. A simplified schematic of this experiment is given in figure 1-2 [34].

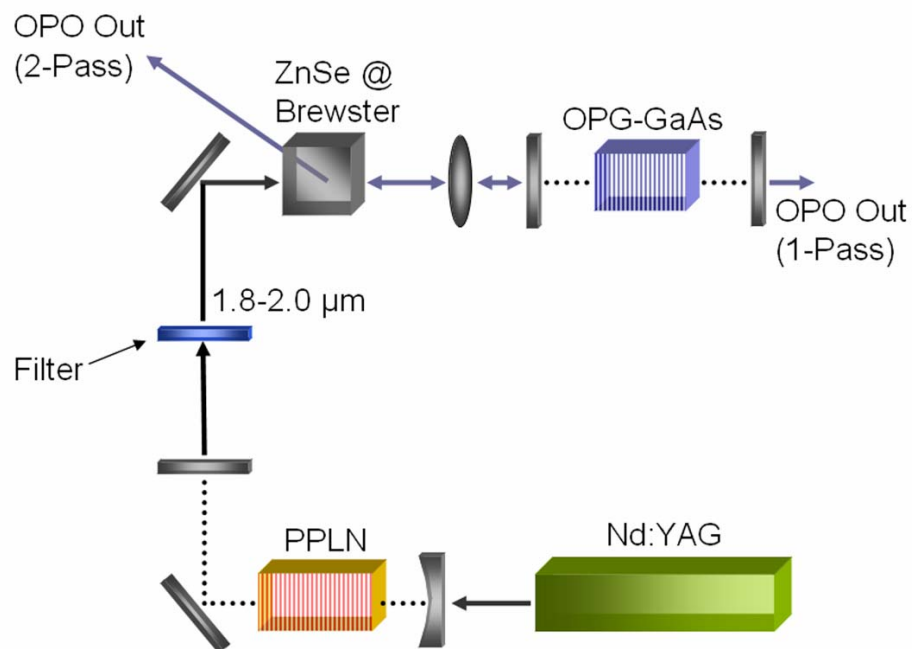


**Figure 1-2 [34] – Simplified schematic of an OPO demonstrated using OPG-GaAs.**

Using the OPG-GaAs, with the appropriate selection of QPM period, efficient THz generation ( $0.5\text{-}3.5 \text{ THz}$ ) has been demonstrated in an intra-cavity configuration [24]. These demonstrations make GaAs a highly competitive source for the generation of optical frequencies which are in a great demand for sensing applications. Additionally, with the use of difference frequency generation (DFG), and using  $775 \text{ nm}$  as a pump source, a monolithically integrated nonlinear optical frequency converter could be realized for application in  $1.5 \mu\text{m}$  telecommunication band [35].

We aim to develop devices operating within this band by monolithically integrating a nonlinear QPM waveguide with an on-chip pump source. The QPM in GaAs has been successfully demonstrated in passive OPG GaAs (given above), and also by employing wafer bonding techniques [36-37]. However, these techniques are limited by the significant challenge of integrating an on-chip laser. Additionally, the losses (e.g., interface losses, scattering, unequal domains, waveguide corrugation, etc.) incurred in these techniques have reduced their predicted nonlinear conversion efficiencies. We have employed post growth, quantum well intermixing (QWI) techniques to achieve QPM in our domain disordered GaAs/AlGaAs superlattice waveguides. These superlattices have been demonstrated to achieve a substantial modulation in the second order nonlinear coefficient  $\chi^{(2)}$ , which is necessary to achieve improved QPM [38]. This post growth technique benefits from its flexibility to achieve QPM over any desired period, unlike in the previously mentioned techniques which are limited to definition at the wafer growth stage. The added benefit which QWI brings is the ease of achieving active-passive integration, which is mandatory in the case of wavelength routing components in our OPO design, discussed in the next section. For similar reasons, the added complexity which arises in other active-passive integration techniques, e.g., selective area growth [39] and asymmetric twin-waveguide technology [40-41], has been circumvented by our design, in which we can achieve the required  $\chi^{(2)}$  modulation and the active-passive integration using a single step post-growth QWI.

In order to enhance the pump power available for nonlinear frequency conversion a ring laser has been employed in our design. It has been discovered in the literature that these lasers achieve a much higher internal power due to their higher quality factor  $Q$  as compared to that of conventional cleaved facet devices. Finally, the nonlinear waveguide has been incorporated within this ring laser in our design, in order to take maximum benefit of this higher internal power.

## 1.4 Device Overview

This investigation finds its roots in the development and demonstration of a novel optical parametric oscillator [22]. This self pumped monolithically integrated device

would produce wavelengths near 1.5  $\mu\text{m}$ ; however, it can be extended further to the mid-infrared wavelengths with the appropriate selection of the phase matching period.

A high power ring laser, with an electroluminescence near 775 nm, excites parametric emission due to the nonlinear nature of the superlattice material. This parametric emission is phase matched with the pump wavelength in a quasi phase matched (QPM) nonlinear waveguide. Finally, the phase-matched signal resonates in the adjoining passive cavity for a maximum power buildup.

Di-chroic multi mode interference (MMI) couplers establish the required routing between the two resonating cavities, in which the pump wavelength is routed from the ring laser cavity into the QPM waveguide and then routed back into the ring for laser action; and due to the di-chroic nature of the couplers, the phase-matched parametric emission is, instead, routed into the passive ring resonator. The design is given in figure 1-3 [22].

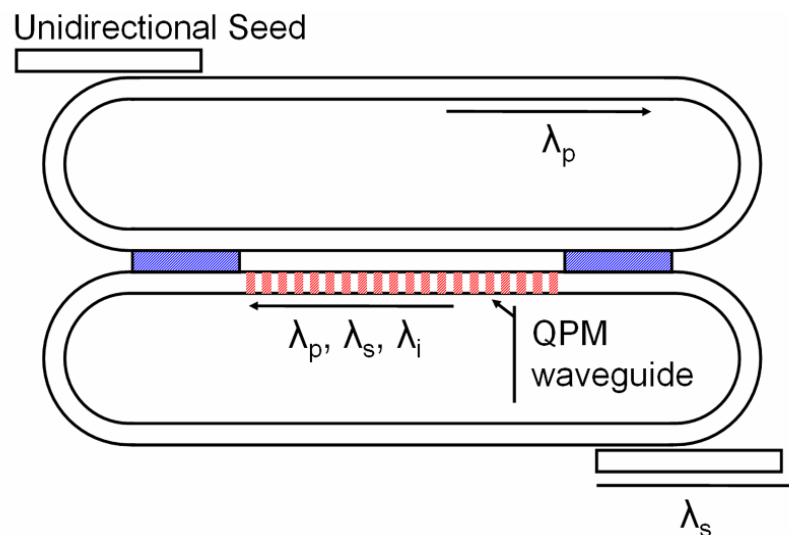


Figure 1-3 [22] – The designed optical parametric oscillator.

The concepts which can be identified in our OPO design and the above stated devices are: 1) the tunability in the pump excitation, and consequently in the signal/idler wavelengths, achieved using a coupled bragg-reflector as a seed to the ring laser, 2) di-

chroic MMI couplers serve exactly the same purpose as the beamsplitter in figure 1-3, and 3) there is a choice of tuning either signal or idler wavelengths to the passive ring's resonances; however, in the conventional approach longer wavelengths (idler) are coupled out, and a singly-resonant cavity is created for shorter wavelengths (signal) only, which has been followed in our design.

## 1.5 Thesis Outline

The thesis is compiled into the following chapters:

**1.5.1 Literature Review and Theoretical Background** — Chapter 2.

**1.5.2 Quasi phase matching waveguides** — Chapter 3 initially presents the material employed for nonlinear experiments, which is followed by the optimization of the intermixing techniques to achieve the necessary quantum well intermixing. The QPM investigation starts with preliminary analyses, followed by the device design and the fabrication process. The experimental demonstrations of various second-order nonlinear processes, with improved conversion efficiencies, cover the optimizations achieved in QPM. Finally, a comprehensive investigation is presented for the fabrication process optimization conducted in order to achieve a monolithically integrated device.

**1.5.3 Di-chroic multimode interference coupler** — Chapter 4 details the required frequency selective routing required in our OPO. The device design has been optimized using beam-propagation-based simulations for the band-gap and the half-band-gap wavelengths. Dry etch optimization is included in this chapter to achieve a precise control over the real time device fabrication. Finally, the fabricated couplers are tested and shown to achieve a good agreement with the behavior predicted through simulations.

**1.5.4 Superlattice lasers** — Chapter 5 presents the design, development, and the experimental characterization of the superlattice laser. The chapter starts

with the material design and covers the details of its design evolution. The material design is supported by the tests which include transmission line measurements and broad area lasers for initial characterization purposes. The main section of ridge waveguide lasers presents the details for device design, fabrication process, and experimental analyses. Finally, the observed resonant tunneling of current is measured in the superlattice diodes, and is analyzed with a theoretical explanation.

**1.5.5 Monolithically integrated devices** — Chapter 6 presents the investigations which have been conducted to demonstrate the feasibility of monolithically integrated devices, i.e., integrated OPOs, and integrated nonlinear optical frequency converters. The ring design for these devices has been achieved by the assessment of bending losses in the half ring superlattice lasers; and the optical routing has been revisited for the modified/thinner superlattice core material structure – thinner than the material used in the nonlinear and the di-chroic coupler experiments. Finally, the detailed designs for these integrated devices have been presented.

**1.5.6 Conclusions** — Chapter 7.

In addition to the thesis outline, a resource distribution map is presented in table 1-1, which shows the activities performed in the overall OPO research, and it highlights the author's specific involvement.

<b>Activities</b>	<b>Author's involvement</b>
<b>QPM waveguides</b>	
Passive material design	—
QPM device design	Partial
Fabrication	Significant
Characterization	—
Fabrication process optimization	Significant
<b>Di-chroic MMI coupler</b>	
Coupler design	Complete
Fabrication	Complete
Characterization	Complete
<b>Superlattice Lasers</b>	
Active material design	Significant
Device design	Complete
Fabrication	Complete
Characterization	Complete
<b>Monolithically integrated devices</b>	
Device design	Significant
Fabrication	Developed
Characterization	—

Table 1-1 – Resource distribution map.

# Chapter 2

## Literature Review and Theoretical Background

This chapter starts with the background theory of the overall processing required in our integrated OPO. Three major sections of the device which have been identified in OPO design are: 1) QPM waveguide, 2) di-chroic MMI coupler, and 3) the ring laser. In the case of QPM waveguide, optical nonlinear theory has been presented in this chapter which also incorporates the quasi phase matching technique – the literature review in this case will be discussed in the next chapter, as a lot of work has been reported in several cases, and it would be simple to place them under individual sections. The image formation and the multimode interference are presented after the QPM section. Finally, the most critical section of the ring laser has been reviewed in the perspective of semiconductor lasers evolution.

### 2.1 Optical Nonlinearity

Nonlinear optical phenomenon dates back to the 19<sup>th</sup> century with the discovery of Kerr and Pockel's effects, but it has been investigated significantly after the demonstration of second harmonic generation in 1961 by Franken et al [42], and with the invention of laser. Optical nonlinearities in a medium become substantial with higher intensity of the propagating electric field, where the polarization of the input field is given as:

$$P = \varepsilon_0 \chi E \tag{1}$$

The constant  $\epsilon_0$  is the permittivity of vacuum, and  $\chi$  is the susceptibility of a medium. Figure 2-1 shows how a second order term will change the overall response of a medium.

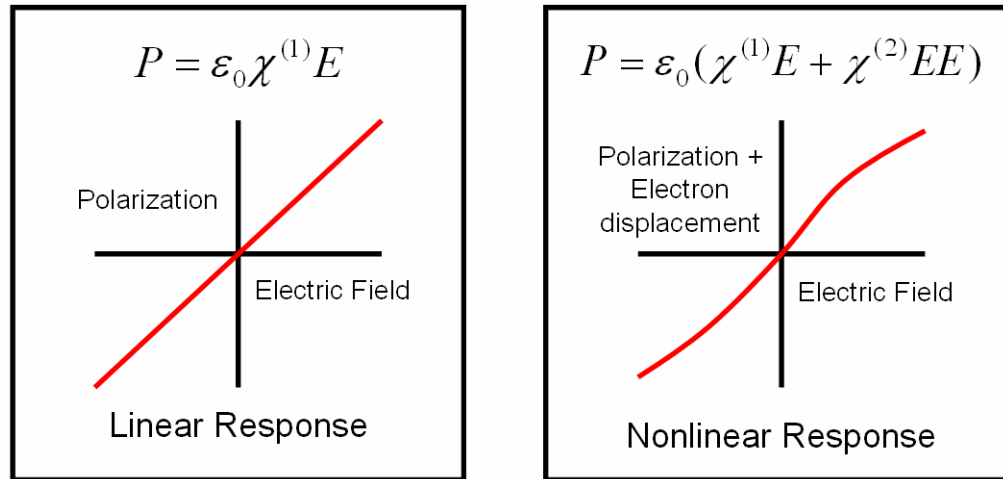


Figure 2-1 – Linear and nonlinear response of a medium.

### 2.1.1 Induced Polarization

The propagating electric field in a medium will induce sub-harmonic polarizations as a consequence of the generated dipoles (figure 2-2 [43]). These induced polarizations can be expanded as a power series in the following:

$$P = \epsilon_0 (\chi^{(1)} E + \chi^{(2)} EE + \chi^{(3)} EEE + \chi^{(4)} EEEE + ..) \quad (2)$$

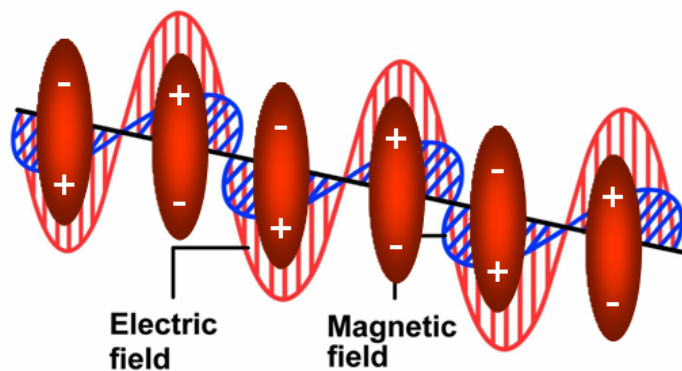


Figure 2-2 [43] – Dipoles which result in the induced polarizations in a medium.

The induced polarizations may not be parallel to the applied field (anisotropic medium); therefore, 3-dimensional susceptibility has to be introduced, in which the first order polarization will become:

$$\begin{pmatrix} P_x^\omega \\ P_y^\omega \\ P_z^\omega \end{pmatrix} = \epsilon_0 \begin{pmatrix} \chi_{xx} & \chi_{xy} & \chi_{xz} \\ \chi_{yx} & \chi_{yy} & \chi_{yz} \\ \chi_{zx} & \chi_{zy} & \chi_{zz} \end{pmatrix} \begin{pmatrix} E_x^\omega \\ E_y^\omega \\ E_z^\omega \end{pmatrix} \quad (3)$$

This first order polarization has a second rank tensor  $\chi_{ij}$  with 9 elements, which can also be written in a more compact form as:

$$P_i^\omega = \epsilon_0 \sum_{j=x,y,z} \chi_{ij}(\omega) E_j^\omega \quad (4)$$

Similarly the second order polarization will have a third rank tensor with 27 elements, and it is written in the compact form as:

$$P_i^{2\omega} = \epsilon_0 \sum_{j,k=x,y,z} \chi_{ijk}(\omega) E_j^\omega E_k^\omega \quad (5)$$

The relation (5) is valid for the induced polarization, which occurs due to a single frequency. However, if there is an interaction of two different frequencies, then the induced polarization will become:

$$P_i^{\omega_1+\omega_2} = 2\epsilon_0 \sum_{j,k=x,y,z} \chi_{ijk}(\omega_1, \omega_2) (E_j^{\omega_1} E_k^{\omega_2} + E_j^{\omega_2} E_k^{\omega_1}) \quad (6)$$

We restrict our self to the second order nonlinearities. Although the sub-order terms are important, but they have a lesser impact in the practical nature of the devices investigated here.

### 2.1.2 Induced Electric Field

The spatial response of the induced electric field can be derived from the wave equation by using slow varying envelope approximation [44].

$E^\omega = \hat{E}^\omega(z)e^{ikz}$ , which can be evolved into:

$$\frac{d \hat{E}^\omega(z)}{dz} = -\frac{\alpha}{2} \hat{E}^\omega(z) + \frac{i\omega^2 \mu_0}{2k} P^{NL}(\omega) e^{-ikz} \quad (7)$$

The material absorption constant  $\alpha$  is equal to  $\omega\mu_0\sigma/k$  ( $\mu_0$  = permeability,  $\sigma$  = electrical conductivity). The above equation shows that the induced electric field not only depends upon the fundamental field, but also, on the spatial modulation of the nonlinear polarization in a medium. Introducing (6) in (7), gives us:

$$\frac{d \hat{E}^{(\omega_1+\omega_2)}}{dz} = -\frac{\alpha_{(1+2)}}{2} \hat{E}^{(\omega_1+\omega_2)} + \frac{i(\omega_1 + \omega_2)^2}{2k_{(1+2)}c^2} \chi_{eff}(\omega_1, \omega_2) : \hat{E}^{\omega_1} \hat{E}^{\omega_2} e^{i\Delta kz} \quad (8)$$

The symbol  $\chi_{eff}$  represents the effective nonlinear susceptibility tensor. Substituting  $\omega_3 = \omega_1 + \omega_2$  in the above equation gives us the sum-frequency case, in which the two

fields at different frequencies add up to give a third frequency. The term  $\Delta k$  is the phase difference between the original and the induced fields:  $\Delta k = k_1 + k_2 - k_3$  (symbol  $k$  is the wave number for a specific field). The phase difference relationship implies that the induced field will have a maximum response if  $\Delta k = 0$ . This takes us to the next section which is the phase matching.

### 2.1.3 Phase Matching

The fields with different frequencies will observe different material dispersion, which will result in the different propagation constants. This gives us a phase velocity mismatch between the fundamental and the induced fields, which results in an oscillating behavior of constructive and destructive interferences at the induced fields in spatial domain. Equation (8) concludes that the induced field has a maximum response if the phase difference is zero, i.e.,  $\Delta k = 0$ . This condition can be written as following:

$$k_3 = k_1 + k_2 \Rightarrow \frac{2\pi\eta_3}{\lambda_3} = \frac{2\pi\eta_1}{\lambda_1} + \frac{2\pi\eta_2}{\lambda_2} \quad (9)$$

For continuous buildup of the induced fields, the phase matching condition must be satisfied. Birefringence phase matching and quasi phase matching (QPM) are important contenders for this solution. However, many materials such as GaAs lack birefringence; therefore, QPM is the available solution which has been employed in our case to achieve the phase matching in GaAs–AlGaAs superlattices. QPM is illustrated in figure 2-3 [44]. The distance for which the phase velocities result in constructive interference is known as the coherence length ( $L_c$ ). Phase matching can be achieved by periodically: 1) reversing the material domains (domain reversal), or 2) disordering the domains (domain disorder). This periodic alteration of the material domains can be generated at any odd integral multiple of  $L_c$ , i.e., 1, 3, 5, and so on, which results in the formation of first order, third order, and fifth order QPM. It can be deduced that the higher order

QPM will require longer devices to achieve the maximum power. Once the required phase-matching has been established, several second-order nonlinear processes can be achieved, summarized in figure 2-4.

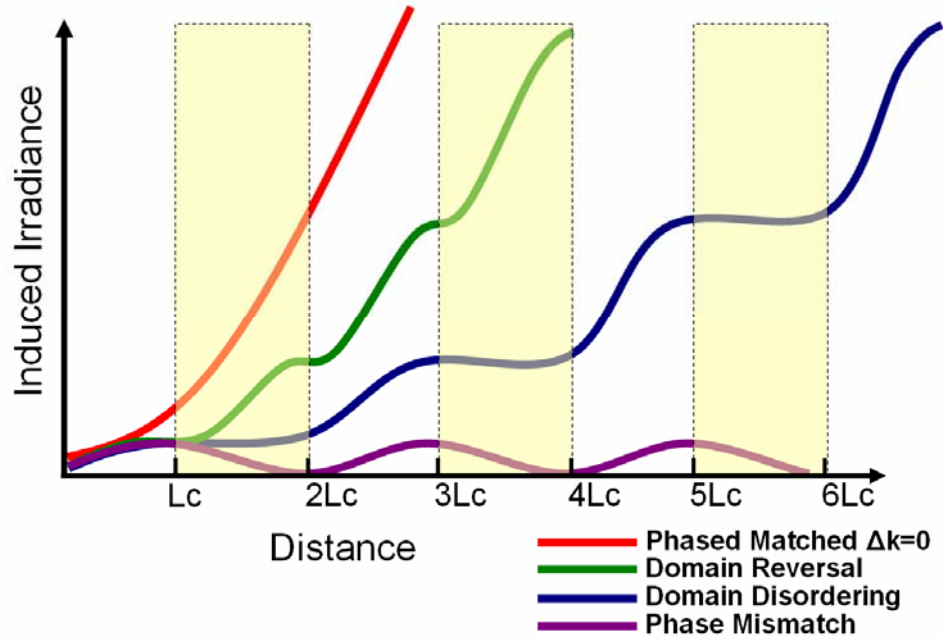


Figure 2-3 [44] – Quasi phase matching.

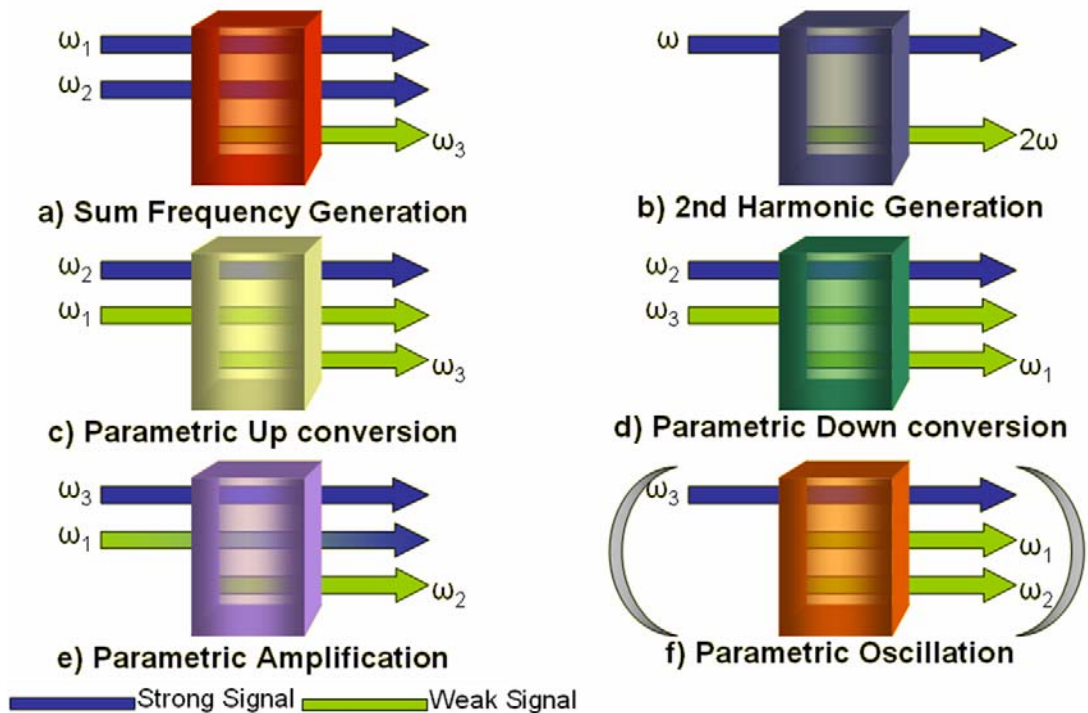


Figure 2-4 – Phase matched second order nonlinear processes.

Parametric oscillation in figure 2-4 (f), illustrate the concept in our designed OPO. The pump excitation (near the material band-gap), excites the parametric emission (near the half-band-gap), due to the nonlinear nature of the material. This parametric emission has to be resonated in a cavity such that the three-wave-mixed signal should achieve maximum conversion in half-band-gap wavelengths.

#### 2.1.4 Parametric Oscillation

In case of parametric amplification and parametric oscillation, in which the pump (intense field) is at the higher frequency, the evolution of spatial optical irradiance can be written in the form of following equations (assuming that the perfect phase matching has been achieved, i.e.,  $\Delta k=0$ ) [44]:

$$I^{\omega_1}(z) = I^{\omega_1}(0) \cosh^2 Gz$$
$$I^{\omega_2}(z) = \frac{\omega_2}{\omega_1} I^{\omega_1}(0) \sinh^2 Gz$$
$$G^2 = \frac{\omega_1 \omega_2}{2 \varepsilon_0 c^3} \frac{\chi_{eff}^2(\omega_1, \omega_2)}{\eta_1 \eta_2 \eta_3} I^{\omega_3}$$

The irradiance is defined as: the optical energy flowing through unit area per unit time, and it can be written in the terms of electric field given below.

$$I^{\omega} = \varepsilon_0 c \eta(\omega) |E^{\omega}|^2 / 2$$

Where  $\varepsilon_0$  is the permittivity of the vacuum,  $c$  is the speed of light,  $\eta(\omega)$  is the refractive index for optical frequency  $\omega$ , and  $|E^{\omega}|^2$  is the modulus of complex electric field.

In the above relations, if  $Gz \gg 1$  then both the signal and the idler irradiances will be dominated by the exponential growth term  $e^{2Gz}$ , which means that the gain coefficient  $2G$  is proportional to the square root of the pump irradiance. Under this amplification, the optical parametric amplifier is used to directly amplify any input signal, given in figure 1-5 (e). Additionally, if the parametric amplifier is placed inside a resonating cavity, then it can produce parametric oscillations from the initial fluorescence, under the same principle of stimulated emission which occurs in a laser cavity. The oscillations in this case will be produced for the maximum gain  $G$ , which depends upon the perfect phase matching; and if the phase matching condition can be controlled by any means then it would result as a tuning mechanism for the OPO. The threshold condition for OPO operation, when the gain exceeds the optical losses (transmission, absorption, scattering, etc), can be written as  $G \propto \sqrt{I^{th}}$ .

## 2.2 Multimode Interference

The idea of multimode interference (MMI), finds its early explanation in the formation of self images using a pinhole array, illuminated by incoherent light, or through the transmission in an optical fiber [45]. The same principle has been studied in detail for optical waveguides by Ulrich [46-47] [48]. In general, the self imaging is said to occur when a single or multiple images of an input field appear at periodic intervals in a multimode guiding structure. This property of multimode structures is widely exploited in modern day optoelectronic devices, like in the case of MMI splitters [49], electro-optic switches [50], ring lasers [51-52], and reconfigurable splitter/switch [53]. The main principle under which these devices work is the phase difference between the multiple modes (mostly guiding).

Generally a multimode cavity supports two or more guiding modes which at certain length of a device add up constructively or destructively to give either: a single inverted (*cross coupler*), a single erected (*bar coupler*), or multiple images of the input field. The input to such a cavity is usually a single mode waveguide, but the number of access waveguides depends upon the device configuration.

MMI devices fabricated in an integrated model are usually etch-based, in which the large width of MMI cavity and the lateral confinement results into multiple guiding modes. The width of an example MMI cavity is assumed to be  $W_e$  (effective width), which is larger than the lithographically defined width, due to the lateral penetration of mode in the guiding structure. The beat length  $L_\pi$  for the two lowest order modes is given by [54]:

$$L_\pi = \frac{\pi}{\beta_0 - \beta_1} \cong \frac{4\eta_r W_e^2}{3\lambda_0}$$

The refractive index is  $\eta_r$ , which is an effective refractive index in the case of a multilayered material. The free space wavelength is  $\lambda_0$ , and propagation constants for the lowest order modes are  $\beta_0$  and  $\beta_1$ . When the propagation length becomes a multiple of this beat length, the field will result in the formation of self/multiple images of the input. MMI is further categorized into general interference and restricted interference.

### 2.2.1 General Interference

In the case of general interference, all guided modes are excited to form images of the input field  $\Psi(y, 0)$  – as given by the modal propagation analysis (MPA) in figure 2-5 [54]. This general interference leads to the formation of a single mirrored image of the input field at  $3L_\pi$ , a single erected image at  $2(3L_\pi)$ , and two-fold images at  $1/2(3L_\pi)$  and  $3/2(3L_\pi)$ . At all these lengths, the excited modes of the input field add up constructively to generate super resonance. The length of a multimode cavity can be formulated in the terms of beat length [55], as:

$$L = \frac{p}{q}(3L_\pi)$$

It can be understood from the above relation, and looking into figure 2-5, that at a specific length  $L$  of the cavity

- 1) The input field will reproduce its image when  $p/q$  is an even integer, i.e., 2, 4, 6, and so on, which is a bar coupler.
- 2) The input field will result into a mirrored image when  $p/q$  is an odd integer, i.e., 1, 3, 5, and so on, which is a cross coupler.
- 3) And, the input field will result into a combination of its original and mirrored image when  $p/q$  is  $1/2$ ,  $3/2$ ,  $5/2$  and so on, to give 3 dB coupling.

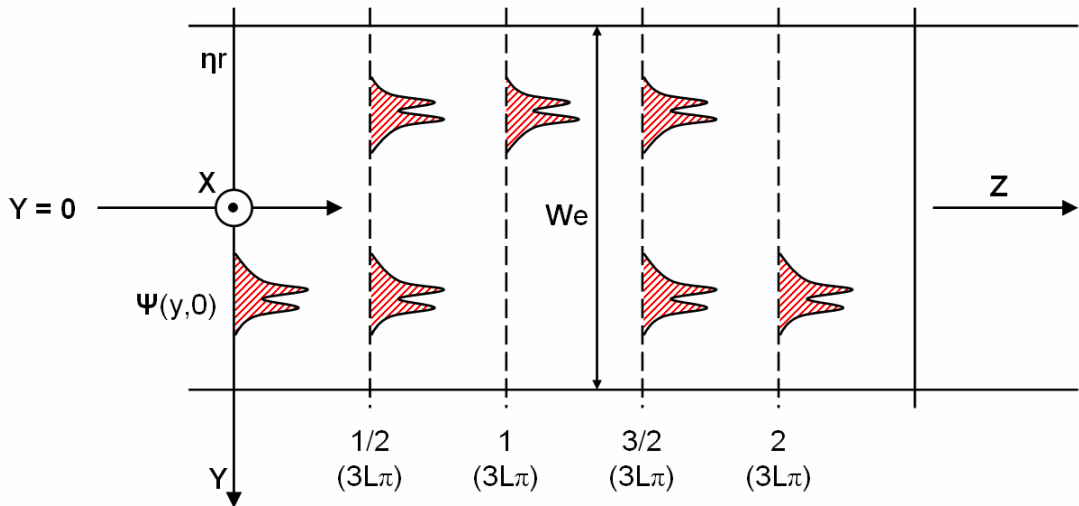


**Figure 2-5 [54] – Field propagation in a multimode cavity.**

The coupling operation can also be achieved by employing a directional coupler (which is also known as evanescent field coupler). In this coupler the two waveguides are placed close to each other in such a way that the evanescent tail of their guided modes overlap; and when the light is launched into one of the waveguides, there is a periodic exchange of power between the guided modes as the light propagates. The coupling operation is very sensitive to the device geometry, especially the spacing between the two waveguides, in the directional coupler as compared to that of a MMI. Additionally, the required fabrication to achieve the desired coupling is very challenging when the spacing between the waveguides is small. Figure 2-6 shows the simulated length of an example directional coupler for a cross operation at 775 nm excitation wavelength. These simulations are performed using the parameters of our material structure, and the

waveguide dimensions are the same which we have employed in our devices, the details on these are presented later in this thesis. It can be seen in these simulations that the coupler length increases exponentially with an increase in the spacing between the waveguides. In our case, where we require cross coupling for the wavelengths near the material band-gap, the minimum length of  $\sim 830 \mu\text{m}$  is achieved with 100 nm spacing between the waveguides (figure 2-6). The fabrication to achieve this small gap is very challenging, and it has been found practically impossible in our case, for which the detailed experimentation is presented in the di-chroic MMI coupler chapter. In conclusion, not only we are limited by the fabrication constraints, but also the required coupling operation requires a longer device in the case of directional coupler; therefore, its was decided to employ MMI in our device design.

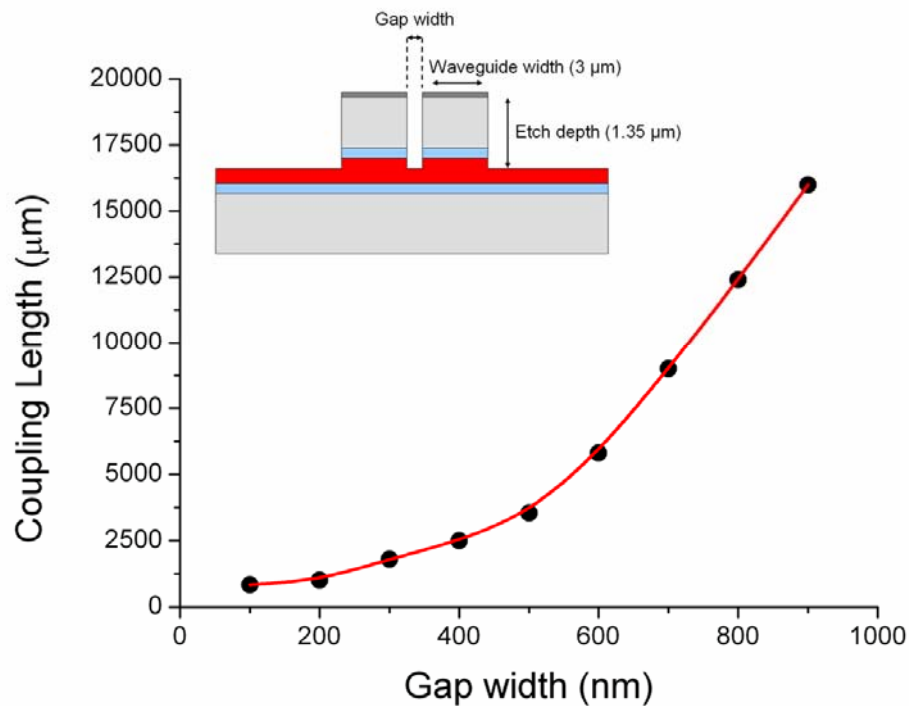


Figure 2-6 – Simulated length of a directional coupler for the cross operation (775 nm wavelength), the inset shows the device geometry.

The geometry of a MMI coupler can also be formulated for a certain cavity length  $L$  [56], as:

$$L = \frac{M}{N} \cdot \frac{3L_{\pi}}{a}$$

Where  $N$  is an integer defining the number of images, and  $M$  is an integer which defines the possible cavity length at which  $N$  images will appear. The integer  $a$  defines the type of MMI coupler. For example, in figure 2-7 [56], the general MMI coupler  $N \times N$  has  $a = 1$ , and the position of input/output ports contain a free parameter  $b$ ; and similarly the symmetric  $1 \times N$  coupler has  $a = 4$ .

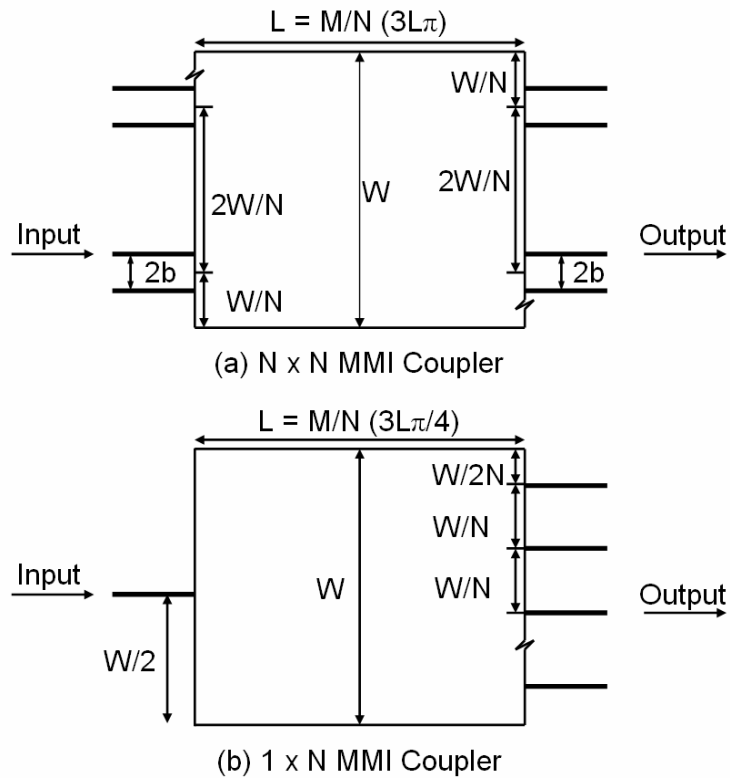


Figure 2-7 [56] – Design of a MMI coupler with length  $L = M/N (3L_{\pi}/a)$ .

The coupler based on general interference principle has been reported as: a 3 dB coupler in [51-52] [55] [57], and as a cross coupler in [55]. The general interference in multiple images configuration has been reported in [50].

### 2.2.2 Restricted interference

The self imaging, in case of MMI devices, is achieved due to the super resonance of all the excited modes which add up constructively. However, it is possible that the modes 2, 5, 8 ... and so on, of MMI cavity are not excited due to specific placement of the input guides at  $\pm W_e/6$  [54]. This configuration of MMI results in the first self image to appear at the length  $L_\pi$ , which makes the length of this device, functioning as a cross coupler, three times less than its general interference equivalent. The selective suppression of the modes and subsequently the interference is said to be paired restricted in this case. Restricted inference mechanism has been employed to make very short length devices, such as 3 dB and cross couplers [54]. An extremely short cavity of only 107  $\mu\text{m}$  long as a 3 dB coupler, and 216  $\mu\text{m}$  long as a cross coupler, has been reported in [58], using deep-etched InP.

Restricted interference is also observed in the multiple images, in which suppressing the odd modes, 1, 3, 5 ... and so on, of MMI cavity result in symmetric interference [54]. The device length in this case, with the placement of input access guide at  $W_e/2$ , is 4 times less than its general interference equivalent. MMI 1 x N splitters fabricated under the said genre have been reported in [49, 59].

## 2.3 Semiconductor Laser

The first demonstration of stimulated emission in a ruby crystal in 1960 [60], derived the determination to achieve coherent radiation in a semiconductor material. GaAs has been reported in many previous studies as an attractive source for such radiation, and the first experiment to report this was performed in 1962 [61]. The emission occurred due to the direct band-gap transitions under pulsed electrical injection in liquid nitrogen. Similar experiments were reported in the same year [62-63]; however, the major drawbacks in these initial efforts were the very high injection current and the pulsed operations at very low temperatures. These shortfalls significantly affected the prospects of semiconductor lasers in research and industrial adoption. This issue was addressed by

a proposal in 1963 by Herbert Kroemer to improve the laser action by Double Heterostructure.

### 2.3.1 Double Heterostructure

(The birth of modern semiconductor lasers)

The earliest work carried out on semiconductor lasers proved that it is almost impossible to achieve a laser action at higher temperature with lower threshold currents. This issue was addressed by the initial proposal of introducing heterojunction injectors on both sides of the active medium (hence double heterostructure lasers). The work under this proposal was formulated independently by Herbert Kroemer and Zhores I. Alferov (Nobel Prize winners in Physics, 2000) in 1963. The work by Kroemer was reported in IEEE proceedings [64], in which he proposed to introduce the material of a higher band-gap energy as heterojunction injectors across the active layer (figure 2-8 [64]). These injectors, which are heavily doped and have opposite polarity, will be able to confine the carriers with much higher density (as compared to the homogenous material) because of their potential barrier at the heterojunction interfaces, and will cause laser action to occur at higher temperatures.

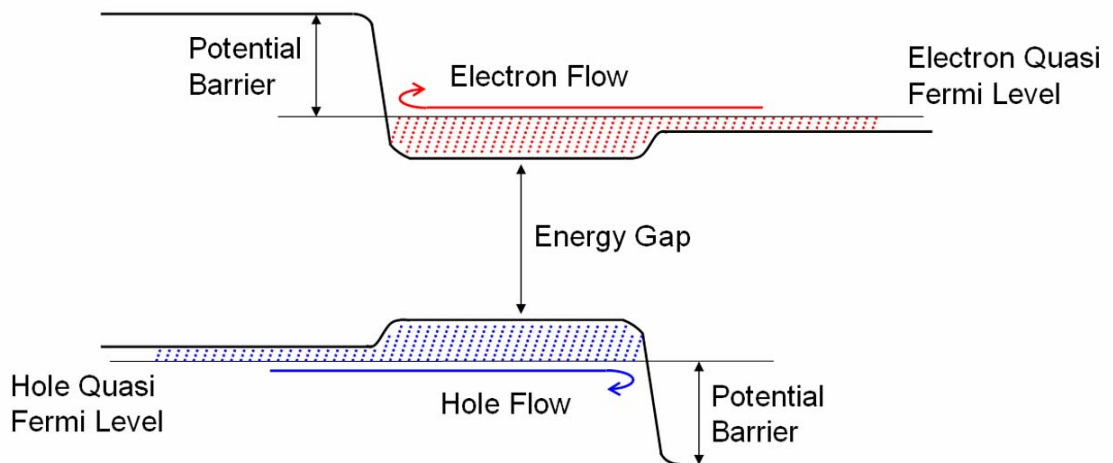


**Figure 2-8 [64] – Double heterostructure laser under applied bias.**

Although the proposed structure was ground breaking, however, it posed significant challenges. The lattice match identified to be the most critical issue in this design, and it

was concluded that the interface dislocations can result in the recombination currents in excess of  $1 \text{ kA/cm}^2$ , even in a very high quality structure. Therefore the epitaxial techniques must avoid the interface dislocations as they will end up carrier traps and degrade the whole idea.

Similarly, the work reported in the same period by Alferov [65], emphasized that the double heterostructure lasers can achieve super injection of the carriers because of their several orders magnitude of the carrier density in the active region, as compared to the adjoining heterojunction injectors. The refractive index differences between the layers shall result the optical confinement within the active layer, and the potential barriers shall restrict the carrier recombination within the active region. He also identified the lattice match between different layers to be highly important. The earliest work reported by his group considered GaAs to be a strong contender as an active region in GaP–GaAs and AlAs–GaAs double heterostructure compounds, and reported the first laser action in a GaAs–AlAs based system in 1969 [66]. Further improvements in their structure demonstrated lower threshold laser action at room-temperature [67], and finally the continuous wave operation at room-temperature [68].

The Bell Telephone laboratories were also actively involved in the investigation of heterostructure lasers in 1960-70's, where the major credits were entitled to I. Hayashi and M. B. Panish [69]. They reported their first laser action in GaAs–AlGaAs double heterostructure in 1970 [70], which achieved a lower room-temperature threshold current density of  $2300 \text{ A/cm}^2$ , as compared to that of  $4300 \text{ A/cm}^2$  by Alferov [67]. The improvements they achieved in their structure through liquid phase epitaxy (LPE) helped them grow high quality wafers, which resulted in the demonstration of continuous wave laser action at room-temperature [71]. They reported to have achieved a threshold current density of  $1000 \text{ A/cm}^2$  for a square diode, and  $1600 \text{ A/cm}^2$  for a Fabry-Pérot diode. They concluded in further studies [72-73], that the double heterostructure lasers have: 1) lower absorption because of the less penetration of optical field outside the active region, 2) perfect optical and electrical confinement within the active region make double heterostructures less effected by temperature if compared to the single heterostructures and the homostructures, and 3) the lasing mode of the optical field is mostly TE polarized because of its higher reflection coefficient.

The developments in double heterostructure lasers were ground breaking; however, the improvements in lowering the threshold current densities than the earlier achieved were not significant. The work conducted on growing high quality structures developed the sophisticated and precision enhanced techniques such as molecular beam epitaxy (MBE) [74-75]; the growth procedure was reported to control the different layers in few nanometers. This achievement led to the developments in quantum well and superlattice heterostructures.

### 2.3.2 Quantum Well

The developments in MBE gave a precise control in the heterostructure growth – in which the individual layers can be achieved with the thickness in few nanometers. Exploiting this, R. Dingle et al. [76], reported the first observation of quantum confinement effects in GaAs potential wells, bounded by AlGaAs barriers. They reported that the number of bound states increases with an increase in the well depth, and the spacing between the bound states increases with a decrease in the well thickness. The absorption spectra measurements (figure 2-9 [76]), they performed on the quantum wells of different thicknesses show the quantum confinement in bound states. These quantum confinement effects were further understood by the earliest demonstration of a multiple quantum well heterostructure laser [77]. The laser action was supported by an optical pump; however, the threshold density was reported to be higher than the conventional double heterostructure lasers. They concluded that the quantum efficiency has been significantly degraded by the recombination centers at the quantum well/barrier interfaces.

The first major achievement in the development of a quantum well laser was reported in 1978 [78]. The GaAs quantum well (~20 nm) with AlGaAs barriers and claddings, grown using metal organic chemical vapor deposition (MOCVD), achieved the very first room temperature injection laser action. These lasers were reported to have the threshold current densities of ~3000 A/cm<sup>2</sup>.

Since then, much work has been reported in quantum well laser structure improvement. The graded index separate confinement heterostructure (GRIN-SCH) symmetric waveguide laser, grown using MBE, reported the threshold current density of 500 A/cm<sup>2</sup> [79], and further improved it down to 160 A/cm<sup>2</sup> [80]. The GRIN-SCH structure (figure 2-10 [80]), not only can achieve very low threshold current density, but also the selection of GRIN layers can result in any desired far-field pattern.

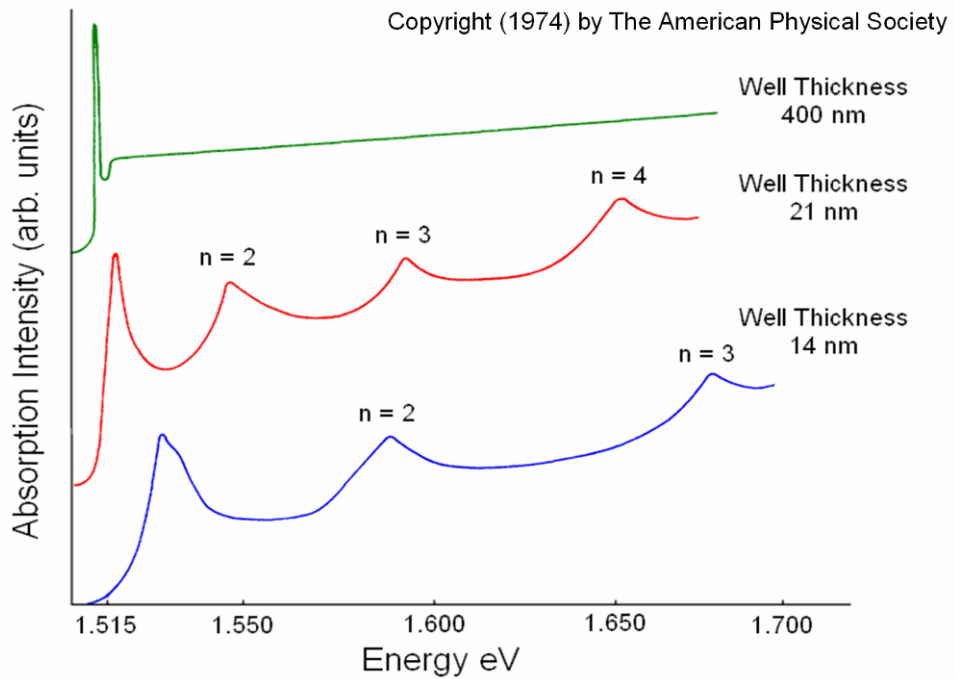


Figure 2-9 [76] – Absorption spectra for quantum wells of different thicknesses, measured at 2 K (Permission to reproduce this figure has been granted by The American Physical Society).

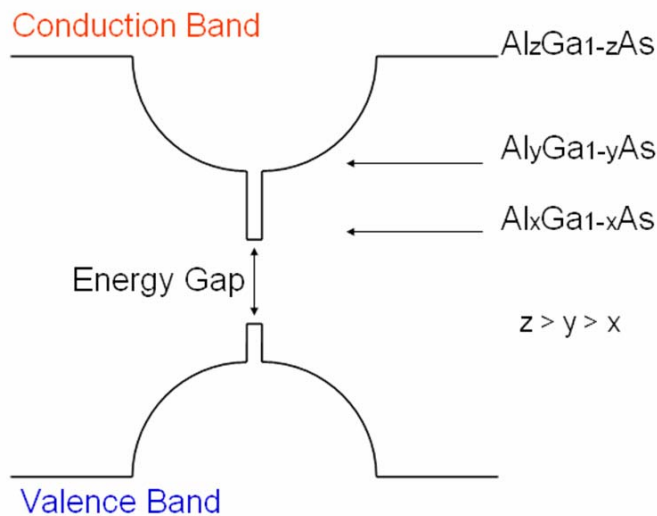


Figure 2-10 [80] – GRIN-SCH energy level schematic.

### 2.3.3 Multiple Quantum Well

Tsang comprehensively investigated the characteristics of a multiple quantum well (MQW) structure [81], and later in [82], author reported an extremely lower threshold of  $250 \text{ A/cm}^2$  in a broad area laser (BAL) with the dimensions  $200(\text{wide}) \times 380(\text{long}) \mu\text{m}$ . This opened an attractive opportunity to achieve an optimized laser action using MQW structures. A detailed study, in which the threshold current was measured for the increasing number of quantum wells in a  $4000 \text{ \AA}$  wide core, has shown a monotonic increase in the threshold current for 2, 4, 10, 20, and 40 GaAs wells bounded by  $\text{Al}_{0.35}\text{Ga}_{0.65}\text{As}$  barriers [83]. Authors concluded the single quantum well structure to be optimum in this case. However, more elaborated analyses [84-85], have identified that the minimum threshold current density is achieved in: short devices with a large number of quantum wells, and long devices with a small number of quantum wells. This is explained by the higher mirror loss for a shorter cavity, which requires a higher gain factor for the laser action to occur, and is provided by an increased number of quantum wells. An experimental demonstration to achieve sub-milliampere threshold current of only  $2.4 \text{ mA}$  at room-temperature for a  $100 \mu\text{m}$  long device under continuous injection is reported in [86], which supports the previous observation. The material structure included 3 GaAs quantum wells bounded by  $\text{Al}_{0.22}\text{Ga}_{0.78}\text{As}$  barriers, given in figure 2-11 [86].

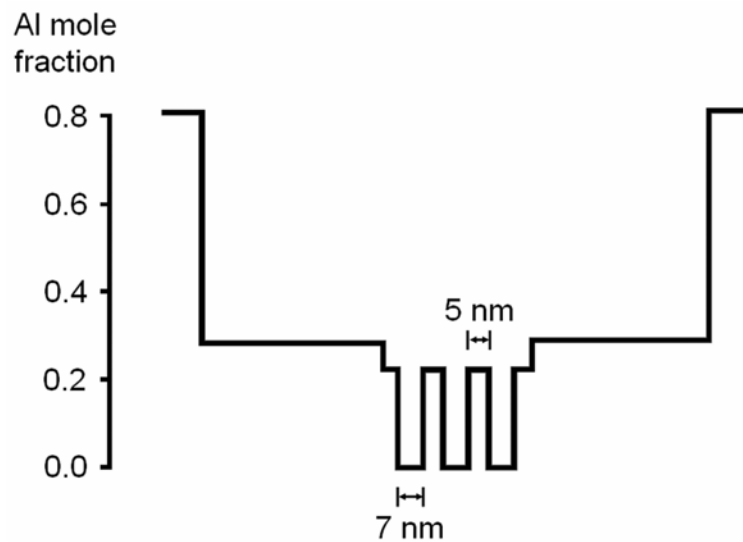


Figure 2-11 [86] – MQW structure which achieved  $2.4 \text{ mA}$  threshold current at the room-temperature.

A very interesting investigation in which the excitation wavelength has been varied as a function of decreasing GaAs quantum well width, bounded by 80 Å Al<sub>x</sub>Ga<sub>1-x</sub>As barriers, is reported in [87]. The pulsed excitation has been observed in 10 and 20 GaAs quantum well material systems, and a red shift of about 20 nm has been reported between the excitation wavelength and the calculated  $n=1(e-hh)$  transition. In a different material system which had 20 GaAs quantum wells (25 Å) bounded by Al<sub>0.31</sub>Ga<sub>0.69</sub>As (40 Å) barriers, has indicated coupling between the quantum confinements among the quantum wells. The excitation in this case also observed a red shift of 18 nm from the calculated  $n=1(e-hh)$  transition which has been attributed to re-absorption.

### 2.3.4 Superlattice Heterostructure

The earliest investigations in the semiconductor superlattices have been reported by Leo Esaki (Nobel Prize winner in Physics, 1973) in 1970 [88-89]. These “man-made” materials exhibit the resonant tunneling of carriers under the applied bias. This tunneling results from the overlay of the electron waves in the bound states of the periodic potential wells. This overlay can either occur among the bound states at the same energy level, or it can occur when the bound states become degenerate among the excited energy levels (in the case of sequential tunneling). The tunneling process has been reported in the case of Zener diodes and Tunnel diodes in 1950’s, whereas in the case of superlattices, it became apparent after the significant advancements in the growth procedures, such as MBE [90]. The use of this procedure, along with its *in-situ* analysis, enabled the scientists to achieve a precise control over the thickness and composition of thin semiconductor layers. The carrier transport measurements performed in GaAs–AlGaAs based double barrier structure [91], and GaAs–AlAs based superlattice structure [92], showed the tunneling at specific bias amplitudes which coincide with the quantum confined states. The sequential resonant tunneling was reported by Capasso et al. in 1985 [93]. They performed photocurrent measurements in a *p-i-n* superlattice diode. Their reported surge in the photocurrent with increasing the reversed bias manifested the resonant tunneling in the ground and the excited states of

the periodic wells. A schematic illustration of the electron tunneling among degenerate energy states in periodic wells is shown in figure 2-12 [93].

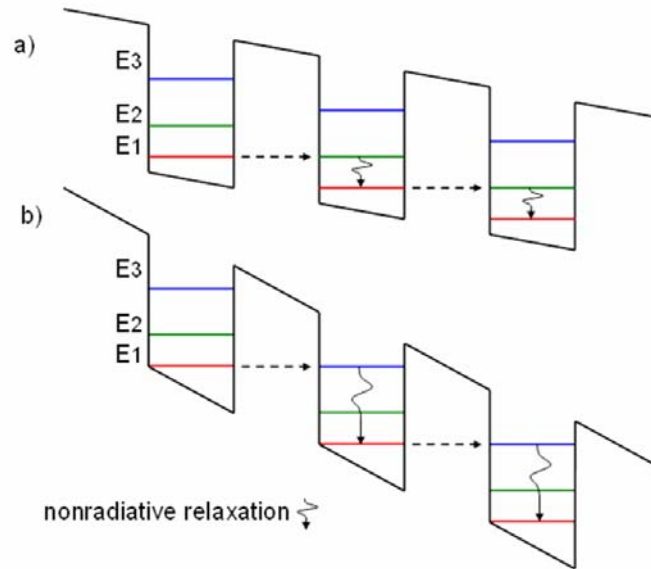


**Figure 2-12 [93] – Sequential resonant tunneling: (a) from the ground state into the first excited state, and (b) from the ground state into the second excited state.**

In 1981, Coleman and Dapkus et al. reported the photo-pumped laser action in AlGaAs–GaAs superlattices [94], and then in AlAs–GaAs superlattices [95]. Their superlattices were grown using MOCVD, and showed the emission lines at 77 K and 300 K, in both pulsed and continuous optical pumping. The first continuous photo-pumped laser action in strained GaAs–InGaAs and GaAs–GaAsP superlattices, grown using MOCVD, was reported in 1983 [96]. These lattice mismatched structures were reported to be unstable and failed quickly within 2-20 min. This experiment considerably questioned the stability of strained superlattice structures.

There has been a significant amount of research reported by the scientists all over the world in the development and the evolution of semiconductor injection lasers, and much work will be under progress. However, the literature presented up to this point can cover the major achievements in this technology. An observation worth mentioning is that the work on the superlattice injection lasers is scarcely reported. While, majority of the stimulated emission measurements in these structures are assisted by optical pumping.

# *Chapter 3*

## Quasi Phase Matching Waveguides

Nonlinear optical conversion is the fundamental requirement in our integrated OPO. This conversion has been achieved using the quasi phase matching (QPM) technique of periodic domain-disordering, as there is no useable material birefringence in GaAs–AlGaAs system. This domain-disordered quasi phase matching (DD-QPM) benefits from the post-growth quantum well intermixing (QWI), which is used to achieve the necessary control of nonlinearity. In addition to this, post-growth QWI techniques are employed to establish the monolithic integration in a fully integrated optoelectronic device. Our GaAs–AlGaAs superlattice core material system can be compared to the GaAs–AlAs superlattice core, which has been previously investigated to achieve a substantive modulation in the optical nonlinearity [38], which in turn facilitates the phase-matched three-wave-mixing. Therefore, using the DD-QPM to achieve the nonlinear optical conversion in GaAs–AlGaAs superlattice is a valued course. The optimization in second harmonic generation (SHG) has been achieved in our periodic DD-QPM waveguides, to achieve the consequent optimization in QPM, i.e., the phase-matching period. The quantum well intermixing has been achieved using the ion-implantation, assisted with the periodic gold mask to retain the as-grown nature of the material. The devices have been later characterized at the University of Toronto for various second order nonlinear processes.

### 3.1 Material

#### 3.1.1 Superlattice Heterostructure

The material which we have employed in this investigation is a GaAs–AlGaAs superlattice core heterostructure. Superlattice heterostructures have been investigated

for the last four decades, and the very first studies are reported by Esaki and Tsu [97]. There have been extensive achievements in the material growth technologies since that time, such as molecular beam epitaxy (MBE) and metal-organic vapor phase epitaxy (MOVPE). In these highly sophisticated growth technologies chemical compositions and thicknesses of a material are controlled precisely under high vacuum [98]. These material structures are grown by atomic/molecular interactions with the crystalline surfaces; and thin layers can be easily grown with a thickness of 2.8 Å, i.e., a monolayer (ML). In these heterostructures, where the layer thicknesses are comparable to the electron/hole wavelengths, the interlayer carrier interactions are apparent. These interactions of carriers with the potential energy barriers result in resonant tunneling (RT), which has been studied and experimentally demonstrated [88, 93]. Resonant tunneling is a quantum effect in which the carrier transport through the barrier layers is transparent, which results in the formation of sub/mini bands in the superlattice region.

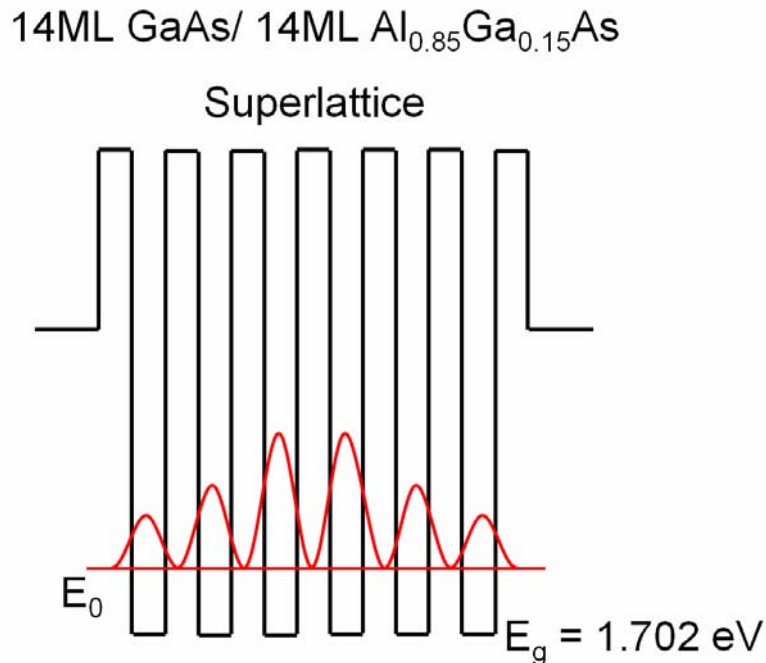


**Figure 3-1 – Schematic conduction band diagram of a six period 14 ML GaAs / 14ML Al<sub>0.85</sub>Ga<sub>0.15</sub>As superlattice with moduli-squared wave-function for the lower edge of  $E_0$  mini-band (the diagram is only for the illustration purpose and none of the energies are up to the scale).**

The studies conducted by Hutchings [38, 99], have given us the calculated modulation in the second order nonlinear susceptibility  $\chi^{(2)}$  in a domain disordered GaAs–AlAs superlattice. It has been concluded that 14ML GaAs/14ML AlAs superlattice structure,

which has a pump transparency close to 775 nm, results in the  $\chi^{(2)}$  modulation of  $\sim 60$  pm/V at the half-band-gap, i.e., 1550 nm. However, the native oxidation of AlAs has compelled AlGaAs as a stable barrier in such periodic heterostructures, which makes GaAs–AlGaAs superlattices a competitive source in nonlinear optical frequency conversion processes.

A schematic conduction band diagram of a six period 14ML GaAs/14ML Al<sub>0.85</sub>Ga<sub>0.15</sub>As superlattice heterostructure is given in figure 3-1 (please note that the diagram is only for the illustration purpose, as the energies depicted are not up to the scale). The red line shows the calculated moduli-squared wave-function for the lower edge of E<sub>0</sub> mini-band. The direct band gap transition E<sub>g</sub> of this composite material is 1.702 eV.

### 3.1.2 Passive Wafers

Our investigation started using the material grown for passive processing, given in figure 3-2. The material has a 600 nm thick 75 periods 14ML GaAs/14 ML Al<sub>0.85</sub>Ga<sub>0.15</sub>As superlattice core. The core cladding has a thickness of 300 nm with Al<sub>0.56</sub>Ga<sub>0.44</sub>As composition, and the outer cladding has a thickness of 800 nm with Al<sub>0.60</sub>Ga<sub>0.40</sub>As composition. Lastly, there is a protective cap of 100 nm GaAs, and a base layer of 1000 nm Al<sub>0.85</sub>Ga<sub>0.15</sub>As to isolate the guided modes from the substrate radiations. For the initial investigations to optimize the nonlinear processing, two wafers were used: BMH1 grown locally by Prof. Colin Stanley (MBE research group, University of Glasgow), and BMH2 received from Sheffield. Both wafers have been grown in [001] crystal axis using MBE, and the devices which were fabricated on these wafers had cleaved facets in [110] axis. The idea here is to exploit the bulk like  $\chi^{(2)}_{xyz}$  coefficient [100], which is reported to be much higher than the typical  $\chi^{(2)}_{zzz}$  in the case of asymmetric quantum well structures [101]. BMH1 has a measured photoluminescence (PL) of 773 nm at room-temperature which is quite uniform over the whole wafer, whereas BMH2 has a room-temperature PL of 770 nm from the centre of the wafer and gradually decreases down to 760 nm at the edge, indicating a non-uniform growth.

The quantum confined wave-functions are subjected to overlap within the successive quantum wells if the mean free path of carriers is comparable to the thicknesses of the wells and their surrounding barriers. These mini-bands which result due to this resonant tunneling, requires a specific approach for energy band calculations in superlattices. A research software Energy levels calculation in GaAs/AlGaAs heterostructures (ECA 4.C), written by Roland Teissier was used to solve the energy bands in our structure. The calculated band-gap energy for 25 periods 14ML GaAs/14ML Al<sub>0.85</sub>Ga<sub>0.15</sub>As structure is 1.702 eV. The corresponding mole fraction of Al<sub>x</sub>Ga<sub>1-x</sub>As is calculated to be 0.22 using the following [102]:

$$E_g^\Gamma(x) = 1.425 + 1.155x + 0.37x^2$$

Refractive index values for subsequent modeling and simulations in the investigation have been obtained from the electronic resource [www.luxpop.com](http://www.luxpop.com). The programmed software on this resource calculates the refractive index for different materials of various mole fractions, operating wavelengths, and temperatures. The calculations are performed using both Gehrsitz [103], and Adachi [102] models.

### 3.2 Quantum Well Intermixing (QWI)

The discovery of QWI has enabled the realization of low loss sections in monolithically integrated devices [104]. Many applications of integrated optoelectronics have been identified in which QWI has been employed [105], such as: low loss waveguide interconnects, distributed bragg-reflector lasers, mode-locked lasers and non-absorbing mirrors. QWI has also overcome the fabrication complexities, which are introduced by substrate patterning, to achieve monolithic integration [106]. Thus to summarize, QWI has proved to be a very effective technology for the active-passive integration in the modern single chip device fabrication.

Over the recent past, QWI techniques like impurity induced disordering (IID) [105], impurity free vacancy disordering (IFVD) [107], sputtered SiO<sub>2</sub> [108], and ion

implantation [109-110] have been investigated. QWI has also been used to modify the linear optical properties [111-112], and the nonlinear optical properties [113], of multiple quantum well structures. The freedom to shift the absorption peak and control the nonlinearities in GaAs–AlGaAs heterostructures using QWI has a fundamental relevance to this investigation. The preferred case of 1<sup>st</sup> order phase matching to achieve the maximum  $\chi^{(2)}$  modulation, requires a phase matching period of 3-5  $\mu\text{m}$  for over the range of wavelengths which we intend to investigate. The required resolution is always compromised by the lateral straggle introduced in any QWI process. However, the lateral straggle in QWI techniques of IID, IFVD, and sputtered SiO<sub>2</sub>, limits their application in our case, and micron-scale resolution has been reported to be achievable using ion-implantation [99-100].

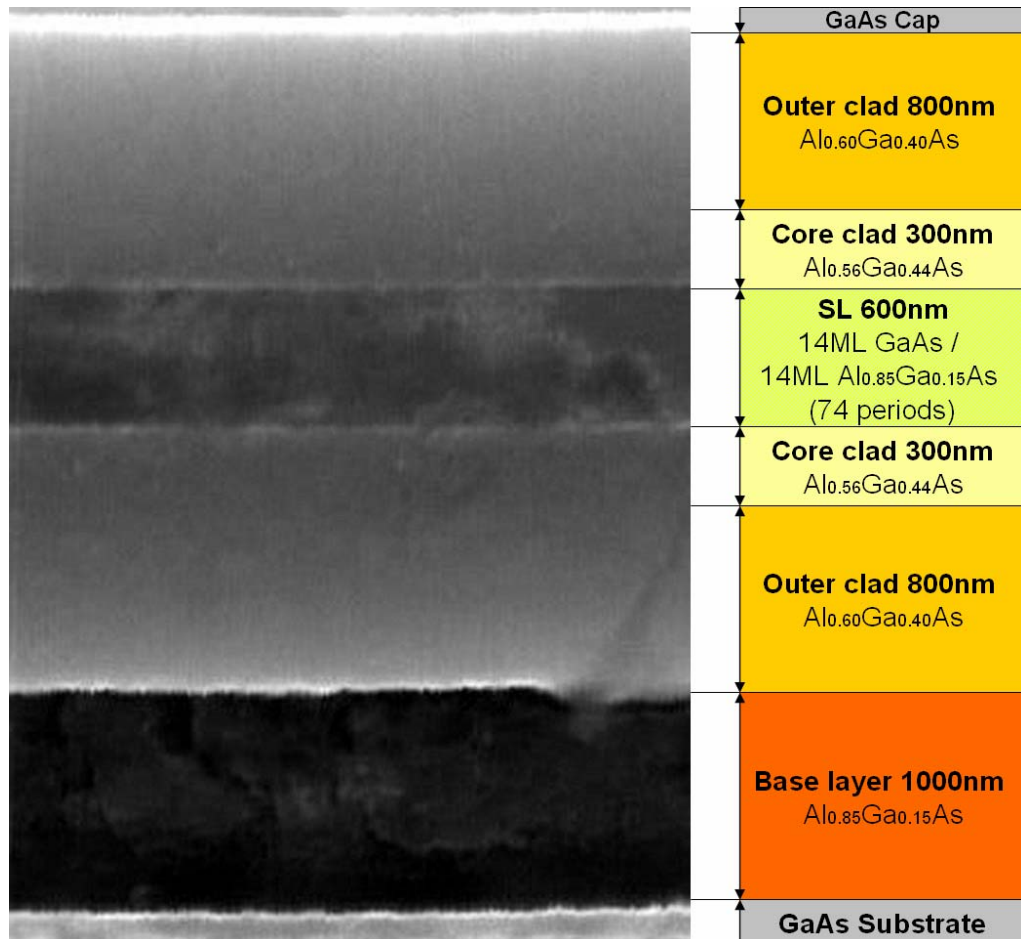


**Figure 3-2 – Cross-sectional scanning electron microscope image of the material.**

Sputtered SiO<sub>2</sub> and ion implantation induced intermixing are presented next, which have been investigated to characterize the band-edge shift and the loss profile in our material.

### 3.2.1 Sputtered Silica Tests

This section covers the experiments, which were performed at first, for the blue shift characterization in BMH1 using sputtered SiO<sub>2</sub>. The motivation here is to show a comparison with ion implantation induced intermixing, and finally identify the technique which exhibits better control over the process parameters, and the required spatial resolution.

The samples were prepared by sputtering an initial layer of 50 nm sputtered SiO<sub>2</sub> on the clean surface. The cleaning procedure used (in all the sample preparations) was a solvent based, in which the samples were placed in: acetone, isopropanol (IPA), and RO water, for 5 min each, in an ultrasonic water bath. On the top of sputtered layer a protective cap of 200 nm plasma enhanced chemical vapor deposition (PECVD) SiO<sub>2</sub> was deposited. The samples were then given a rapid thermal annealing (RTA) treatment for 60 s at different temperatures – samples were placed on a silicon carrier wafer in RTA chamber, and a small piece of clean silicon was used to fully cover the samples' surface to minimize the arsenic desorption. Finally, the low temperature (70 K) PL measurements were performed. The PL measurement setup (figure 3-3) had a green frequency-doubled (Nd:YAG) source from which the light was shined on the surface of the samples kept in liquid nitrogen (77 K), and the reflected light was coupled back into the optical fiber and measured on optical spectrum analyzer (OSA).

The results obtained are given in figure 3-4, which show that with increasing the RTA temperature the blue shift increases; and a maximum shift of 71 nm has been achieved at 600 °C. The diminishing power of the reflected PL signal, from the high temperature annealed samples, indicates a fully intermixed core; and also, the devices which would be fabricated with these intermixing parameters will have higher losses.

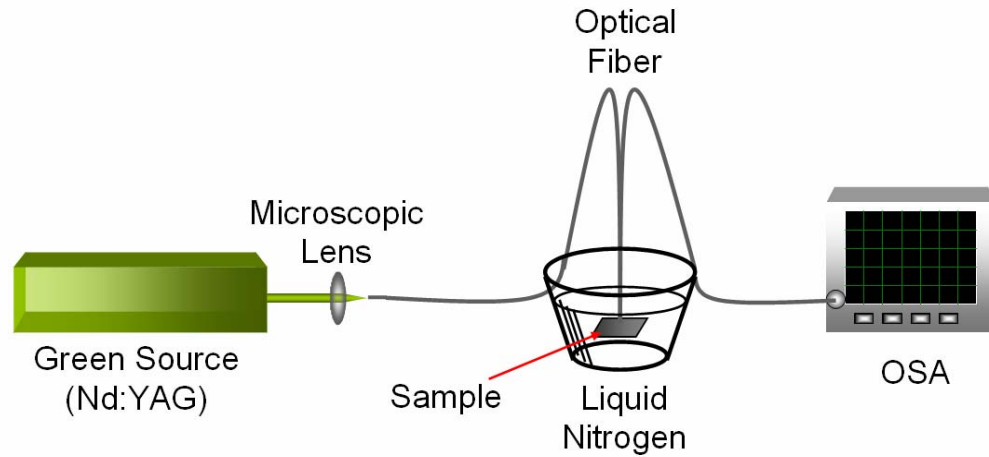


Figure 3-3 – Photoluminescence measurements setup.

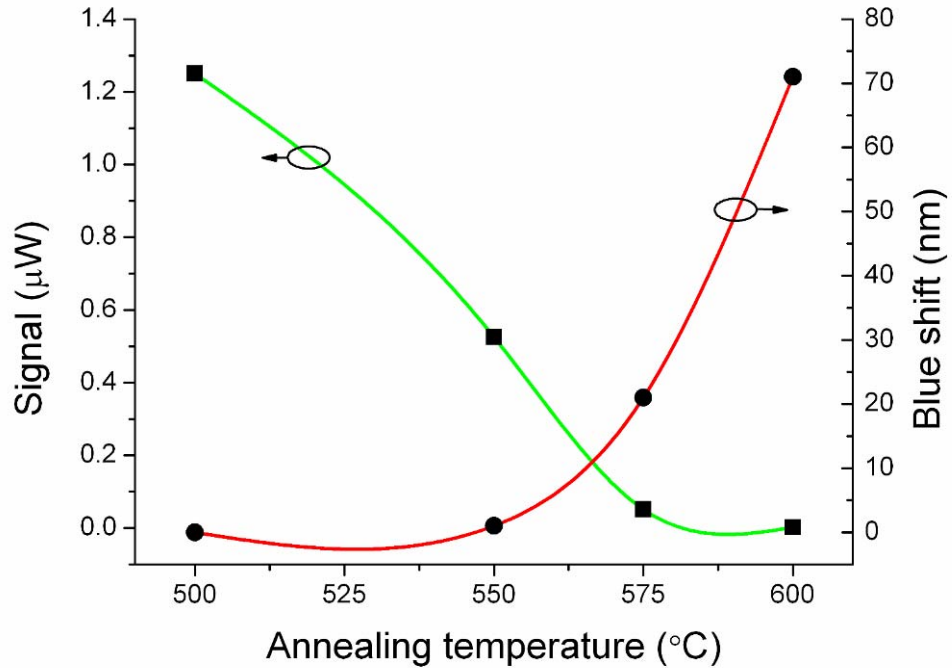


Figure 3-4 – Photoluminescence measurements of sputtered silica induced QWI at different annealing temperatures – annealing time is 60 s (solid lines are a smoothed fit to the data).

The point defects created by sputtered SiO<sub>2</sub> underneath the sample’s surface create the group III vacancies, and at higher temperatures these defects migrate deep into the epitaxial layers. It is understood that at these higher temperatures, the inter-diffusion of group III atoms is increased at the vacancies, which is also enhanced by desorption of Ga atoms into the deposited SiO<sub>2</sub> layer. The result of these effects increases the Al composition in the intermixed regions, and thus the band-gap of the material increases

to a higher energy. This diffusion based process is a temperature dependent [108], and higher annealing temperatures will result in an increased band-edge shift. However, at such higher temperatures, depending upon the material profile, the intermixing will result in a fully disordered structure, which has been observed in our case. This would degrade the optical transmission in the intermixed devices as the large defect concentration causes the scattering of light; and also, higher diffusion can significantly compromise the micron-scale resolution required for a 1<sup>st</sup> order phase-matching process. Although, sputtered SiO<sub>2</sub> can achieve the band-edge shift which is required to suppress the  $\chi^{(2)}$  in our case, the spatial resolution of this process is found to be poor in the literature and a value of tens of microns is reported [114].

### 3.2.2 Ion Implantation Tests

The mechanism by which ion implantation induced intermixing achieves QWI in the target material is significantly different to that of the sputtered SiO<sub>2</sub> process. In this process, high energy ions are bombarded on the surface of the material which can easily penetrate deep into the epitaxial layers. Each ion on collision with an atom dislocates it from its site (only nuclear/heavy-ion collisions can transfer the sufficient energy to cause the lattice dislocations), and also the energy which is transferred to the dislocated atom enables it to cause further dislocations. This gives a “tree like” dislocations effect, given in figure 3-5 (a). After implantation, the optical properties of the material are severely degraded, and a high temperature annealing treatment is required to repair this damage. At these higher temperatures the inter-diffusion of group III atoms occur at the dislocations, and consequently the relative Al composition increases in the regions which are ion implanted to cause QWI, figure 3-5 (b). This inter-diffusion is also assisted by desorption of Ga atoms into the SiO<sub>2</sub> layer, which is deposited on the sample surface prior to annealing. Similar to any QWI process, the optical transmission in ion implantation induced devices is degraded when higher doses of the ion-beam are employed; however, the lateral straggle in the case of ion implantation is much lower. A value of  $\sim 0.45 \mu\text{m}$  is predicted for this lateral straggle in [100], for 4 MeV As<sup>2+</sup> ion beam with an estimated ion range of 1.7  $\mu\text{m}$  in a similar material system as ours. We

estimate the ion straggle of  $<1 \mu\text{m}$  in our experiments using the same ion implantation parameters (more details are given in section 3.2.2.1).

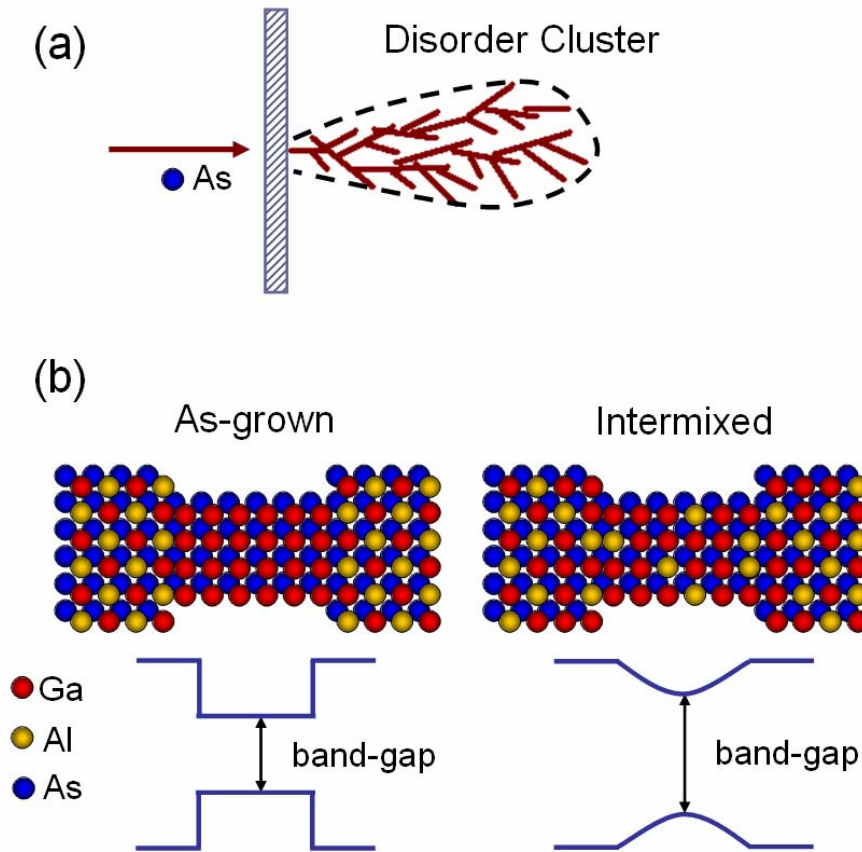


**Figure 3-5 – Ion implantation induced QWI, (a) Disorder cluster created in the result of high energy ion collisions, (b) The inter-diffusion of group III atoms increase the band-gap of intermixed material.**

Ion implantation for our samples was performed at Surrey Ion Beam Centre<sup>1</sup>. We have employed  $\text{As}^{2+}$  ion implantation to achieve the necessary QWI in our material. Selection of  $\text{As}^{2+}$  ions avoids introducing an impurity in the intermixed structure. The ion energy of 4 MeV, calculated by Transport of Ions in Matter (TRIM) software, and correspondingly reported in [100], has been used for the implantation.

The samples prepared for the ion implantation were initially cleaned with solvent based process, and a 200 nm protective cap of PECVD  $\text{SiO}_2$  was deposited. Intermixing tests

<sup>1</sup> <http://www.ee.surrey.ac.uk/IBC/>

were performed for various implantation doses and annealing temperatures (60 s anneal time), to characterize the blue shift in the material BMH1, which has a room temperature PL of 773 nm. Figure 3-6 summarizes these findings – implantation doses are in the scale of  $10^{13}$  ions/cm<sup>2</sup>. An average blue shift of 80 nm has been achieved using higher ion beam doses, which is 52 nm larger than previously reported in a conventional multiple quantum well (MQW) structure with half-band-gap at 1550 nm [115].

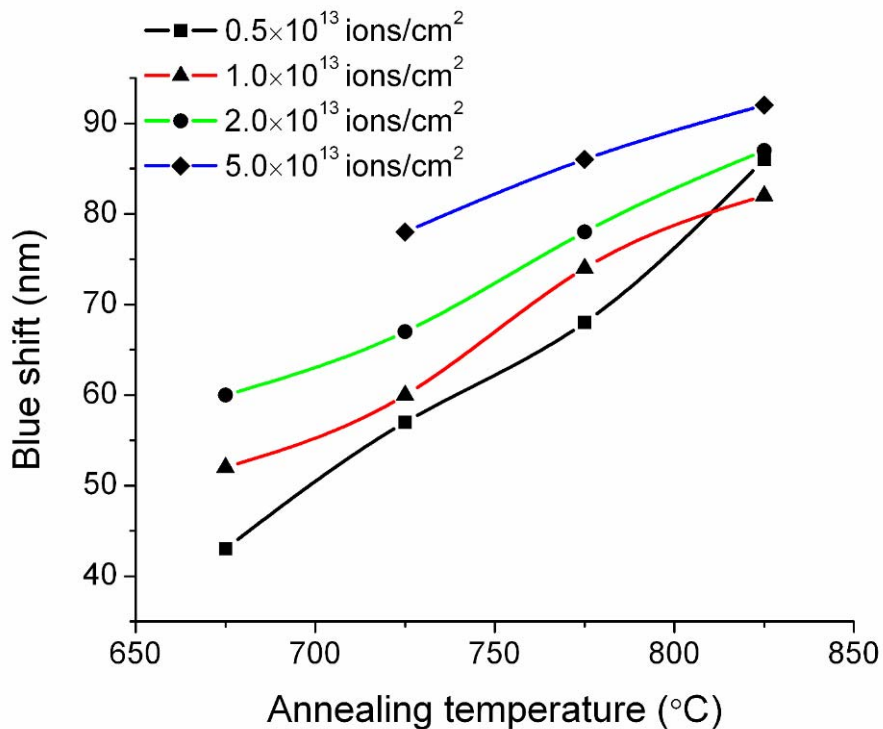


Figure 3-6 – Photoluminescence measurements of ion implantation induced QWI at different annealing temperatures – annealing time is 60 s (solid lines are a smoothed fit to the data).

In order to measure the linear losses for different implantation doses, 2 mm long Fabry–Pérot (FP) waveguides were fabricated in each case. The samples which were used for these devices were given an initial RTA treatment of 775 °C for 60 s. Figure 3-7 shows these measurements over a range of transmission wavelengths, which have been obtained using the FP resonance method [116]. The losses for the as-grown material have an average value of  $0.55 \text{ cm}^{-1}$ .

As we increase the implantation dose the transmission loss increases, e.g., in the case of  $2 \times 10^{13}$  ions/cm<sup>2</sup> dose a blue shift of 78 nm has been measured, and the loss coefficient

in this case is  $2.5 \text{ cm}^{-1}$ . This shows that the optical properties of intermixed material are fairly retained, which makes ion implantation much appreciated to achieve the necessary band-edge shift. These measurements have been reported in [117]. In comparison to ion implantation, the transmission loss in the case of sputtered  $\text{SiO}_2$  has been reported to be  $4\text{-}4.4 \text{ cm}^{-1}$  in InGaAsP material system for a blue shift of 110 nm [118], and similarly, an average value of  $4.25 \text{ cm}^{-1}$  has been reported for AlGaInAs material system which is  $>100 \text{ nm}$  blue shifted [119]. The transmission loss for the sputtered  $\text{SiO}_2$  intermixing was not measured in our material system.

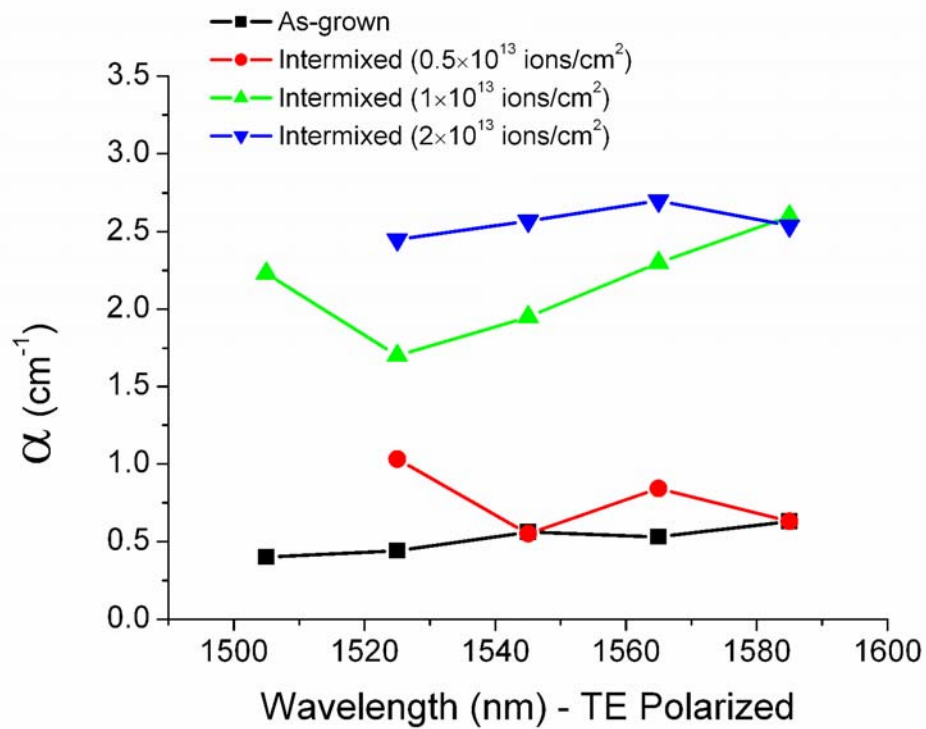


Figure 3-7 – linear loss measurements for different implantation doses, samples were annealed at  $775 \text{ }^\circ\text{C}$  for 60 s.

Another issue which was considered while selection of the dose for subsequent fabrication is the ions flux in smaller gaps. The values which have been reported above were all obtained from the intermixed samples on which no patterns were created; however, in the case of final devices the implantation has been performed using a periodic gold mask ( $3\text{-}5 \text{ }\mu\text{m}$  periods). It is understood that in these small openings, the concentration of ions reaching the core is spread, due to straggle, and is, therefore, lower than the surrounding open regions on the sample. This deviates the desired ion

implantation required in these small openings and affects the required periodic  $\chi^{(2)}$  modulation. Taking these effects into account, after analyzing all the measurements and the physical constraints, the dose of  $2 \times 10^{13}$  ions/cm<sup>2</sup> was selected for the various second order non-linear process demonstrations, which have been given later in this chapter.

### 3.2.2.1 Lateral Straggle in Ion Implantation

It has been reported earlier [99], that the spatial resolution of the intermixing process is highly critical to achieve a maximum modulation in the nonlinear coefficients. The intermixing processes in which the point defects are migrated into the buried layers by diffusion at high temperature annealing could compromise the required resolution for a 1<sup>st</sup> order QWI grating. Therefore, it is imperative to identify the lateral straggle of an intermixing process in the wave-guiding core.

The ion implantation for the test samples was performed assisted with a 2  $\mu$ m thick gold mask. The periodic mask was grown into the patterned E-beam resist on the sample's surface using the gold electroplating. Gold has a high density of 19.3 g/cm<sup>3</sup> which can protect the as-grown properties in our superlattice core, provided that the mask thickness is large enough for 4 MeV implantation energy. These test samples were prepared with various duty cycles of the periodic gold mask – the duty cycle in this case is the designed E-beam mask which is slightly different from the actual duty cycle of the developed E-beam resist, more details of the fabrication process are presented later in this chapter.

Figure 3-8 (a) shows the top view of one of the test samples, with gold mask at the surface which has a period of 3.5  $\mu$ m and the designed duty cycle is 60% masked: 40% exposed. This sample, which was implanted with As<sup>2+</sup> ions  $2 \times 10^{13}$  ions/cm<sup>2</sup> dose and 4 MeV energy, is presented in a cross-sectional view in figure 3-8 (b). Material contrast is clearly visible under the SEM in figure 3-8 (b) – the light shade in the middle which spans horizontally is the superlattice core, the horizontal dark shade is Al<sub>0.85</sub>Ga<sub>0.15</sub>As base layer, and the tear-drop shaped implantation pattern is also visible in the lighter shade. The implantation duty cycle is approximately 55% intermixed: 45% as-grown,

which has been reported to result the maximum conversion in a phase-matched process [120]. The lateral straggle from these measurements is estimated to be  $\sim 0.9 \mu\text{m}$ . This straggle will slightly increase after annealing the samples due to domain diffusion which could not be measured. It should be mentioned here that the material contrast was only visible in un-annealed samples after the implantation, whereas, no contrast was observed in the same samples after RTA treatments, which is attributed to the damage repair at such high temperatures. A synopsis of all these implantation tests is provided in appendix II.

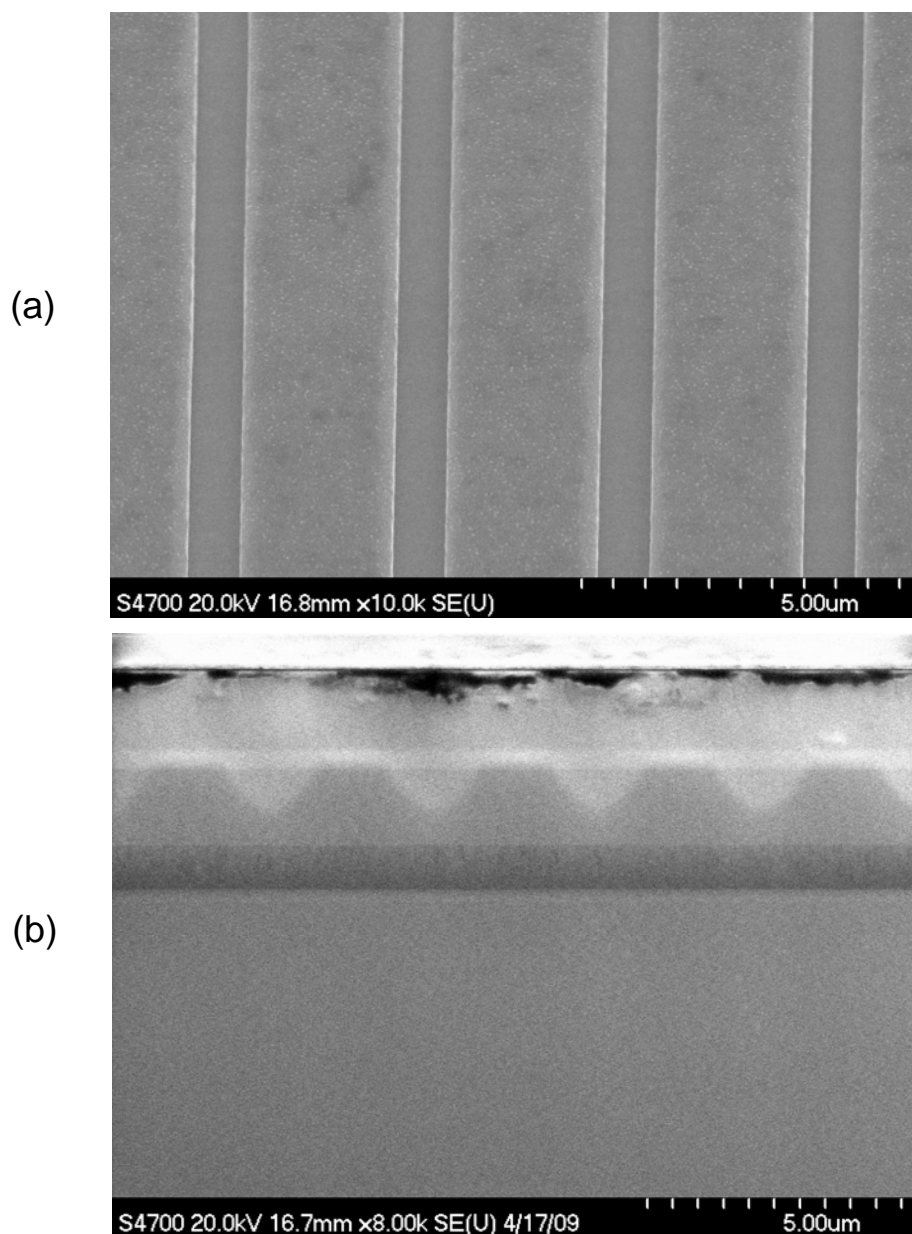


**Figure 3-8 – (a) Top view of the periodic electroplated gold (designed as: 60% masked / 40% exposed), (b) Cross-sectional SEM micrograph of the same duty cycle after ion implantation.**

Table 3-1 summarizes the two intermixing processes for the selection criteria which have been considered when deciding the course of action in this research.

	<b>Sputtered SiO<sub>2</sub></b>	<b>Ion Implantation</b>
<b>Blue shift</b>	Large (maximum achieved is 70 nm in our case; however, more than 100 nm has been reported in the literature).	Large (maximum achieved is >90 nm in our case for a higher ion beam dose).
<b>Transmission loss</b>	Reported to be 4-4.5 cm <sup>-1</sup> for >100 nm blue shift [118-119].	Measured to be 2.5 cm <sup>-1</sup> for 78 nm blue shift.
<b>Lateral straggle control</b>	Poor, and is reported to be tens of microns in the literature [114].	Very promising, and is estimated to be <1 μm in our experiments.
<b>Cost</b>	Low, as fairly simple processing is required.	High, as the implantation can only be performed at the specialist facilities.

**Table 3-1 – Intermixing process selection criteria**

In conclusion, sputtered SiO<sub>2</sub> is a fairly robust intermixing technology, and it has been proven to achieve good quality devices; however, its application is limited by its poor spatial control which is critical in our case. One can reason to circumvent this control by selecting a higher order QPM period, and it has been demonstrated using 3<sup>rd</sup> order grating with periods in the range of 10.5-12.4 μm [121]. However, the higher order period requires much longer devices to achieve the same conversion efficiency which can be achieved in a 1<sup>st</sup> order grating, and also, this efficiency is limited by the optimum length of the device which is related to the losses at the band-gap wavelengths. Therefore, to proceed further in this research it was decided to use the ion implantation induced intermixing which has been demonstrated to give improved conversion efficiency in the previous literature for various second order nonlinear processes.

As identified earlier in the chapter introduction, we have employed the optimization in second harmonic generation to achieve the optimization in QPM, which is presented next.

### 3.3 Second Harmonic Generation (SHG)

The earliest demonstration of SHG [42] in a quartz crystal established one of the research foundations in optical harmonics. The follow up of this demonstration, and the studies of the nonlinear properties in potential materials [122-123], have lead the way forward in realizing tunable coherent sources. The operational environment and the large footprint of these sources have made their integration not viable in modern optoelectronics. GaAs has been much investigated as a potential material in such integrated coherent sources, as it benefits from the sophisticated fabrication technologies, and its large nonlinear second order susceptibility  $\chi_{xyz}^{(2)}$  of  $\sim 340$  pm/V for near-infrared wavelengths [124], which is much larger than that of the ferroelectrics.

A detailed study has been conducted to optimize QPM SHG in our material, and subsequently, to optimize the generation of phase-matched parametric fluorescence at the half-band-gap – which is the main aim in our designed OPO. Phase matching results in a higher signal buildup when the domain reversal techniques are employed, as compared to the domain disordering techniques. In these lines, SHG has been demonstrated using periodic domain inversion achieved by wafer bonding in [36]. Higher scattering losses, unequal domain dimensions, and bonding losses, have been identified as the main contributing factors in the lower efficiency reported in this experiment. Fabricating a domain inverted structure is a significant challenge which also limits its applications in the integrated optoelectronics. An efficient way of achieving periodic domain inversion has been demonstrated by orientation patterned growth (OPG) in GaAs–AlGaAs [125-126]. In this technique a thin layer of Ge is deposited on GaAs substrate, which is followed by a thin layer of GaAs deposition with a  $90^\circ$  rotation around the growth axis of the underneath GaAs substrate (usually [001]). This rotation results in the inversion symmetry in the zinc-blende crystal structure of GaAs–AlGaAs. In order to define the periodic domain inversion, a photolithographic

and a wet-etch procedure is performed for the required QPM period. Finally, the claddings and the wave-guiding layers are grown. Using this OPG method, an efficient continuous wave SHG has been demonstrated in AlGaAs material system for 1.55  $\mu\text{m}$  pump wavelengths [127]. However, the shortfalls include the lack of monolithic integration in a single chip device, and the waveguide corrugation which arises from the initial template layout causes scattering.

This leads us to the techniques, as identified in section 2.2, to achieve QPM and hence the modulation in the second order nonlinearity. The demonstration by Helmy et al. [121], shows that the sputtered  $\text{SiO}_2$  has been employed to modulate  $\chi_{zxy}^{(2)}$ , but the 3<sup>rd</sup> order grating has compromised the necessary QPM resolution, and it has resulted in a lower efficiency. Ion implantation induced intermixing has been found to be the most effective to achieve sub-micron lateral straggle, required for a 1<sup>st</sup> order QPM grating. This intermixing technique has also been recommended earlier in [99], and has been experimentally demonstrated in [100-101]. Authors in reference [101], have used 5 MeV  $\text{As}^+$  ion beam to achieve QPM in asymmetric quantum wells, but the modulation in the lower  $\chi_{zzz}^{(2)}$  (as compared to bulk like  $\chi_{xyz}^{(2)}$ ) has limited the efficiency. Therefore, we have modulated  $\chi_{zyx}^{(2)}$  and  $\chi_{xyz}^{(2)}$  in our periodically intermixed superlattices to achieve SHG in type-I and type-II polarization configurations.

The next details in this chapter include initial analyses, followed by the fabrication process to achieve QPM waveguides, and the tests performed on these passive devices to demonstrate second order nonlinear processes. The fabrication related issues and findings have also been included, and a complete process is presented which has been developed to achieve the monolithic integration in a fully integrated OPO.

### 3.3.1 QPM Period

The quadratic dependence of the SHG power on the fundamental power requires the phase matching period to be closer to the degeneracy point, i.e., the period for which the

band-gap wavelength is converted equally into the half-band-gap wavelengths. The phase matching condition for SHG is given as:

$$\Delta k = k_{2\omega} - 2k_{\omega}$$

The signal build-up in the case of SHG is much higher if the phasing matching condition stated above is equal to the period of QWI.

$$\Delta k = \frac{2\pi}{\Lambda} \quad (\Lambda \text{ is the period of QWI})$$

This equates the phase matching condition in term of QWI period as:

$$\frac{2\pi}{\Lambda} = \frac{2\pi\eta_{eff}2\omega}{\lambda_{2\omega}} - 2 \times \frac{2\pi\eta_{eff}\omega}{\lambda_{\omega}}$$

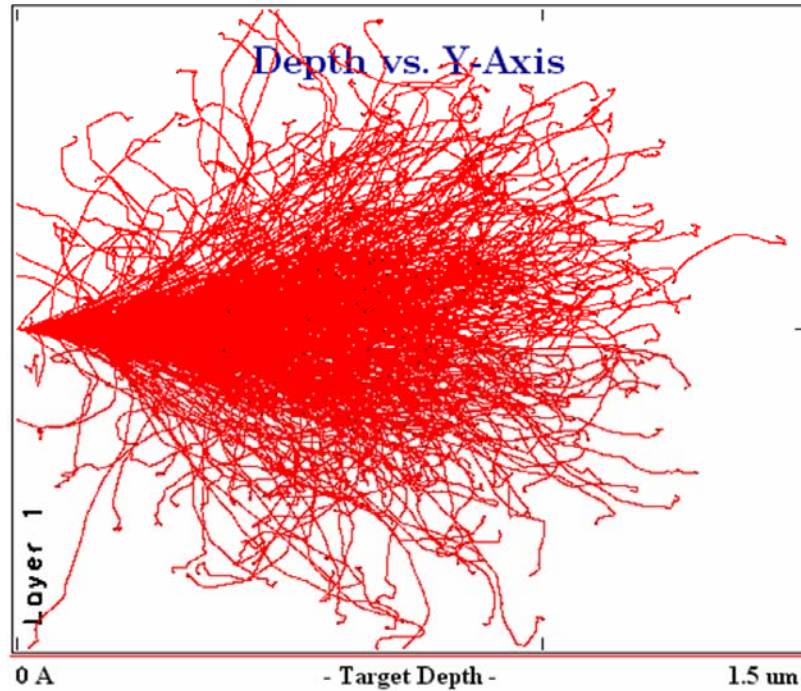
(Where  $\eta_{eff}$  is the effective refractive index of the guiding structure)

The earlier study [99], has given an estimate of 3-7  $\mu\text{m}$  phase matching period, for a 1<sup>st</sup> order grating.

### 3.3.2 Ion Implantation Mask

The ion implantation induced QWI has proven to be the suitable choice to achieve the required phase matching spatial resolution. Therefore, it is necessary to identify the materials that can be used as a protective mask for implantation. The higher density of

gold ( $19.32 \text{ g/cm}^3$  at room temperature) has made it an attractive choice [100-101]. The maximum penetration of 4 MeV  $\text{As}^{2+}$  ions is  $1.5 \mu\text{m}$  in gold, given in figure 3-9 – which is a snap-shot of Transport of ions in matter (TRIM) software.

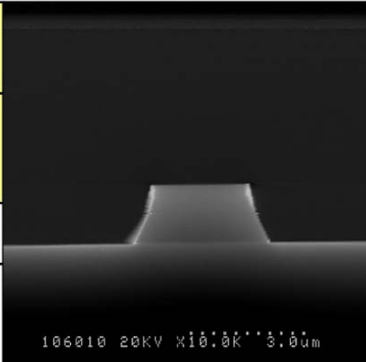


**Figure 3-9 – Simulated penetration of  $\text{As}^{2+}$  ions in gold.**

Gold mask requires a seed conducting layer at the sample's surface, and a patterned resist on top of it which provides protection against the gold growth; electroplating process then grows the metal mask starting from the sample's surface. The vertical profile of gold mask is critical for the ions flux to reach the sample's surface, which depends upon the resist profile. Some tests were conducted initially for the resist selection based on the said criteria.

Photolithography, which can easily achieve  $1\text{-}2 \mu\text{m}$  size features with high precision [128], had been a fine start. The tests in this case were performed using photo-resists that can achieve a height of  $1.5 \mu\text{m}$  after patterning. The process development in this case was comprehensive and various photolithography parameters were experimented and tuned to reach an optimized process. For example, the standard photolithography employed in the clean room for S1818 resist is: 30 s spin at 4000 RPM (which gives the

resist height of 1.8  $\mu\text{m}$ ), 30 min oven bake at 90 °C, 4 s exposure under Maskaligner-6 (MA-6) tool, and finally 60 s development in 1:1 Microposit:H<sub>2</sub>O developer. In these lines, our experiments were designed for the same resist spinning parameters; however, the hotplate baking was performed on one set of samples, along with the oven bake on the other set. It should be mentioned that the specification sheet of the resist identify hotplate baking to be an optimum course (115 °C for 60 s). In addition to different baking procedures, the exposure of the resist was also performed for various times, i.e., starting from 3.8 s it was increased up to 5 sec over a range of samples. Finally, each set of samples was developed for different times, i.e., 50 s, 60 s, and 75 s. the resist profile in each case was measured under the SEM, and it was found unacceptable in almost all the cases. The best resist profile achieved using the developed photolithography is given in figure 3-10, which shows the cross-sectional view (the details of some these experiments are given in appendix III).

R9	Category	Spin Speed	Thickness	Bake	
<b>Resist</b>	S1818	4000 RPM x 30 sec	1.8 $\mu\text{m}$	125 °C / 2 min (Hotplate)	
<b>Exposure</b>	4 sec exposure (MA-6)				
<b>Development</b>	60 sec (1:1 Micro Dev:H <sub>2</sub> O)				

**Figure 3-10 – Cross-sectional view of the developed photolithography.**

It is observed that the intended side wall verticality has not been achieved; this could be caused by an improper exposure, as it has been found in the literature that the resist edge beads introduce a gap between the mask and the resist surface and causes interference. To resolve this, some tests were performed in which the resist was carefully removed from the edges of the samples; however, this did not give us the required profile. Another reason for an improper exposure could be the MA-6 lamp. It has been discovered in the specifications sheet that the resist has been optimized for the g-line exposure (435 nm), and it can be effective over the spectrum of a standard mercury lamp (g-line 436 nm, h-line 405 nm, and i-line 365 nm). One can argue that

this exposure could be optimized by using appropriate filters; however, this could not be performed in our case where the maintenance of the MA-6 tool is restricted only to the staff.

The unsatisfactory results using photolithography, compelled us to develop the fabrication process using Electron-beam (E-beam) lithography. For this purpose, positive tone Poly Methyl Methacrylate (PMMA) resist has been used. The bi-layer 15%15% PMMA has given us the thickness of  $\sim 2.5 \mu\text{m}$  resist at 4000 RPM (spinning speed) for 60 sec – this should suffice the later gold growth. Several dose tests were conducted, and one of them is given in figure 3-11. The cross-sectional SEM micrograph of the resist shows that the required vertical side wall profile has been achieved – the charging effects under E-beam are also visible in the image.

### 3.3.3 Protective Dielectric Cap

Gold mask, which has been grown using electroplating, required a protective cap on the sample's surface against potential penetration of the metal into the semiconductor. Also, this protective cap would prevent any surface damage which has been observed during subsequent cleaning in various wet-etch chemicals [100]. The selection of protective dielectric cap was decided after performing some tests. These tests included the PL measurements of the annealed material with a protective cap, and an effective removal of this cap. The tested protective layers were PECVD  $\text{SiO}_2$  and inductive coupled plasma (ICP)  $\text{Si}_3\text{N}_4$ . It has been identified in [107], that  $\text{Si}_3\text{N}_4$  cap layer does not introduce IFVD in the material at the annealing temperatures near  $800^\circ\text{C}$ , but  $\text{SiO}_2$  cap layer does introduce a slight band-edge shift. Similar tests were performed on our material, and the measured PL of the samples with 200nm thick ICP  $\text{Si}_3\text{N}_4$  deposited and then annealed at  $775^\circ\text{C}$  did not indicate any blue shift; however, PECVD  $\text{SiO}_2$  with similar thickness and annealing temperature introduced a blue shift of 5 nm. Therefore  $\text{Si}_3\text{N}_4$  seemed a better choice, but the cracks which were observed on the surface after annealing indicated a stress. On the other hand, the samples which were deposited with  $\text{SiO}_2$  had their surface intact and clear after annealing. The wet-etch of protective layers in buffered Hydrofluoric (HF) solution showed that  $\text{SiO}_2$  is easily removed to give a

clean surface, whereas  $\text{Si}_3\text{N}_4$  is difficult to remove and has a very slow etch rate once it is annealed. Therefore, these tests conclude the robustness of PECVD  $\text{SiO}_2$  against ICP  $\text{Si}_3\text{N}_4$  during different process stages, even if there is a slight compromise in the band-edge shift.

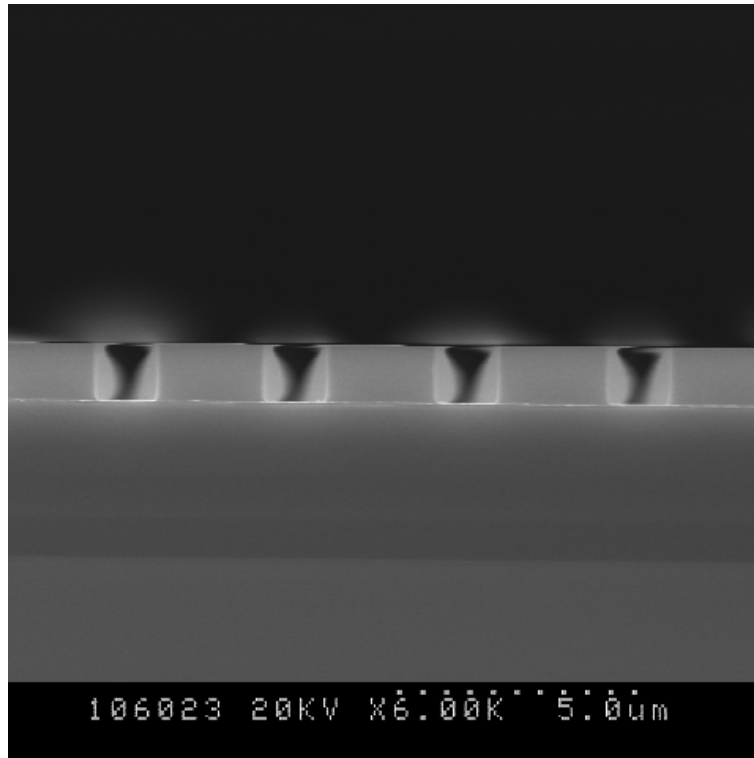


**Figure 3-11 – Cross-sectional view of a dose test performed using 15% PMMA.**

### 3.3.4 Device Design

The optimization consideration required us to identify the QPM period for which the maximum SHG power is achieved. For this purpose, E-beam mask was designed with various even ( $3.6 - 4.4 \mu\text{m}$ ) and odd ( $3.5 - 4.5 \mu\text{m}$ ) periods to achieve the 1<sup>st</sup> order phase matching, given in figure 3-12. Each period incorporated three different duty cycles: 40:60, 60:40, and 50:50, and a single grating pattern of E-beam mask (single period with a specific duty cycle) had the designed width of  $100 \mu\text{m}$  – this dimension would accommodate four waveguides defined in the later stage for a single grating pattern. The waveguide dimensions were designed to be  $3.5 \mu\text{m}$  wide and  $1 \mu\text{m}$  deep ridges – the design was optimized with multiple beam-propagation-based simulations

using commercial software BeamPROP<sup>2</sup>. The mode profile at half-band-gap wavelength is given in figure 3-13.

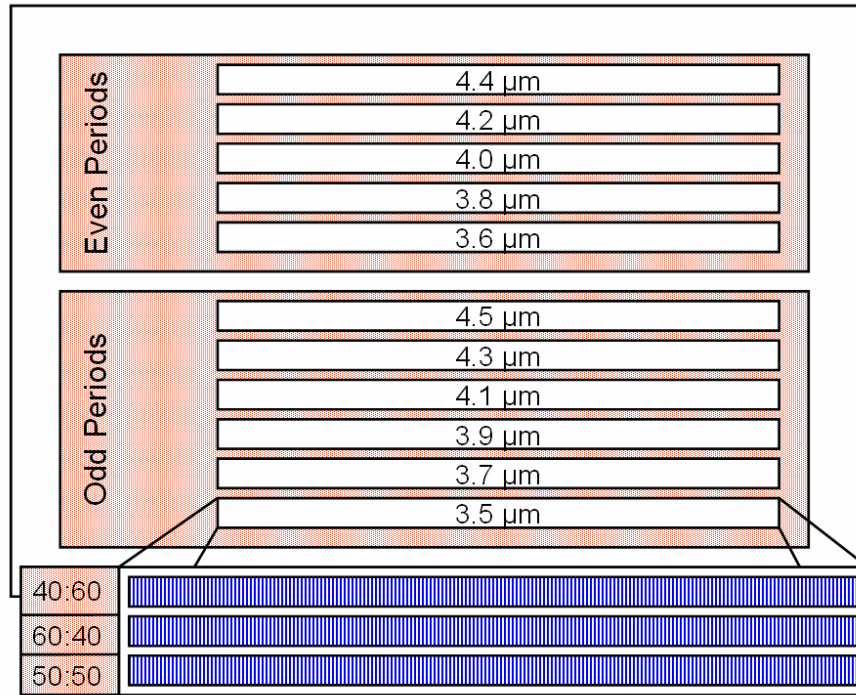


Figure 3-12 – Designed E-beam mask for QPM samples.

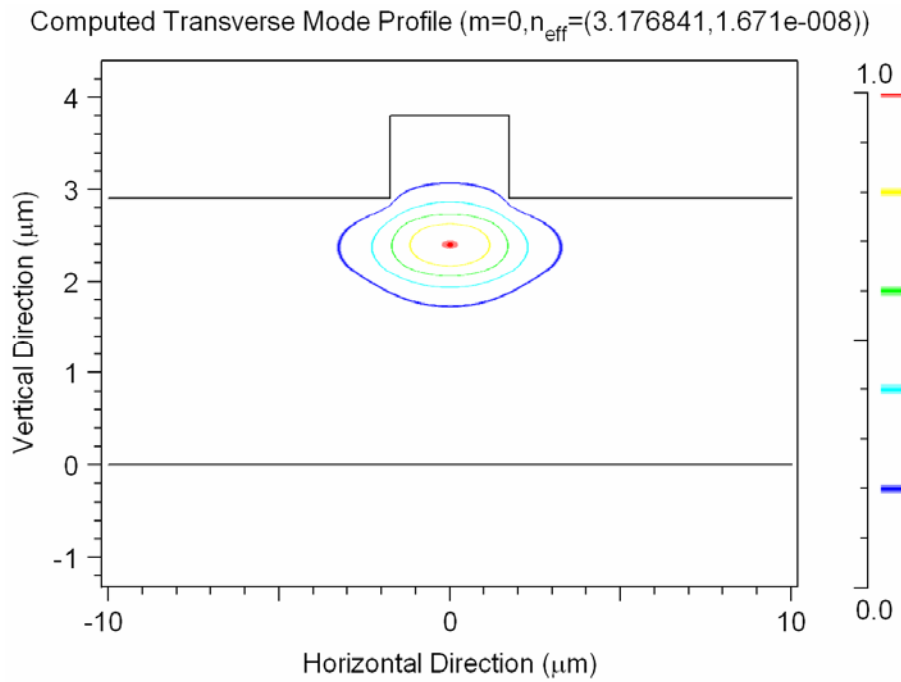
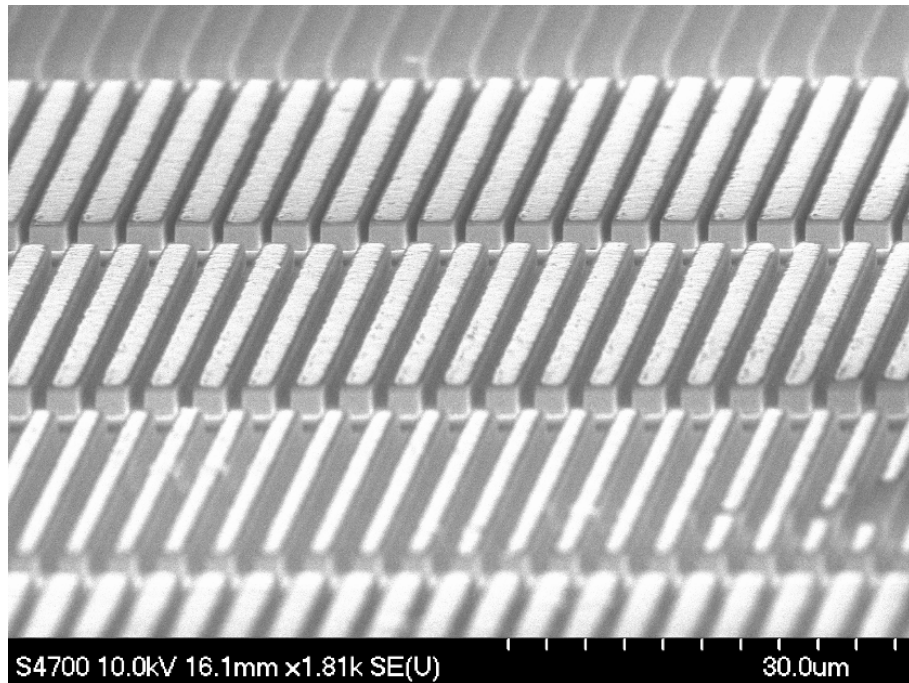


Figure 3-13 - Mode profile of the designed waveguide at 1550 nm.

<sup>2</sup> BeamPROP from Research Software (Rsoft) Inc.

### 3.4 Sample Fabrication

The fabrication process involved: 1) deposition of 200 nm thick PECVD SiO<sub>2</sub> protective layer, 2) sputtering of 40 nm Au/5 nm Ti seed layer, 3) patterning the samples with 15%15% PMMA (in E-beam), and 4) 2 μm thick gold mask. The samples were then placed in SVC-14 resist stripper in a hot water bath (50 °C), and mounted on a carrier wafer to be sent for ion implantation. Figure 3-14 shows the SEM image of a test sample, the periodic gold mask is visible from the top view.



**Figure 3-14 – SEM image of the periodic gold mask created over a test sample.**

The samples were then sent to Surrey Ion Beam Centre to be implanted with 4 MeV As<sup>2+</sup> ions, with a dose of  $2 \times 10^{13}$  ions/cm<sup>2</sup>. After implantation, the gold was removed by wet-etch in potassium iodide/iodine (KI/I<sub>2</sub>) solution – the etch rate was found to be ~700 nm/min. SiO<sub>2</sub> protective cap was then removed by wet-etch in HF solution (which would remove the Ti adhesion layer as well), and a fresh layer of 200 nm SiO<sub>2</sub> was deposited for annealing at 775 °C, which was removed later again by HF cleaning. Lastly, a quick treatment of GaAs cap removal was performed on the samples using citric-acid: hydrogen-peroxide (5:1) solution. This cleaning, which selectively etched

GaAs as compared to AlGaAs, was employed for the passive material only; as the contamination, which has been later investigated and presented in detail under the fabrication optimization, was very challenging to remove.

The waveguides were patterned using negative tone hydrogen silsesquioxane (HSQ) E-beam resist, and were finally defined using reactive ion etching (RIE) in  $\text{SiCl}_4$  plasma. Dose and developing processes for each of these steps were optimized. Figure 3-15 shows the SEM image of a final sample which has been used for further characterization.

## 3.5 Characterization

### 3.5.1 Type-I SHG

Type-I phase matching is occurred when the fundamental field is TE polarized and the induced SHG is TM polarized [129]. The linearly polarized pump is coupled into the device which generates the linearly polarized second harmonic, figure 3-16 (a).

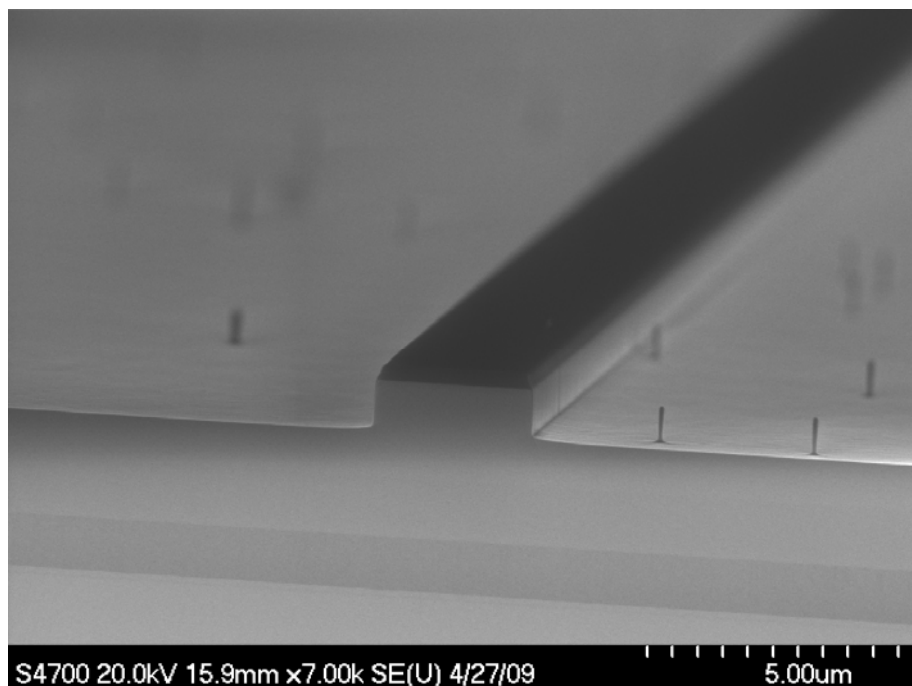


Figure 3-15 – Cross-sectional view of the final sample – dark shaded HSQ resist is visible.

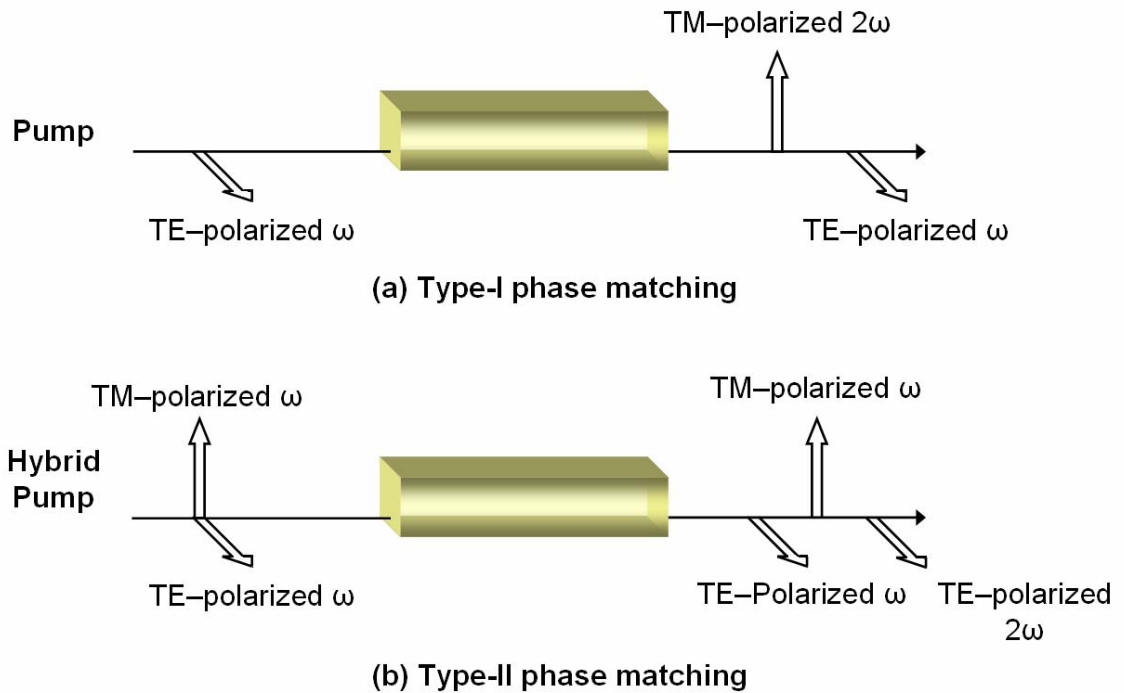


Figure 3-16 – SHG phase matching polarization configurations.

**Pulsed SHG** — has been measured in our devices cleaved to the length of 0.7 mm. The calculated group velocity mismatch for 1.3 ps pulses in a related material has limited the optimal length to be at 0.6 mm for maximum SHG [120]. Characterization was done using an OPO synchronously pumped by mode-locked Ti: Sapphire laser. Input light of 1.35-1.5 ps pulses with a maximum power of 185 mW at the facets was end-fire coupled into the waveguides using a microscopic objective lens. The output SHG was measured using a silicon photo-detector. Figure 3-17 shows the schematic diagram of the experimental setup. An average SHG power of 2.04  $\mu\text{W}$  was measured, which has been achieved due to the higher fundamental transmission (explaining the better sample quality). Linear loss at the fundamental was measured to be  $0.9 \text{ cm}^{-1}$  for a 3.5 mm long sample cleaved from the same chip. Peak SHG power was  $\sim 3.65 \mu\text{W}$ , measured for 3.8  $\mu\text{m}$  period (50:50 duty cycle) with 123 mW input power at the facet, and at a phase matching wavelength of 1583 nm. The pulse spectrum of the phase matched type-I SHG is given in figure 3-18 [130].

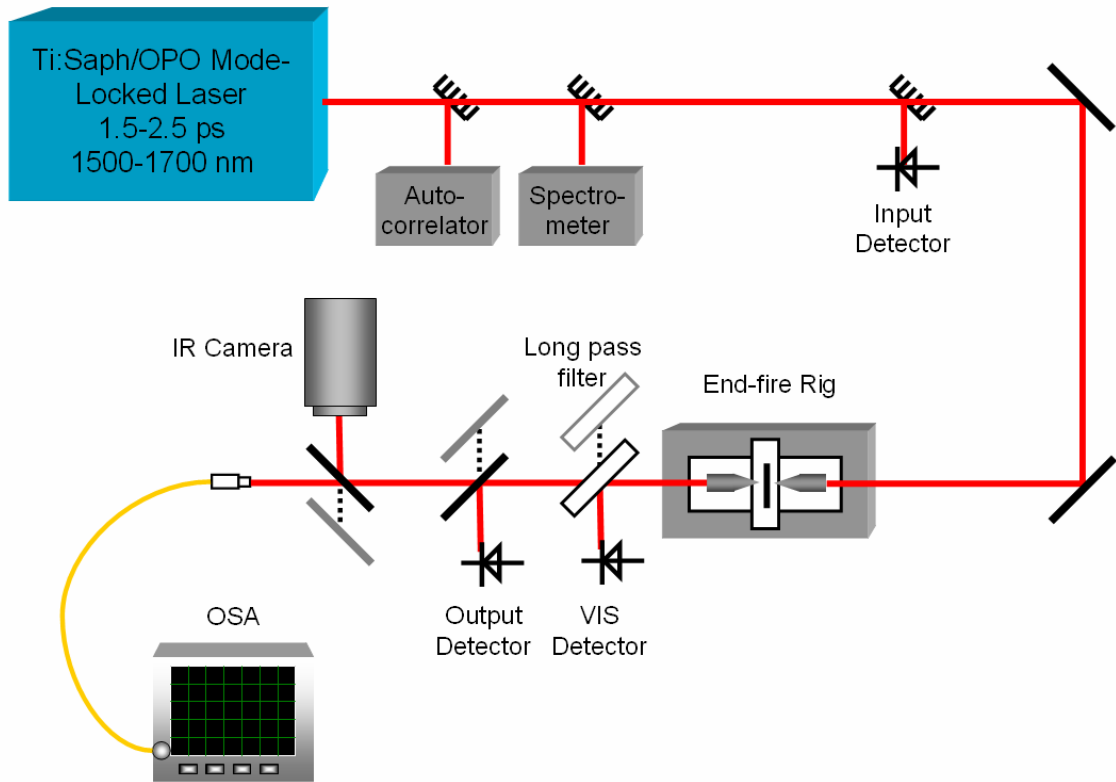


Figure 3-17 – Schematic diagram of the type-I SHG measurements setup.

A figure of merit for the SHG is given by the internal conversion efficiency, which is calculated for the type-I phase matching as:

$$\eta_I = \bar{P}_{2\omega}^{TM} / (\bar{P}_{\omega}^{TE} L)^2$$

The peak type-I SHG conversion efficiency in our case is calculated to be 250 % W<sup>-1</sup> cm<sup>-2</sup>, after accounting for the losses (output optics, facet reflectivity, etc). The peak SHG for type-I phase matching reported in the literature is ~1.5 μW (~40 % W<sup>-1</sup> cm<sup>-2</sup>) for a 1<sup>st</sup> order QPM using ion implantation induced intermixing [100], and it is ~110 nW (~13 % W<sup>-1</sup> cm<sup>-2</sup>) for a 3<sup>rd</sup> order QPM using sputtered SiO<sub>2</sub> [121]. The improvement in our case has been achieved due to the significant fabrication process optimization and a good QWI control.

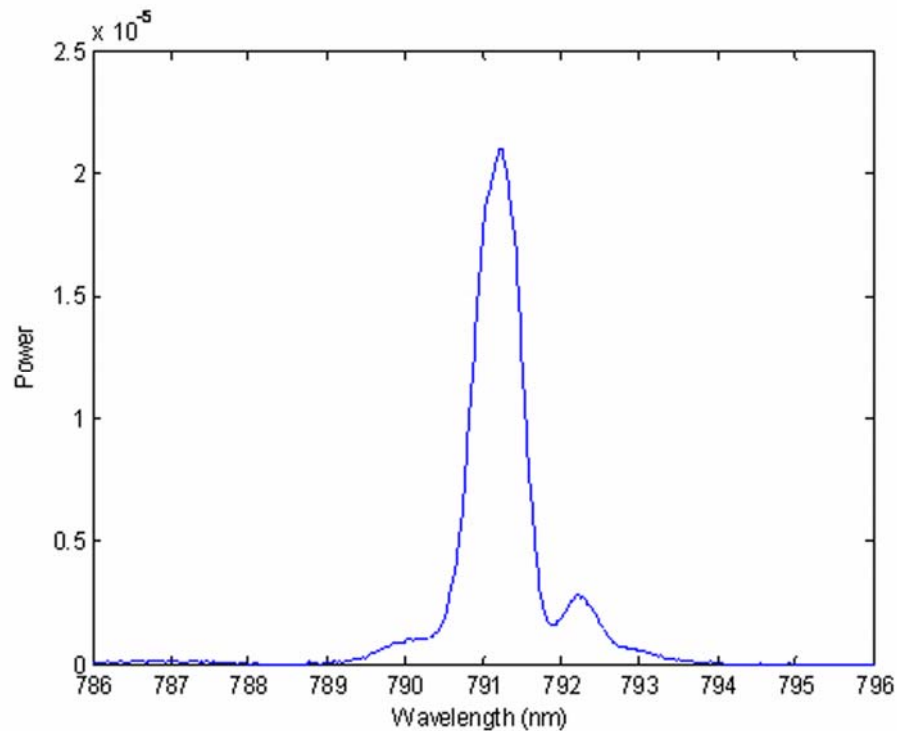


Figure 3-18 [130] – Pulse spectrum of the phase matched type-I SHG – the curve resembles  $\text{Sinc}^2$ -function which is consistent with the phase-matched process.

**Continuous wave (CW) SHG** — has been measured for the first time in our devices, and subsequently reported in [131]. Samples were cleaved to the length of 3.5 mm and the characterization was conducted using a tunable CW C-Band (1530 nm – 1565 nm) laser. The input power was enhanced up to 350 mW using an erbium-doped fiber amplifier (EDFA). The light was end-fire coupled into the waveguides using a microscopic objective lens, and was measured using a silicon photo-detector. Linear optical losses were measured to be  $0.9 \text{ cm}^{-1}$  using the FP method. The maximum SHG power of  $1.6 \text{ }\mu\text{W}$  was achieved on a FP peak, with an input power of 310 mW at the input facet. The normalized conversion efficiency in this case has been calculated to be  $0.18 \text{ \% W}^{-1} \text{ cm}^{-2}$ . The tuning curve, figure 3-19 [131], shows the asymmetric FP features while scanning from shorter to longer wavelengths. The scan interval is 0.01 nm which is kept shorter than measured 0.1 nm free spectral range (FSR) at the input fundamental. A delay of 3 sec was added between the scan points to account for the measured settling down time for 310 mW input. The scan shows a dotted red line obtained by filtering the data which resembles the  $\text{Sinc}^2$  phase matching behavior of the

SHG. The  $\text{Sinc}^2$  asymmetry in this case could be the result of absorption, as this feature is at the band-edge for the second harmonic. However, the exact source for this asymmetry is unclear and requires further investigation. The filtered tuning curves for three different input powers are given in figure 3-20 [131]. Increased input power shifts the phase matching wavelength to the longer side, which is an affirmation of the change in the effective refractive index.

The inset in figure 3-19 [131], shows a bistable hysteresis loop when performing forward and reverse scans with a reduced scan interval of 0.002 nm. This bistability is attributed to the thermo-optical effects which occur due to the whole sample heating [132]. Bistability is observed for the fundamental wavelength outside the phase matching band width, and also, in the as-grown samples with no QPM periods at all; therefore, SHG has unnoticeable effect in this process. The linear optical loss of  $0.9 \text{ cm}^{-1}$  which is dominating these heating effects, gives us the calculated absorbance of 64 % for a 3.5 mm long sample, which results in tens of mW of the absorbed power.

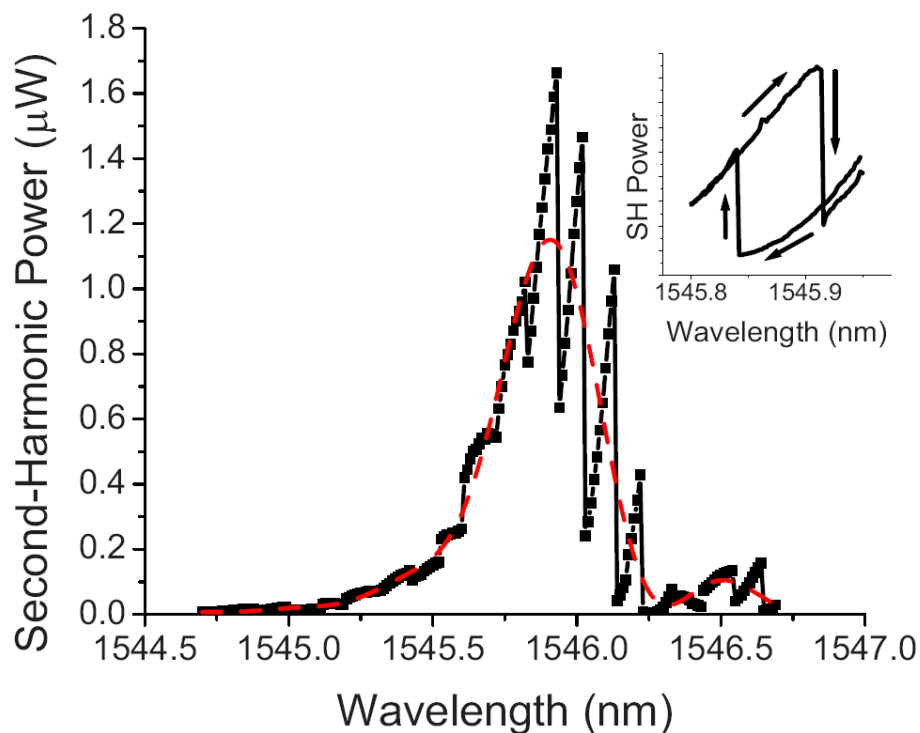


Figure 3-19 [131] – Tuning curve for CW SHG.

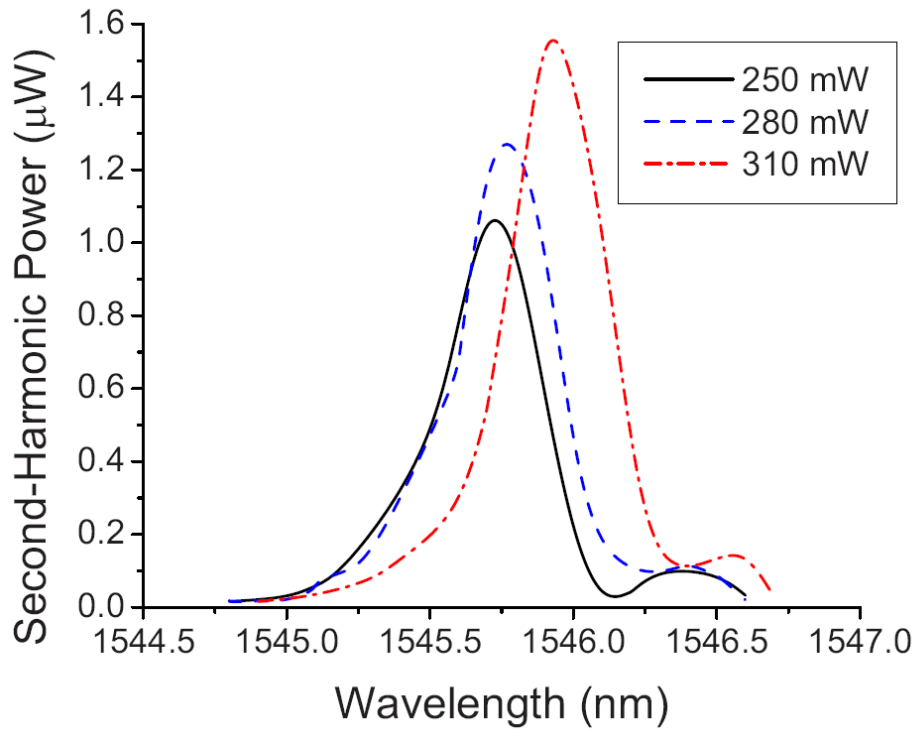


Figure 3-20 [131] – Filtered tuning curves for CW SHG with increasing input powers.

In summarizing, we have been able to measure CW SHG for the very first time in this material regime, which confirms our claim of achieving highly optimized fabrication process, and the periodic QWI control in a sub-micron scale.

### 3.5.2 Type-II SHG

The second order susceptibility is non-degenerate in GaAs–AlAs superlattices [38]. The calculated modulation in the  $\chi^{(2)}_{xyz}$  is  $\sim 60$  pm/V, which is larger than the modulation in  $\chi^{(2)}_{zxy}$  for 14/14 ML GaAs/AlAs superlattice. Further more, the material we have employed is grown in [001] crystal axis, which will result the waveguide facets in [110]. The Type-I phase matching in this case, corresponds to the modulation in  $\chi^{(2)}_{zxy}$ , and the Type-II phase matching corresponds to the modulation in  $\chi^{(2)}_{xyz}$ . This concludes that the Type-II phase matching will result in higher SHG power in our devices. The eventual motive of this investigation is to monolithically integrate the phase matched nonlinear section with an on-chip pump superlattice laser. The selection rules identify

the pump to produce laser action in TE polarization, which makes it critical to measure the device performance in type-II polarization configuration, given in figure 3-16 (b).

**Pulsed SHG** — has been measured in our devices cleaved to the length of 0.6 mm — and subsequently reported in [133-134]. The characterization was conducted using an OPO synchronously pumped by mode-locked Ti: Sapphire laser. Input light was end-fire coupled into the waveguides using a microscopic objective lens. The characterization specifications include 1.9 ps pulses with an average power of 180 mw at the input facets. A half wave plate was used to inject a hybrid TE/TM polarized input fundamental, and a polarization beam cube was used to measure TE polarized SHG at the output using a silicon photo-detector. Figure 3-21 shows the schematic diagram of the experimental setup.

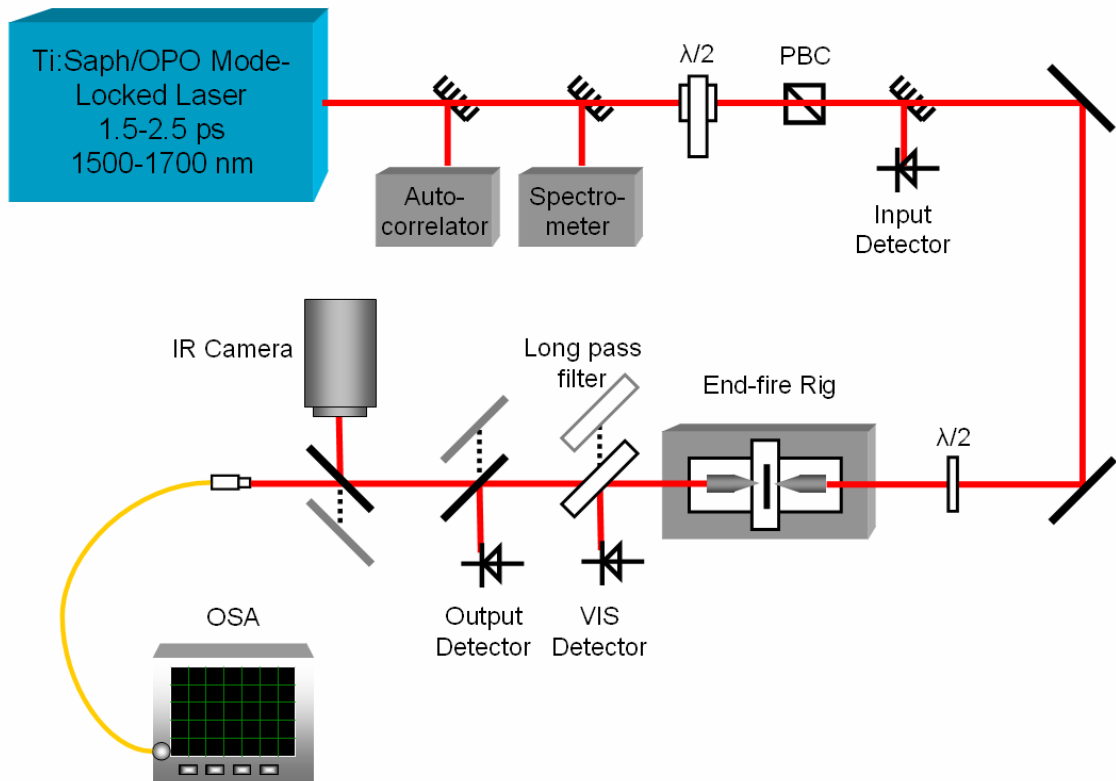


**Figure 3-21 – Schematic diagram of the type-II SHG measurements setup**

Average linear loss at the fundamental for this chip is  $0.9 \text{ cm}^{-1}$ . Peak SHG power is measured to be  $2.0 \text{ }\mu\text{W}$  for  $3.5 \text{ }\mu\text{m}$  period, with  $130 \text{ mW}$  of input power at the facet. The phase matching wavelength for the best performing waveguide is found to be  $1577.4 \text{ nm}$ . SHG tuning curve which has been measured using an OSA is given in figure 3-22 [133]. The output SHG power has a polarization ratio of 4.4:1 (TE: TM), which establishes the dominance of type-II phase matching process.

The observed output is lower than the expected, which is attributed to the higher losses at SHG. These losses could arise from the proximity of the TE polarized SHG to the material band-edge, or the radiation losses associated with poor TE polarized optical mode confinement. A mode solution for TE polarized band gap excitation is given in figure 3-23.

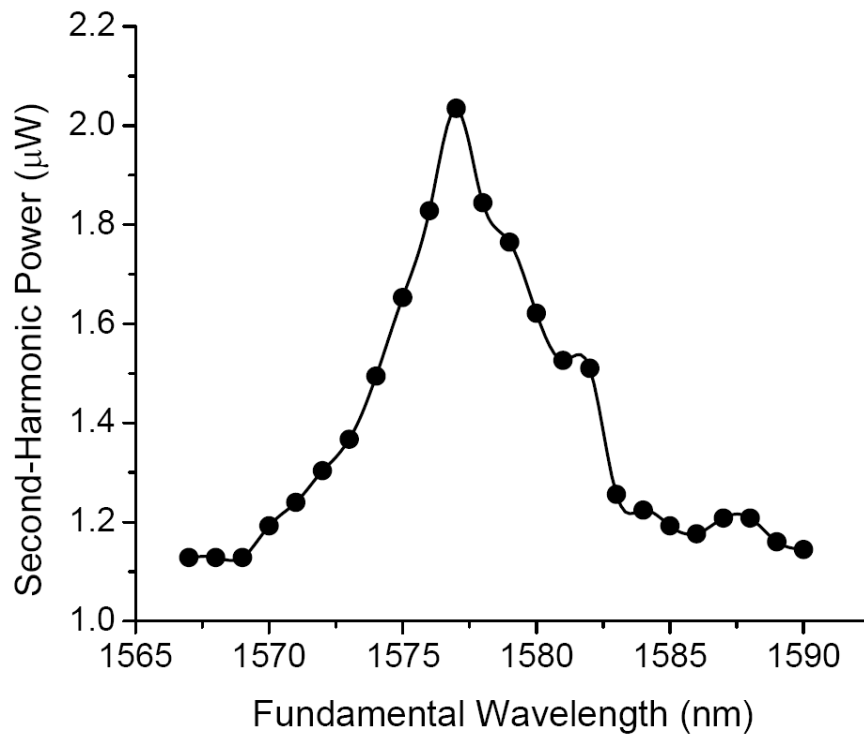


**Figure 3-22 [133] – Tuning curve for type-II SHG.**

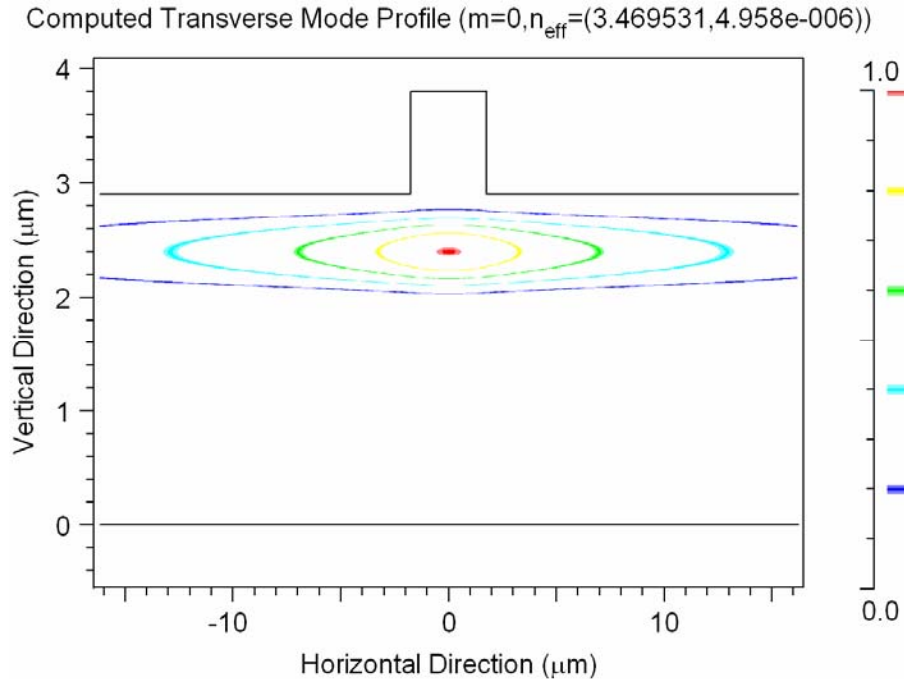


Figure 3-23 – Mode solution for TE polarized band-gap excitation.

### 3.5.3 Difference Frequency Generation (DFG)

Difference frequency generation is a promising three-wave-mixing process in order to achieve a direct wavelength conversion in an optical domain. Especially GaAs–AlGaAs materials, which have half-band-gap near  $1.5 \mu\text{m}$  telecommunication band, are highly attractive for an all optical wavelength division multiplexing (WDM) network. Moreover, it is possible to achieve a monolithically integrated optical frequency converter with the inclusion of an on-chip pump source. Direct conversion near  $1.5 \mu\text{m}$  wavelengths has been demonstrated previously in the periodic domain inverted AlGaAs waveguides [37]; however, they suffer a drawback of their inability to integrate with an on-chip pump laser source. Our developed process to achieve post-growth QWI is a solution to achieve this monolithic integration.

The lower confinement for TE-polarized band-gap wavelength has been observed in type-II SHG tests, and it has been attributed as a source of radiation loss which degraded the expected conversion efficiency. Therefore, new samples were fabricated with deep etched ridge structures to increase the optical confinement. These samples,

which have 3  $\mu\text{m}$  wide and 1.3  $\mu\text{m}$  deep ridge waveguides, were measured for type-I DFG test.

**Continuous wave type-I DFG** — The sample which has been used to perform DFG experiments was cleaved to the length of 1 mm, and it has the measured linear loss of  $2.5 \text{ cm}^{-1}$  in waveguides; this higher loss is explained by the light scattering in a deep etched structure. Pulsed SHG measurement was initially performed to identify the degeneracy point which would result in the maximum conversion for the three-wave-mixing process. Peak SHG was achieved for 1583.4 nm phase-matching wavelength in type-I polarization configuration. After this, the DFG measurements were performed using CW Ti:sapphire laser which was tuned to the degeneracy wavelength of 791.7 nm, and the output beam of the laser was set to TM. C-Band tunable laser, followed by EDFA, was used as the TE-polarized signal. The composite input of pump and signal, combined using a beam splitter, was end fire coupled into the waveguides using a microscopic objective lens. The collected output was separated using a long pass filter to measure the pump and the signal/idler wavelengths on different photo-detectors. Finally, the idler was detected by measuring it on OSA.

The input pump and signal powers at the waveguide facets were 45 mW, and 250 mW, respectively. More details of this experiment are presented in [135], but to summarize, TE-polarized idler wavelength at 1620.7 nm was produced for a signal wavelength of 1550.1 nm. The signal wavelength was scanned from 1535 nm to 1555 nm to observe the idler tuning, and a measured spectrum of 20 nm has been achieved with the conversion efficiency within 5dB. This shows an extensive phase-matching bandwidth of signal/idler close to the degeneracy, given in figure 3-24 [135].

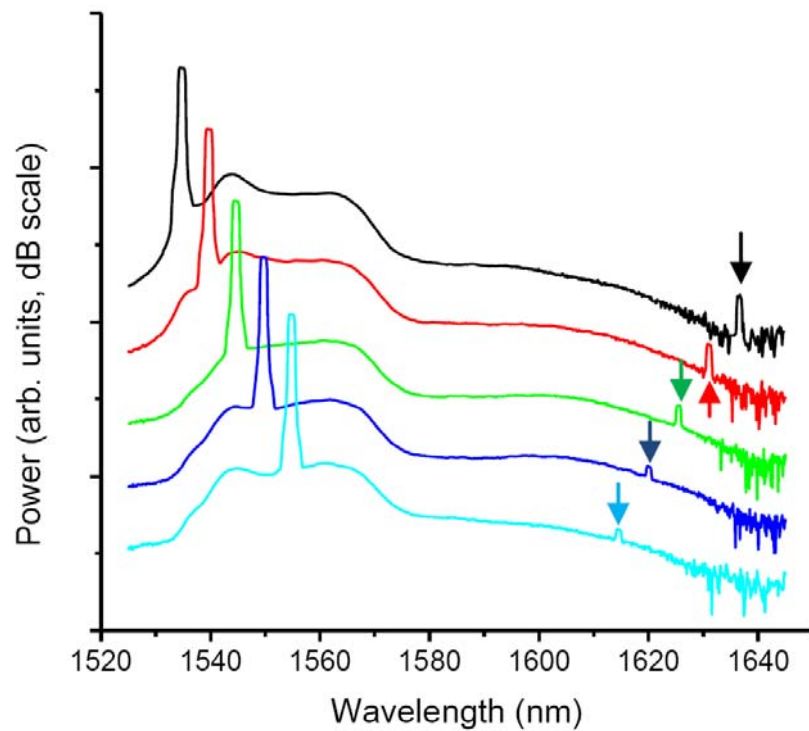


**Figure 3-24 [135] – The output spectra of measured DFG – the signal wavelengths are between 1535-1555 nm, and the arrows indicate the generated idler wavelengths.**

This direct conversion of C-Band wavelengths, into L- and U-Band wavelengths, has demonstrated the realization of an all optical frequency converter, which could achieve a higher efficiency using the appropriate filtering and amplification. However, the monolithic integration for such a WDM device require an on-chip pump source, which has been achieved by the laser action in our superlattice material structure presented in the lasers chapter.

### 3.6 Fabrication Process Optimization

The fabrication process flow, in our case, is lengthy and requires the sample to go through many electro-chemical and chemical processing steps, in addition to the standard lithography. For instance, the formation of the gold mask early on in the process flow involves immersing the sample in a sulphite-based gold electroplating solution. If the solution becomes contaminated, and/or is used incorrectly, this may

degrade the sample and/or the plated metal. Existing electroplating procedures and shared equipment had to be revised to establish reliable plating. Further, there were some issues related with effective removal of the metal mask. Poor surfaces after RIE suggested the presence of residual Au/Ti. Investigations were conducted in which test samples were prepared to understand the source of this contamination. As a result, we established a fabrication process flow that enables the monolithic integration of required OPO components.

The fabrication process flow chart for a complete monolithically integrated device is given in figure 3-25. The flow chart has been divided into two sections, in which the left section covers the fabrication up to the QPM waveguides, and the right section continues the fabrication to achieve the on-chip lasers. Please note that the individual recipes for each step have not been provided, and one can easily develop them to their requirements.

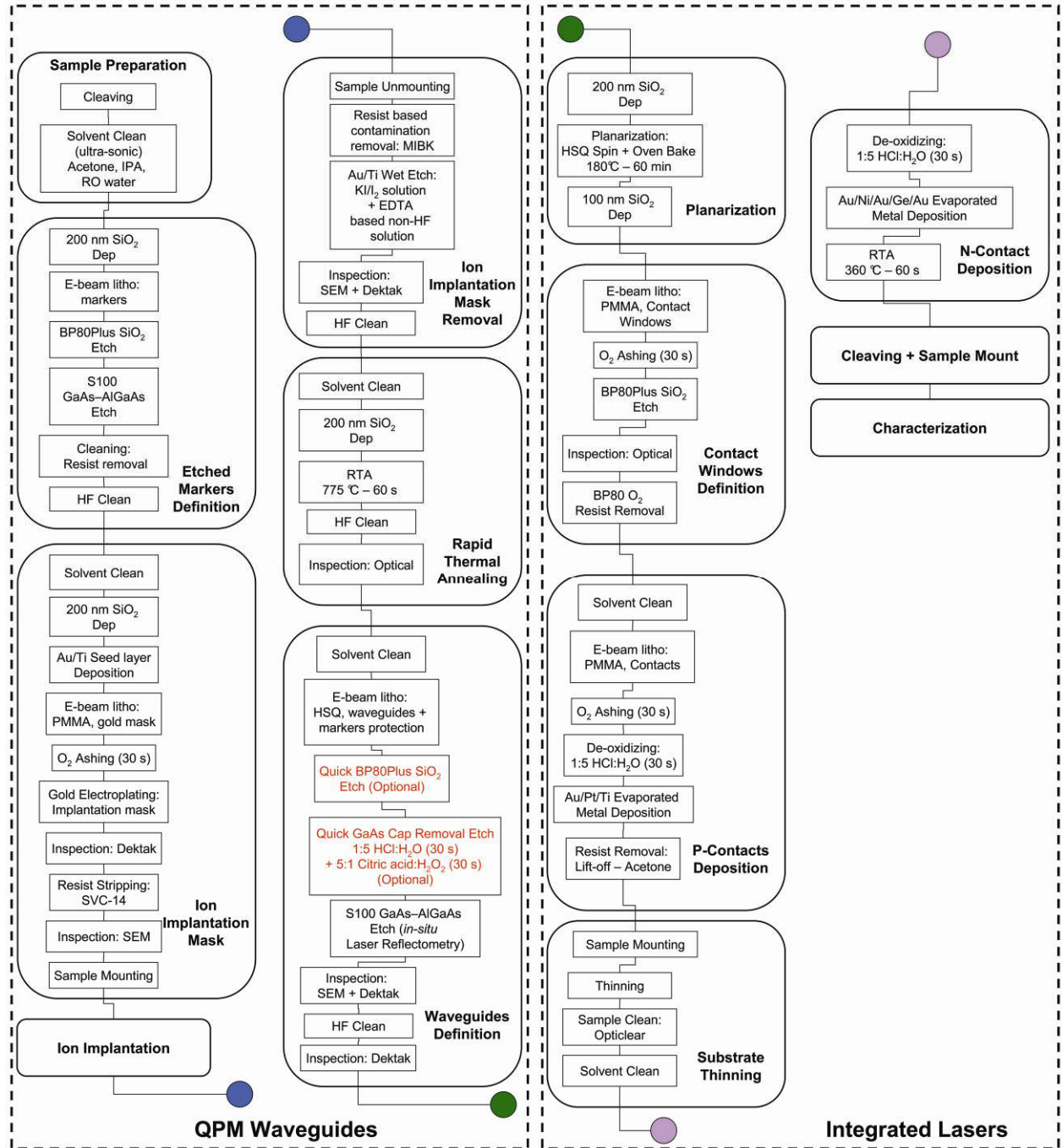
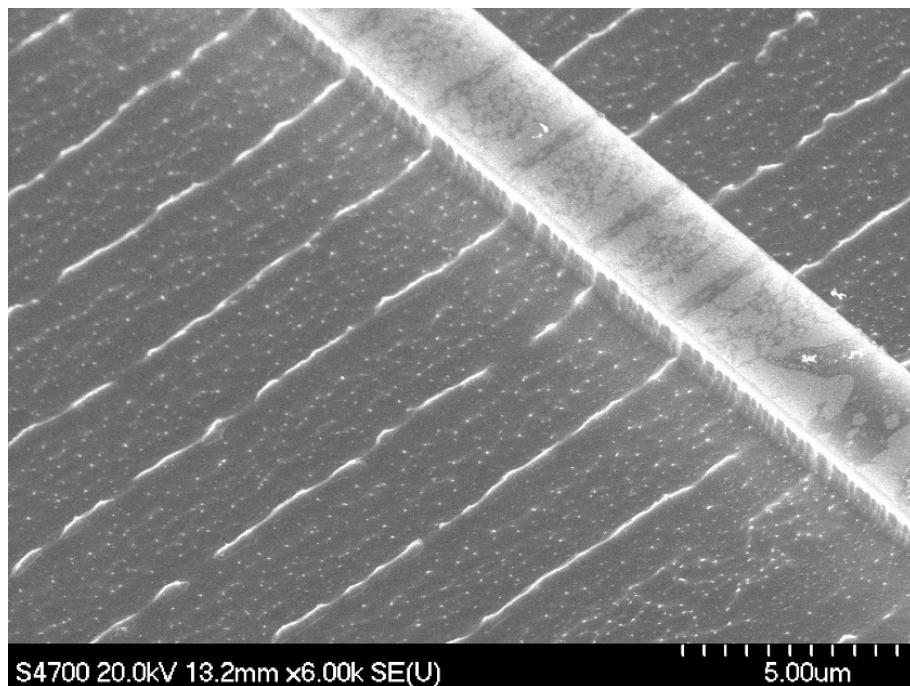


Figure 3-25 – The fabrication process flow chart for a monolithically integrated device. The left section provides the process if one wishes to achieve only the passive nonlinear waveguides; however, the right section continues with the fabrication to achieve the on-chip lasers in the case of an active device.

The selective etch of GaAs cap layer in the passive material, using citric acid based solution, resulted in a very clean sample surface suitable for subsequent RIE. The improved conversion efficiencies in various second order nonlinear measurements in these samples are an affirmation of this. However, the highly-doped GaAs cap is not always expendable; it must be conserved in electrically active regions in order to obtain ohmic contacts for the electrical injection. Therefore, it is mandatory to protect the GaAs cap while removing the Au/Ti based contamination. Test samples in which the GaAs cap removal stage was not included exhibited degradation, apparent in the form of grass on sample's surface after the subsequent RIE step. Figure 3-26 elaborates more on this issue.



**Figure 3-26 – SEM image of a test sample – no GaAs cap removal etch.**

This contamination, which has been observed on the sample's surface (figure 3-26), probed an investigation into the entire fabrication process. The test samples were initially cleaned with solvents before depositing a protective layer of 200 nm PECVD SiO<sub>2</sub>. The seed layer of 60 nm Au/10 nm Ti was deposited using E-beam assisted metal evaporation, instead of sputtering – the sputtering process requires the sample to be taken out of the clean room which itself is a contamination risk. The samples were then

patterned with 15%15% PMMA using E-beam, and a gold mask was grown using electroplating.

### 3.6.1 Improved Gold Electroplating

For gold electroplating, some new recommendations were followed, as demonstrated by Dr. C. D. Farmer [136]:

- 1) A new solution of gold electrolyte was obtained to ensure the absence of any contamination.
- 2) New sample holders (cathode) with Poly-tetra-fluoro-ethylene (PTFE) coated wire and screw were used.
- 3) A new platinum anode was used.
- 4) The anode and the cathode were immersed simultaneously into the electroplating solution with voltage-bias enabled.
- 5) The anode and the cathode were simultaneously taken out of the electroplating solution and placed in a beaker full of RO water before disabling the applied voltage-bias.

Table 3-2, summarizes the findings of the gold electroplating tests. The color of the electroplating solution and the anode did not change after multiple runs, and the gold mask was observed to be very smooth and shiny under the optical microscope. This is in contrast to runs performed previously.

<b>Gold electroplating</b>				
Initial settings:				
Set temperature		50 °C		
Measured temperature		48 °C		
Set voltage		10 V		
Set current		40 mA		
Feature size		40 μm		
<b>Test No.</b>	<b>Voltage in the solution (V)</b>	<b>Current in the solution (mA)</b>	<b>Electroplating time (min)</b>	<b>Measured thickness (μm)</b>
1	0.71	39	13	1.44
2	0.74	39	12	1.2
3	0.75	40	12	1.18

**Table 3-2 – Gold electroplating tests.**

After electroplating, the PMMA resist was stripped by placing the samples in SVC-14, in a hot water bath. The gold mask was partially removed from one of the test samples using potassium iodide/iodine (KI/I<sub>2</sub>) wet etch, and the sample was observed in SEM (figure 3-27). The attacked gold mask and the contaminated surface are clearly visible in the image. This contamination has been classified in to two categories: 1) caused by the resist, 2) caused by the Ti adhesion layer.

### 3.6.2 Resist Contamination Removal

The resist-based contamination, as identified in figure 2-27, has been observed at the Au / PMMA interface after electroplating. This can possibly be attributed to the change in PMMA properties due to higher electric field at the metal/polymer interface. The resist was found to be insoluble in generally identified cleaning solutions for polymers, i.e., acetone and SVC-14. Two approaches have been used to get rid of this contamination: 1) oxygen plasma clean [137], otherwise known as O<sub>2</sub> *Ashing*, and 2) placing the sample in Methyl-isobutyl-ketone (MIBK) – the latter is a solvent for polymers and is widely used as a developer in PMMA based lithography. We have employed MIBK

cleaning to remove the resist based contamination in all the later fabrications; a 10 min immersion in MIBK solution is recommended followed by a 1 min in IPA.

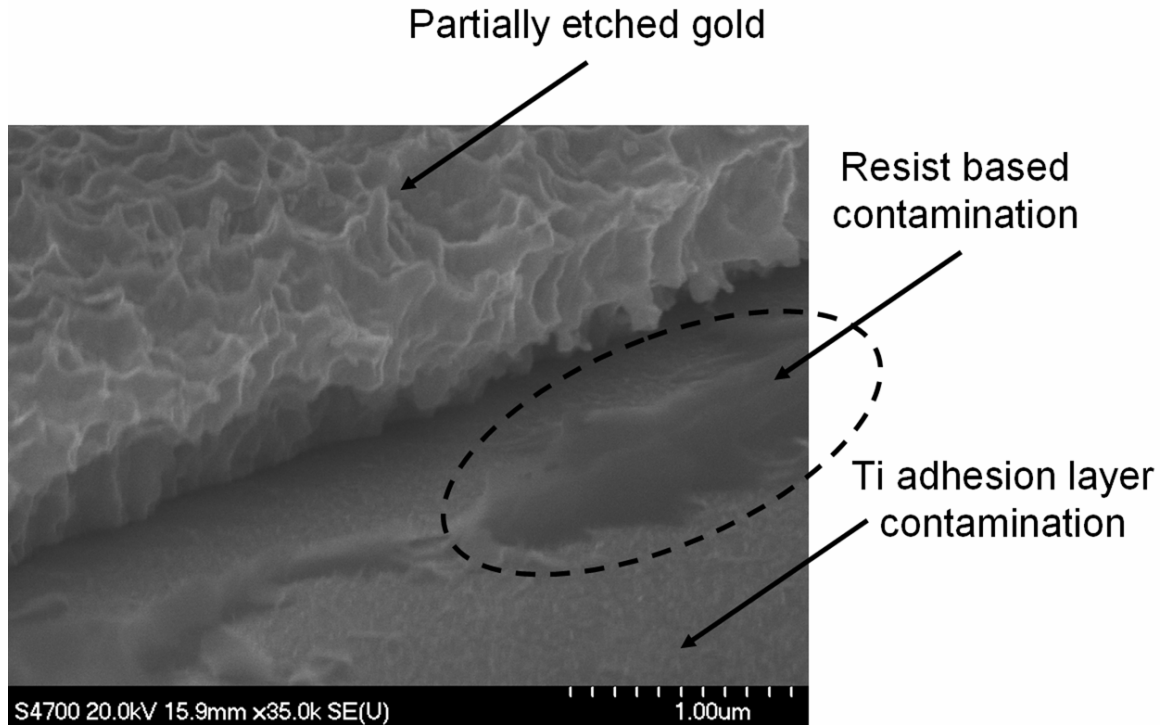


**Figure 3-27 – SEM image of a partially gold etched sample.**

### 3.6.3 Ti Layer Contamination Removal

The HF clean which was given initially to remove SiO<sub>2</sub> protective cap (underneath the Au/Ti seed layer) is also an etchant for Ti. However, cleaning procedures using HF-based solutions have been found to be unreliable. Therefore, it was mandatory to identify a non-HF based etchant for Ti adhesion layer. The test samples for this process development were cleaned initially in MIBK solution, and were masked with photo-resist to perform the gold etch. An image of one of these samples is given in figure 3-28, in which the masked surface and the exposed surface is clearly visible. Although the exposed surface has been attacked with KI/I<sub>2</sub>, still some contamination is visible in the electroplated grating regions, which could be left-over gold, perhaps due to insufficient etch time used. Ti adhesion layer is also visible in the image.

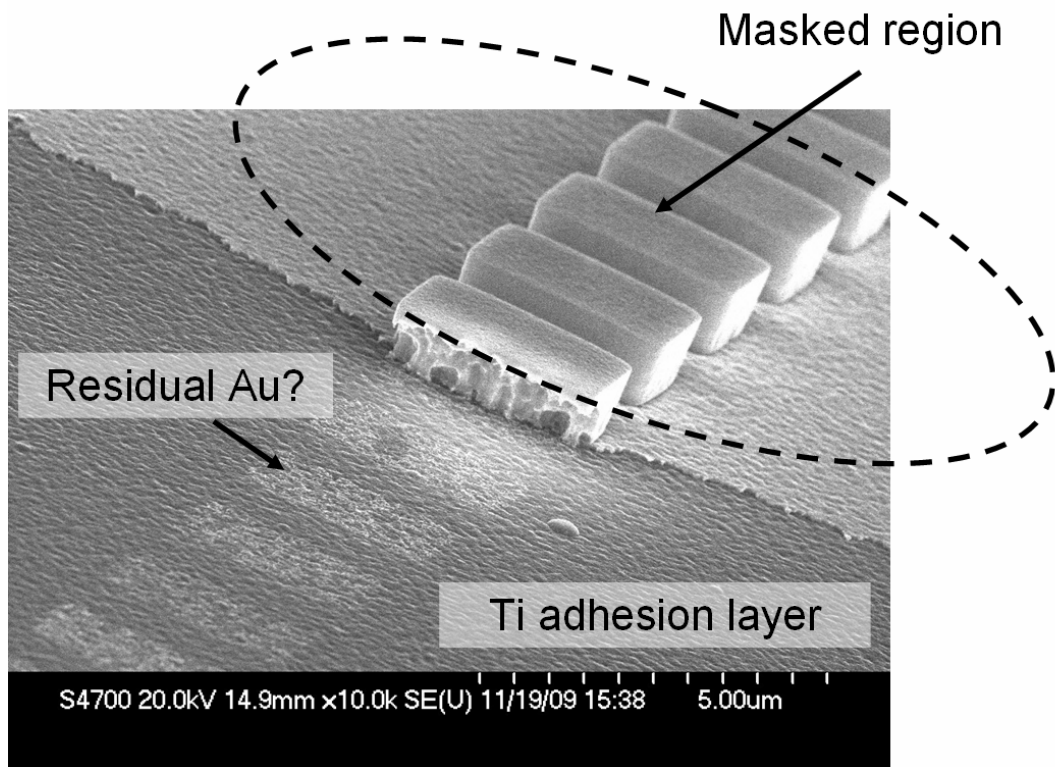


Figure 3-28 – SEM image of a gold etched sample – masked region and exposed region are visible.

**HF-based Ti etch** — Ti layer is employed for adhesion in many thin metal depositions on semiconductors. However, Ti is known to diffuse along grain boundaries of Au (Pt, Pd) overlayers [138]. Another potential problem arises since, once it is exposed, the surface of Ti quickly oxidizes to create a composite of Ti/TiO<sub>x</sub>. Furthermore, oxides and silicides of titanium are able to be formed at the interface between SiO<sub>2</sub> and Ti [139]. HF-based etchants attack the Ti rapidly, but the dissolution process is very slow for TiO<sub>x</sub>; and the same etchant rapidly dissolves the SiO<sub>2</sub> protective cap underneath. This expected behavior has been observed in the tests performed using HF: H<sub>2</sub>O (1:26) etchant. Figure 3-29 shows the edge-on view of the same sample (figure 3-28), which has been processed through Ti wet-etch. The dissolution of SiO<sub>2</sub> layer is clearly visible in the exposed region; however, the main concern is the presence of Ti/TiO<sub>x</sub> layer. A possible solution would be to perform this wet-etch for a longer time (or at an increased temperature), but it would risk the GaAs cap which is critical in an active device [140].

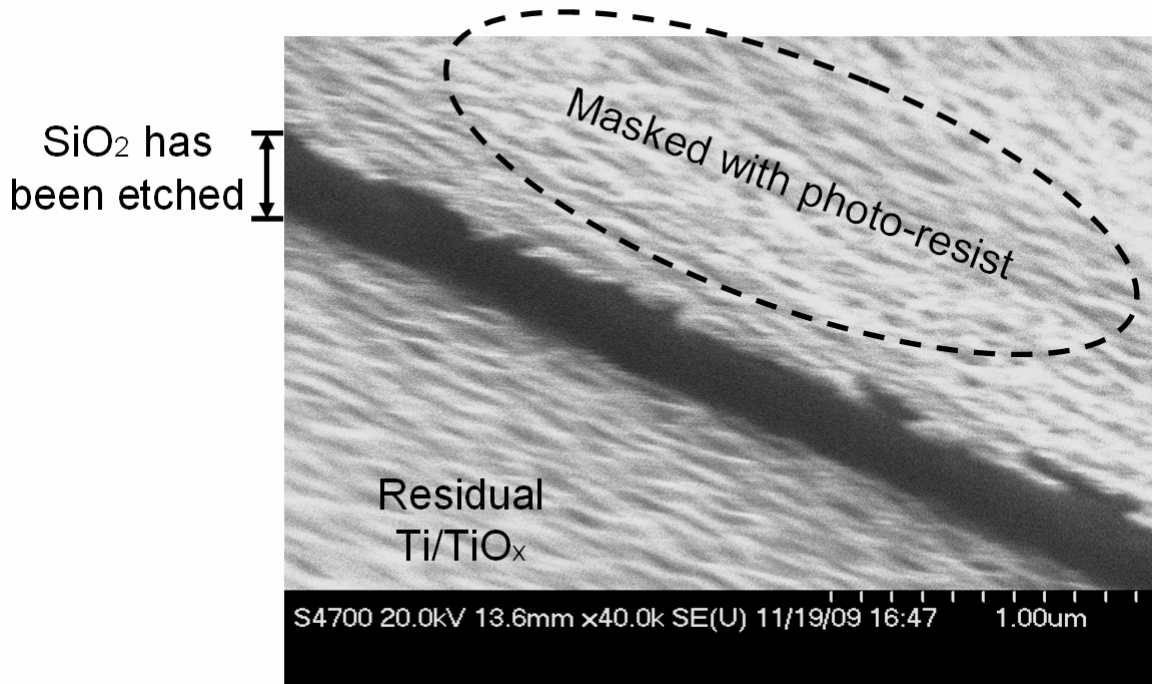
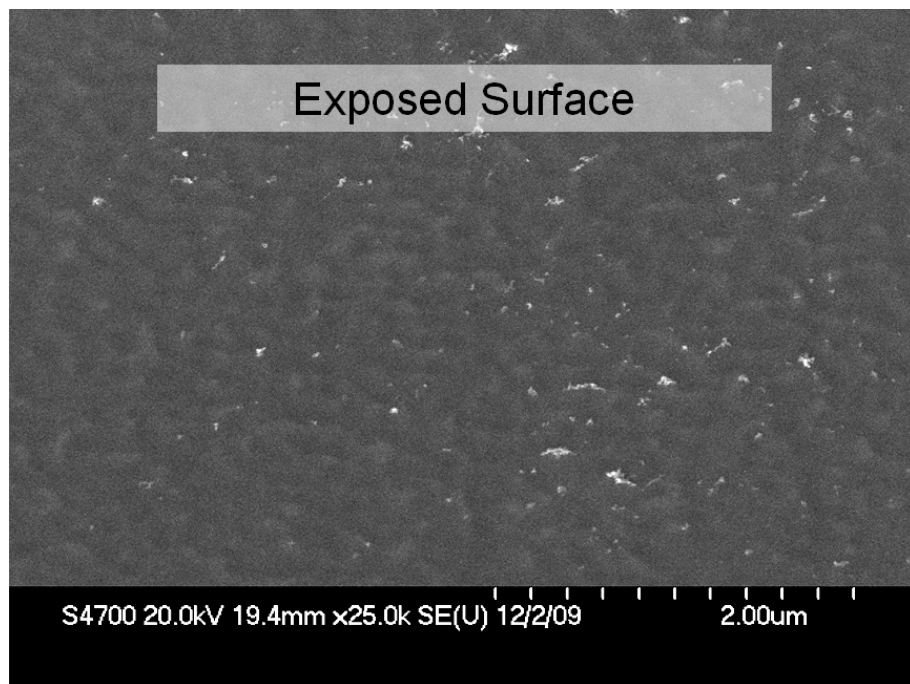


Figure 3-29 – Edge-on view of the sample partially exposed to Ti wet-etch.

**Non-HF-based Ti etch** — An alternative and more effective etchant based on non-HF chemistry was investigated, as proposed for our application by Dr. C. D. Farmer [141]. This etchant has the benefit of having a similar etch rate for Ti and its oxide, along with a slow etch rate 5 nm/min, that together provide high process controllability when etching thin layers [142-143]. Another useful trait is that it does not etch  $\text{SiO}_2/\text{SiN}_x$ , unlike HF acid. However, it does attack GaAs–AlGaAs, so protection of the exposed semiconductor surface (e.g., using  $\text{SiO}_2/\text{SiN}_x$ , photo-resist) is needed to avoid etching of those layers.

The preparation of stock solution involved: 1) mixing 93.3 ml  $\text{NH}_4\text{OH}$  solution (28-30 %) in 2 L  $\text{H}_2\text{O}$ , 2) adding 50 g EDTA powder into the solution such that it was completely dissolved, and finally 3) storing the stock solution in an air tight bottle to avoid any loss of  $\text{NH}_3$  gas. In order to perform the etch, a fresh solution of 5 g (~4.5 mL)  $\text{H}_2\text{O}_2$  was mixed into 53.1 g (~52 mL) stock EDTA solution. A completely protected sample (exposed semiconductor covered with an adhesive tape and photo-resist) was initially given quick  $\text{O}_2$  plasma clean, followed by an immersion in  $\text{H}_2\text{O}$  to

wet its surface. Ti/TiO<sub>x</sub> wet-etch process was performed immediately after this H<sub>2</sub>O soak. The sample was placed in the solution for 16 mins to completely etch 10 nm Ti adhesion layer. It is recommended to perform a Au etch followed by a Ti etch for at least two cycles – such that the first cycle is performed for the etch time required to etch the thick gold layer, and further iterations are designed to remove any residual Au-Ti composites. Figure 3-30 shows the sample's surface after the said procedure; Ti/TiO<sub>x</sub> based contamination has been significantly removed in this case.



**Figure 3-30 – Top view of a sample exposed to non-HF-based Ti wet-etch.**

In conclusion, during the fabrication process optimization, a number of factors have been identified which proved critical in effective realization of monolithic integration of our final device. The cleaning procedures which have been thoroughly investigated to overcome these factors have shown visible improvements, of which the very last stage of Ti contamination removal has been the most significant. Once the effective removal of gold mask and the underneath Ti adhesion layer is established, the later fabrication process for the final device is similar to the laser fabrication which has been presented in the lasers chapter.

This chapter concludes with the demonstration of improved conversion efficiencies in various second order nonlinear processes measured in our devices. This proves significant improvements in the fabrication process as compared to the work reported earlier, and also, it indicates a better control in selectively achieving QWI for the required periodic nonlinear modulation. Finally, the fabrication related issues have been investigated in complete, and the optimization in each case has been achieved.

# *Chapter 4*

## Di-chroic Multimode Interference Coupler

Our design of a fully integrated OPO requires us to have essential routing components on the chip. The simultaneous conversion of different wavelengths in the QPM waveguide section would be degraded if the multi-wavelength transmission does not follow the designated paths, i.e., the band-gap wavelength has to fully couple into the QPM waveguide section to ensure maximum three-wave-mixing, and it has to completely couple back into the ring laser cavity for stimulated emission. Similarly, the half-band-gap wavelengths must maintain their transmission confined within the adjoining resonator, after they have been routed through the QPM waveguide. Therefore, it is mandatory to achieve such routing on the integrated chip, while keeping its fabrication inline with the overall fabrication process of the final device; and subsequently establish the monolithic integration.

This chapter starts with the MMI coupler design, which is fully understood with the beam-propagation-based simulations. The fabrication process optimizations, specific for this component, have been presented. Finally, the device characterization has been performed and presented.

### 4.1 Coupler Design

Our OPO design requires a cross coupler for the band-gap wavelengths. The coupler should exhibit maximum coupling of the pump mode into the QPM waveguide section, as given in figure 4-1 (a). The resonating parametric fluorescence near the half-band-gap, requires a coupler in a bar configuration, given in figure 4-1 (b). Moreover, the constraints include a short cavity length for minimal foot print, and the avoidance of any

back reflections into the pump cavity. Following subjects, which have been considered as priorities in our coupler design, have been found in the literature:

- 1) MMI has been identified as a better design than the directional coupler, as the coupling parameters: etch depth, waveguides separation, and device length, do not have a significant effect on the performance in MMI [57, 144].
- 2) MMI couplers can furnish a very broad bandwidth in the same design [59, 145] [56].
- 3) The performance of even a weakly guiding MMI coupler can satisfy the theoretical requirements [52], and has the benefit of lesser back reflections [145].
- 4) MMI coupler can be critical in the case of an integrated ring laser. The undesirable resonating modes and back reflections in MMI cavity end up in the spectral response of the device [51-52] [145]. The remedies include: a weakly guided structure, passive MMI cavity, and tapered access waveguides [145].

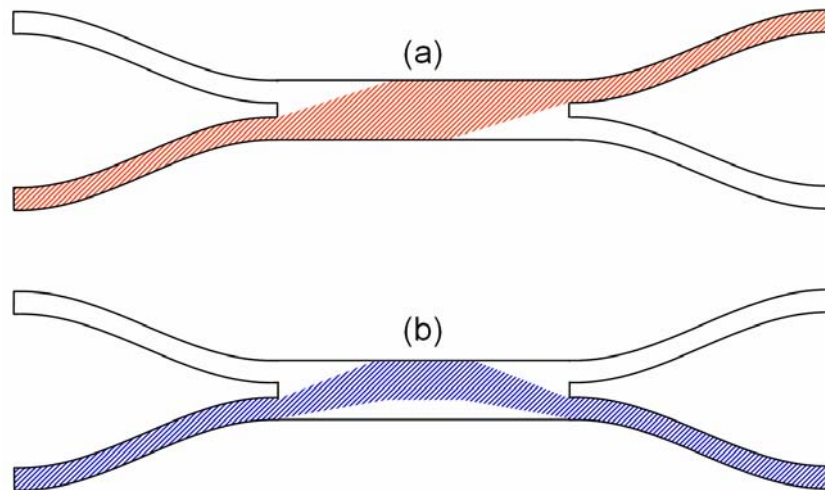


**Figure 4-1 – Required design: (a) cross coupler near the band-gap (775 nm), (b) bar coupler near the half-band-gap (1550 nm).**

It has been identified in the previous chapter that the shallow etch waveguides have poor confinement; therefore, the access waveguides have to be etched deep enough to

cause minimum transmission loss in the bended sections. An acceptable approach would be a completely etched waveguide core; however, this will exhibit the scattering losses and will bring in the higher order modes. The mode solutions, for the bended sections, identified the required etch depth of 1.3-1.4  $\mu\text{m}$  as an acceptable agreement in this case. This etch depth will partially expose the superlattice region for the current material structure BMH1; however, in the case of lasers, the superlattice core thickness has been reduced and an additional layer has been included in the waveguide core to circumvent the non-radiative recombinations (this is presented in the lasers chapter). Once the etch depth of 1.3-1.4  $\mu\text{m}$  has been established, the mode simulations were performed to find the optimum waveguide width of 3  $\mu\text{m}$ , given in figure 4-2.

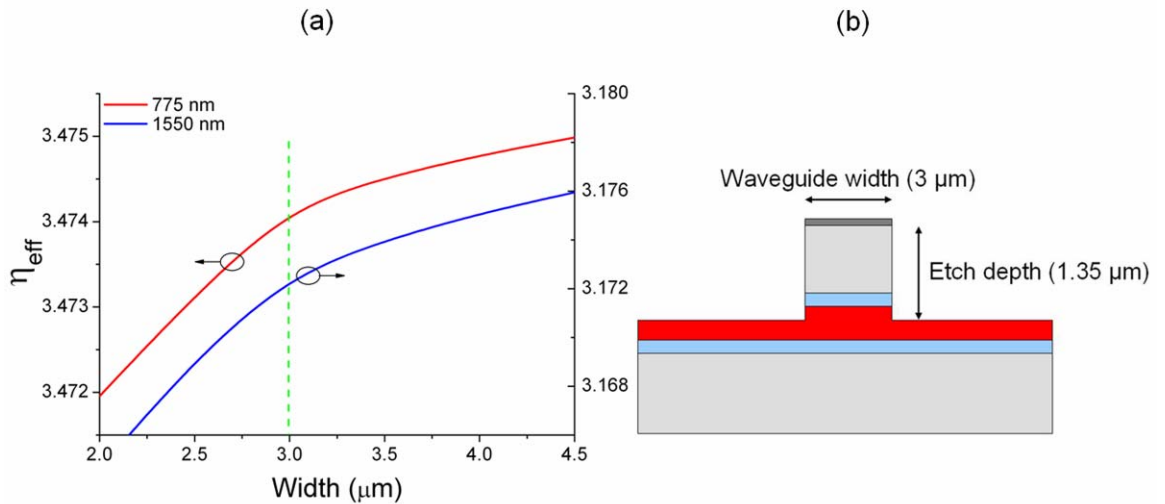


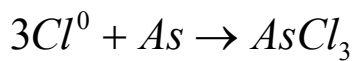
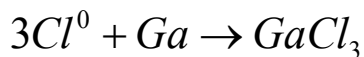
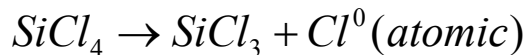
**Figure 4-2 – (a) Mode solutions of the designed waveguide structure for the band-gap and the half-band-gap-wavelengths, (b) the designed access waveguide structure.**

Single mode access waveguides to the MMI cavity were designed to have a width of 3  $\mu\text{m}$ . The width of the MMI cavity has to be less in order to keep the length (which is dependent upon the width of the cavity) at the minimum possible. The ideal case would be a two-mode interference (TMI) coupler [57], which will result in the cavity width of 6  $\mu\text{m}$  in our case, and will provide the smallest possible length under restricted interference. But fabrication limitations could vary this length in the curved input sections; therefore, it was mandatory to identify these limitations. The fabrication process optimization is given in the next section.

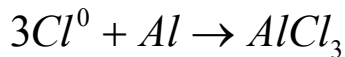
## 4.2 Dry Etch Optimization

Reactive ion etching (RIE) is used to achieve the anisotropic etch in the semiconductor device fabrication; and it has a better control and reproducibly on the etch depth than the isotropic wet etch. Chlorine based plasma is generally employed for GaAs etch [146-147] [148] [149], but there are several parameters that effect the anisotropy and the etch rate. These parameters include: the gas pressure, gas flow in the RIE chamber, the chamber design, and the applied bias across the electrodes; and most critical is the gas composition.

The chemistry generally used for GaAs–AlGaAs etch in the dry etch facility at University of Glasgow is SiCl<sub>4</sub> based. This chemistry has been identified to produce comparable etch rates for both GaAs and AlGaAs [148]. The application of high power RF-bias creates a plasma of charged ions and radicals of the injected gas between the two electrodes; and the main contributing factor which reacts with the semiconductor is chlorine [150]. The chemical reaction for this process is reported in [149], and is given below:



and



The process parameters which have been used in our experiments were: 18 sccm SiCl<sub>4</sub> gas flow, 9 mT of pressure, and 250 W of power. Although, these parameters were ensured in many tests performed initially; however, it has been observed that the process is dependent upon the sample size. An available solution is the real time monitoring of etch depth using laser reflectometry in an *in-situ* RIE process.

### 4.2.1 RIE with Laser Reflectometry

Laser reflectometry is a process in which a monochromatic beam is shinned on the substrate, normal to its surface, and the reflected light is measured using a photo-detector, and recorded on an onboard computer. The real time interference in the reflected optical signal provides a precise control of the etch depth in an *in-situ* RIE [149, 151]. Using this analysis tool, a number of tests were performed for our material, in which the etch depth was monitored by the real time interferometer data (figure 4-3); and the resultant etch depth was measured using surface profiler Dektak. Various etch tests were performed for different number of oscillations in the reflected signal (figure 4-4), and an average etch rate of ~85 nm/oscillation has been obtained for our material. The etch rate per oscillation has been reported to be 86 nm for GaAs, and 91.5 nm for  $Al_{0.28}Ga_{0.72}As$  in [149]. Although our material has a higher aluminium concentration than these; however, the measured etch rate is in a good agreement with the reported values. This *in-situ* RIE was used in all the later fabrications, and the required etch depths have been achieved within  $\pm 20$  nm tolerance.

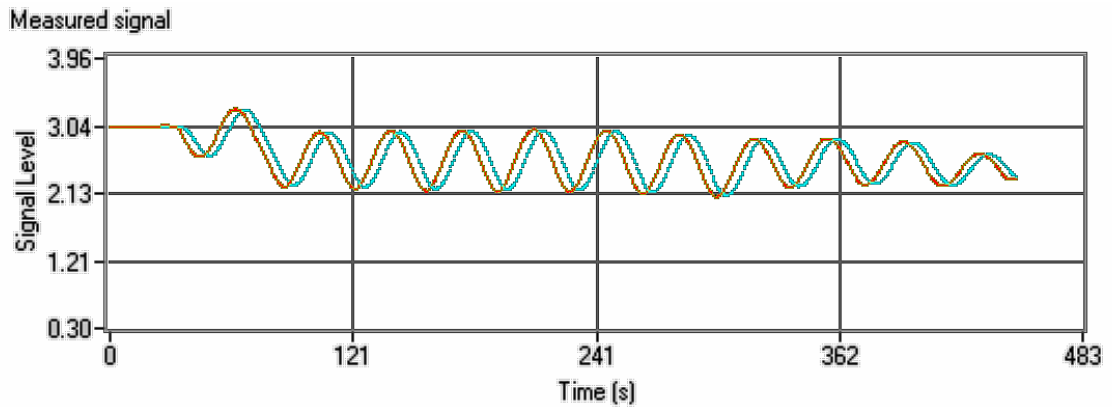


Figure 4-3 –Recorded plot of a real time RIE signal (the oscillations in the signal are seen as the etch depth increases with time).

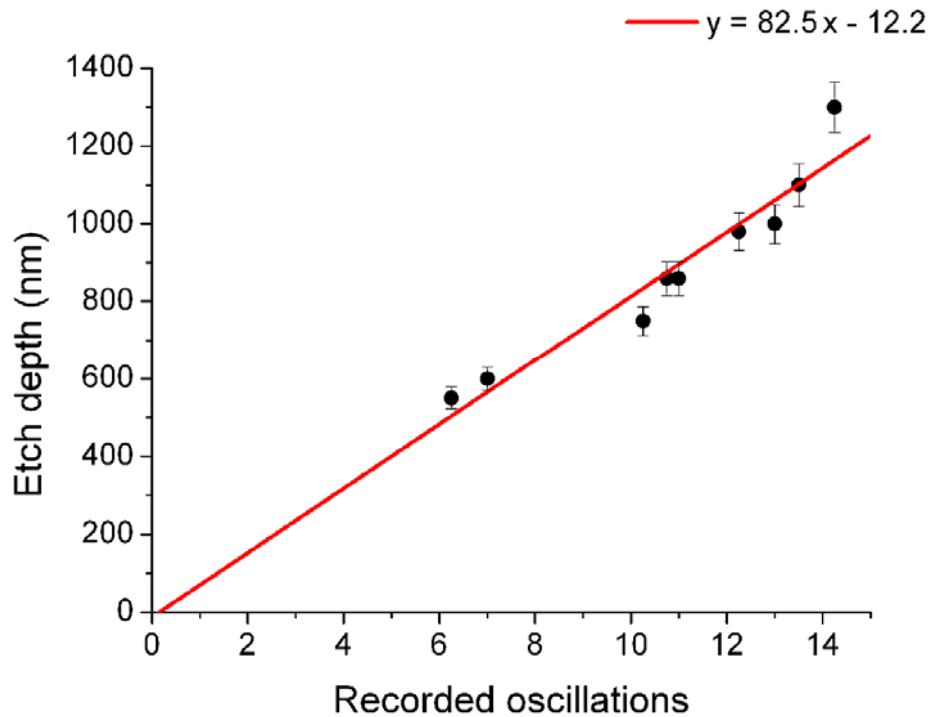


Figure 4-4 – The measured RIE etch depth against the number of oscillations recorded.

#### 4.2.2 RIE Lag

Dry etch is a process in which the ions react with the substrate's surface under the influence of applied process parameters. This process is effected significantly when the exposed gaps (in which RIE is desired), are small enough to reduce the ions flux. The optimum performance in our coupler requires the gap between the access waveguides to be completely etched up to the depth of MMI cavity; however, RIE in its general application is not able to completely open the converging gaps. Two options are identified to resolve this issue:

- 1) The optimization of RIE process, in which etch is stopped on the bigger exposed surface of the sample, but is continued in the smaller gaps – this is usually done by introducing an etch stop layer in the initial epitaxial growth.
- 2) The identification of a minimum width for the smaller gaps in which the etch depth is practically similar to the large features.

This RIE lag in smaller opening has been measured by performing tests on the exposed gaps of various widths. The test sample was fabricated by patterning neat (100%) HSQ under E-beam, and subsequently etching in SiCl<sub>4</sub>, using the previously mentioned parameters. As expected, the measured gaps were not completely open for the decreasing width of the exposed surface, which can be seen in the cross-sectional SEM images, figure 4-5. It was found that a gap of 500 nm is practically achievable with the similar etch depth as that of the surrounding exposed surface.

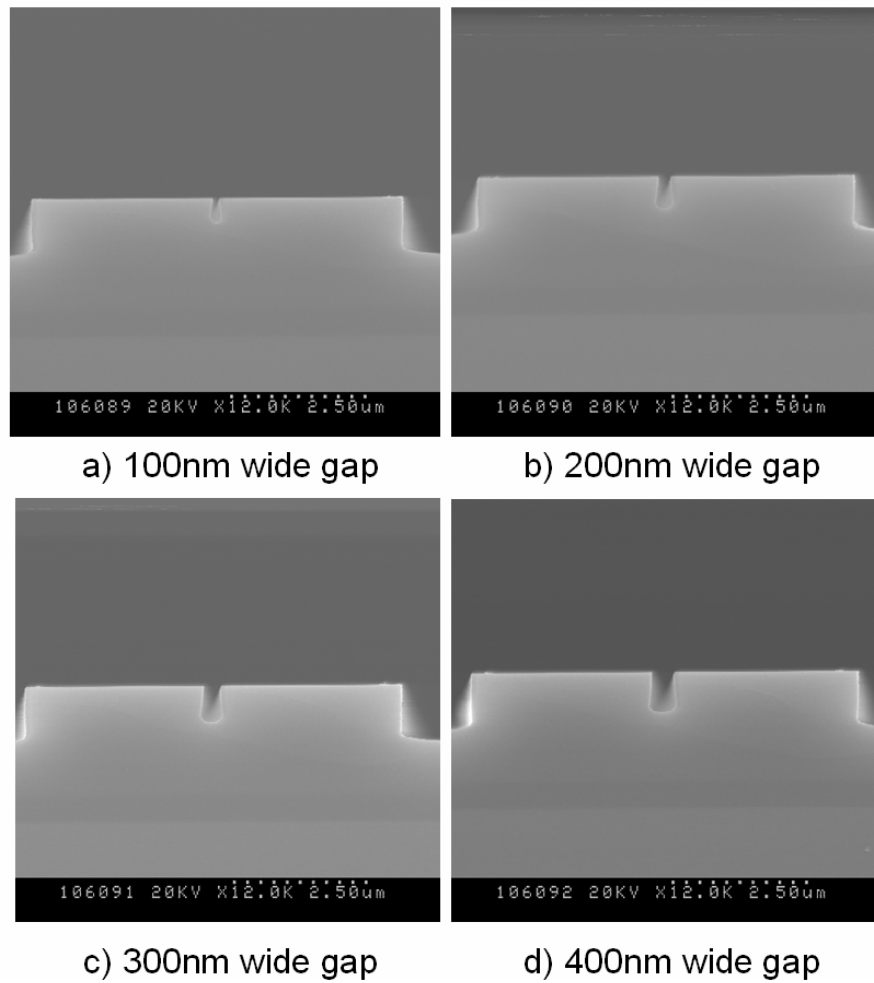


**Figure 4-5 – Cross-sectional SEM micrographs of the small gaps depicting RIE lag.**

### 4.3 Simulations and Tests near Band-gap

The designed access waveguides which have the width of 3  $\mu\text{m}$ , and the added fabrication tolerance as identified in RIE lag tests, has given us the minimum cavity

width of 6.5  $\mu\text{m}$  for the MMI coupler. The restricted paired interference has been employed, in which the cross operation should occur at the beat length of the first two modes. The calculated length of MMI for excitation wavelength 780 nm (near band gap) is  $L_\pi = 250 \mu\text{m}$ . The coupling operation has been optimized by simulating different cavity lengths using BeamPROP, and the optimum length has been identified to be 220  $\mu\text{m}$ , given in figure 4-6.

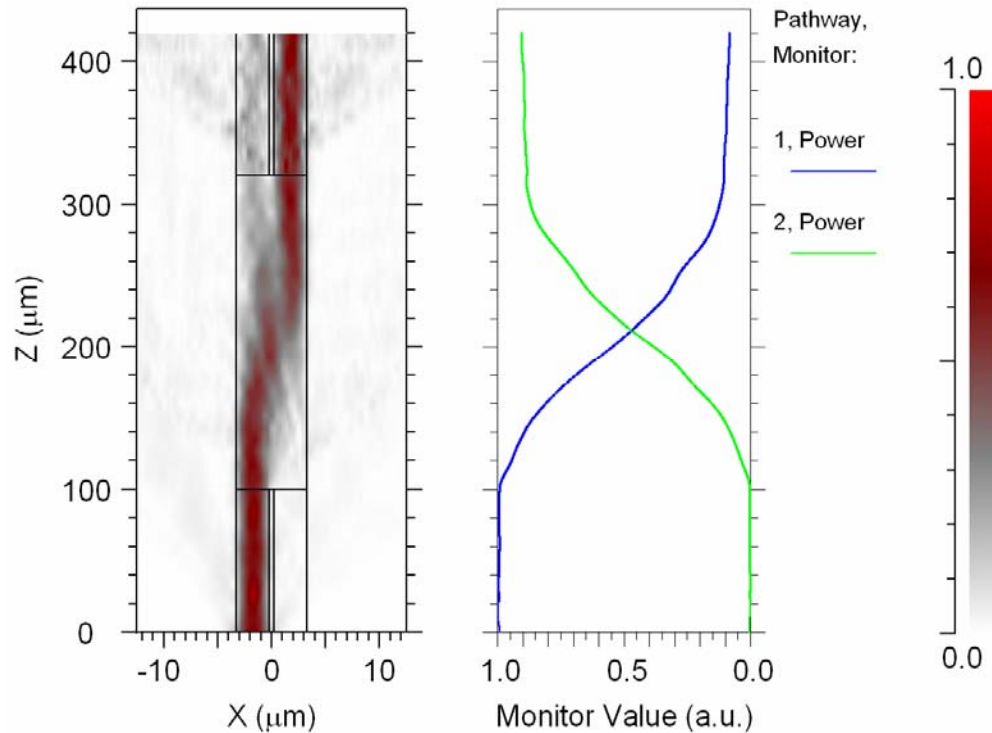


**Figure 4-6 – Simulated cross operation at the excitation wavelength of 780 nm (MMI cavity dimensions: 6.5  $\mu\text{m}$  wide, 220  $\mu\text{m}$  long, and 1.35  $\mu\text{m}$  deep etched).**

MMI cross coupling tests were performed by fabricating couplers of various lengths, i.e., 180 – 240  $\mu\text{m}$  long. The E-beam mask was designed with a skew such that the cleaved samples will have angled waveguides at the facets; this helps to avoid the FP effects in the measurements. The sample fabrication included neat (100%) HSQ patterning using E-beam, and subsequent definition using RIE. The fabricated samples were measured to have an etch depth of  $1.35 \pm 0.02 \mu\text{m}$ . SEM image of one of the test samples is given in figure 4-7. The converging gap between access waveguides is practically open in the inset (top left corner).

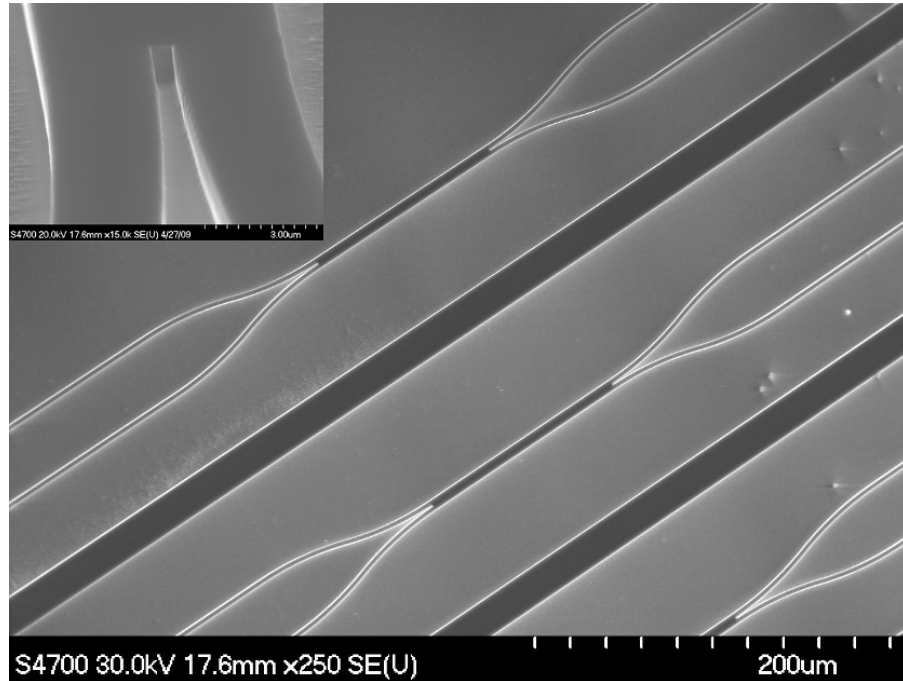


Figure 4-7 – SEM image of a test sample with various coupler lengths.

The measurements near the band-gap wavelengths were performed using a tunable Ti: Sapphire CW laser, pumped by an argon ion laser. The measured output of the laser was in hundreds of mW, but it was reduced down to a few mW using the neutral density filters. The light was not set to any polarization for these measurements; however, the TE polarized component of the field was significantly dominant. The light was end-fire coupled into the waveguides using a microscopic objective lens, and the output of the couplers was measured using a silicon photo-detector attached to a lock-in amplifier & an optical chopper. The measurement setup is given in figure 4-8.

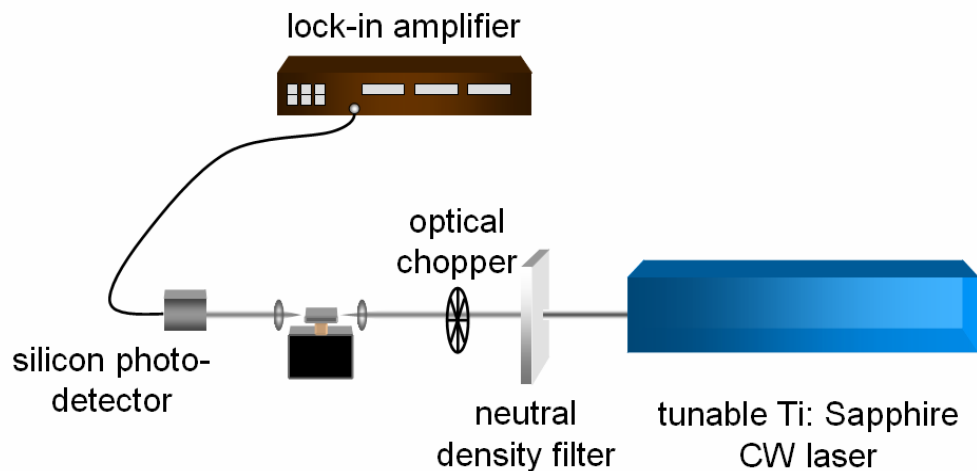
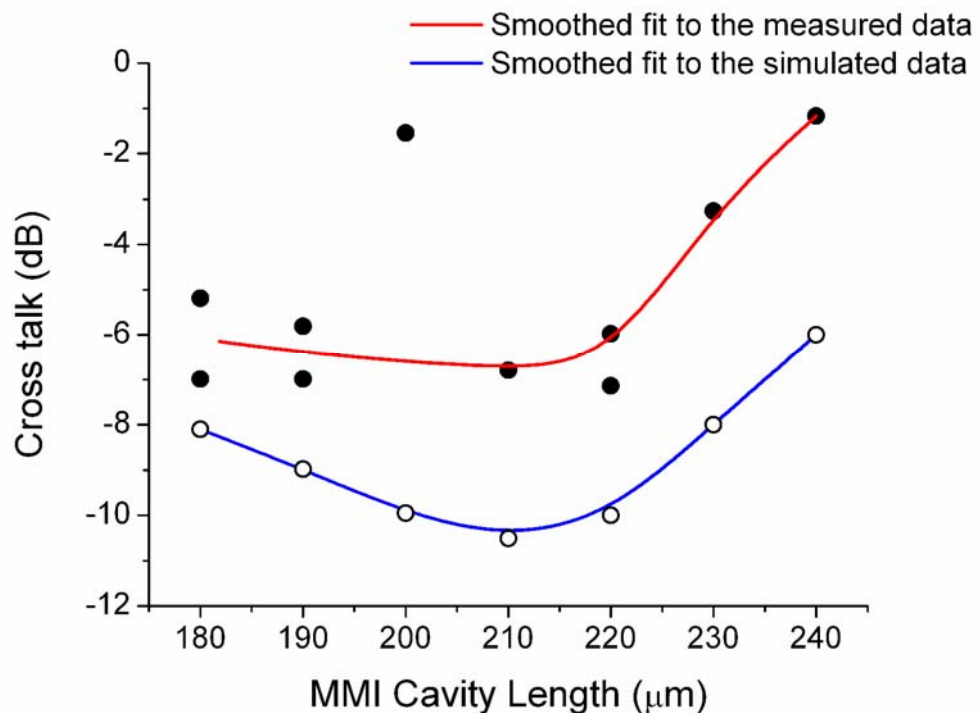


Figure 4-8 – Measurement setup for the near band-gap wavelengths.

The measured cross talk, which in this case is the ratio between the unwanted signal and the wanted signal ( $10 \log_{10} \frac{P_{bar}}{P_{cross}}$ ) dB [152], for the wavelength 797 nm, is given in figure 4-9. It has been observed that the coupler is working in a cross configuration for 190-220  $\mu\text{m}$  long MMI cavities, which is in agreement with the simulated cavity length. An unexpected behavior is observed in the case of the 200  $\mu\text{m}$  long coupler, it is believed to be damaged. The normalized cross + bar state power is plotted in the figure 4-10, which identifies the lower transmission for 200  $\mu\text{m}$  long coupler.

The minimum cross talk in the case of simulations is  $-11$  dB, which is lower than the minimum cross talk achieved in the measurements. However, the measured coupling trend seems to follow the simulated coupling trend. These measurements were repeated for 788 nm wavelength, and the coupler performance was found consistent. A minimum cross talk of  $-7$  dB has been observed in this case. The optical bandwidth ( $2|\partial\lambda|$ ) [56], is calculated to be  $\sim 100$  nm for a  $220\mu\text{m}$  long coupler.



**Figure 4-9 – Measurements for 797 nm wavelength, and simulations for 780 nm wavelength (quasi-TE polarized light in both cases). Solid lines are a smoothed fit to the data. Solid circles represent the measured data, and the empty circles are the simulated data.**

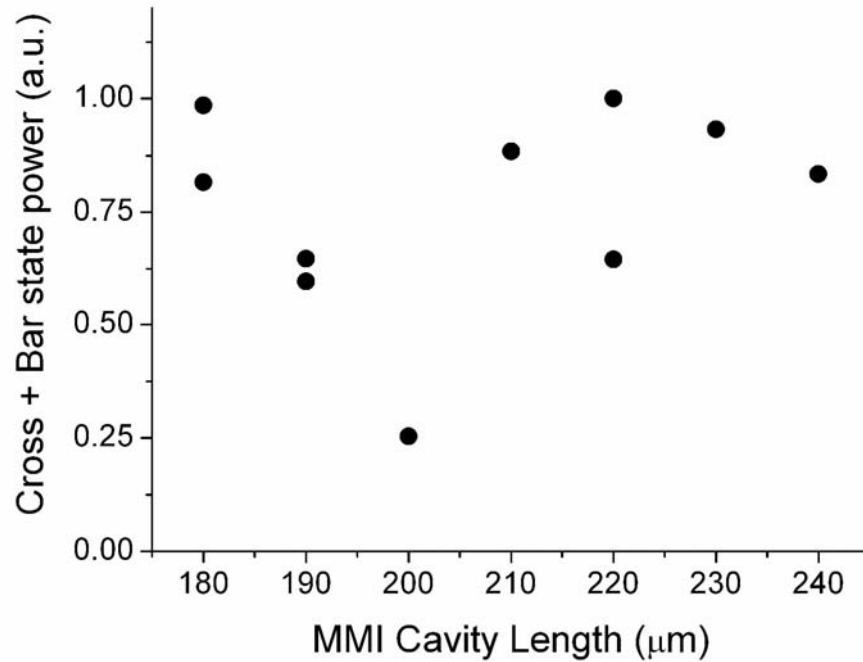


Figure 4-10 –Cross + bar state power.

#### 4.4 Simulations and Tests near Half-Band-gap

The designed MMI cavity (6.5  $\mu\text{m}$  wide and 220  $\mu\text{m}$  long), has been simulated for the bar coupling near the half-band-gap wavelength (1560 nm), which is depicted in figure 4-11. The calculated beat length  $L_\pi$  for this excitation wavelength is 114  $\mu\text{m}$ , and the bar operation should occur at twice the beat length, i.e., 228  $\mu\text{m}$ , which is within  $\pm 10$   $\mu\text{m}$  tolerance measured for the cross coupling.

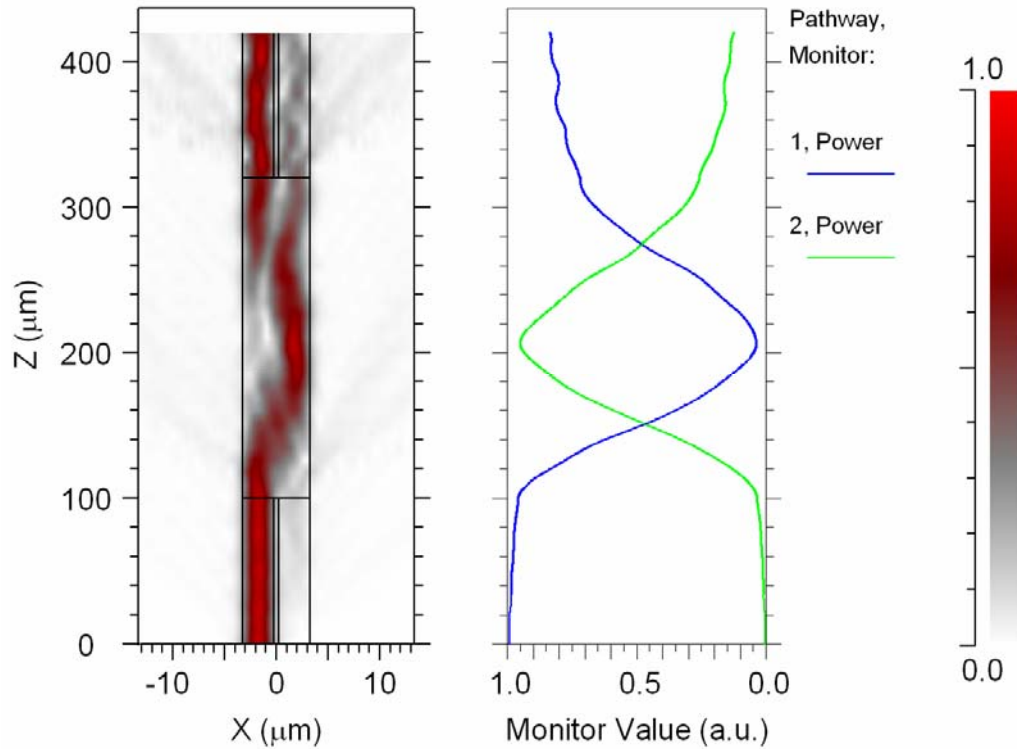
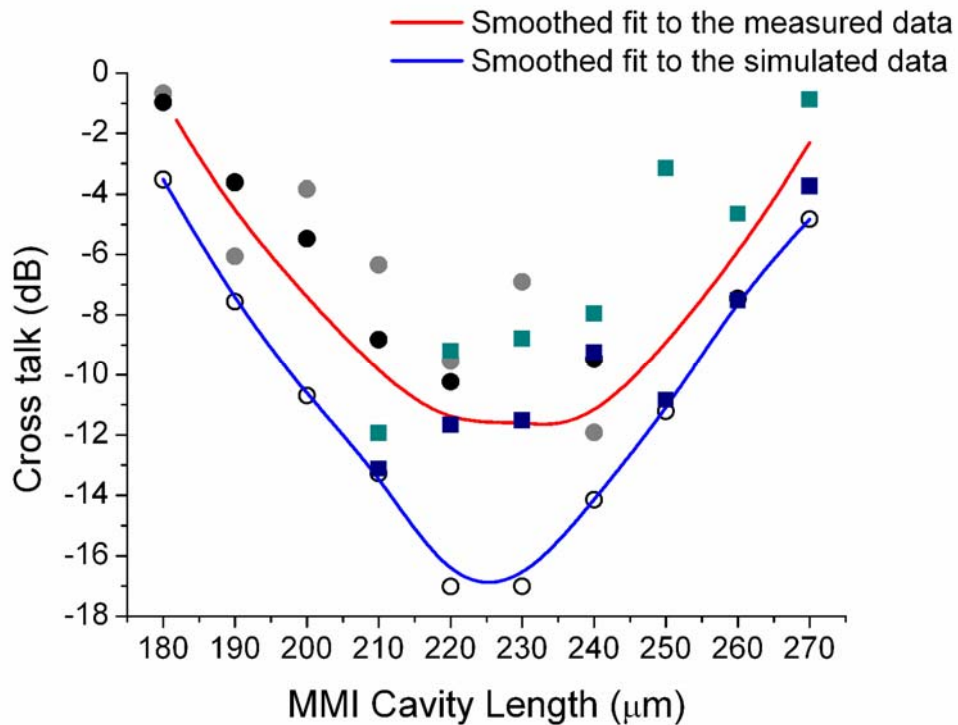


Figure 4-11 – Simulated bar operation at the excitation wavelength of 1560 nm.

The measurement setup for bar operation was similar to the previous; however, tunable Ti: Sapphire laser was replaced with tunable 1.5  $\mu\text{m}$  CW laser. Again, no polarization was set for the quasi-TE polarized input light. Input power of 2 mW was end-fire coupled into the waveguides using a microscopic objective lens, and a germanium photo-detector was used to measure the output power. Two samples, with MMI cavities of various lengths, were measured for the cross talk ( $10 \log_{10} \frac{P_{cross}}{P_{bar}}$ ) dB, given in figure 4-12. Again, the minimum cross talk has been observed for 210-240  $\mu\text{m}$  long MMI cavities, which is in agreement with the optimum cavity length. Moreover, the measurements performed using two different samples establish the fabrication process repeatability.



**Figure 4-12 – Measured and simulated performance of the coupler for 1560 nm wavelength (quasi-TE polarized light). Solid lines are a smoothed fit to the data. Solid circles and squares represent the measured data, and the empty circles are the simulated data.**

The measurements for both coupling operations demonstrate that the required di-chroic behavior is consistent with the designed structure. It is anticipated that the coupler would be able to accommodate sufficient tunability and required fabrication tolerance in the final integrated devices. The polarization dependent operation of the coupler is complimented by the type-II phase-matching of the three-wave-mixing, in which the pump wavelength is TE polarized, and there is choice for signal in TE (TM) and idler in TM (TE) polarizations.

## 4.5 Tapered Coupler

It has been found in the literature that the tapered access waveguides improve the performance by reducing back reflections in the MMI cavity. In order to asses this improvement, the coupler design was modified and tapers were introduced in the inner

side of the access waveguides. The modified design and the fabricated couplers in this case are given in figure 4-13.

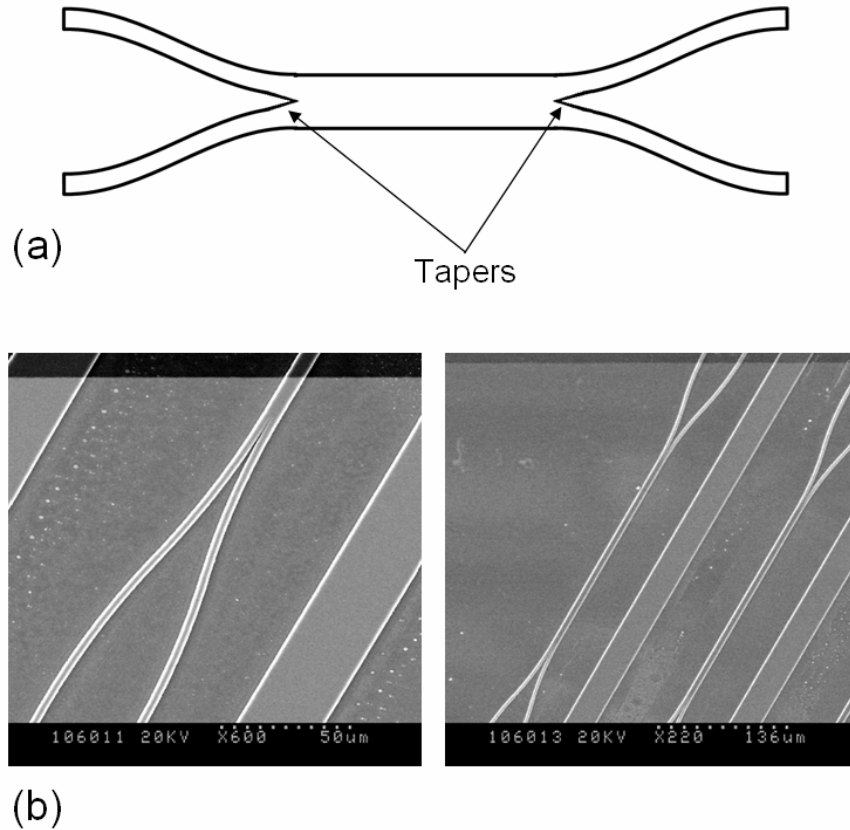


**Figure 4-13 – Tapered couplers, (a) tapers have been introduced in the inner side of the access waveguides, (b) SEM images of the fabricated couplers.**

The measurements over a range of MMI cavity lengths in this case are given in figure 4-14. The minimum cross talk for the half-band-gap wavelength has not been improved in this case; however, there is an improvement observed when the coupler cavity is away from the designed length (220 μm), as compared to that of the measurements in figure 4-12. This improvement could be the result of reduced back reflections in the MMI cavity. The cross talk for the band-gap wavelength of 788 nm in this case is measured to be -6.9 dB for 210 μm long cavity, which is also consistent with the previous values. It should be mentioned here that the actual cavity length is slightly longer in the case of tapered couplers due to the RIE lag in the converging gaps on either side. Again, the measurements performed using two different samples establish the fabrication process repeatability.

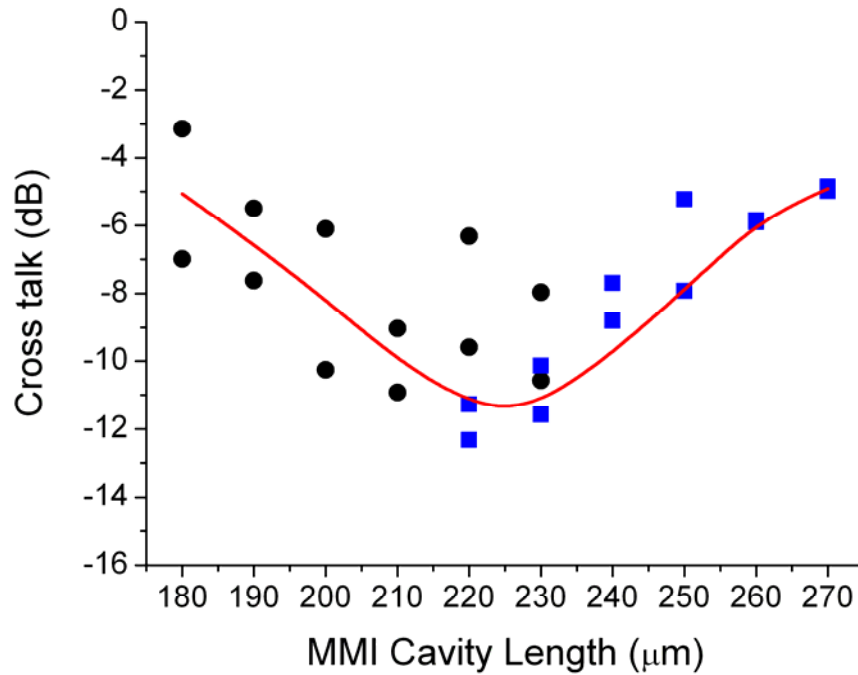


**Figure 4-14 – Measured performance of the tapered coupler for the half-band-gap wavelength (quasi-TE polarized light). Solid line is a smoothed fit to the data, solid circles and squares represent the measured data.**

This chapter has covered the optical routing components in our integrated OPO. Required di-chroic coupling has been demonstrated with a MMI coupler – the design for which has been optimized using BeamPROP. The fabrication challenges have been identified, and achieved, while keeping this process inline with the over-all fabrication to demonstrate monolithic integration. The minimum cross talk of -14 dB for the half-band-gap wavelengths will introduce the transmission loss in the final device, and the minimum cross talk of -7 dB for the band-gap wavelength will affect the Q of the ring laser.

# *Chapter 5*

## Superlattice Lasers

The inclusion of an integrated pump source in an optoelectronic device has the benefits of reduced losses (which are un-avoidable in the case of coupling an external source), higher performance (as more power is available for processing), higher irradiance for intra-cavity processing, and a reduced size. However, the critical issue of monolithic integration of the passive and the active components on a single chip is prevalent. At first, a material has to be designed which can incorporate laser action and does not compromise the passive processing significantly. Secondly, the fabrication process has to be identified in which the complete chip should be processed while protecting the as-grown properties of the material in the active sections.

The identified challenges are completely applicable in our device, where we had to incorporate a ring laser in the integrated chip. The foremost challenge was to design a lasing material, and the complexity became paramount as the laser action in superlattice heterostructures has been reported scarcely. It was identified in initiation that we will be requiring a number of wafers for the laser action to be observed, which became true at last as we had to optimize the structure in more than 7 wafers, and above 20 devices were fabricated and tested. The discussion starts with the superlattice heterostructure materials.

### 5.1 Materials

The integrated design requires us to have an on-chip pump source; therefore, it was prerequisite to achieve the laser action in a similar material structure which has been used previously for the nonlinear experiments.

The material design initially started with the active version of the wafer BMH1. The 75 periods 14ML GaAs/14 ML Al<sub>0.85</sub>Ga<sub>0.15</sub>As superlattice core was left un-doped, to form the active region of a waveguide, which had p- and n-doped upper and lower cladding layers respectively. The wafer design identified as BMH3 (table 5-1), was grown using MBE at EPSRC National Centre for III-V Technologies, Sheffield. The growth information, including the impurity concentration, is unavailable.

It has been identified in the previous chapters, that the initial shallow etched device design is unable to provide the necessary mode confinement for the wavelength near the band-gap, especially in the curved sections. It has also been observed that the increased etch depth will partially expose the superlattice active layer. Keeping this in view, the wafer design was modified to reduce the superlattice thickness to 300 nm, and subsequently adding the buffer layers on each side of the superlattice to keep the core at 600 nm thickness. The modified design BMH4 is given in table 5-2. This wafer was also provided by the MBE growth facility at Sheffield. The measured PL of BMH4 at room-temperature is 769.5 nm, with full width at half maximum (FWHM) of 18.8 nm from the centre of the wafer. The PL map identified a gradual red shift of ~20 nm as the PL is obtained from the centre to the edge of the wafer, given in figure 5-1.

<b>Layer</b>	<b>Thickness</b>	<b>Doping (cm<sup>-3</sup>)</b>
Cap GaAs	100 nm	P+
Outer cladding Al <sub>0.60</sub> Ga <sub>0.40</sub> As	800 nm	P (~5×10 <sup>17</sup> )
Core cladding Al <sub>0.56</sub> Ga <sub>0.44</sub> As	300 nm	P (~5×10 <sup>17</sup> )
(finishing with) Al <sub>0.85</sub> Ga <sub>0.15</sub> As	(4 nm)	Intrinsic
14ML GaAs/ 14ML Al <sub>0.85</sub> Ga <sub>0.15</sub> As SL layers (74 periods)	596 nm	Intrinsic
Al <sub>0.85</sub> Ga <sub>0.15</sub> As	4 nm	Intrinsic
Core cladding Al <sub>0.56</sub> Ga <sub>0.44</sub> As	300 nm	N (~5×10 <sup>17</sup> )
Outer cladding Al <sub>0.60</sub> Ga <sub>0.40</sub> As	800 nm	N (~5×10 <sup>17</sup> )
Base layer Al <sub>0.85</sub> Ga <sub>0.15</sub> As	800 nm	N (~5×10 <sup>17</sup> )
(100) GaAs substrate		N+

**Table 5-1 – Designed active wafer BMH3.**

Layer	Thickness	Doping (cm <sup>-3</sup> )
Cap GaAs	100 nm	P+
Outer cladding Al <sub>0.60</sub> Ga <sub>0.40</sub> As	800 nm	P (~5×10 <sup>17</sup> )
Core cladding Al <sub>0.56</sub> Ga <sub>0.44</sub> As	300 nm	P (~5×10 <sup>17</sup> )
Buffer Al <sub>0.43</sub> Ga <sub>0.67</sub> As	150 nm	Intrinsic
(finishing with) Al <sub>0.85</sub> Ga <sub>0.15</sub> As	(4 nm)	Intrinsic
14ML GaAs/ 14ML Al <sub>0.85</sub> Ga <sub>0.15</sub> As SL layers (37 period)	296 nm	Intrinsic
Al <sub>0.85</sub> Ga <sub>0.15</sub> As	4 nm	Intrinsic
Buffer Al <sub>0.43</sub> Ga <sub>0.67</sub> As	150 nm	Intrinsic
Core cladding Al <sub>0.56</sub> Ga <sub>0.44</sub> As	300 nm	N (~5×10 <sup>17</sup> )
Outer cladding Al <sub>0.60</sub> Ga <sub>0.40</sub> As	800 nm	N (~5×10 <sup>17</sup> )
Base layer Al <sub>0.85</sub> Ga <sub>0.15</sub> As	800 nm	N (~5×10 <sup>17</sup> )
(100) GaAs substrate		N+

Table 5-2 – Designed active wafer BMH4.

The wafer structure BMH4, was also requested to be grown locally (MBE research group, University of Glasgow), by Prof. Colin Stanley. The private communication resulted in a modification in the structure, in which the outer and the core cladding layers were merged into a single cladding of Al<sub>0.60</sub>Ga<sub>0.40</sub>As (1100 nm thick). The doping profile was also modified. This design (table 5-3), was grown locally using MBE, and also by MOVPE at Sheffield. The wafers were identified as BMH5 & BMH6 respectively.

The measured PL of BMH5 is 780 nm at room-temperature. Also, the PL measurements across the whole wafer are uniform and close to 780 nm. The growth information for this wafer (BMH5) is unavailable; whereas, a comprehensive growth information has been made available by Sheffield for BMH6. The measured electroluminescence (EL) for the wafer BMH6 is 770 nm. The doping concentration is 2×10<sup>19</sup> cm<sup>-3</sup> in the GaAs cap, and 9×10<sup>17</sup> cm<sup>-3</sup> in the upper cladding layer. The wafer was grown 10° towards the [111] plane.

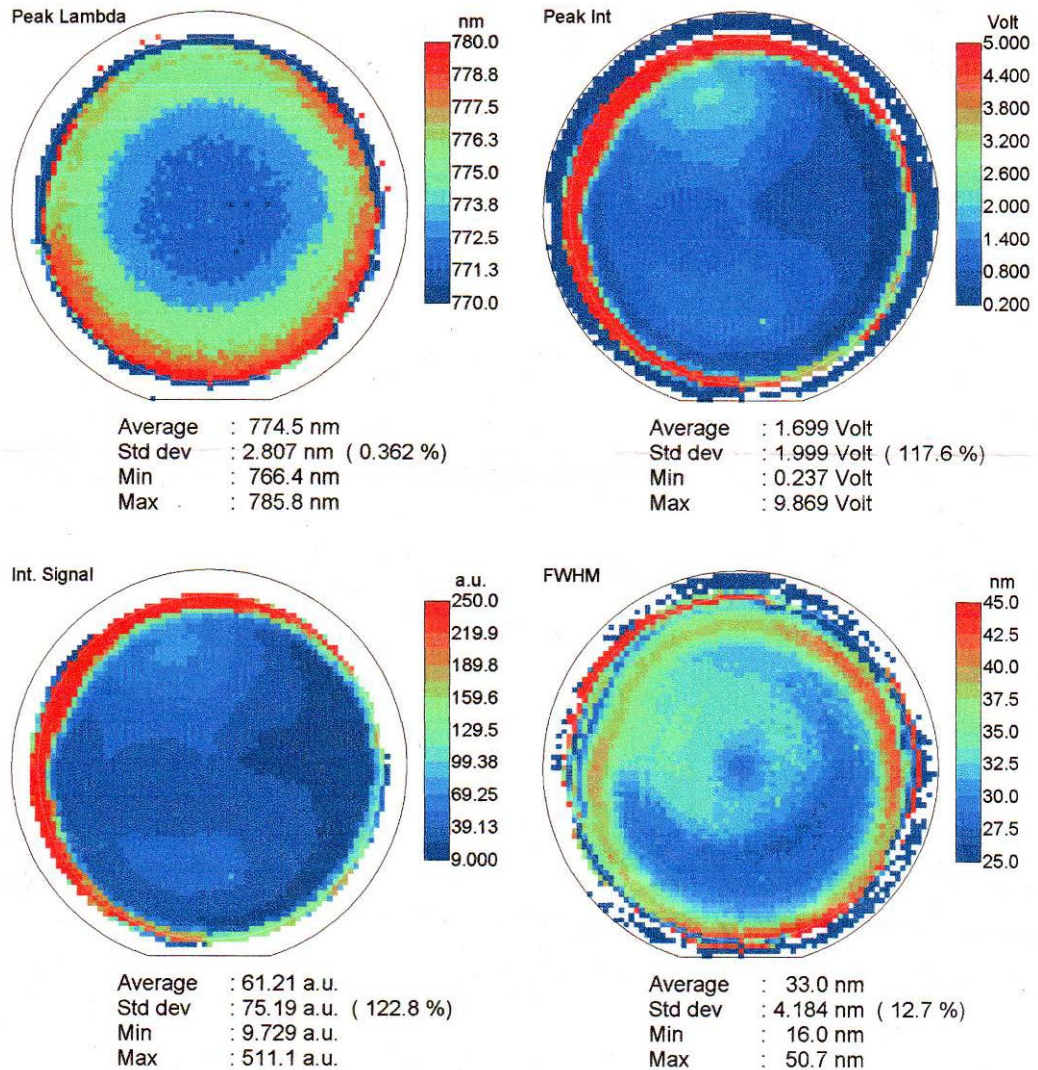


Figure 5-1 – PL map of the wafer BMH4.

The growth information for BMH6, along with the real time laser reflectometry and the surface temperature, is given in figure 5-2. The reflectometry was performed simultaneously with two sources: 1) 950 nm source, and 2) 633 nm source. The reflectivity oscillations (red oscillations for the longer source, and blue oscillations for the shorter source), clearly identify the different growth layers; especially the blue oscillations in the case of core layer can count 37 periods of the superlattice. The pyrometer measurement shows that the surface temperature has been kept practically constant during the wafer growth.

Layer	Thickness	Doping (cm <sup>-3</sup> )
Cap GaAs	100 nm	P+ [Carbon] ( $\sim 1 \times 10^{19}$ )
Cladding Al <sub>0.60</sub> Ga <sub>0.40</sub> As	1100 nm	P [Carbon] ( $\sim 2 \times 10^{18}$ )
Buffer Al <sub>0.43</sub> Ga <sub>0.67</sub> As	150 nm	Intrinsic
(finishing with) Al <sub>0.85</sub> Ga <sub>0.15</sub> As	(4 nm)	Intrinsic
14ML GaAs/ 14ML Al <sub>0.85</sub> Ga <sub>0.15</sub> As SL layers (37 period)	296 nm	Intrinsic
Al <sub>0.85</sub> Ga <sub>0.15</sub> As	4 nm	Intrinsic
Buffer Al <sub>0.43</sub> Ga <sub>0.67</sub> As	150 nm	Intrinsic
Outer clad Al <sub>0.60</sub> Ga <sub>0.40</sub> As	1100 nm	N [Silicon] ( $\sim 2 \times 10^{18}$ )
Base layer Al <sub>0.85</sub> Ga <sub>0.15</sub> As	800 nm	N [Silicon] ( $\sim 2 \times 10^{18}$ )
(100) GaAs substrate		N+

Table 5-3 – Designed active wafers BMH5 &amp; BMH6.

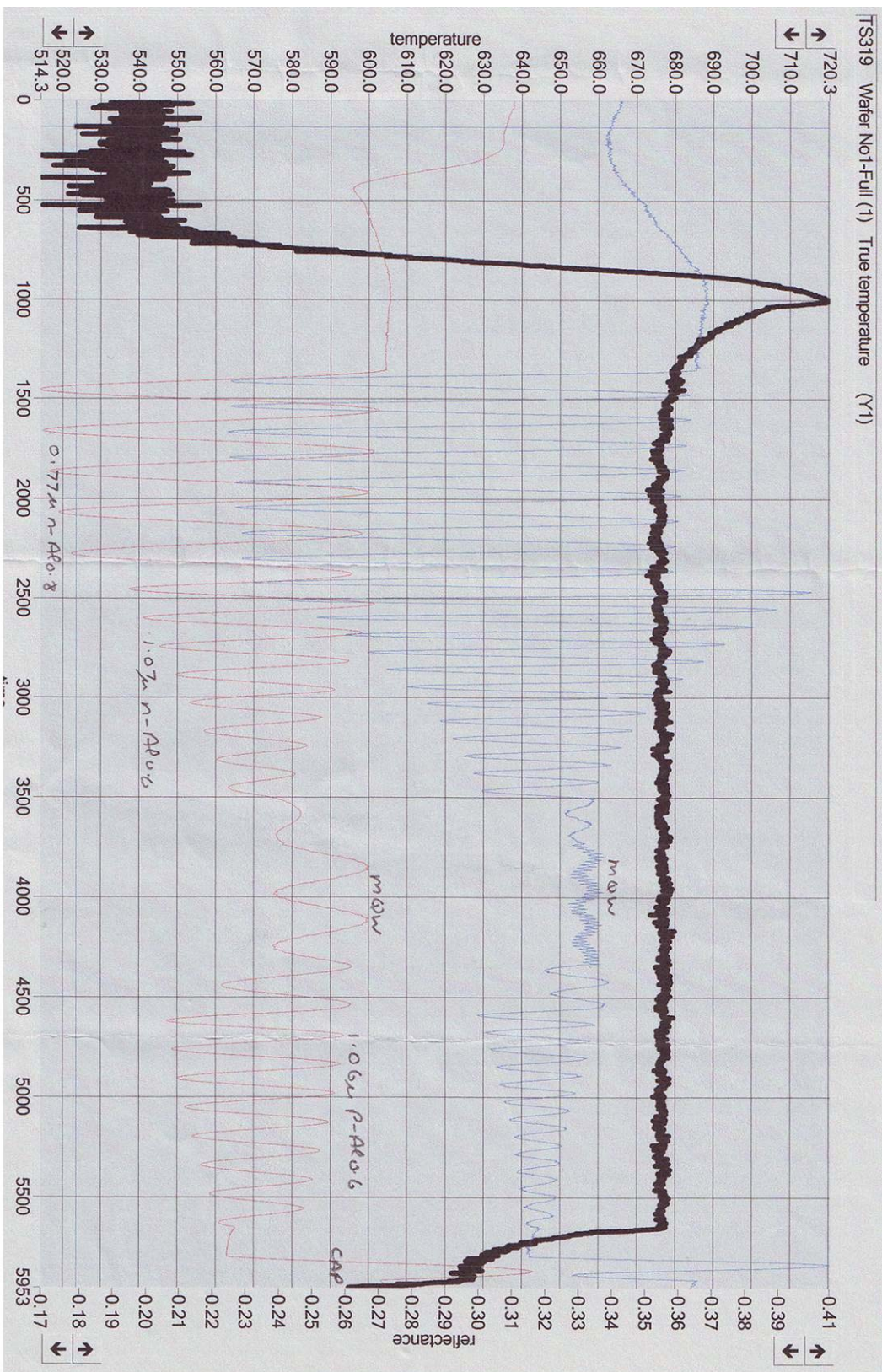


Figure 5-2 – The real time growth information for BMH6. Black trace is the surface temperature, red trace is the reflectivity data from a 950 nm source, and blue is from a 633 nm source.

It was instigated that the buffer  $\text{Al}_{0.43}\text{Ga}_{0.67}\text{As}$  layers, in conjunction with the 4 nm finishing layers of  $\text{Al}_{0.85}\text{Ga}_{0.15}\text{As}$ , on either side of the superlattice might end up as carrier traps, and degrade the performance. In order to avoid this, the core structure was modified. The buffer layers were removed, and the transitional thin layers were introduced between the superlattice and the claddings. The supporting argument for the selection of the thicknesses of 1 nm and 2 nm for GaAs and  $\text{Al}_{0.8}\text{Ga}_{0.2}\text{As}$  in the transitional layers comes from the energy band calculation. The ECA research software (mentioned earlier), identified that the GaAs quantum well (having thickness less than 3 nm and bounded by  $\text{Al}_{0.8}\text{Ga}_{0.2}\text{As}$  barriers), will possess an indirect energy band. This 3 nm or less GaAs well, coupled with a 2 nm  $\text{Al}_{0.8}\text{Ga}_{0.2}\text{As}$  barrier, will support the smooth carrier transport into the superlattice active layer.

This modified design is given in table 5-4 (the transitional thin layers are highlighted), it was grown using MOVPE at Sheffield, and was identified as BMH7. This wafer, which was grown  $10^\circ$  to the [111] plane, has the measured carbon concentration of  $3.3 \times 10^{19} \text{ cm}^{-3}$  in the GaAs cap, and  $1.6 \times 10^{18} \text{ cm}^{-3}$  in the upper cladding. The measured PL of the wafer is 777 nm from the centre of the wafer.

Layer	Thickness	Doping ( $\text{cm}^{-3}$ )
Cap GaAs	100 nm	P+ [Carbon] ( $\sim 1 \times 10^{19}$ )
Cladding $\text{Al}_{0.60}\text{Ga}_{0.40}\text{As}$	1250 nm	P [Carbon] ( $\sim 2 \times 10^{18}$ )
GaAs	1 nm	Intrinsic
$\text{Al}_{0.8}\text{Ga}_{0.2}\text{As}$	2 nm	Intrinsic
GaAs	2 nm	Intrinsic
14ML GaAs / 14ML $\text{Al}_{0.8}\text{Ga}_{0.2}\text{As}$ SL layers (37 period)	296 nm	Intrinsic
$\text{Al}_{0.8}\text{Ga}_{0.2}\text{As}$	4 nm	Intrinsic
GaAs	2 nm	Intrinsic
$\text{Al}_{0.8}\text{Ga}_{0.2}\text{As}$	2 nm	Intrinsic
GaAs	1 nm	Intrinsic
Cladding $\text{Al}_{0.60}\text{Ga}_{0.40}\text{As}$	1000 nm	N [Silicon] ( $\sim 2 \times 10^{18}$ )
$\text{Al}_{0.80}\text{Ga}_{0.40}\text{As}$ Buffer	1000 nm	N [Silicon] ( $\sim 2 \times 10^{18}$ )
GaAs Buffer		N+
(100) GaAs substrate		N+

Table 5-4 – Designed active wafer BMH7.

Another design was also worked out, in the light of previous work done on the superlattice lasers by Dr. M. Sorel & Prof. D. Hutchings [153] (the laser action was observed in AlAs–GaAs superlattice; however, the information is unavailable on this experiment, as the material degraded most likely due to the oxidation of AlAs layers). The designed material (in our case), was also a complete superlattice heterostructure in which the core and the wave-guiding layers were alternating thin layers of X ML GaAs / Y ML  $\text{Al}_{0.8}\text{Ga}_{0.2}\text{As}$ . This design, given in table 5-5, was grown using MBE at Sheffield. The initial material tests performed on the first wafer showed a very high material resistance (the details of these tests are given in the next section). Therefore, a new wafer was made available by Sheffield (The first wafer is identified as BMH8a, and the improved second wafer is identified as BMH8b). The room-temperature PL for the wafer BMH8a is 774 nm, where as the information for BMH8b is unavailable.

Layer	Thickness	Doping (cm <sup>-3</sup> )
Cap GaAs	100 nm	P+ [Carbon] ( $\sim 1 \times 10^{19}$ )
Cladding 6ML GaAs / 14ML Al <sub>0.8</sub> Ga <sub>0.2</sub> As (SL layers XX period)	1250 nm	P [Carbon] ( $\sim 1 \times 10^{18}$ )
14ML Al <sub>0.8</sub> Ga <sub>0.2</sub> As	4 nm	Intrinsic
10ML GaAs	2.8 nm	Intrinsic
14ML GaAs / 14ML Al <sub>0.8</sub> Ga <sub>0.2</sub> As SL layers (37 period)	296 nm	Intrinsic
14ML Al <sub>0.8</sub> Ga <sub>0.2</sub> As	4 nm	Intrinsic
10ML GaAs	2.8 nm	Intrinsic
Cladding 6ML GaAs / 14ML Al <sub>0.8</sub> Ga <sub>0.2</sub> As (SL layers XX period)	1250 nm	N [Silicon] ( $\sim 1 \times 10^{18}$ )
Base Cladding Al <sub>0.8</sub> Ga <sub>0.2</sub> As	1000 nm	N [Silicon] ( $\sim 2 \times 10^{18}$ )
(100) GaAs substrate		N+

**Table 5-5 – Designed active wafer BMH8 (a/b).**

In concluding this section, one final design is presented which actually demonstrated the laser action. The repeated cycle of material design and test, identified a lower gain in the thick superlattice core. Therefore, the active layer thickness was reduced down to 100 nm superlattice (table 5-6). The design of BMH7 was repeated in this case, but the intrinsic buffer layers (which were present in BMH6) were brought back. The wafer BMH9 was grown using MOVPE at Sheffield, and this wafer (like all other MOVPE grown wafers) was grown with a 10° offset to the [111] axis. The growth information identifies: 1) the measured EL of 772 nm, from the centre of the wafer, 2) the doping concentration of  $\sim 4 \times 10^{19}$  cm<sup>-3</sup> in the GaAs cap, and 3) the doping concentration of  $\sim 2 \times 10^{19}$  cm<sup>-3</sup> in the upper cladding. The wafer design BMH9 was also grown with a slightly thicker superlattice core of 150 nm, which is identified as BMH9\_REV in the later discussions.

Layer	Thickness	Doping (cm <sup>-3</sup> )
Cap GaAs	100nm	P+ [Carbon] ( $\sim 1 \times 10^{19}$ )
Cladding Al <sub>0.60</sub> Ga <sub>0.40</sub> As	1000nm	P [Carbon] ( $\sim 1 \times 10^{18}$ )
Buffer Al <sub>0.45</sub> Ga <sub>0.55</sub> As	250nm	Intrinsic
GaAs	1nm	Intrinsic
Al <sub>0.8</sub> Ga <sub>0.2</sub> As	2nm	Intrinsic
GaAs	2nm	Intrinsic
14ML GaAs / 14ML Al <sub>0.8</sub> Ga <sub>0.2</sub> As SL layers (12 period)	96nm	Intrinsic
Al <sub>0.8</sub> Ga <sub>0.2</sub> As	4nm	Intrinsic
GaAs	2nm	Intrinsic
Al <sub>0.8</sub> Ga <sub>0.2</sub> As	2nm	Intrinsic
GaAs	1nm	Intrinsic
Buffer Al <sub>0.45</sub> Ga <sub>0.55</sub> As	250nm	Intrinsic
Cladding Al <sub>0.60</sub> Ga <sub>0.20</sub> As	1000nm	N [Silicon] ( $\sim 1 \times 10^{18}$ )
Al <sub>0.80</sub> Ga <sub>0.40</sub> As Buffer	500nm	N [Silicon] ( $\sim 1 \times 10^{18}$ )
GaAs Buffer		N+
(100) GaAs substrate		N+

Table 5-6 – Designed active wafer BMH9.

## 5.2 Material Tests

The material design, as presented in the previous section, had been a repeated process in our aim to demonstrate the laser action. Over the period of one and half year, this effort drove us to: design, process, and optimize the structure, and subsequently report our feed back to the grower. The basic material tests, which include TLM and BAL, are highly recommended in the circumstances where optimum structural parameters are unknown. These basic tests identify the material gain and the electrical properties of the structure in a short period of time; in which the required devices can be easily prepared using photolithography.

### 5.2.1 Transmission Line Measurement (TLM)

The specific contact resistance of any ohmic contact is identified with a well known model of transmission line measurement. The TLM information helps the selection of a thin film (ohmic contact), which subsequently affects the device performance; and also, it is a quick test to validate the appropriate doping of the material.

The TLM in our case was performed on most of the wafers, and the measurements were reported back to the grower for further optimization. It is necessary to mention that the measurements were only performed for the top/polished side (P-contact) of the wafers. The sample preparation was a quick photolithographic process, in which: firstly the evaporated metal contact pads (240 nm Au/15 nm Pt/15 nm Ti) were deposited using a lift-off photo-resist mask, and secondly the shallow etched mesas were defined (in  $\text{SiCl}_4$  RIE), also using the photo-resist mask. After the mesa definition, the samples were given a 60 s annealing treatment in the RTA at 360 °C (figure 5-3b), with an initial ramp of 320 °C for 20 s.

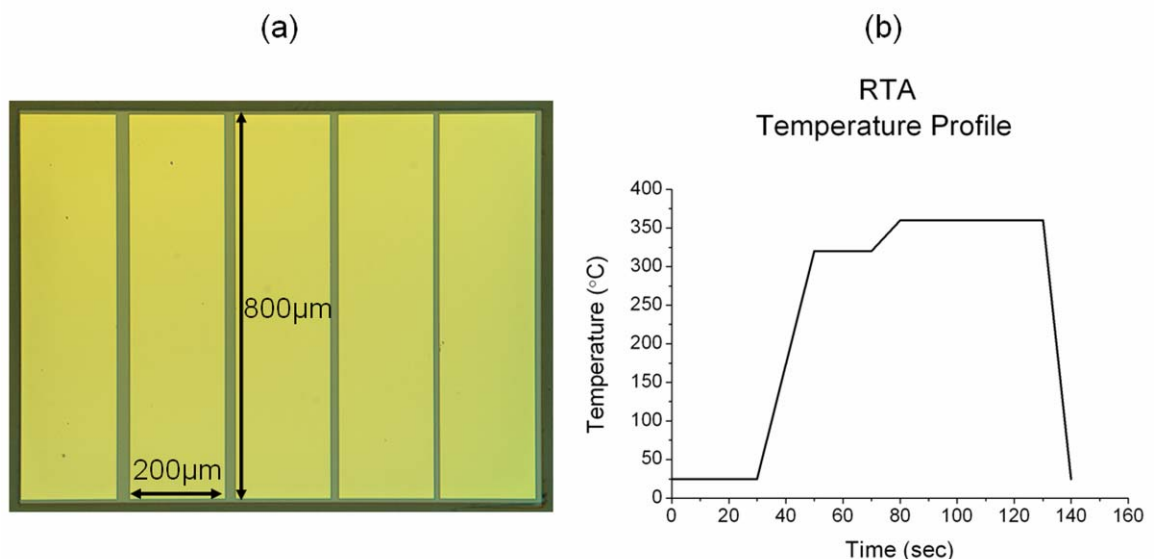


**Figure 5-3 – Left a) A mesa etch section with 5 contact pads having multiple gaps in between them; Right b) RTA profile of the annealing treatment provided to the samples after mesa definition.**

A sample used for TLM (given in figure 5-3a), had multiple mesa sections, each having 5 contact pads (800  $\mu\text{m}$  long and 200  $\mu\text{m}$  wide). These contact pads had a gap of 25  $\mu\text{m}$ ,

20  $\mu\text{m}$ , 15  $\mu\text{m}$  and 10  $\mu\text{m}$  between them (as shown in the figure, from left to right). It is worthy to mention that the above given gaps were defined on the photolithography mask; whereas for the TLM, actual gaps on the samples were measured using optical microscope.

The prepared samples were measured on the four-probe station. Two probes each were brought into contact with the consecutive pads, with one designated for the voltage and second for the current. The measurement was done by applying bias voltage across the pads, and measuring the current flow from one contact to the other. The automated script on the four-probe station calculated the resistance between the two ohmic contacts. This process was repeated such that the four measurements (four resistances) were obtained for the four individual gaps in a single mesa section. A schematic of the four-probe station measurement is given in figure 5-4. Measurements were performed on the multiple mesa sections across the sample to obtain a scatter of the resistances.

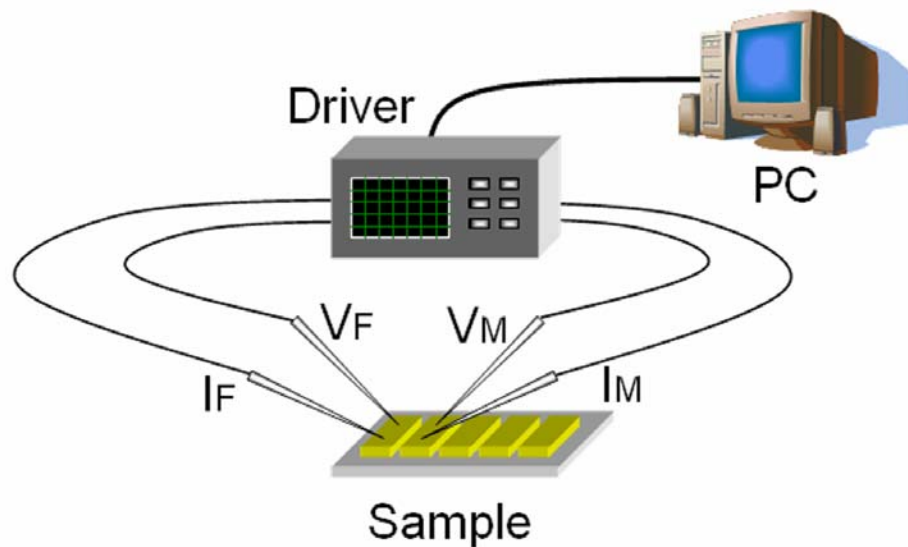


**Figure 5-4 – Schematic of the four-probe station measurement. The bias voltage is applied across VF & VM, and the current flow is measured from IF to IM.**

The scatter of resistances has been plotted against their respective gaps (between the contact pads) in the case of measurements from BMH5, given in figure 5-5.

The linear fit to this scatter gives information about the contact resistance and eventually the specific contact resistance, which can be calculated as under [154]:

$$L_T = \frac{R_c}{R_{sheet}/W}$$

- $L_T$  = Transfer length (half of the x-intercept of the linear fit).
- $R_c$  = Contact resistance (half of the y-intercept of the linear fit).
- $R_{sheet}$  = Sheet resistance (resistance of the thin semiconductor region in which lateral current flows).
- $W$  = Width of the pad (which in this case is 800  $\mu\text{m}$ ).
- $R_{sheet}/W$  is the slope of the linear fit.

The specific contact resistance  $\rho_c$  is calculated by:

$$\rho_c = R_{sheet} L_T^2$$

The above given relation has been used to calculate the specific contact resistances of the active wafers, which are given in table 5-7. It can be identified in the table that the resistances of the wafers grown using MOVPE technology have very low values; the major contribution in this case is the highly doped ( $\sim 1 \times 10^{19} \text{ cm}^{-3}$ ) GaAs cap. The wafers grown using MBE technology have very high resistances, with the exception of BMH5 which was grown locally by MBE research group at Glasgow. The reason for these higher values are unclear; however, when these values were reported back to the grower (Sheffield), the growth challenges were identified for the  $\text{Al}_x\text{Ga}_{1-x}\text{As}$  claddings, in which the Al compositions were higher than 0.6 [155].

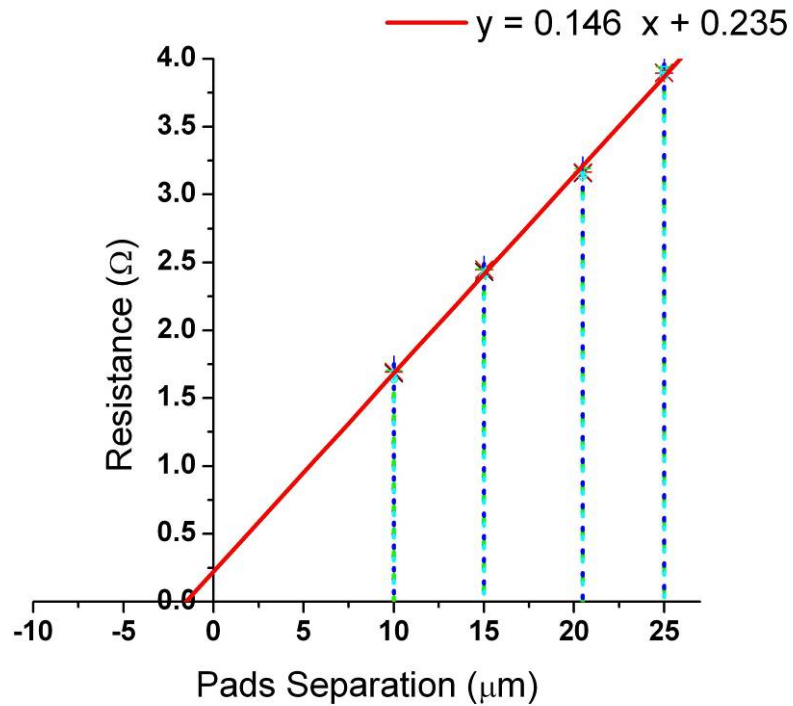


Figure 5-5 – The measured resistances’ scatter, plotted against their respective pads separation.

Active Wafer	Specific contact resistance ( $\Omega\text{mm}^2$ )	Equivalent resistance for 1 mm long ridge ( $\Omega$ )	Growth Technology
BMH3	Unavailable	-	-
BMH4	$6.628 \times 10^{-3}$	3314000	MBE
BMH5	$5.287 \times 10^{-4}$	0.264	MBE
BMH6	$9.348 \times 10^{-5}$	0.046	MOVPE
BMH7	$3.426 \times 10^{-5}$	0.017	MOVPE
BMH8a	$5.772 \times 10^{-2}$	28.86	MBE
BMH8b	Unavailable	-	-
BMH9	$7.601 \times 10^{-5}$	0.038	MOVPE

Table 5-7 – Measured specific contact resistances of the different active materials.

After performing the TLM tests, it has been established that the MOVPE growth has been a better choice as compared to the MBE. Acceptable electrical conductivity has also been achieved for the deposited P-contacts.

### 5.2.2 Broad Area Lasers (BAL)

Broad area laser is a quick and an effective way to identify the gain in any active material, in which the laser action is provided by the FP cavity formed between the two cleaved facets. The vertical beam confinement results from the wave-guiding layers in the material, whereas the lateral beam confinement is provided by the higher gain section just under the wide contact pad, caused by the higher current injection. Given the simplicity of the device fabrication, the BAL is one of the basic material tests performed in our case.

The fabrication process for the BAL involved: 1) the solvent cleaning of the samples, 2) the evaporated metal P-contact (240 nm Au/15 nm Pt/15 nm Ti) deposition, using a lift-off photo-resist mask, 3) mechanical thinning of the substrate, using the calcined aluminium-oxide powder, 4) solvent cleaning and the deposition of evaporated metal N-contact (240 nm Au/11 nm Ni/14 nm Au/14 nm Ge/14 nm Au), and finally 5) a 60 s annealing treatment in the RTA at 360 °C. The fabricated samples, which had measured P-contact pad-width of 78  $\mu\text{m}$ , were then cleaved to the different lengths and mounted (N-side/bottom side) on the brass pads using conductive silver epoxy. The samples were measured using Keithley 2520 Pulsed Laser Test system, in which the electrical pulse width was set to 10  $\mu\text{s}$  with a 1 ms pulse delay. The laser action was not observed in any of the wafers, except BMH9; however, the voltage current (V-I) measurements from the different wafers (samples cleaved to the length of 0.5 mm) are give in figure 5-6. It can be seen that the turn-on voltage for most of the diodes is in the acceptable limit, with the exceptions of BMH6 and BMH8a. The case of BMH8a has been previously discussed, and the growth challenges have been concluded for the low quality material structure. A peculiar case of BMH4 is apparent in the figure 5-6, in which the turn-on voltage of 3 V is observed; however, in the previous section, the same material was measured to have a very high specific contact resistance. After this, the TLM was repeated on BMH4 a couple of times, and it was found that the dependency of current flow over the applied bias is not linear (figure 5-7), which is contrary to an ohmic contact. An explanation for this behaviour could be the growth defects in the cladding layers (as identified by the grower), which are resulting as a variable sheet resistance to the lateral current flow (in

case of TLM); however, the vertical current flow might not be undermined, given that these defects are only confined within a region somewhere in the cladding.

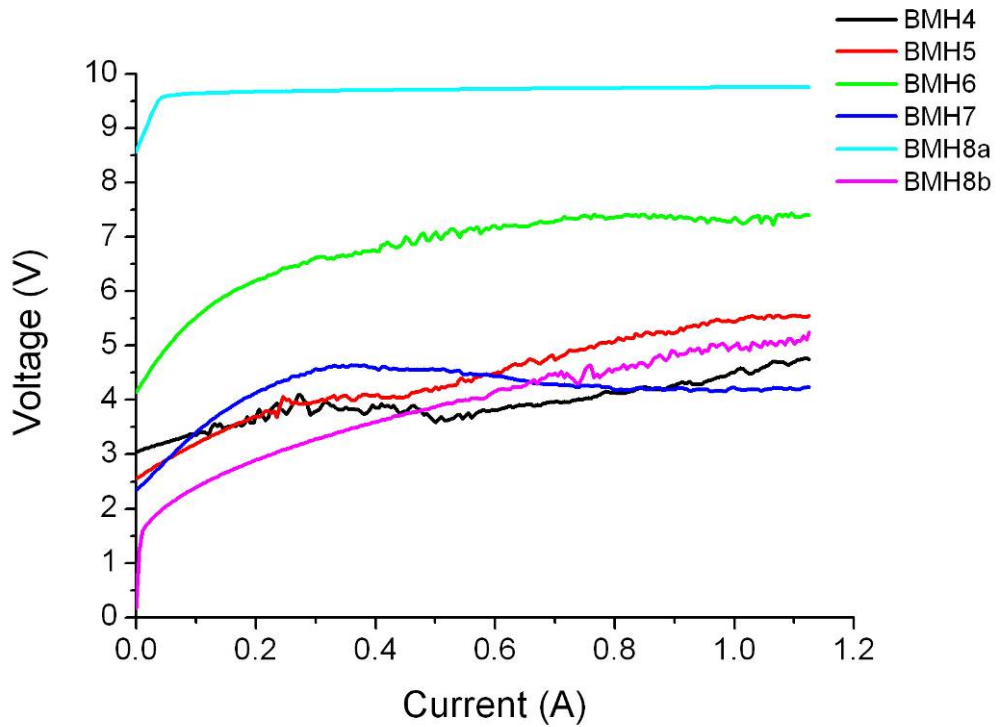


Figure 5-6 – V-I curves for the measured BAL.

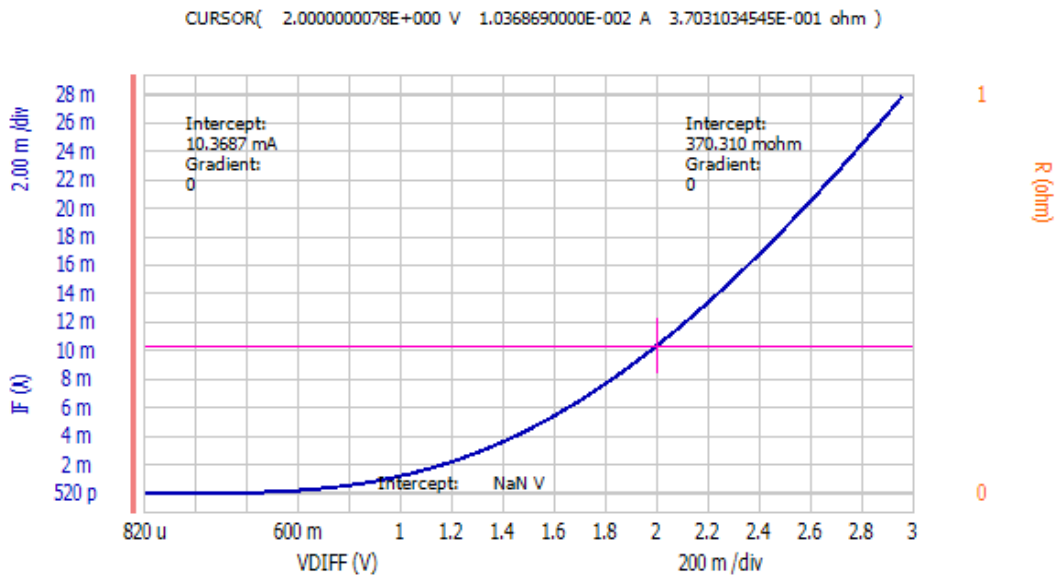


Figure 5-7 – TLM, current flow measurement (BMH4).

BAL fabricated on the wafer BMH9 demonstrated the laser action. Figure 5-8 shows the L-I-V curves over a range of the cavity lengths. The light was measured using a silicon photo-detector, which has a typical responsivity of 0.505 A/W near the wavelength of

interest, i.e., 780 nm. The lower turn-on voltage ( $\sim 1.8$  V) reflects the high quality growth of the material. It should be noted that these measurements are crude to some extent; however, they were obtained as a quick test to estimate the laser performance.

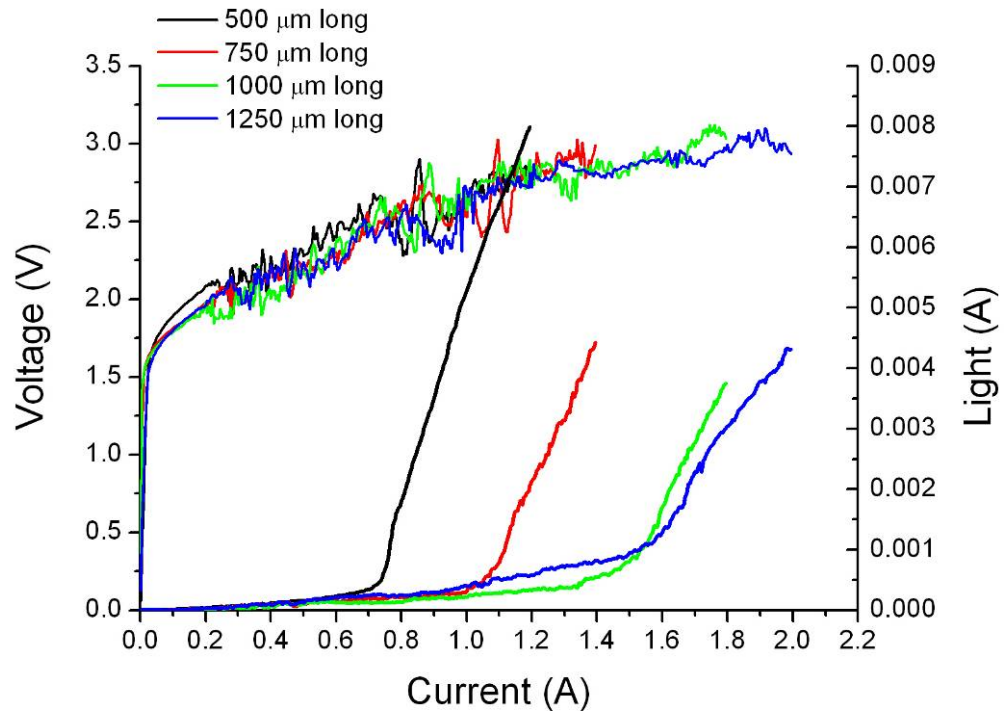


Figure 5-8 – L-I-V curves for the BAL (BMH9).

The threshold current density  $J_{th}$  obtained from the above measurements has been plotted against the inverse of the cavity length to determine the  $J_{th}(\infty)$  of an infinite length laser. The resulting  $J_{th}(\infty)$  is  $1500 \text{ A/cm}^2$ , which is tolerable considering it is a novel design.

In a separate test where the material BMH9 was initially given a 60 s annealing treatment at  $775 \text{ }^\circ\text{C}$  in RTA, a lower threshold has been observed for the similar device structures. The L-I-V curves (given in figure 5-9) show this reduced threshold for the annealed BMH9; whereas no significant change is observed in the turn-on voltage. The detailed investigation in this behavior is presented later in this chapter.

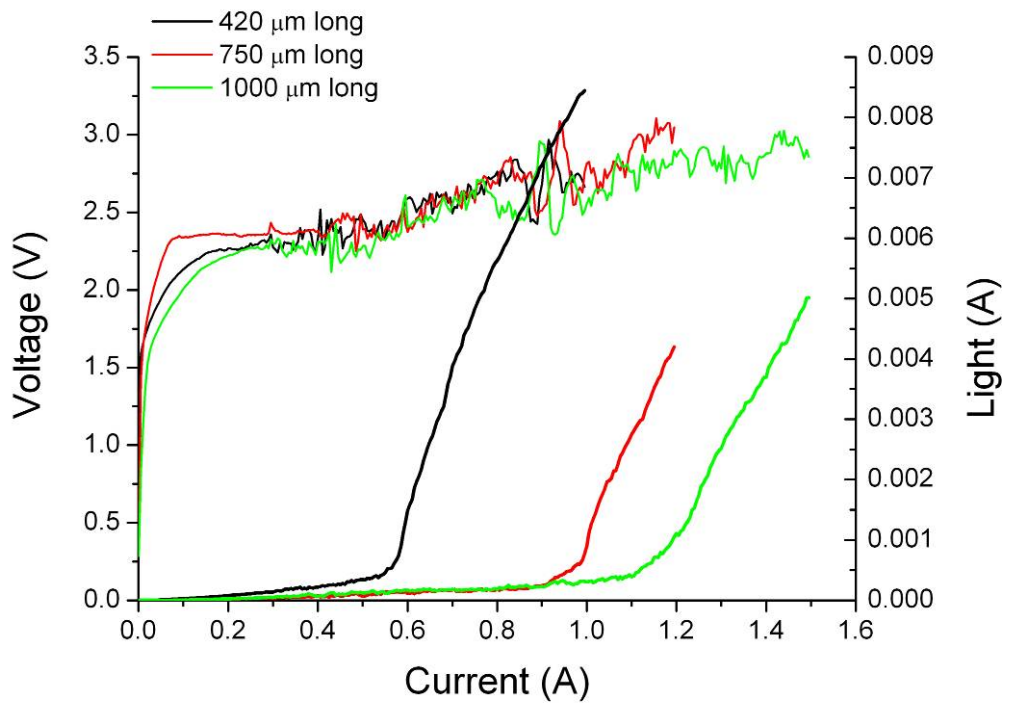


Figure 5-9 – L-I-V curves for the BAL (BMH9 annealed at 775 °C).

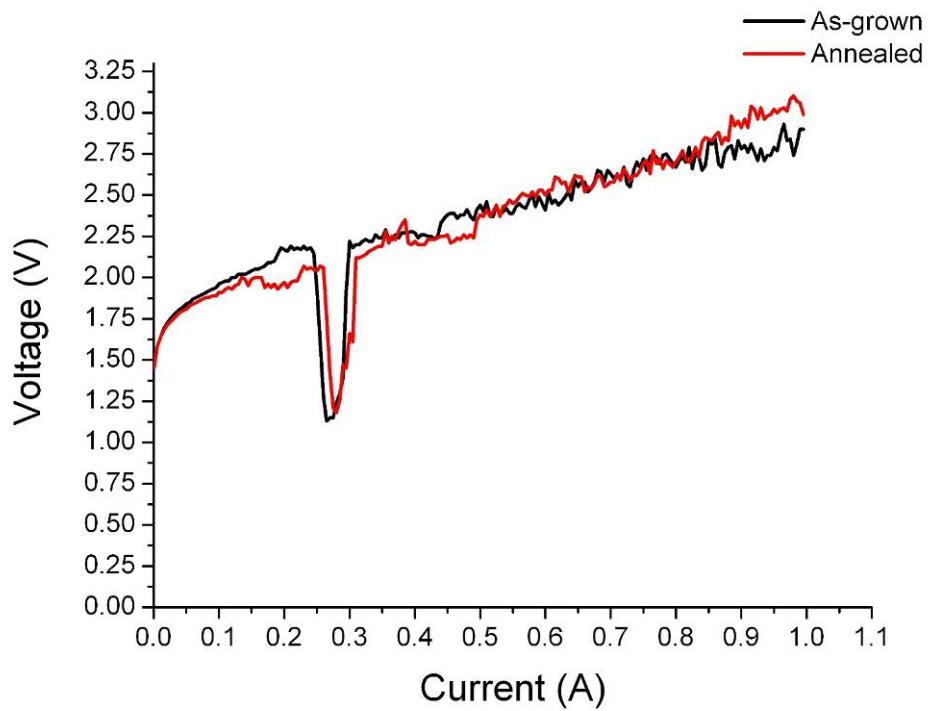


Figure 5-10 – V-I curves for the BAL, fabricated with as-grown and annealed (775 °C) BMH9\_REV.

A final BAL test was performed on the 150 nm thick superlattice core structure BMH9\_REV. The measurements in this case, and similar to all the previous BAL measurements, were done using the pulsed current injection at room-temperature. The laser action was not observed in both as-grown and annealed materials. However, a negative differential resistance (NDR) zone has been identified in the V-I curves, as shown in figure 5-10. This NDR is attributed to the increased carrier transport caused by the resonant tunneling.

As for now, it has been established that only BMH9 has demonstrated the laser action; therefore, only BMH9 was used for all the later investigation, including the ridge waveguide lasers and the ring lasers.

The next section of ridge waveguide lasers starts with the device design, and is supported by the simulations which have been performed to achieve an agreement with the waveguide design for the passive sections in a fully integrated device. The device design is followed by the fabrication process development and its optimization. Finally, the characterization and discussions on the results are presented.

### 5.3 Ridge Waveguide Lasers

Ridge waveguide laser is a class of semiconductor laser in which the light is confined in both transverse directions. The optical confinement in the vertical direction is provided by the index guiding, and the confinement in horizontal direction is provided by the etched surfaces. The laser action is achieved in a Fabry-Pérot cavity formed between the two cleaved facets, which makes ridge waveguide laser an edge emitting semiconductor laser. The lasers made in this geometry are widely applicable, and can achieve a good beam quality. In addition to it, they have a benefit of monolithic integration in a photonic integrated circuit, if the optical feedback to achieve the laser action is provided, e.g., by bragg reflectors, or in a ring laser.

The designed OPO requires us to achieve the laser action in a ring laser. Therefore, the optimum start should be the development of a ridge waveguide laser, and subsequently

develop the structure into the ring geometry. But initially, the ridge waveguide parameters have to be identified, i.e., the width and the etch depth, which ensure the single mode operation of the laser and incorporate low losses in the bended sections of the ring.

### 5.3.1 Device Design

The waveguide structure, which has been discussed in the previous chapters of QPM waveguides and di-chroic couplers, has been revisited for the lasers; and the new wafer design has been incorporated into the simulations for this structure. It was found previously that the etch depth required for the bended sections of the device should be increased to lower the bending losses, and it should not be increased too much to expose the superlattice active medium. Therefore, the optimum starting point for a ridge waveguide laser would be a completely etched upper cladding. Such a deep etched structure does introduce the transmission loss due to light scattering. This loss is reduced in the waveguides which have smooth side walls, and it could be achieved by optimizing the RIE during fabrication. However, it is a compromise that has to be made in order to avoid the bending losses which are much higher in the shallow etched structures.

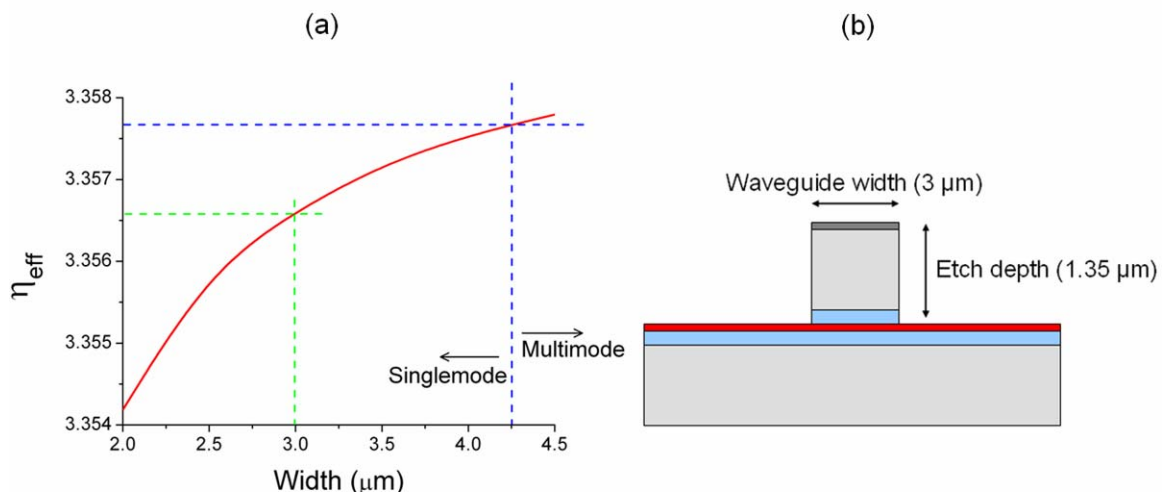


**Figure 5-11 – Left a) Effective refractive index calculations with varying the waveguide width (the upper cladding has been etched completely). Right b) The proceeded ridge structure (also highlighted by the green markers in (a)).**

Further investigation in the design has been supported by the mode solving simulations, given in figure 5-11. The increasing effective refractive index with the increasing waveguide width, indicates the higher confinement, and more power available for the laser action; however, it has been mentioned in the earlier work that the wider structure brings the higher order modes in the bended cavity [114]. It was decided to keep the width of the waveguides at 3  $\mu\text{m}$ , which is consistent with the width of the QPM waveguide and the access waveguides to the di-chroic couplers.

With the above mentioned parameters for the waveguide structure, the simulated mode diagram for the fundamental mode is given in the figure 5-12.

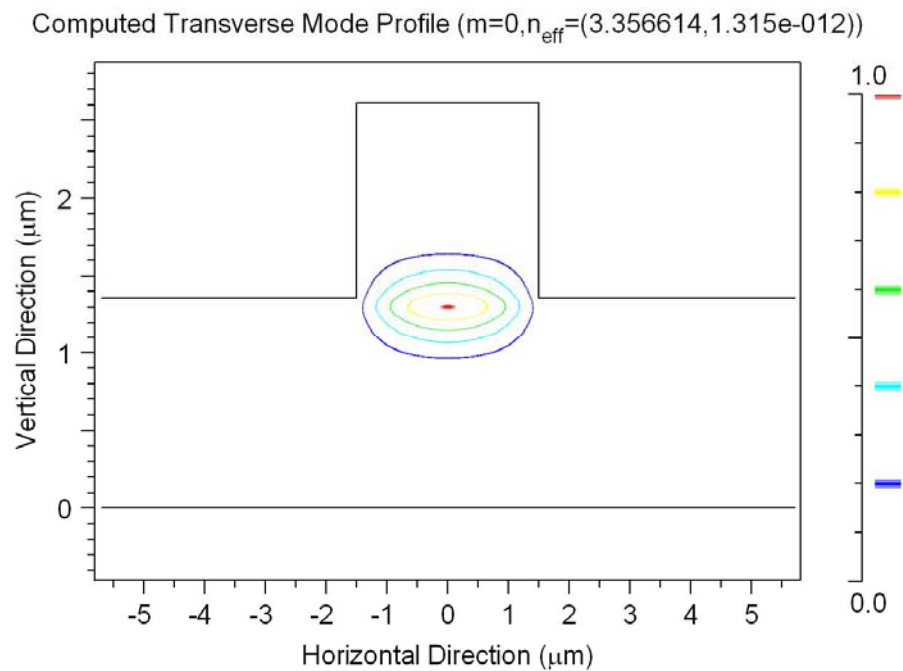


Figure 5-12 – Mode profile for 3  $\mu\text{m}$  wide waveguide, etched down to the core.

### 5.3.2 Fabrication Process

The fabrication process in the case of lasers is a lengthy procedure, and it requires considerate fragile handling and cleanliness. This multiple lithographic, etching, and metallization, process can be categorized into the following stages:

- Pre-fabrication cleaning.

- Registration markers.
- Waveguides patterning and subsequent definition using RIE.
- Waveguides insulation using PECVD SiO<sub>2</sub> deposition.
- Planarization.
- Contact windows patterning and subsequent definition using RIE.
- P-contact metallization.
- Mechanical thinning.
- N-contact metallization.
- RTA treatment and device mount.

The above given process is a standard procedure for any light emitting semiconductor device fabrication [114]; however, a new step of planarization has been introduced. This step has ensured a better control on the subsequent metallization, which has been compared with the standard sputter metal deposition. Moreover, planarization can provide a certain degree of protection while probing the waveguides in later device characterization. It is recommended to follow the whole process sequentially, where subtleties required in each stage, if overlooked, can easily degrade the complete device. It should be mentioned that almost all of the fabrication has been performed in the James Watt nano fabrication (JWNC) centre, except the thinning and cleaving/device mount stages.

#### 5.3.2.1 Sample Cleaning

The solvent cleaning techniques were employed after cleaving the samples to their required dimensions – which is a pre-requisite for further fabrication. The ultra-sonic assisted solvent cleaning involved: a 5 min soak of the sample in Acetone, a 5 min soak in Isopropanol (IPA), a 5 min soak of the sample in RO water, and then N<sub>2</sub> blow dry. The samples were also given a quick O<sub>2</sub> plasma cleaning (commonly known as O<sub>2</sub> Ash), to ensure any left over contamination removal. In addition to it, the sample boxes for subsequent placement were also swipe cleaned with the above given solvents to prevent any contamination. This cleaning process was employed before all the sample preparation stages of the lithography. A general cleanliness was maintained during any

inspection stage, e.g., SEM; however, for any unintentional contamination the samples were also cleaned after all the inspections.

### 5.3.2.2 Registration Markers

As mentioned earlier, the laser fabrication involves multiple lithographic stages. Therefore, it is mandatory to define a set of markers that would ensure the required alignment of the resist exposures in successive lithography.

The lithography employed in our samples has been Electron Beam (E-beam), so the registration/alignment techniques set for the machine were followed accordingly. The complete information about the alignment functionality in Leica Vectorbeam (VB6<sup>3</sup>), is available in the operator's manual (chapter 11, page 87) [156]. In summarizing this process, an alignment cross is defined on the sample's surface by the user initially, which E-beam identifies through a sequential search assisted by its internal algorithm. After the cross identification, a set of global markers is scanned across the surface, where the specific co-ordinates of these markers (in reference to the alignment cross) are defined by the user. It is mandatory to define the global markers across the substrate in four different locations. The E-beam can search these global markers and subsequently perform the alignment with 1  $\mu\text{m}$  precision – to achieve a higher precision a set of local markers can also be incorporated around a specific pattern. Each individual global marker is defined in a set of four markers, which ensures the redundancy if the markers' edges get degraded in subsequent searches by the high brightness E-beam.

The registration jobs in our case were mostly performed using the etch-pit markers. The samples were deposited with 200 nm of PECVD SiO<sub>2</sub> as a hard mask, followed by the PMMA resist spinning. After the E-beam exposure and development, the markers were defined using the CHF<sub>3</sub> RIE (an etch depth of 0.6-1  $\mu\text{m}$  is usually accepted in a multilayered GaAs substrate, for which the video level contrast can be easily detected by the machine). The resist was removed by the O<sub>2</sub> Ash – resist removal at this stage

---

<sup>3</sup> The VB6 E-beam writer was employed in all the electron beam lithography

can also be performed by placing the sample in acetone for about an hour in a hot water bath. The SiO<sub>2</sub> hard mask was finally etched in buffered HF solution, and the samples were solvent cleaned for further processing.

An exposed and developed registration job is given in figure 5-13. The sequential E-beam scan for the etch-pit marker is visible for the bottom left marker on the substrate.

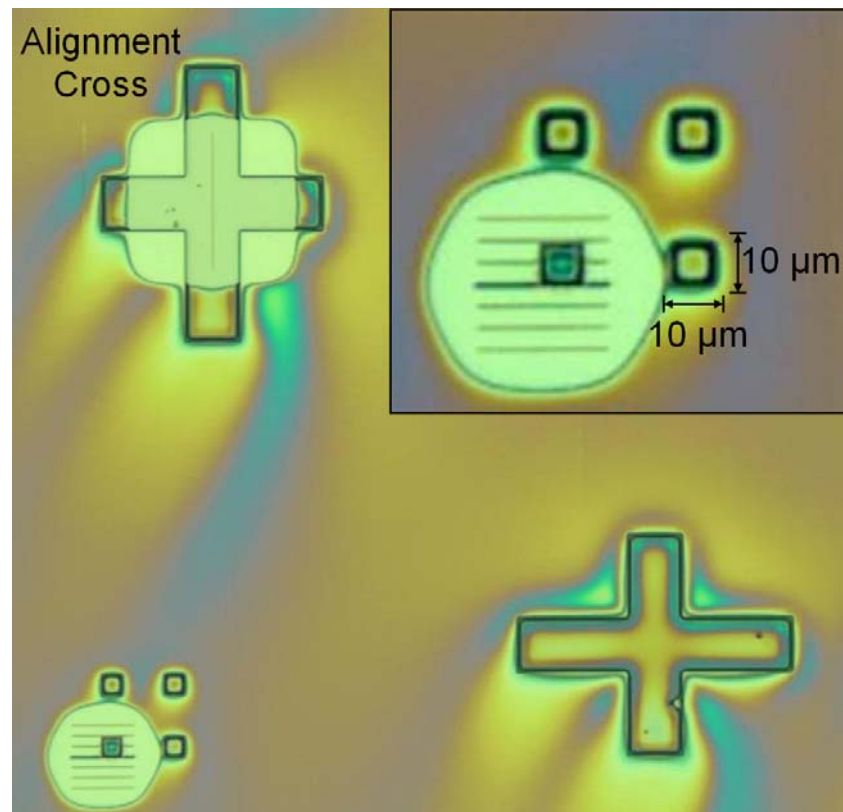


Figure 5-13 – Optical micrograph of an exposed and developed E-beam registration job.

### 5.3.2.3 Waveguides Definition

The negative tone E-beam resist Hydrogen Silsesquioxane (HSQ) was used for the waveguides patterning in a single step mask fabrication. The process included: HSQ (neat/100%) spinning, exposure in E-beam, and then development in the Tetramethylammonium hydroxide (TMAH) solution. The HSQ patterning is a much faster fabrication as compared to that of the PMMA based patterning. HSQ not only has

a high etch resistance (similar to that of PECVD SiO<sub>2</sub>), but also with the proper dose selection the sub-micron features with very high resolution can be easily achieved.

The final definition of waveguides was done using the SiCl<sub>4</sub> RIE assisted with an *in-situ* laser reflectometry, which has been discussed previously in the dry etch optimization section of the di-chroic couplers. The aim was to achieve the etch depths of 1.35 μm for the material structure BMH9. It has been identified previously that the deep etched waveguides suffer the light scattering, therefore some tests were performed to improve the etch process. The process parameters which were identified to give the best results are: 13 sccm SiCl<sub>4</sub> gas flow, 5 mT of pressure, and 250 W of power. This recipe, which is slightly different from the one used for couplers fabrication, was used in all the subsequent devices. The recipe not only ensured the side walls verticality, but also an improvement was observed in side walls. The edge-on view of an etched ring is given in figure 5-14, in which the very smooth side walls are conspicuous.

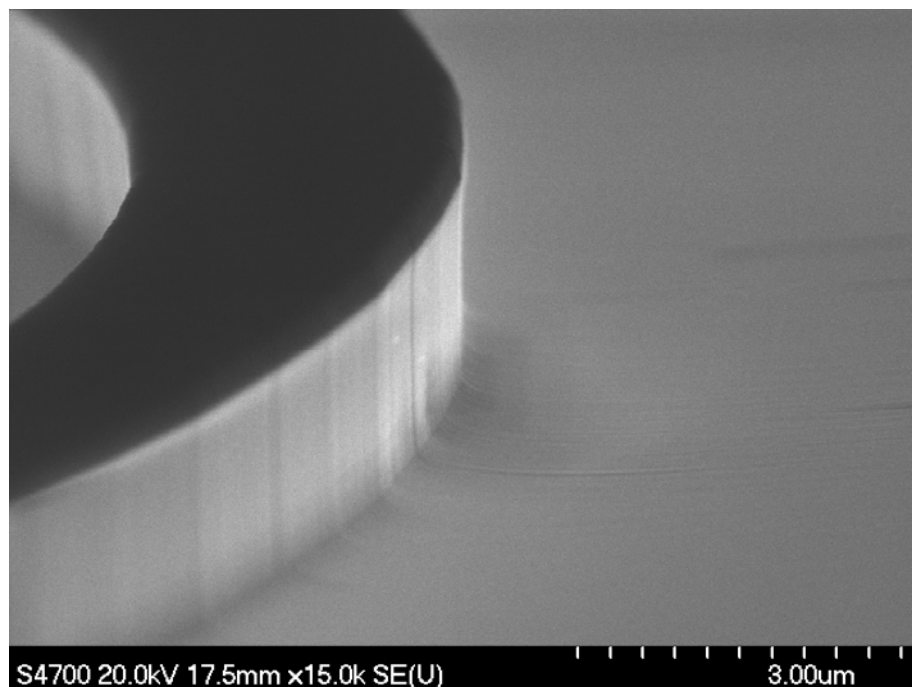


Figure 5-14 – The edge-on SEM image of an etched ring (HSQ mask is visible on the waveguide).

After the waveguides definition, the mask was removed with a wet etch in buffered HF solution. The samples were solvent cleaned, and an insulation layer of 200 nm PECVD SiO<sub>2</sub> was deposited.

#### 5.3.2.4 Planarization

The E-beam metal evaporation, which is a highly directional process, was employed to deposit the electrical contacts. This electron gun assisted vertical beam is very precise in providing the required thin film thickness on a flat surface; however, for a vertical edge this relationship cannot be ensured. The resultant thinner contacts covering the side walls are unstable at higher current injections. An alternate process of sputter metal coating after the evaporated metal deposition has been mentioned earlier [114]. The devices which were fabricated using the sputter metal deposition have been reported to perform effectively. The only criticism one can argue for this process is that it comprises two stages, which not only requires more time, but also, an additional care is required to move the samples to the sputter metal coater which is located in the Rankine building. For these constraints, a planarization technique was developed, which not only reduced the fabrication time for metal contacts, but also, an additional protection was ensured during the probe measurements in the later device characterization. The process involved the HSQ spinning on the samples, and subsequent oven bake for an hour at 180 °C. The HSQ formed an insulation on the samples' surfaces, where the thickness of this insulation was lowest in the open areas and gradually increased as it approached the waveguides. The thickness of HSQ at the top of the waveguides is dependent upon the initial spin speed; however, in our case where we used 4000 RPM, it resulted in 100-150 nm thick. Finally an additional 100 nm PECVD SiO<sub>2</sub> was deposited to provide better adhesion to the metal contacts.

#### 5.3.2.5 Contact Windows & P-contact Metallization

The next stage inline after the waveguides definition and the subsequent insulation is the contact windows. The samples were prepared for the E-beam registration job by spinning bi-layer 15%4% PMMA, and baking it at 180 °C for an hour and a half. After expose and solvent development, the samples were given short O<sub>2</sub> plasma clean to remove any leftover mask. The contact windows were finally defined in RIE using CHF<sub>3</sub>/Ar chemistry. The contaminated PMMA mask can then be removed in O<sub>2</sub> plasma clean, or it can be dissolved in Acetone placed in a hot water bath.

The final E-beam patterning (registration job) for P-contacts was conducted using a bi-layer 15% (2010) 4% (2041) PMMA mask. The baking and solvent development was similar to the previous step. The P-contacts were deposited in E-beam assisted metal evaporator Plassys. The metallization recipe was same as used earlier in the broad area lasers, i.e., 240 nm Au/15 nm Pt/15 nm Ti. The excess metal was removed by placing the samples in Acetone for two hours in a hot water bath, and finally cleaned in IPA.

### 5.3.2.6 Mechanical Thinning & N-contact Metallization

The semiconductor substrates, used for the laser fabrication, had thicknesses in the range of 500-600  $\mu\text{m}$ . Therefore it was mandatory to reduce it down to  $\sim 250 \mu\text{m}$  for a low series resistance of the diode. The process employed to achieve this was a mechanical thinning procedure. The first step was to mount the samples up-side-down on the glass slides using S1818 photo-resist, and baking them in a 90  $^{\circ}\text{C}$  oven for 15 min (to make sure that the samples were well adhered to the glass slides). The thinning process started with gluing the sample-mounted glass slides on a metal rod using wax, and then gently sliding the rod on a thick glass plate in a colloid of water and Calcined Aluminium-oxide powder. After achieving the required thickness, the samples were detached from the metal rod, and were thoroughly cleaned in Opticlear.

The N-contacts deposition was similar to the previously mentioned P-contacts; however, the samples were solvent cleaned in Opticlear, Acetone, and IPA (5 min each), without any ultra-sonic agitation. The samples were mounted again up-side-down on the glass slides to avoid any damage to the waveguides, which could occur if the samples are loaded directly on the evaporator's metallic chucks. The metallization recipe in this case was 240 nm Au/11 nm Ni/14 nm Au/14 nm Ge/14 nm Au. Finally, the samples were removed from the glass slides, and an annealing treatment of 360  $^{\circ}\text{C}$  was given for 60 s in RTA.

The samples were cleaved to the required device dimensions, and were mounted on the brass pads using silver epoxy for characterization. A cross-sectional SEM micrograph

of one of the fabricated ridge waveguide laser is given in figure 5-15, in which the surface planarization is clearly visible.

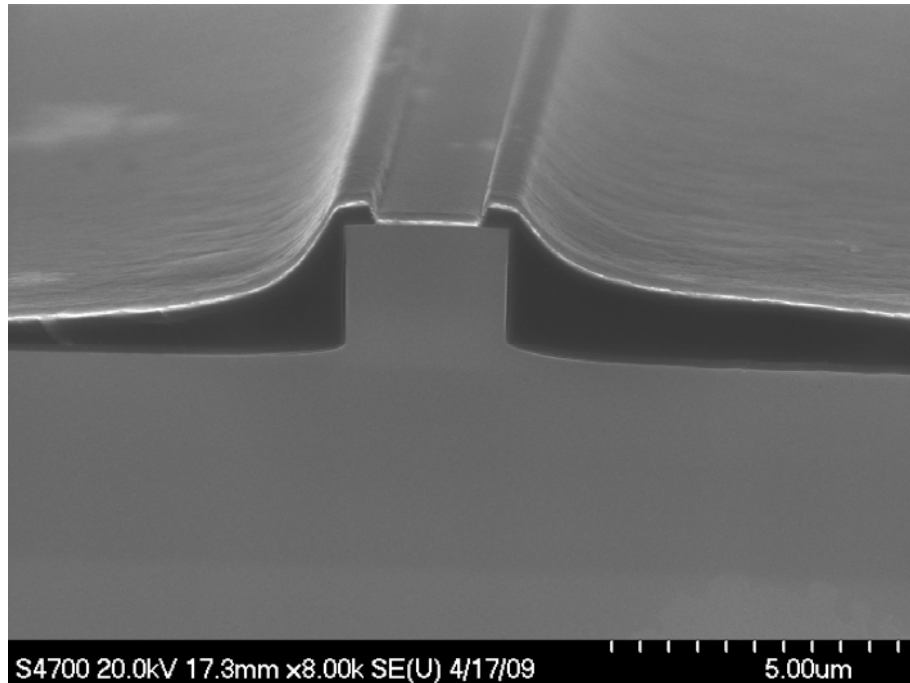


**Figure 5-15 – Cross-sectional SEM image of a 3  $\mu\text{m}$  wide ridge waveguide laser.**

### 5.3.3 Basic Device Characterization

(Annealed semiconductor chip)

The previously discussed optimized process was used in the fabrication of various cavity length Fabry-Pérot ridge waveguide lasers. The waveguides were defined in sets of three widths, i.e., 3  $\mu\text{m}$  wide, 2.5  $\mu\text{m}$  wide, and 2  $\mu\text{m}$  wide. It is a good practice to fabricate multiple device designs in different configurations on a same chip, as it saves time on the fabrication, and it also provides the redundancy for establishing the device functionality. Keeping this in mind, a range of half ring ridge waveguide lasers were also fabricated on the same chip – the half ring lasers will be discussed in the next chapter. The semiconductor chip was fabricated using annealed material, for which the substrate was given an initial RTA treatment of 775  $^{\circ}\text{C}$  for 60 s – which is a mandatory post QWI procedure. The optical micrograph of one of the fabricated chip is given in figure 5-16.

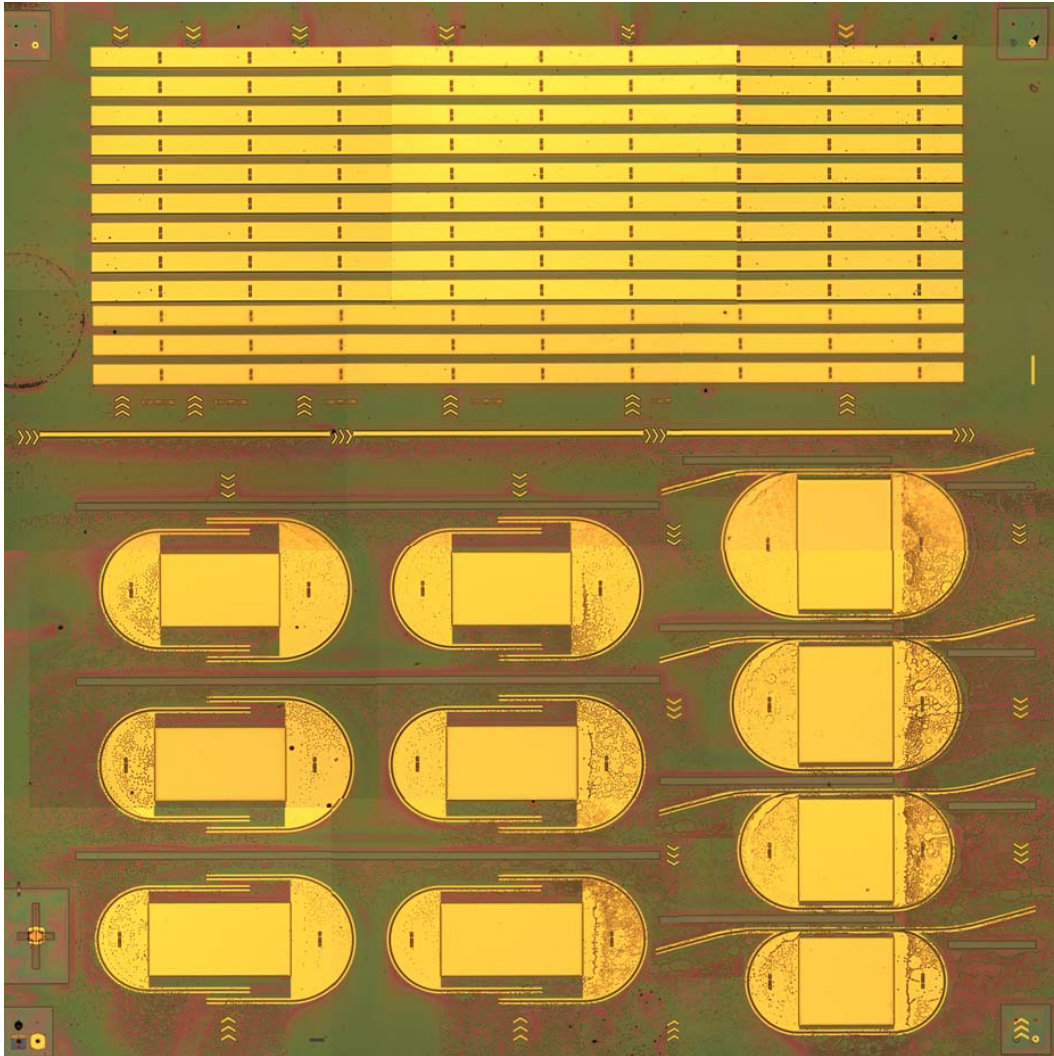


**Figure 5-16 – Optical micrograph of a fabricated chip, using the annealed material.**

Continuous wave characterization was conducted for various cavity length ridge waveguide lasers. The temperature for measurements was 20 °C, controlled by a thermoelectric cooler, and the optical power was measured using an optical power meter – the power meter saturated above 12 mW. The L-I curves for 3  $\mu\text{m}$  wide ridge waveguide lasers, fabricated using the annealed material with various cavity lengths, are given in figure 5-17.

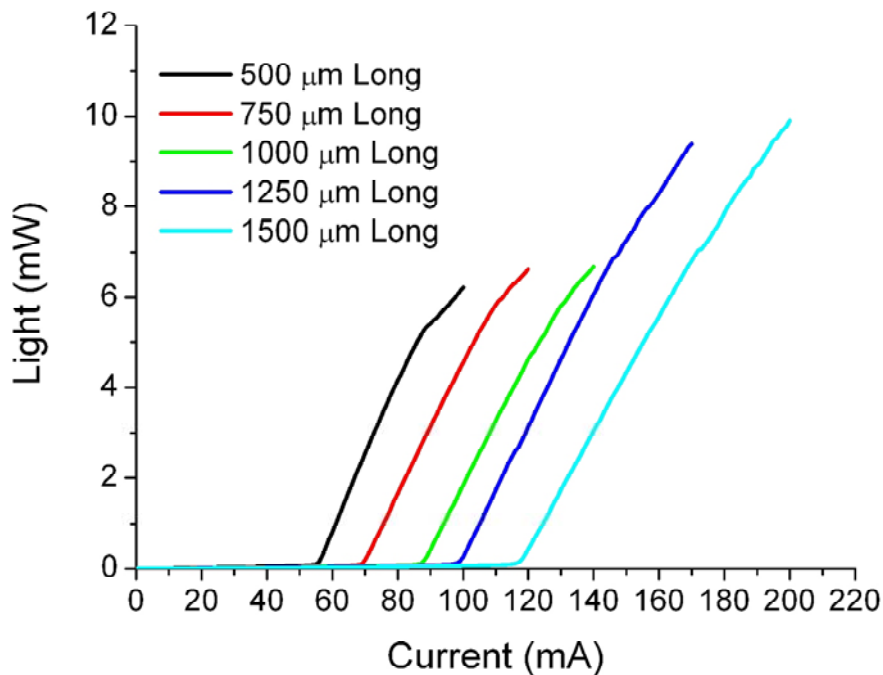


Figure 5-17 – L-I curves for various cavity length ridge waveguide lasers (3  $\mu\text{m}$  wide ridges).

The L-I curves for 500  $\mu\text{m}$  long FP cavities with different ridge widths are given in figure 5-18. Lasing threshold for 2  $\mu\text{m}$  wide ridge should be less than 2.5  $\mu\text{m}$  and 3  $\mu\text{m}$  wide ridges, given that the etch depth and the cavity length is same. This is not the case in figure 5-18, and also, the optical power of 2  $\mu\text{m}$  wide ridge saturates at a lower value. Theory suggests that the devices of similar dimensions (cavity length) should have a similar lasing threshold current density, given that the losses are same. This is clearly not the case in the figures 5-18. In order to understand this unexpected behavior, the threshold current density over a range of devices is plotted in figure 5-19.

It has been observed that the threshold current density is higher in the case of thinner devices, especially the 2  $\mu\text{m}$  wide ridges. This might be caused by a combination of increased scattering losses, surface recombination and current spreading effects. However, a more detailed investigation is required to establish them. In addition to this, the threshold current density increases with a decrease in the cavity length due to the higher gain required for short cavity devices (increased mirror loss term in the gain-loss equation). The dotted black line in figure 5-19 shows the calculated threshold current density using the material gain-curve (gain calculations are presented later in this chapter).

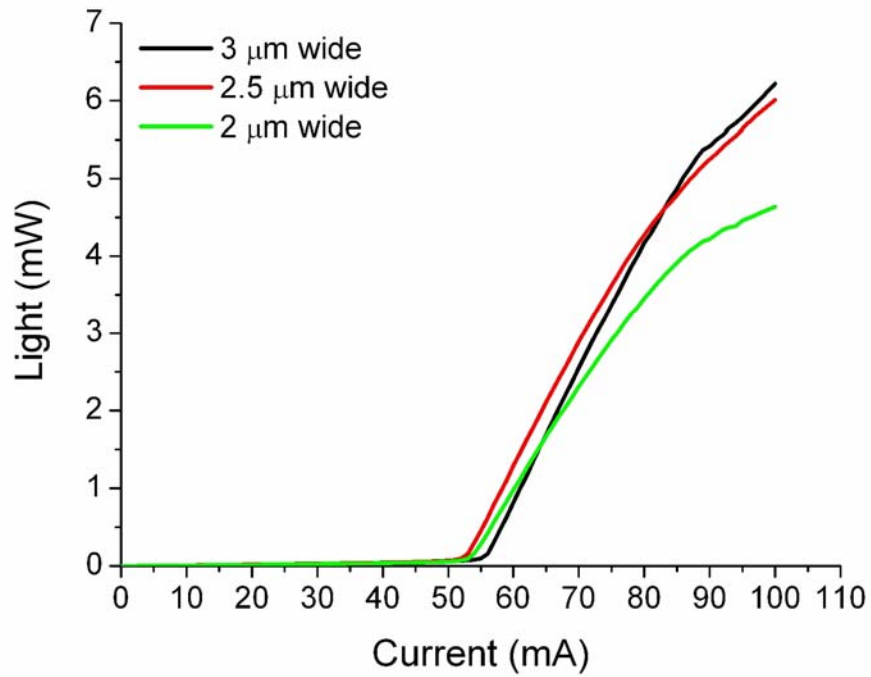


Figure 5-18 – L-I curves for different ridge widths (500  $\mu\text{m}$  long FP cavities).

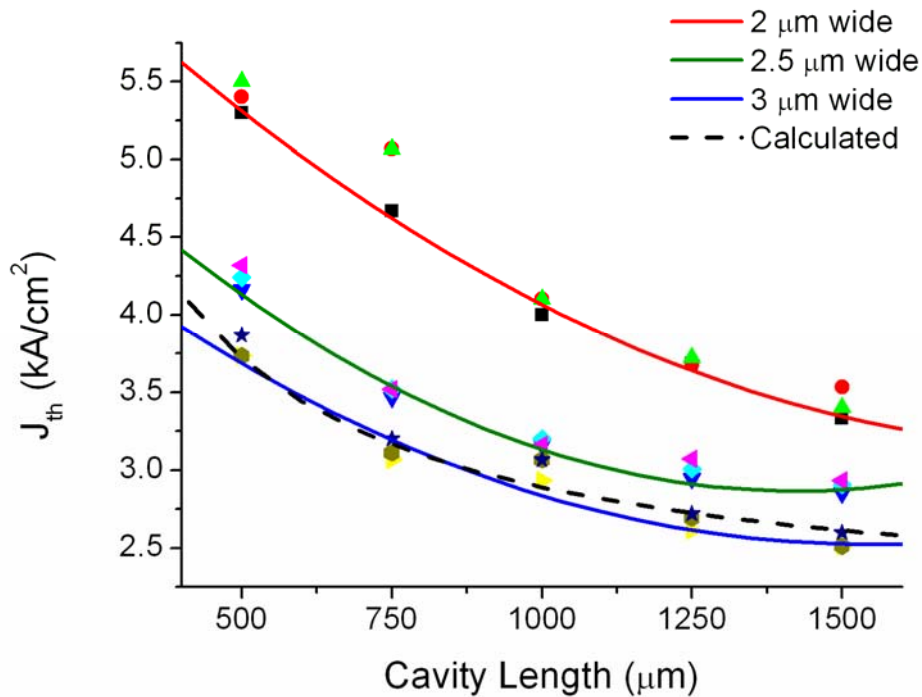


Figure 5-19 – Room-temperature CW threshold current density for various FP cavity lengths (solid lines are a smoothed fit to the data).

### 5.3.4 Material Parameters

The material parameters, including the internal quantum efficiency  $\eta_i$  (which quantifies the conversion of electrical carriers into photons), and the material loss factor  $\alpha_i$ , have been obtained by using the L-I curves given in figure 5-17. The external differential quantum efficiency  $\eta_D$  above threshold, which is obtained from the slope of the laser action, is plotted against the cavity length, given in figure 5-20. This gives us a linear relationship [157] (see eq. 7.4-1).

$$1/\eta_D = (1/\eta_i) [1 + \alpha_i L / \ln(1/R)]$$

$L$  symbolizes the cavity length in the above equation, and  $R$  is the Fresnel reflectivity which is calculated to be  $\sim 0.3$  for the cleaved facets.

The calculated value for  $\eta_i$  in our case using the above given method is  $\sim 23\%$ , and the material loss factor  $\alpha_i$  is calculated to be  $3.2 \text{ cm}^{-1}$ .

The equation 7.4-4 in reference [157], distinguishes the loss factor into different terms as following:

$$\alpha_i = \Gamma \alpha_{fc} + (1 - \Gamma) \alpha_{fc,x} + \alpha_s + \alpha_c$$

The symbol  $\Gamma$  identifies the optical confinement factor within the active region, and  $(1 - \Gamma)$  is the confinement outside of it. The free carrier loss  $\alpha_{fc}$  for an active region, in which the carrier concentration is less than  $10^{17} \text{ cm}^{-3}$  scale, is estimated to be  $\sim 10 \text{ cm}^{-1}$  (see figure 3.8-9 [157]). Which is applicable in our case, as the measured doping concentration in the buffer layers and the superlattice is within  $10^{16} \text{ cm}^{-3}$ . Similarly, the loss factor  $\alpha_{fc,x}$  in the case of buffer layers in our material is estimated to be less than  $1 \text{ cm}^{-1}$  [80]. Scattering losses  $\alpha_s$  are significant for the waveguide structures which have exposed active region. The etch depth in our case is controlled above the superlattice, therefore scattering can be neglected. Coupling losses  $\alpha_c$  effect the laser performance if

the optical field can couple into the regions outside of the active medium; however, they have been considered negligible for claddings thicker than  $1\ \mu\text{m}$  [157] (figure 7.4-13).

In our ridge waveguide lasers, the calculated  $\Gamma$  is less than 0.4 in the superlattice active region; whereas the confinement in the buffers layers is around 0.6. The optical field in claddings layers is calculated to be less than 0.01 and can be easily disregarded. These calculations, along with the values given for different loss factors, give us the loss factor  $\alpha_i$  of  $4\ \text{cm}^{-1}$  which is slightly higher than experimentally observed value of  $3.2\ \text{cm}^{-1}$ . However, the calculated and experimentally observed values for  $\alpha_i$  are in a good agreement. This low optical loss factor is also an indication of an excellent material growth, and it has been complimented by typical growth information as given previously in figure 5-2.

The internal quantum efficiency  $\eta_i$ , which is experimentally calculated to be 23% in our case, is lower than the typical values of 60-80 % for a good quality material. This could potentially be caused by a leakage electron/hole current in a diode if the electric potential barriers at the cladding/active-medium interface become lower than the electron/hole quasi Fermi levels. However, it has been ruled out in our structure where the aluminium composition in the claddings is higher than the intrinsic superlattice core to result a potential barrier of  $\sim 0.554\ \text{eV}$ . Another reason for this lower efficiency could be the presence of carrier traps, either in the superlattice active region or in the surrounding intrinsic buffers. In the later case, these traps would resist the carrier transport into the superlattice active region, and would significantly degrade the thermal stability acting as localized heating sources. Growth defects can be ruled out as a source of these traps, as fairly good optical properties of the material have been established so far. However, the existence of traps due to the presence of high potential energy barriers cannot be ruled out. Later investigation in this hypothesis indicates the presence of such energy barrier at the superlattice/buffer-layer interface, and it is discussed in the resonant tunneling experiments in this chapter.

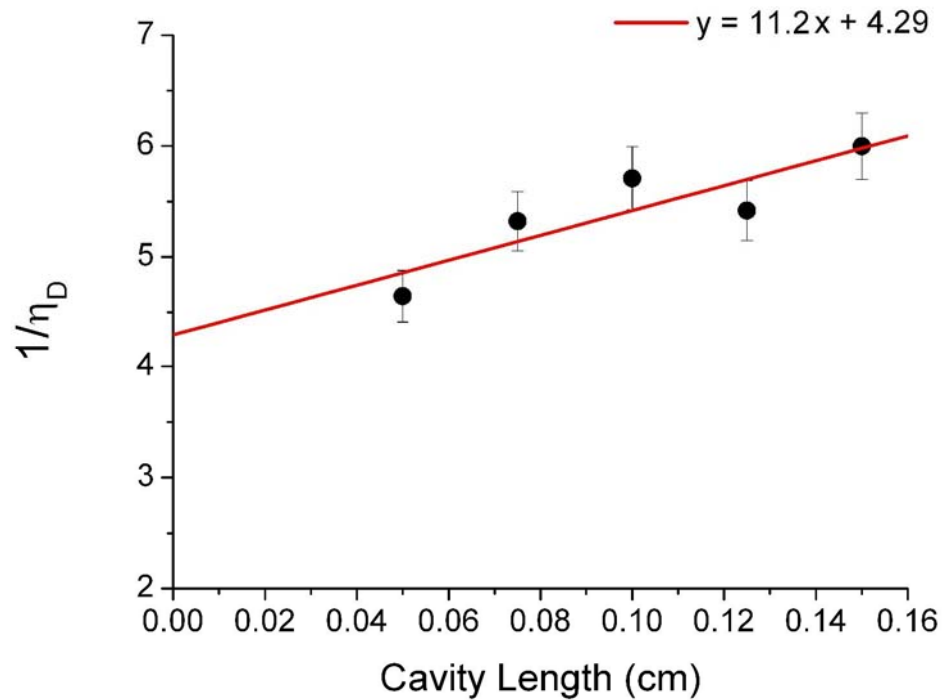


Figure 5-20 – The external differential quantum efficiency plotted against the cavity length.

### 5.3.5 Gain Calculation

The laser action requires the material gain at the threshold to equate all the losses, which include the material losses and the reflection losses. This relationship is depicted by the following equation [157] (eq. 7.4-3).

$$g_{th} = (1/\Gamma)[\alpha_i + (1/L)\ln(1/R)]$$

The gain coefficient calculated by the above given method, and using the experimentally obtained parameters identified in previous section, is plotted against the nominal threshold current density  $J_{nom}$  for different cavity lengths, given in figure 5-21.

Where  $J_{nom}$  is calculated as following:

$$J_{nom} (A/cm^2 \cdot \mu m) = J_{th} \frac{\eta_i}{d}$$

The idea above is to normalize the threshold current density as a function of internal quantum efficiency and the active region thickness  $d$  in  $\mu\text{m}$ .

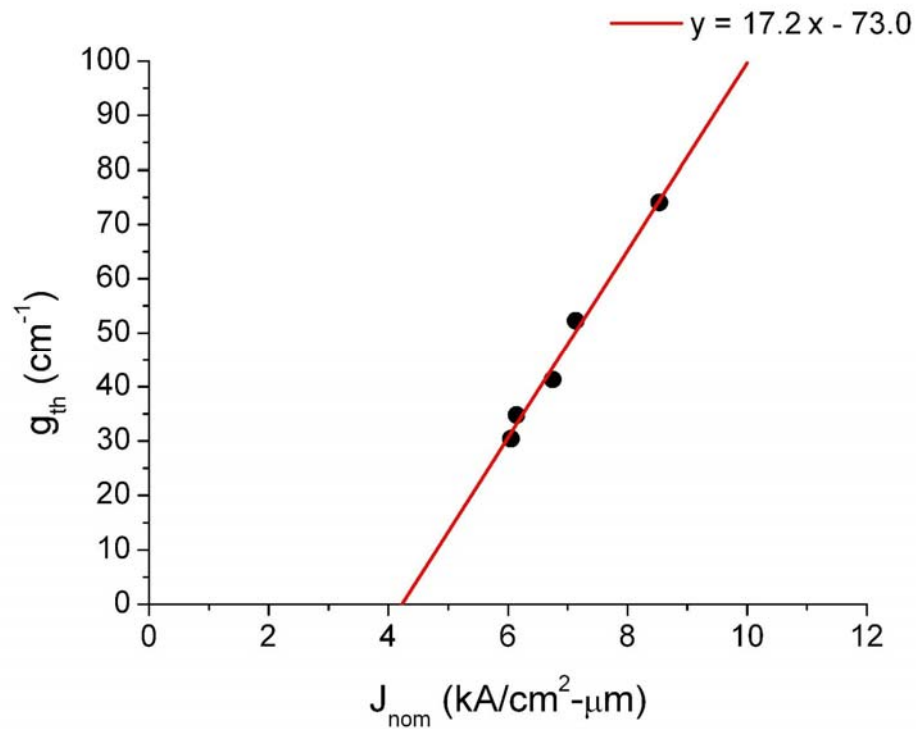


Figure 5-21 – Gain at threshold is plotted against the  $J_{nom}$ .

The linear relationship between the threshold gain and the  $J_{nom}$  is used to calculate the higher gain region in the gain curve, given next – gain curve is the dependence of the gain coefficient on the threshold current density.

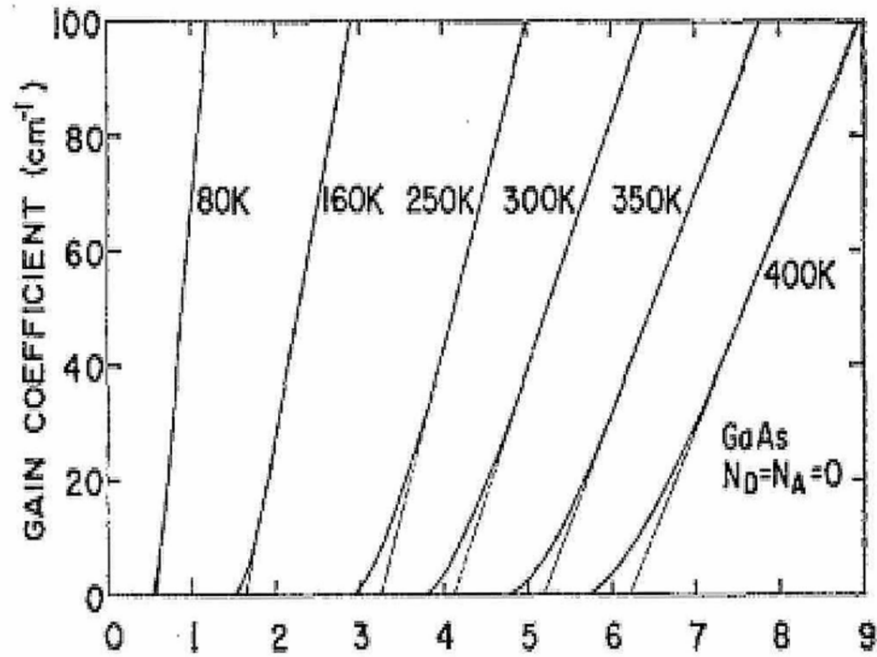
$$g_{high} = \beta(J_{nom} - J_0)$$

The symbol  $\beta$  is defined as the gain constant or the gain factor in this case (this should not be confused with the propagation constant), and  $J_0$  is the current density at which the gain coefficient becomes zero.

The gain coefficient calculated for our material is compared with the gain coefficient calculated by Stern for an un-doped GaAs [158], given in figure 5-22. Although the

comparison is between two completely different material systems; however, a satisfactory agreement can be seen at the temperature 300 K.

(a) © 1973 IEEE



(b)

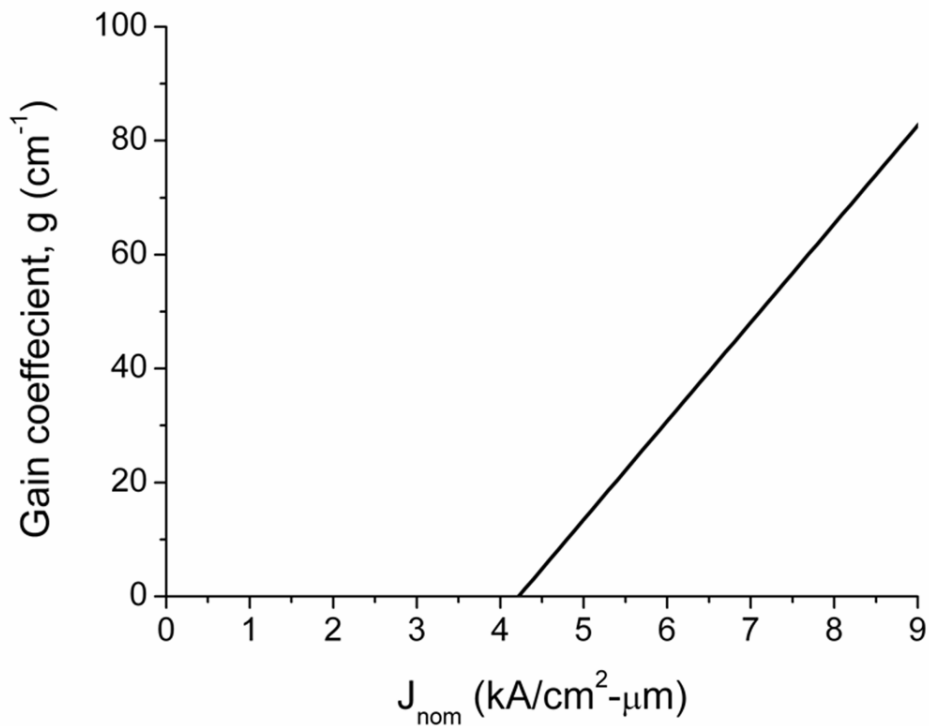


Figure 5-22 – a) The calculated gain for an un-doped GaAs [158] (Permission to reproduce this figure has been granted by IEEE), b) Gain calculated for BMH9 using the experimentally obtained parameters.

### 5.3.6 Spectrum Analysis

The optical spectrum was obtained for a 500  $\mu\text{m}$  long ridge waveguide laser by coupling the light into a lens fiber and measuring it on the optical spectrum analyzer (OSA). The threshold current for this device is 55 mA (as shown in figure 4-16); however, the first noticeable peak is observed at 78 mA. The laser excitation of 801 nm for this device is given in figure 5-23.

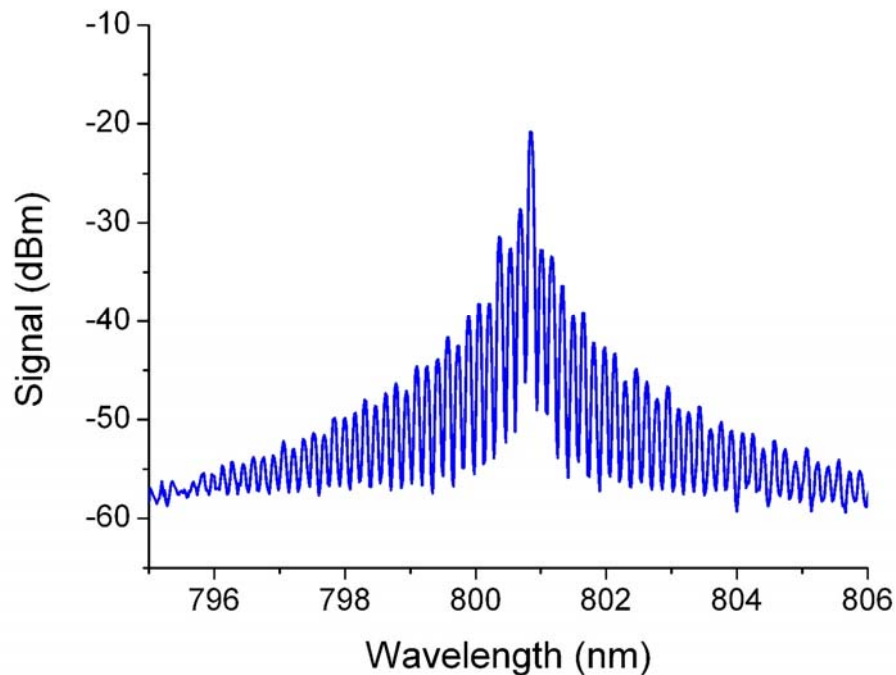


Figure 5-23 – Excitation wavelength of 801 nm for a 500  $\mu\text{m}$  long annealed FP ridge.

A red shift of 29 nm is observed between the laser excitation and the measured EL of 772 nm, which has been mentioned earlier for the wafer BMH9. The potential sources for this behavior could be the: 1) growth defects, which has been ruled out previously by the growth data and a low optical loss factor, 2) relaxation or increase in the thickness of superlattice quantum wells which might arise after the initial RTA treatment – although this effect is highly unlikely to occur as it is completely against the quantum well intermixing observed at the high temperature; however, this hypothesis can not be established unless the excitation wavelength for the as-grown structure is obtained, 3) non-uniformity of the PL/EL across the wafer - the PL map of this wafer is unavailable; however, a PL shift of up to 20 nm has been observed previously in the

active wafers from Sheffield (figure 5-1), and 4) localized thermal effects. This last explanation requires some initial assessment of the temperature that can cause such wavelength shifts. The thermo-optic coefficient  $\partial n/\partial T$  is calculated to be  $3.6 \times 10^{-4} \text{ K}^{-1}$  for bulk  $\text{Al}_{0.22}\text{Ga}_{0.78}\text{As}$  (which is the equivalent composition for the superlattice in this case), using the Gehrtsitz model at 300 K [103]. A wavelength shift of 29 nm, which is correspondingly equal to the index shift of  $\Delta n=0.033$  (calculated using the same model), requires a temperature change of 91.6 K. The temperature dependent wavelength shift in 980 nm GaInAs–AlGaAs QW lasers has been reported to be  $\sim 0.35 \text{ nm/K}$  [159-160]. Therefore, in our case, increased temperature of the waveguide core under CW injection could induce this wavelength shift.

In order to resolve a possible relaxation in the superlattice quantum wells, the optical spectrum of BAL fabricated on as-grown and annealed BMH9 was measured. The laser emission, obtained using the pulsed current injection, was coupled into an optical fiber by a microscopic objective lens and measured on OSA. The pulsed injection will circumvent any thermally induced effects which are observed in the CW injection, where as the BAL configuration does not introduce any changes in hetero-structure, which have a low probability to occur during ridge waveguide laser fabrication. The recorded spectrum for as-grown and annealed BAL is given in figure 5-24 (a) and (b), respectively.

The excitation wavelength of 796 nm for the as-grown BAL can confidently rule out any occurrence of relaxations in the superlattice quantum wells after the annealing. However, a blue shift of  $\sim 8 \text{ nm}$  is observed in the annealed BAL excitation, which is an indication of the intermixing, often originated by high temperature annealing.

The recorded spectrum data for different device configurations can fairly identify the existence of a localized heating in the intrinsic core of the material. This heating could occur in the presence of carrier traps in the core which resist the carrier transport into the active medium. The presence of a high potential energy barrier at the superlattice/buffer-layer interface has been observed in the resonant tunneling experiments in a similar material structure, and it is found to be the reason for non-radiative recombinations. These details are presented in the next section.

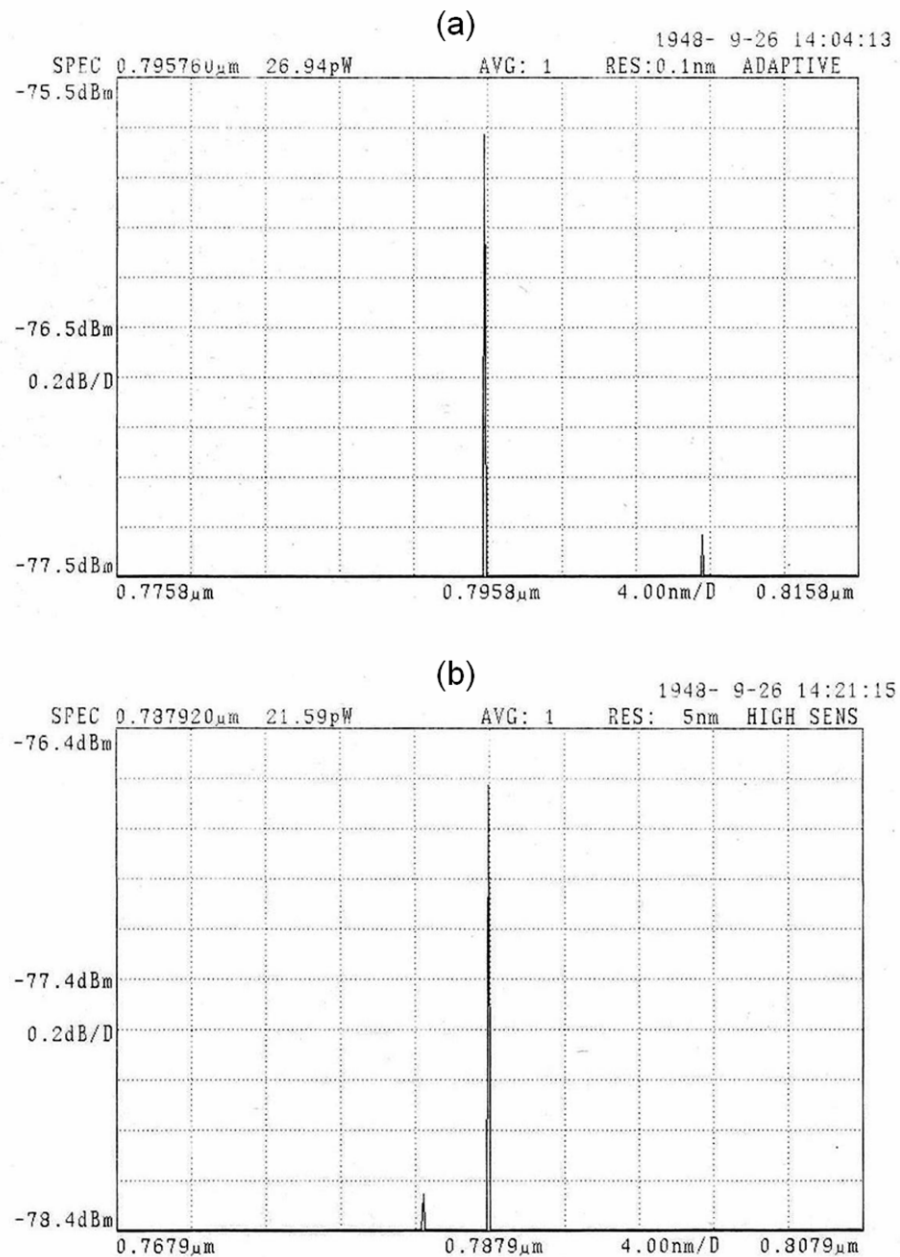


Figure 5-24 – Measured excitation wavelength using pulsed injection for: (a) As-grown BAL, (b) Annealed BAL.

### 5.3.7 As-grown Semiconductor Chip

In concluding this section of ridge waveguide lasers, a final experiment is presented in which the chip design given in figure 5-16, was repeated for the as-grown material. The fabrication process was similar as in the previous chip; however, the initial RTA treatment was excluded. No laser action was observed in any of the ridge waveguide

lasers and also the half ring cavities, and the turn-on voltage was at least  $\sim 2$  V higher than the annealed ridges in this case. The V-I curves for a range of cavity lengths are given in figure 5-25. The slope of all the curves is approximately similar ahead of turn-on, and a higher series resistance is seen in the case of as-grown diodes. Whereas, the low series resistance for the annealed diode indicates that the initial RTA treatment has overcome a structural defect.

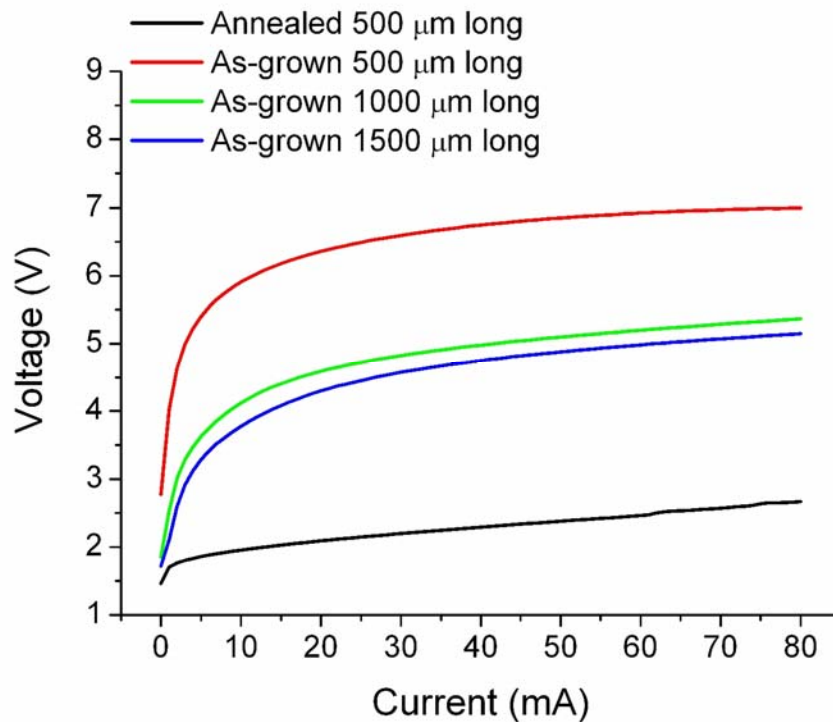


Figure 5-25 – V-I curves for the as-grown diodes in comparison with the annealed diode.

## 5.4 Resonant Tunneling in Superlattices

A relatively low performance of the laser diodes in our case, as compared to any good quality modern semiconductor light emitting source, has been observed in the previous sections. The laser action, which has been quantized with 23 % internal quantum efficiency, is observed with a 29 nm red shift from the measured EL of the material. So far, the growth defects and the fabrication process have been ruled out as a source for this behavior; and the laser action has proven to be improvised with the initial RTA treatment. The presence of a high potential energy barrier in the intrinsic core which

could act as a carrier trap has been recommended. In this case the laser dynamics could be significantly affected by the localized heating as a result of the non-radiative recombinations. This hypothesis has been supported by the spectrum analysis and the electrical properties of the as-grown and the annealed material. However, a critical test which has validated the existence of a structural/design defect is the observation of resonant tunneling in a 150 nm thick superlattice material, BMH9\_REV.

This section presents the details for the resonant tunneling experiments. But before that, the material design of BMH9/BMH\_REV has been revisited with the energy band calculations.

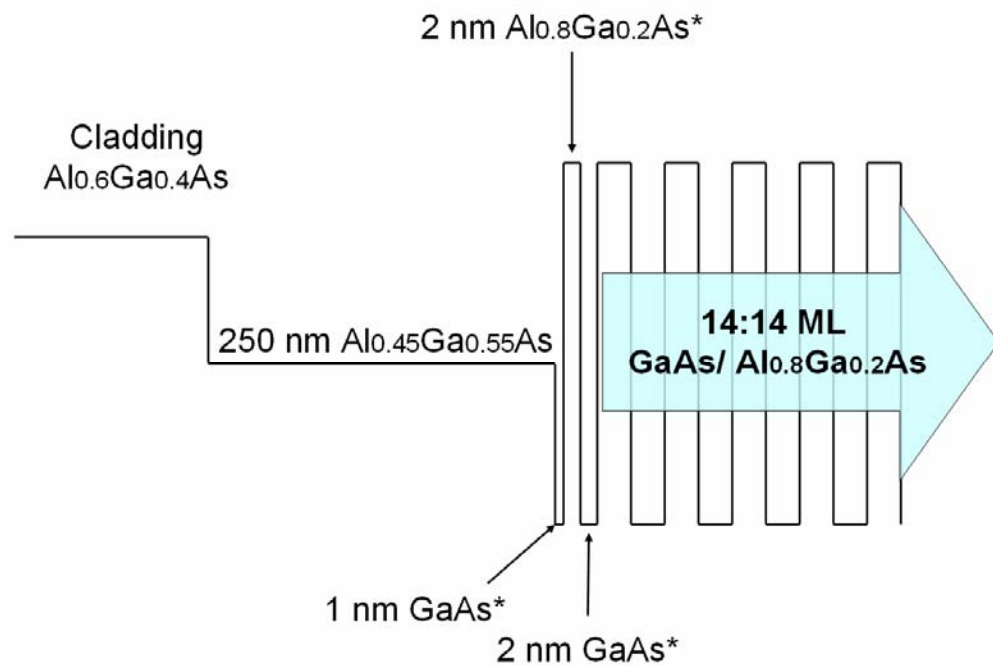
#### 5.4.1 Energy Band Calculation

The material structures BMH9 and BMH9\_REV are simulated with the ECA software for the energy band calculations. The software employs the effective-mass model to scan for the energy levels using the transfer matrices, and introduces infinite potential barriers as the boundary conditions at both ends of the structure. The calculations are performed for the electron states from the center of Brillouin zone, for light holes and heavy holes, and also for the X- and L-valley electron states. The energy scan is performed during these calculations until a value for the wave-function which fulfills the boundary conditions is achieved.

The detailed design of the wafer is given earlier in table 5-6, and is repeated schematically in figure 5-26. The material has 250 nm thick intrinsic  $\text{Al}_{0.45}\text{Ga}_{0.55}\text{As}$  layers on either side of the superlattice core, and the thin transitional layers are intended to provide smooth carrier transport into the superlattice active medium.

Energy band calculations for BMH9 are initially performed without any applied electric field across the superlattice, which reveal the first quantum confined mini-band  $E_0$  at 1.663 eV (bottom of the mini-band). This ground state/mini-band, along with the calculated heavy-hole (HH), gives us a direct band-gap transition  $n=1(e-hh)$  of 1.69 eV.

However, after adding a room temperature red shift of  $\sim 43$  nm (which has been measured during the initial QWI optimization), this transition is 1.6 eV or 772 nm, which is equal to the measured EL of the wafer. Similarly, the zero-field excited states  $E_1$  and  $E_2$  have the calculated energies of 1.835 eV and 1.932 eV, respectively. These excited states, which are localized in the transitional layers on both sides of the superlattice core, occur due to the thin GaAs quantum wells. Among these excited states, the state  $E_1$  can be a potential trap for the carrier transport into the superlattice core due to its  $\sim 170$  meV energy difference from the ground state  $E_0$ , and insignificant coupling with the next 4 nm wide quantum well. The zero-field calculations for BMH9\_REV are consistent with the above given values.



\*These layers are referred as the transitional layers

Figure 5-26 – Schematic representation of BMH9/BMH9\_REV.

The doping concentrations, which have been obtained from the real-time growth information for BMH9, are:  $2 \times 10^{18}$  cm<sup>-3</sup> carbon in p-type,  $1 \times 10^{18}$  cm<sup>-3</sup> silicon in n-type, and the carbon concentration in the intrinsic core is estimated to be  $6 \times 10^{16}$  cm<sup>-3</sup> (this value was recorded from the polaron measurements performed for BMH6). It is worthy to mention that all the MOVPE wafers including BMH9 and BMH\_REV were grown with a  $10^\circ$  tilt to the [111] axis in order to reduce the carbon concentration in the

superlattice region, which arises from the aluminium precursor [161]. Using these values, the built-in voltage for BMH9 is calculated to be 0.164 V, and under the application of an equivalent electric field, the energy shift between the localized excited states  $E_1$  on either side of superlattice is calculated to be  $\sim 500$  meV, presented schematically in figure 5-27.

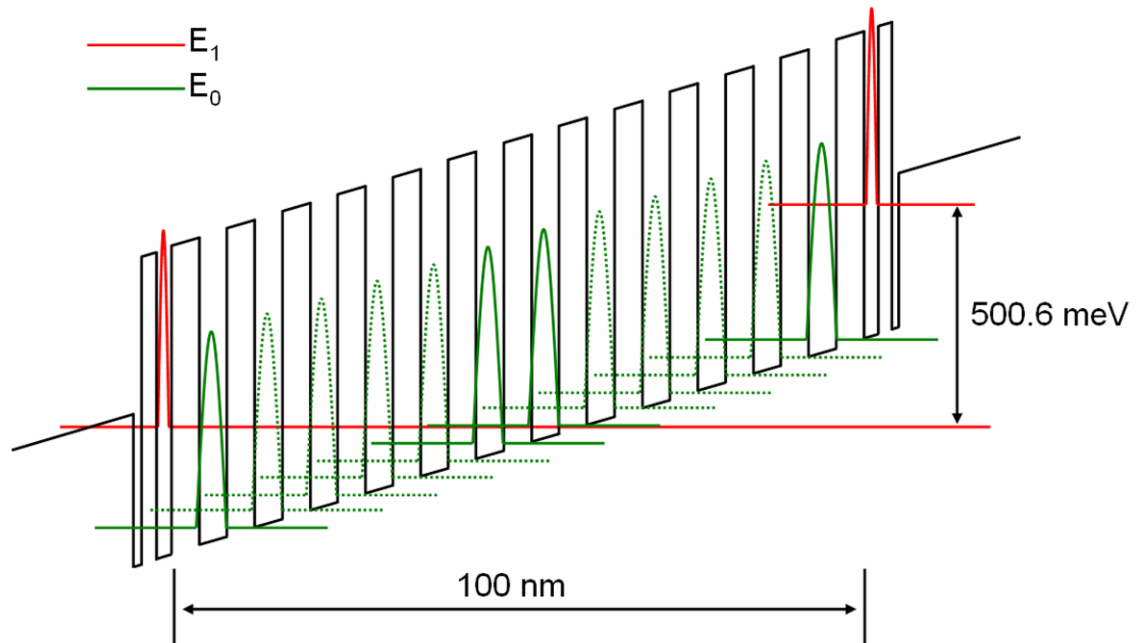


**Figure 5-27 – Schematic representation of the calculated conduction band under the application of an electric field in BMH9.**

The real-time growth information for BMH9\_REV is unavailable; however, assuming the similar doping profiles presented earlier, the calculated shift between the excited states  $E_1$  on either side of a 150 nm thick superlattice is  $\sim 440$  meV. If the carbon concentration is  $1 \times 10^{17} \text{ cm}^{-3}$  in the superlattice core, which is most likely in this case [161], the energy difference between the excited states reduces down to 360 meV.

In summarizing, the estimated Stark shift in both the wafers BMH9 and BMH9\_REV suggests the occurrence of resonant tunneling, if the applied external bias can cause the energy bands to align with each other. Especially in the case of BMH9\_REV, the resonant tunneling is highly plausible, and it has been measured experimentally in the later experiments.

### 5.4.2 Experiments

The detailed analysis for the resonant tunneling required the voltage driven sweeps across the smaller diodes. For this purpose the mesa etched squares diodes with 80  $\mu\text{m}$  edges were fabricated, using the same process which was used for the laser diodes. The diodes were measured on the four-probe station using continuous injection – the injection current was limited to 100 mA. This measurement should ideally be performed at low temperature; however, the expected NDR zone was observed in the voltage range 2–2.25 V at the room-temperature. Figure 5-28 shows one of these measurements, in which the tunneling current peaks at  $\sim 2.2$  V during the forward scan, and then drops when the band alignment is discontinued at a higher bias. The reverse scan shows the intrinsic bistability in the form of a hysteresis loop which is attributed to the space-charge buildup in the wells once the resonant tunneling has been established [162-163].

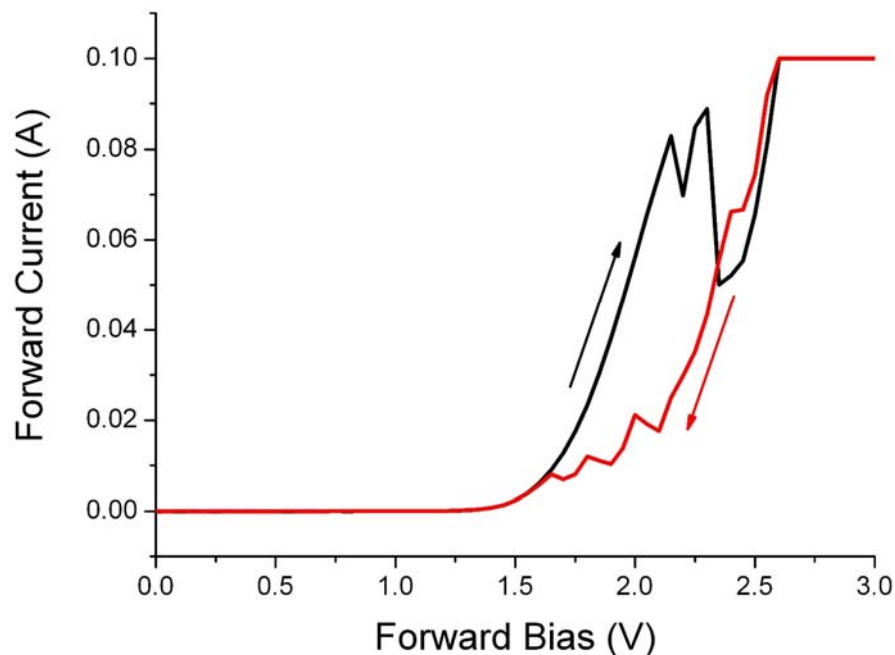


**Figure 5-28 – I-V curves for the resonant tunneling measurements in BMH9\_REV which has 150 nm thick superlattice core.**

These experiments establish the hypothesis in which the presence of a high potential energy barrier has been proposed in the intrinsic core of the superlattice lasers. This

barrier has effected the laser action by significantly reducing the internal quantum efficiency; and it has also caused the non-radiative recombinations, which shifted the laser excitation at a longer wavelength. These effects have been paramount in the case of as-grown devices, whereas the initial RTA treatment in the fabrication of annealed lasers has reduced the height of this barrier.

This chapter has covered the details required to develop the monolithic integration in our integrated OPO by achieving the laser action in a superlattice core. The active wafers, which evolved our superlattice heterostructure design, have been presented and tested. The laser action has been achieved in an optimized structure; however, the limited performance has been observed, and it has been investigated in detail. The reasons for this relatively lower performance have been identified and established through detailed experimentation.

# Chapter 6

## Monolithically Integrated Devices

This chapter covers the experiments and the studies which have been performed to demonstrate the monolithic integration for nonlinear optical frequency conversion. The chapter starts with the ring design which has been supported by the demonstration of the laser action in half ring cavities of various radii, and consequently the bending losses have been assessed. The coupler design has been revisited with the beam-propagation-based simulations for the material system BMH9, and the optical routing in different sections of the integrated devices has been evaluated. Finally, the designs for the integrated OPO and the integrated nonlinear optical frequency converter have been presented, along with their layout on the semiconductor chip. In order to demonstrate the process development for the final monolithically integrated chip, the integrated devices are presented which were fabricated using the material system BMH5.

### 6.1 Ring Design

The losses which occur due to the propagation of optical field in the bended sections of the device are the most critical in the design of a ring structure. One way to observe the minimum losses in this case is to completely etch the wave-guiding core; however, this could not be incorporated in our design in which the monolithic integration requires the waveguide structure to be similar in all sections. For this, an accurate assessment of the bending losses for different ring radii in the given waveguide structure (presented previously) was performed. The half ring lasers which have been discussed as the most accurate method to conduct the bending loss assessment [114], were fabricated in our case for various ring radii. The E-beam pattern was initially designed in such a way that the final cleaved devices would have the same cavity length of  $\sim 2200 \mu\text{m}$ , given in figure 6-1.

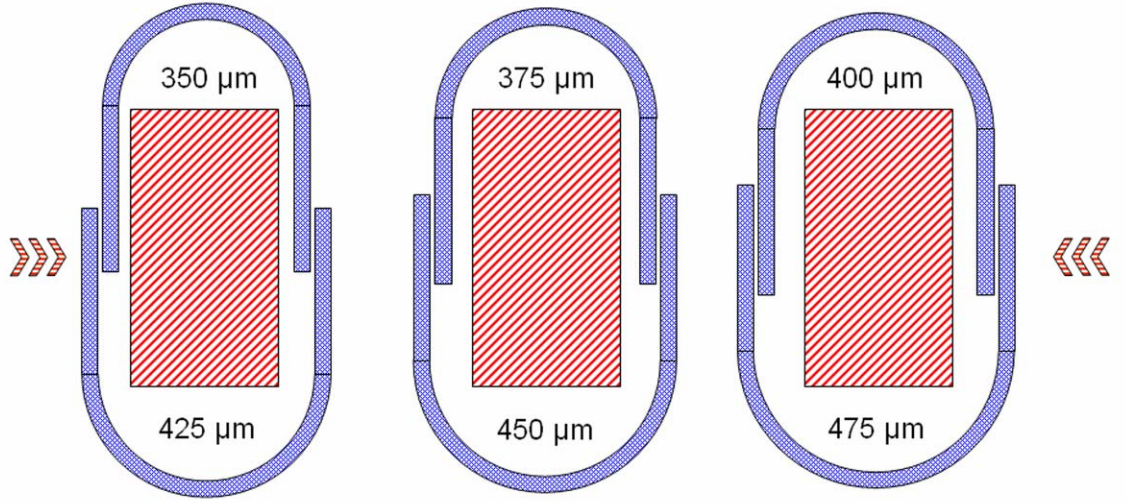


Figure 6-1 – The designed E-beam pattern for the half ring lasers.

In such a half ring structure the laser action is achieved in the FP cavity formed between the two cleaved facets. As the cavity length and the fabrication is similar for all the half rings in our case (figure 6-1), the transmission and the optical loss can be assumed as constant. The linear relationship to formulate the external quantum efficiency as a function of cavity length [157], with the inclusion of bending loss, is given as:

$$1/\eta_D = (1/\eta_i) \left[ 1 + (\alpha_i(L + \pi r) + \alpha_b \pi r) / \ln(1/R) \right]$$

Where  $L$  is the length of the straight sections in a device, and  $\pi r$  symbolizes the half ring section. Solving the above relationship for  $\alpha_b$  (bending loss factor), gives us:

$$\alpha_b = \frac{1}{\pi r} \left[ \left( \frac{\eta_i - \eta_D}{\eta_D} \right) \ln(1/R) - \alpha_i(L + \pi r) \right]$$

The half ring lasers fabricated on the annealed chip, and given in figure 5-16, were tested for the CW laser action. The calculated external quantum efficiency from the L-I curves of these lasers, and the experimentally obtained parameters which are given in section 5.3.4, have been used to calculate the bending losses for the different ring radii,

given in table 6-1. Although the process parameters were constant for the complete chip fabrication, but the placement of the half rings at different sections of the chip resulted in slightly different etch depths, which caused higher bending losses for the shallow etched devices.

<b>Ring Radius (<math>\mu\text{m}</math>)</b>	<b>Etch Depth (<math>\mu\text{m}</math>)</b>	<b>Bending Loss – <math>\alpha_b</math> (<math>\text{cm}^{-1}</math>)</b>
350	$1.3 \pm 0.07$	25.7
375	$1.25 \pm 0.07$	45.6
400	$1.25 \pm 0.07$	44.5
425	$1.25 \pm 0.07$	45.2
450	$1.3 \pm 0.07$	14.5
475	$1.3 \pm 0.07$	10.8

**Table 6-1 – Bending losses for various rings.**

In order to estimate the sensitivity of the bending losses upon the ring radius and the etch depth of the structure; various ring radii have been simulated. These simulations have been performed using the simulated bend feature of the BeamPROP, which calculates the complex values of the effective refractive index of the guided mode in a curved waveguide. These values have been used to calculate the bending losses, and are plotted in the figure 6-2. It can be seen in the figure that the bending losses are very sensitive to the etch depths, such that, only 25 nm difference from the desired value can significantly increase the losses. This could be explained by the higher confinement of the mode in a 100 nm thick superlattice core in the laser structure BMH9, as compared to that of BMH1. The bending losses calculated in our case using the measured values are also given in the figure, and a fair comparison can be seen for  $1.20 \pm 0.07 \mu\text{m}$  deep etched rings.

The bending losses clearly identify that the etch depth is very critical in the efficient performance of the ring laser, and consequently of the final device. Therefore, the scattering can be compromised in a slightly deep etched structure, i.e., 1.35-1.45  $\mu\text{m}$ .

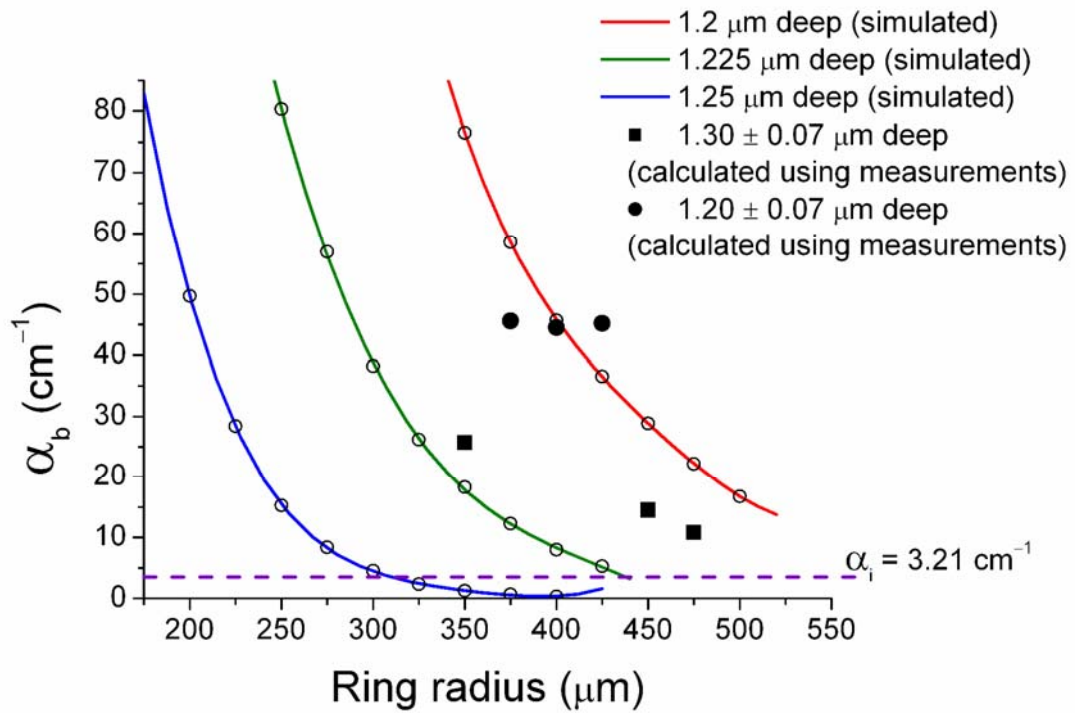


Figure 6-2 – The bending losses calculated using the simulations. Solid lines are a smoothed fit to the data. The solid circles and squares are the values calculated using measurements from the half ring lasers, and the empty circles represent the simulated data.

The L-I curves for the best performing half rings are given in figure 6-3.

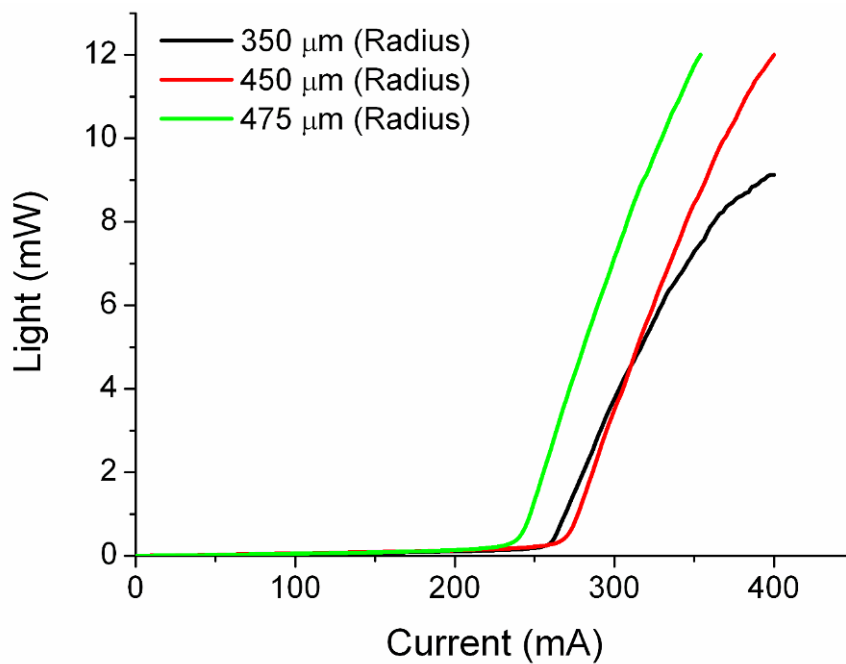
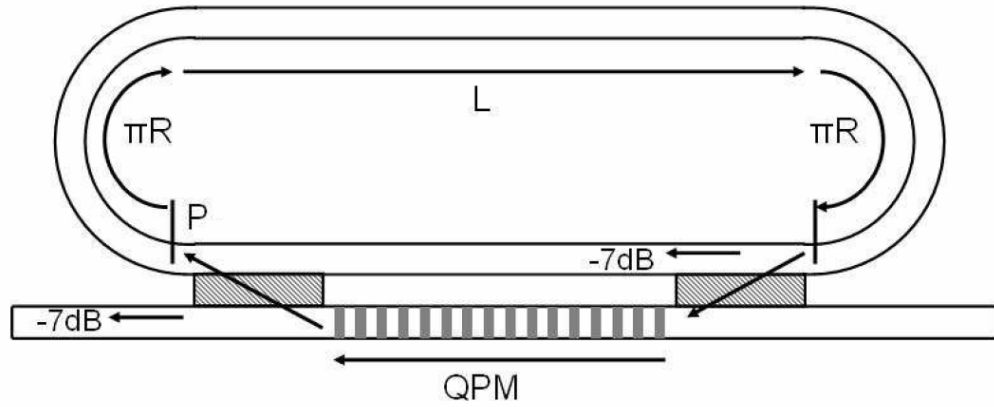


Figure 6-3 – L-I curves of the half ring lasers with different ring radii (all rings had the same etch depth of  $1.3 \pm 0.07$ ).

Another assessment which has to be performed for the ring design is the internal power calculation. The threshold condition for the ring dictates that the gain must equalize all the losses inside the ring, and in our case this includes: bending loss, linear loss, coupling loss, and the loss in the QPM waveguide, figure 6-4.



**Figure 6-4 – Losses of the ring cavity**

The threshold condition for the ring in this case can be written as:

$$\frac{1}{\text{coupling}^2} = e^{g(L+2\pi R) - \alpha_i(L+2\pi R) - \alpha_b(2\pi R) - \alpha_{SHG}(L_{QPM})}$$

The values which have been used to calculate the gain at the threshold are given in table 6-2; and using these values, the threshold current has been obtained for different ring radii using  $g_{th}/J_{nom}$  relationship (figure 5-21). Finally, the internal power of the rings (above threshold) has been calculated using the internal quantum efficiency, before the saturation effects become significant. The rings have been biased at the same current density of  $6.6 \text{ kA/cm}^2$ . These calculations are plotted in figure 6-5.

The internal power is observed to increase monotonically for the large rings in which the bending losses are lower. However, one should also recognize that the large rings will have a bigger footprint on the semiconductor chip; and the estimated size of the  $375 \text{ }\mu\text{m}$  radius ring is  $2 \text{ mm}^2$ , which increases up to  $3 \text{ mm}^2$  for  $475 \text{ }\mu\text{m}$  radius ring.

<b>Ring dimensions</b>	
$L$	1760 $\mu\text{m}$
$L_{QPM}$	1000 $\mu\text{m}$
$R$	350-475 $\mu\text{m}$
<b>Coupling</b>	0.8336—calculated by the coupler's throughput (-7 dB cross talk)
<b>Losses</b>	
$\alpha_i$	3.21 $\text{cm}^{-1}$
$\alpha_b$	10-25 $\text{cm}^{-1}$ (over a range of ring radii) <sup>4</sup>
$\alpha_{SHG}$	$\sim 25 \text{ cm}^{-1}$ [131]

Table 6-2 – The ring parameters used for the internal power calculation.

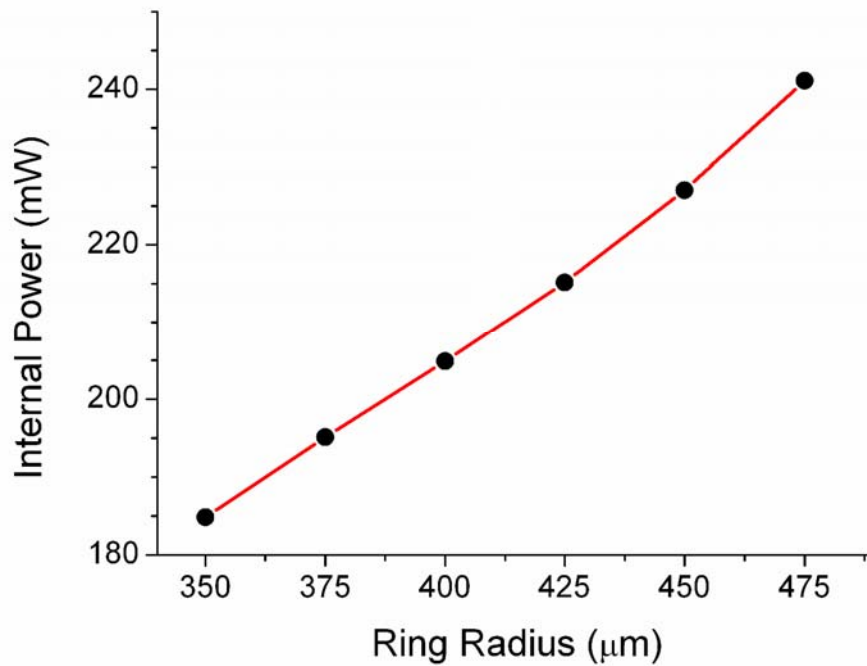


Figure 6-5 – The internal power estimates of the rings before the saturation effects become significant. All the rings are biased at same current density of 6.6  $\text{kA}/\text{cm}^2$ .

The selected radius for the final device is 400  $\mu\text{m}$  for the ring laser cavity. There is significant room for improvement in the performance if the laser structure can be optimized to increase the internal quantum efficiency from its present value of 23 %;

<sup>4</sup> It can be seen in the table 6-1, that the ring radii 375-425  $\mu\text{m}$  have higher bending losses because of their lower etch depth. Therefore, for the internal power estimates, the bending loss values are assumed to be 17-23  $\text{cm}^{-1}$  for these radii, such that the estimates could be given for the devices of similar etch depths.

and also, the MMI coupler must be optimized because the present throughput costs about 17 % of the internal power of the ring as a loss. The ring radius for the adjoining OPO cavity has been selected to be 300  $\mu\text{m}$ , as the bending losses for the half-band-gap wavelengths are estimated to be  $< 1 \text{ cm}^{-1}$  in this case.

## 6.2 Coupler Simulations Revisited

The di-chroic MMI coupler, which has been presented in chapter 4, was investigated and demonstrated using the 600 nm thick superlattice core material structure (BMH1). However, the laser action has been achieved in a 100 nm thick superlattice core (BMH9). Therefore, it was mandatory to revisit the coupler design for this modified structure; for which the MMI coupler has been simulated with the same dimensions as demonstrated previously, i.e., 220  $\mu\text{m}$  long, 6.5  $\mu\text{m}$  wide, and 1.35  $\mu\text{m}$  deep, and it has 3  $\mu\text{m}$  wide access waveguides to the cavity. The excitation wavelength used in these simulations is 801 nm with quasi-TE polarization. The coupler design is found to be consistent with the earlier case of 600 nm thick superlattice core – the simulated coupler using the new material structure is given in figure 6-6.

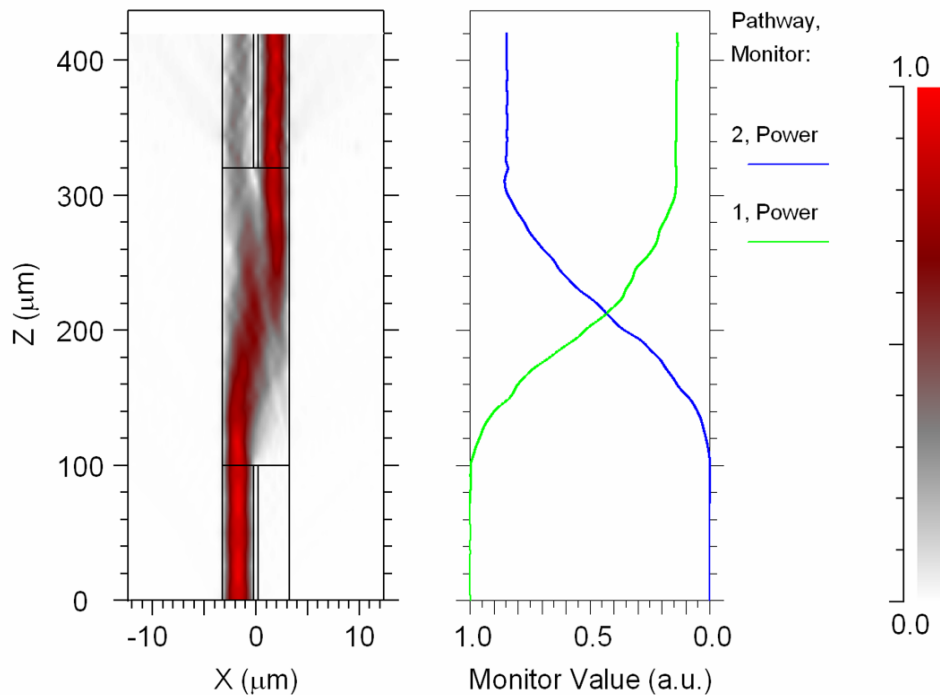


**Figure 6-6 – Cross coupler for the 801 nm laser excitation (MMI cavity dimensions: 6.5  $\mu\text{m}$  wide, 220  $\mu\text{m}$  long, and 1.35  $\mu\text{m}$  deep etched).**

Similarly, the simulations for the half-band-gap wavelengths are also found consistent with the earlier case presented in the chapter 4.

It can be assessed from these simulations that the required coupling is unchanged in the modified structure BMH9, and that the coupler's performance will compliment the desired functionality of the OPO.

### 6.3 Integrated OPO Design

The OPO design is given below in figure 6-7, in which the components have been optimized after analyzing their measured performance and their fabrication tolerance. Most of the individual components in this integrated device have been discussed earlier, and are highlighted in the figure. The exceptions are: 1) the QPM period, which will be 3.1-3.6  $\mu\text{m}$  over a range of devices, 2) excluding the ring laser cavity and the QPM section, the whole device will be intermixed, 3) and 350  $\mu\text{m}$  long output directional coupler for the longer wavelengths, which has been estimated to couple out 20% of the power from the resonating cavity – the simulated coupling in this case is given in figure 6-8.

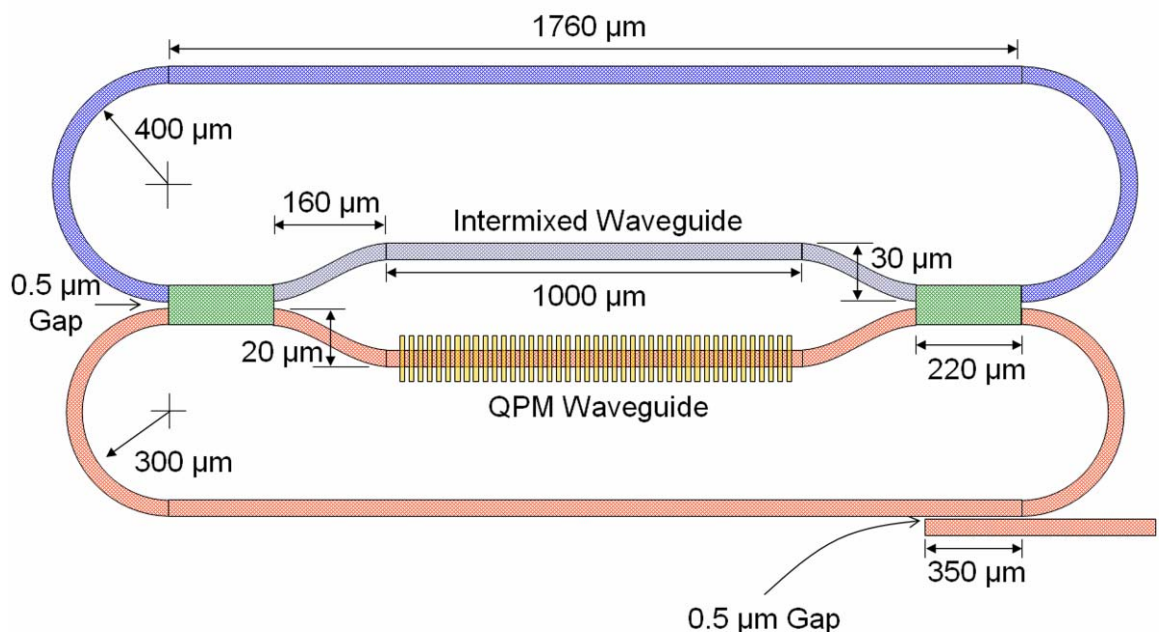


**Figure 6-7 – The designed integrated OPO.**

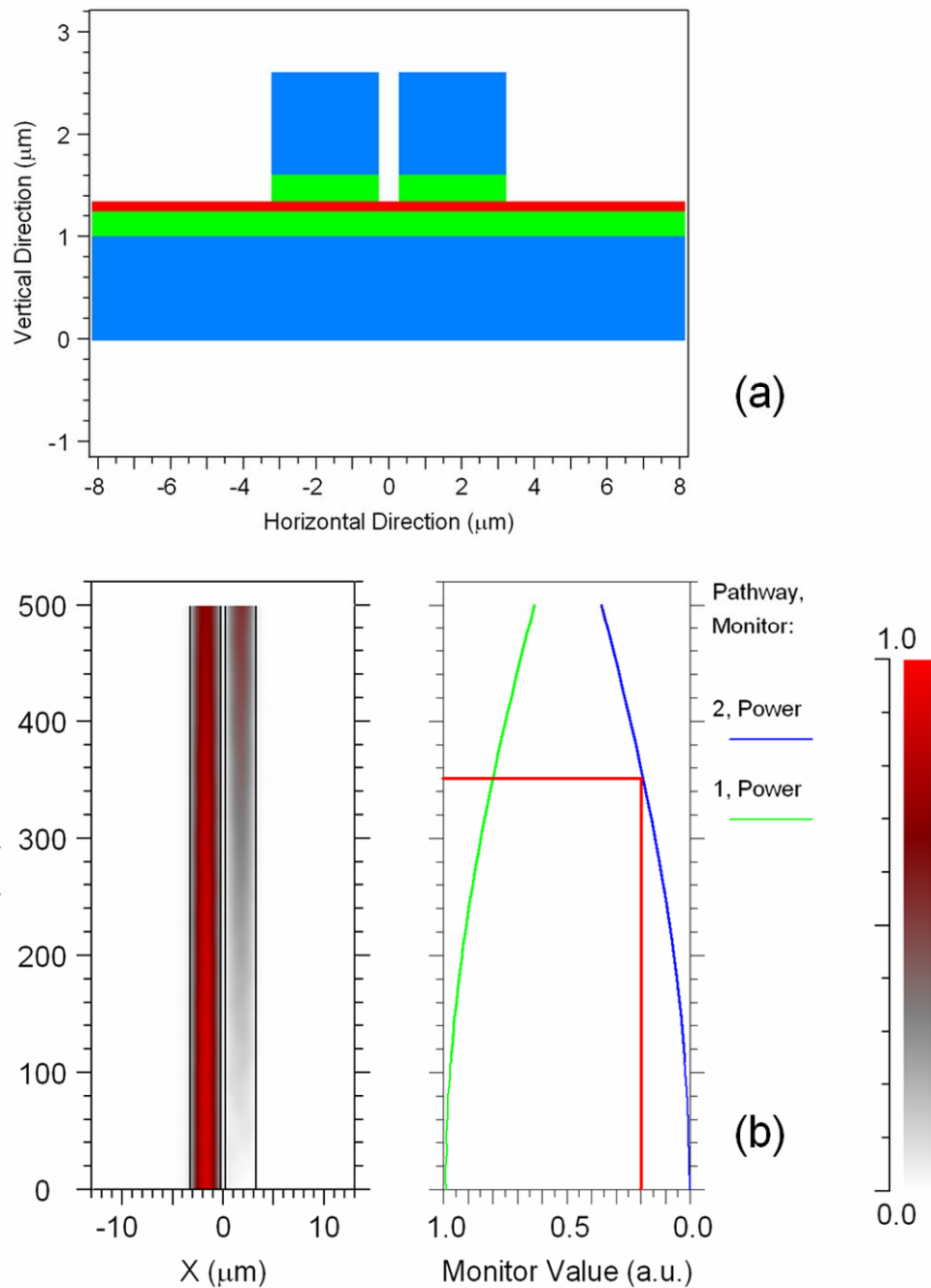
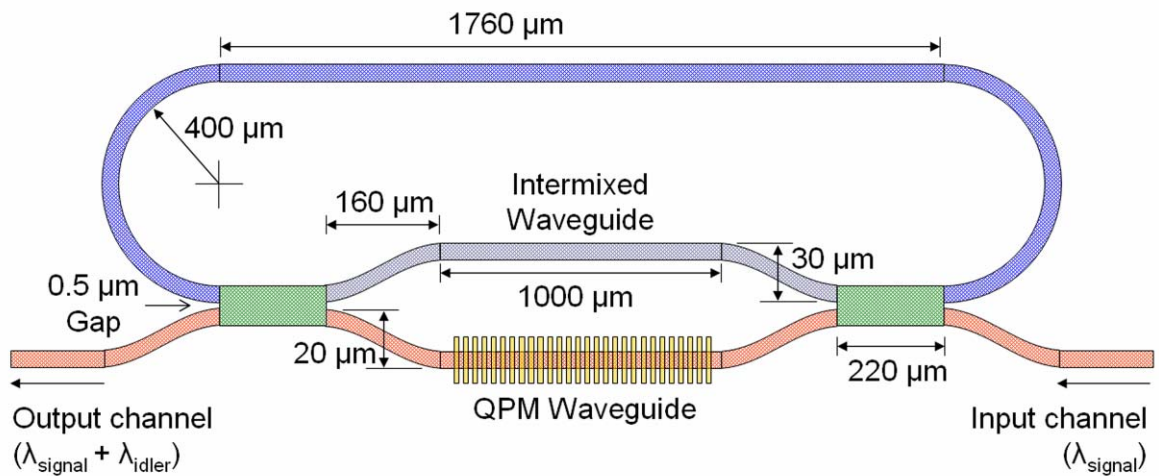


Figure 6-8 – Simulated directional coupler for the longer wavelengths, (a) cross-sectional view of the structure, (b) 350  $\mu\text{m}$  long coupler is estimated to couple out 20% of the power.

## 6.4 Integrated Frequency Converter Design

The concept of monolithically integrated nonlinear frequency converter has been indicated earlier in the section 1.1. The feasibility for such a device is complimented by

the DFG we have achieved in our QPM waveguides, and with the inclusion of an on-chip pump source which has been demonstrated by the laser action in our superlattice material structure. The routing of different wavelengths has also been established by the di-chroic MMI coupler. Placing all the components together, the detailed design for this all-optical frequency converter is given in figure 6-9, which would convert the optical frequencies in 1.5  $\mu\text{m}$  telecommunication band.



**Figure 6-9 – The designed nonlinear optical frequency converter for 1.5  $\mu\text{m}$  telecommunication band.**

The design for this frequency converter is based on the integrated OPO, in which the passive resonator has been replaced by the input channel waveguide  $\lambda_{\text{signal}}$ , and the output channel waveguide  $\lambda_{\text{signal}} + \lambda_{\text{idler}}$ . It can be seen that the optical conversion is achieved using the three-wave-mixing in nonlinear QPM waveguide, for which our DFG experiments have demonstrated direct C-band to L- and U- band wavelength conversion [135].

## 6.5 Integrated Chip

This section presents the design of the semiconductor chip which includes the monolithically integrated devices, i.e., OPO and the nonlinear frequency converter, given in figure 6-10. Both of these devices have been designed for the QPM periods of 3.1-3.3  $\mu\text{m}$  on this chip, and 3.4-3.6  $\mu\text{m}$  on the second chip.

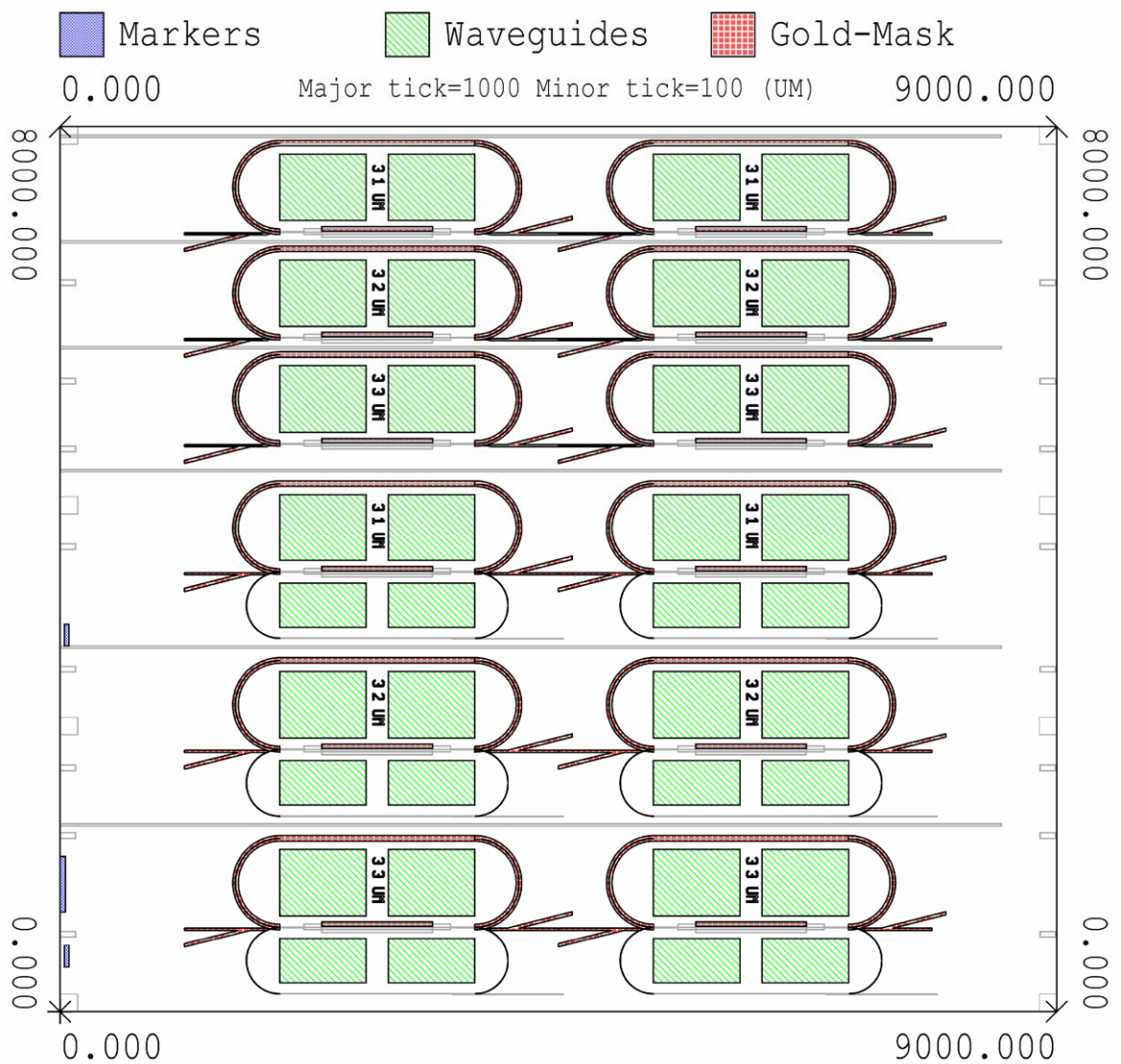


Figure 6-10 – The designed semiconductor chip which includes monolithically integrated devices.

The different fabrication layers of the E-beam mask are visible in the above image, which is consistent with the multi-layered fabrication performed in case of all the devices presented in this thesis – except the couplers. Figure 6-10 also highlights the different fabrication steps involved to achieve these single-chip devices, which include: 1) the definition of registration markers for the alignment of subsequent lithography, 2) the formation of the gold mask for ion-implantation, 3) the definition of waveguides which realize the device design, and finally 4) the fabrication involved for the device metallization, i.e., contact windows definition, P-contact metallization, mechanical thinning of the substrate, and finally the N-contact metallization. The details for each of

these fabrication steps have been presented earlier in the QPM waveguides and the superlattice lasers chapters.

The fabrication for these chips has not been completed at the submission of this thesis (May 2010), due to the initial fabrication related issues for which the chips had to be revised, and also, over two months of the down time in the case of ion-implantation. However, the findings which would be observed from these devices will be reported in the near future.

## 6.6 Monolithic Integration Demonstrated

The fabrication of the final chips could not be completed at the submission; however, the process development for this has been demonstrated by the integrated OPO and the integrated DFG, which were fabricated on the active wafer BMH5. The improved fabrication process, which has been discussed earlier in the QPM waveguides chapter and the superlattice lasers chapter, has been employed in this case. Figure 6-11 shows the SEM image of the gold mask for the DFG section of this test chip.

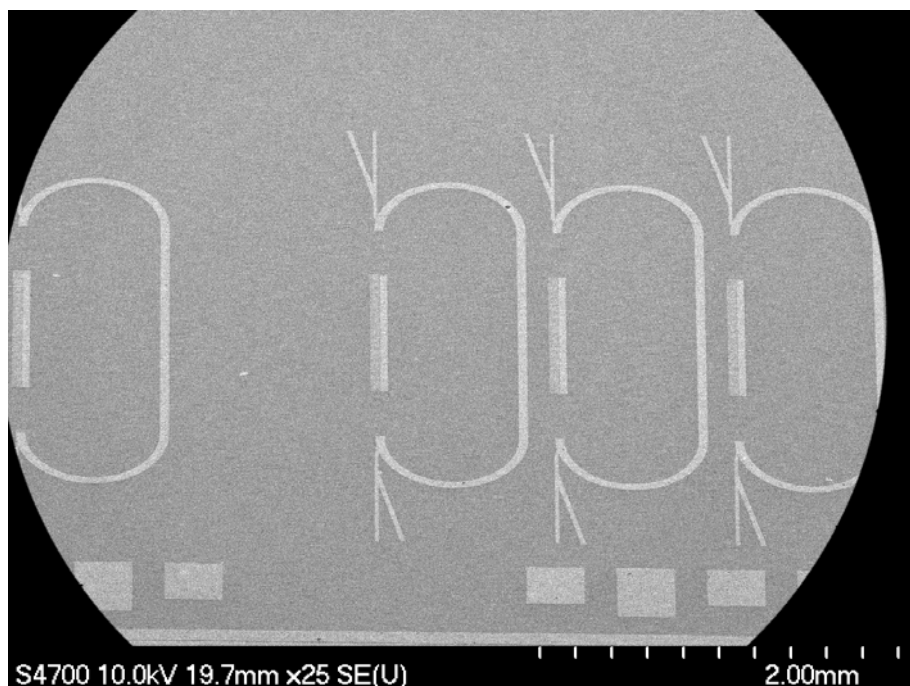


**Figure 6-11 – The SEM image of the gold mask for the integrated DFG.**

After performing the Au/Ti clean and the RTA stages of the fabrication, the waveguides were defined in dry etch, given below in the figure 6-12. The SEM image shows the process improvements which have been achieved in order to define the low loss waveguides – thin layers of the superlattice core are also visible around this deep etched waveguide.

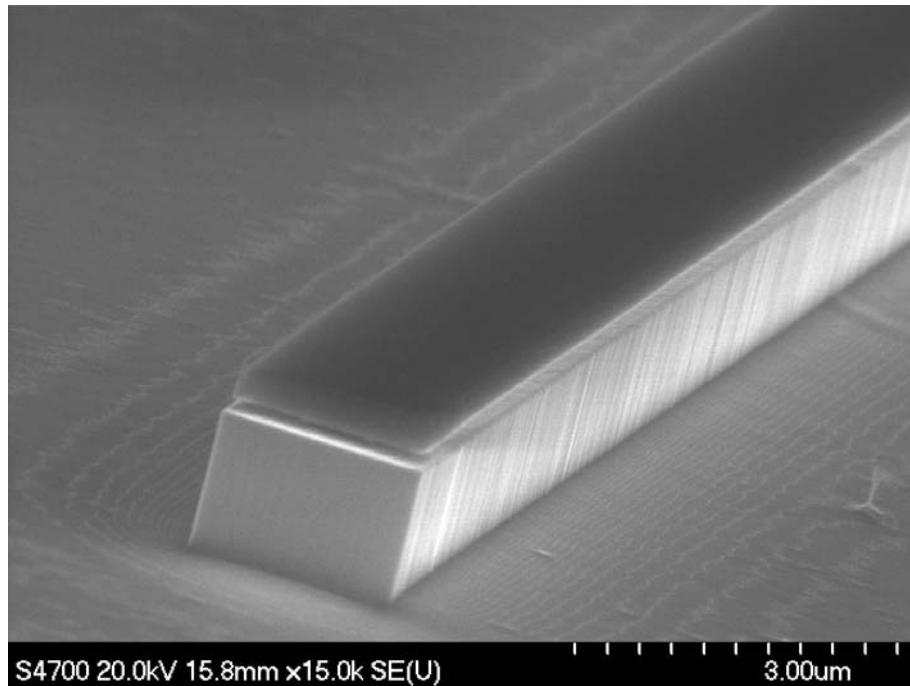


**Figure 6-12 – The SEM image of the deep etched waveguide.**

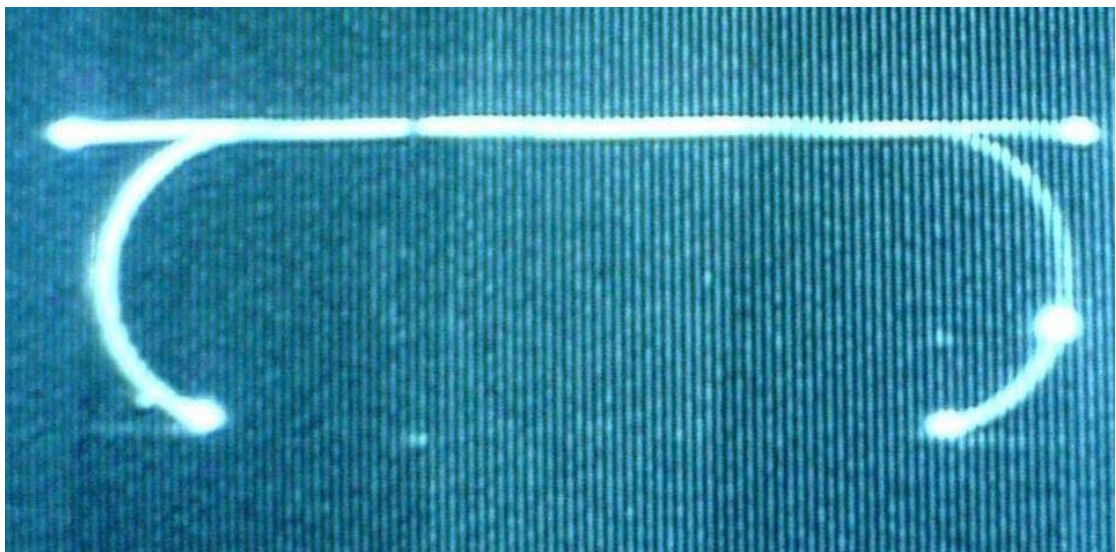


**Figure 6-13 – The IR image of an integrated DFG being tested.**

Finally, after the P- and N-contact metallization, the devices were electrically probed to observe any light generation, which was unlikely in this case as the material BMH5 did not show any laser action in the first place. However, an IR image of the tested DFG is given in figure 6-13, in which the cladding glow is visible from the top.

This chapter concludes with the investigations and the studies which have been performed to demonstrate our monolithically integrated OPO, and the monolithically integrated nonlinear optical frequency converter. The design for the ring laser has been finalized after achieving the laser action in the half ring lasers, and the di-chroic MMI coupler has been simulated for the thinner superlattice core material structure. In both of these cases, the results have been found highly encouraging towards the monolithic integration. The detailed design of the integrated chip has been presented, and the fabrication for these devices is incomplete.

# *Chapter 7*

## Conclusions & Future Recommendations

This thesis has presented a detailed study into the feasibility of producing a monolithically integrated OPO, and a monolithically integrated nonlinear optical frequency converter, in a GaAs/AlGaAs superlattice material system. The motivation for using GaAs for such nonlinear applications comes from its large nonlinear susceptibility, broad transparency range, low absorption, and very mature fabrication technologies. Furthermore, selective area intermixing in GaAs/AlGaAs superlattices can achieve a substantial modulation in the inherent nonlinearities of the material system; and for this purpose, they are highly attractive for nonlinear optical processing. A principle challenge in realizing such nonlinear sources is the intrinsic requirement to phase match the different wavelengths involved, for which, we have employed a quasi phase matching approach.

Our GaAs/AlGaAs superlattice core material system has initially been studied with the help of energy band calculations, and an understanding of the mini-bands formation has been developed. We have engineered a domain-disordered quasi phase matching (DD-QPM) technique to periodically intermix the superlattice core. In order to achieve this periodic quantum well intermixing (QWI), two different QWI techniques have been investigated in detail: 1) sputtered SiO<sub>2</sub>, and 2) Ion Implantation. A large band-edge shift has been observed in the case of sputtered SiO<sub>2</sub>; however, the relatively low spatial resolution achievable using this intermixing technique has been identified as a shortfall in its application. In the case of ion implantation, a comprehensive study has been conducted to understand the intermixed material parameters, i.e., the band-edge shift, and the optical loss factor, by using various implantation doses and annealing treatments at different temperatures. In addition, the tests performed to quantify the spatial resolution of ion implantation strongly favor its application in achieving a sub-micron control of the intermixing. Through a detailed characterization of the second harmonic

generation (SHG) produced in test samples, using various phase matching periods, each with different duty cycles, we have optimized the design of the QPM period and duty factor. Our optimized fabrication process, and greatly improved periodic QWI, has enabled us to achieve enhanced conversion efficiency in various second order nonlinear processes. We have achieved: 1) Type-I pulsed SHG up to 3.65  $\mu\text{W}$ , 2) continuous wave (CW) type-I SHG up to 1.6  $\mu\text{W}$ , for the very first time in GaAs/AlGaAs superlattice waveguides, 3) Type-II pulsed SHG up to 2.0  $\mu\text{W}$ , again for the very first time, and recently 4) we have demonstrated difference frequency generation (DFG), which converts C-band wavelengths into L- and U- band wavelengths – the conversion bandwidth is 20 nm with 5dB conversion efficiency. This last result is of critical importance when considering the feasibility of an all-optical nonlinear frequency converter for 1.5  $\mu\text{m}$  telecommunication band. Lastly, the fabrication process for QPM waveguides has been completely reevaluated to identify the optimization of each step. The resulting, significantly improved fabrication processes which have been developed are a pre-requisite for the potential performance of a monolithically integrated device.

The wavelength dependent optical routing, which is required in our integrated devices, has been designed and demonstrated using a di-chroic MMI coupler. Fabrication challenges have been identified for the designed MMI structure, and an improved dry-etch process has been developed to overcome these – this dry-etch process has been developed towards the monolithic integration of the final device. The coupler characterization has been performed for the band-gap and the half-band-gap wavelengths, and a minimum cross-talk of  $-14$  dB has been achieved for the half-band-gap wavelengths, which is found to be consistent with the initial design.

The material structure for the superlattice core laser has been designed and presented in the thesis. The final design has been achieved by incremental improvements identified in growth of more than seven wafers, and also by employing different growth technologies – in latter, the challenges faced in each of the growth technologies have also been discussed, and metalorganic vapour phase epitaxy (MOVPE) has been found to offer a highly promising approach for the growth of such complex heterostructures. The material tests which have been performed using several wafers include: 1) transmission line measurements, and 2) broad area laser characterization. Laser action

has been achieved in a 100 nm thick superlattice core material structure, as a result of these tests and the improvements achieved in the growth of active wafers. Ridge waveguide lasers have been developed initially to achieve lasing action in a ring laser – which has been designed as an on-chip pump source. The ridge waveguide design has been kept consistent with the overall waveguide structure of the complete device. The fabrication process for the ridge waveguide laser has been developed, and it has been presented in detail in the thesis. A new step of waveguide planarization has been incorporated into the fabrication process, in order to achieve an overall process optimization through improved contact deposition. The lasers have been tested CW at room-temperature, and the results from various devices of different dimensions have been discussed in detail. The characteristics of these lasers, e.g., the optical loss factor, the internal quantum efficiency, and the material gain, have been evaluated using the experimentally obtained values. A good agreement has been observed between the experimentally evaluated parameters and theoretically predicted values. The reduced device performance, in lasers with 23% internal quantum efficiency, is attributed to several causes. In order to understand each of these, the required measurements have been performed and are presented, including information relating to the growth conditions and also the pulsed spectrum. However, the reason for this behavior is suggested to be the presence of a high energy barrier in the intrinsic core. The presence for this barrier has been established by the observation of resonant tunneling in a slightly thicker superlattice core of 150 nm. The band alignment calculations, and the V-I measurements, are in an agreement for the resonant tunneling to occur at ~2 V applied bias.

Consequently, it seems that the laser action in our superlattice core material may be improved, as much as, any commercially available light source in a GaAs–AlGaAs material system. This requires further study, and it is recommended as a future course of action. One solution could be the inclusion of graded alloys in the wave-guiding core, which have been employed to provide a smooth carrier transport in the quantum cascade lasers [6].

The final part of this thesis covers the monolithically integrated devices, i.e., integrated OPO, and the nonlinear optical frequency converter. The ring design, in these devices,

has been achieved by the demonstration of lasing action in half ring lasers. In these tests, the etch-depth has been found critical in reducing the bending losses; hence, a slightly deep etched structure has been recommended for the final devices. The coupler design has also been revisited for the 100 nm thick superlattice core, and the required coupling is found consistent with the previously measured behavior. Finally, the detailed design of our OPO and the optical frequency converter has been presented, along with the semiconductor chip layout for the final design, the fabrication of which is incomplete at the submission of this thesis, primarily due to machine downtime at the University of Surrey and also at the JWNC. However, the fabrication processes and design of a fully integrated device have been developed, and it is highly recommended as a near term future activity that these devices be completed and characterized.

A dual core, mid-infrared wavelength source is proposed as a future extension of this research. Orientation patterned growth (OPG) GaAs has previously been employed to demonstrate this [34]; however, to achieve a monolithically integrated source, a longer wavelength on-chip pump is required. InP could be employed to provide this on-chip pump, and its high quality growth on [001] GaAs has recently been demonstrated [164]. In this device, the QPM waveguide would be formed in the superlattice GaAs/AlGaAs material, for which the phase matching period has to be studied in detail for mid-infrared generation. The laser pump would then be provided by the InP source grown on the top of GaAs/AlGaAs substrate. The lateral wave-guiding in this structure could be achieved by the asymmetric waveguide coupling technology (AWG) [40-41].

# APPENDIX I

Prints of the selected articles published in collaboration with University of Toronto.

The physical prints of the journal articles have been included in the printed version of the thesis; however, the live links (hyperlinks) are provided for the online version, in order to comply with the University's copyright policy.

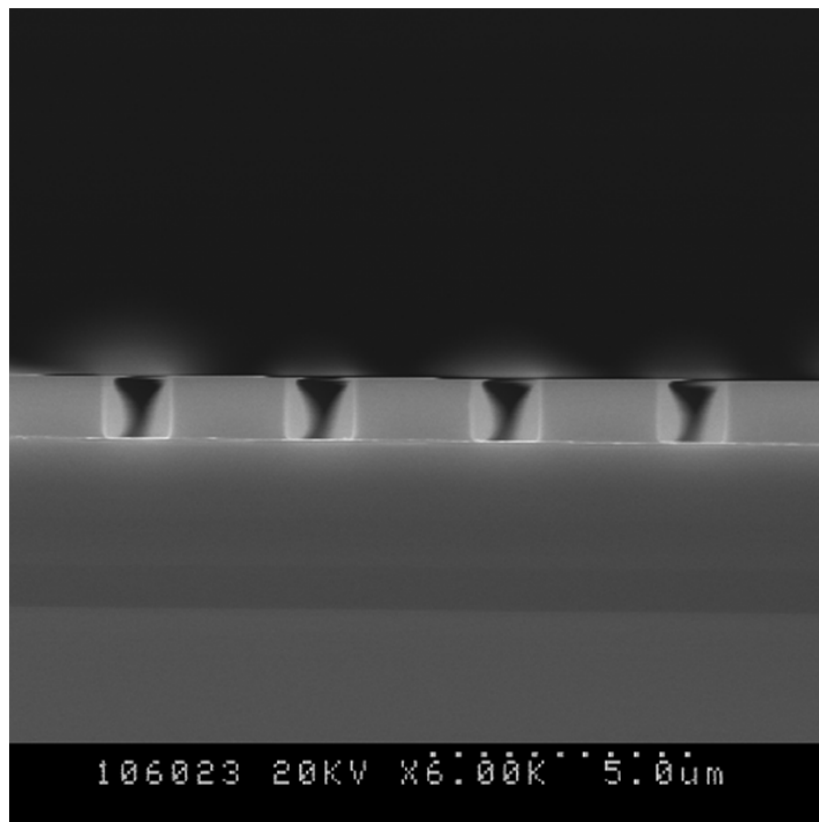
- 1) Sean J. Wagner, Barry M. Holmes, **Usman Younis**, Amr S. Helmy, J. Stewart Aitchison, and David C. Hutchings, "Continuous wave second-harmonic generation using domain-disordered quasi-phase matching waveguides", *Applied Physics Letters*, vol. 94, pp. 151107, Apr. 14 2009.
- 2) David C. Hutchings, Sean J. Wagner, Barry M. Holmes, **Usman Younis**, Amr S. Helmy, and J. Stewart Aitchison, "Type-II quasi phase matching in periodically intermixed semiconductor superlattice waveguides," *Optics Letters*, vol. 35, pp. 1299-1301, Apr. 15 2010.
- 3) S. J. Wagner, I. Sigal, A. S. Helmy, J. S. Aitchison, **U. Younis**, B. Holmes, and D. C. Hutchings, "Difference Frequency Generation in Domain-Disordered Quasi-Phase-Matched Semiconductor Waveguides," *Conference on Lasers and Electro-optics (CLEO)*, San Jose, CA, May 2010.

## APPENDIX II

### Ion Implantation Tests

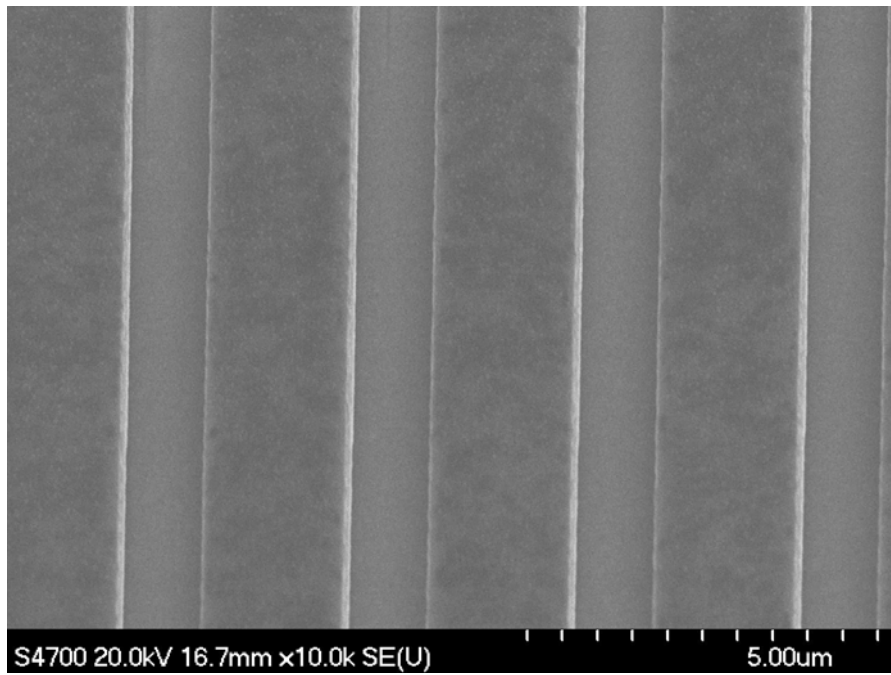
The masked and the exposed ratios are designed figures, and there is a fabrication tolerance which has to be included. E-beam dose has been kept higher to fully expose the 2.5  $\mu\text{m}$  thick bi-layer PMMA resist – this higher dose increases the pattern dimensions.

- 1) 50 : 50 (50 % Gold Mask: 50 % Exposed)
- 2) 55 : 45 (55 % Gold Mask: 45 % Exposed)
- 3) 60 : 40 (60 % Gold Mask: 40 % Exposed)
- 4) 65 : 35 (65 % Gold Mask: 35 % Exposed)
- 5) 70 : 30 (70 % Gold Mask: 30 % Exposed)

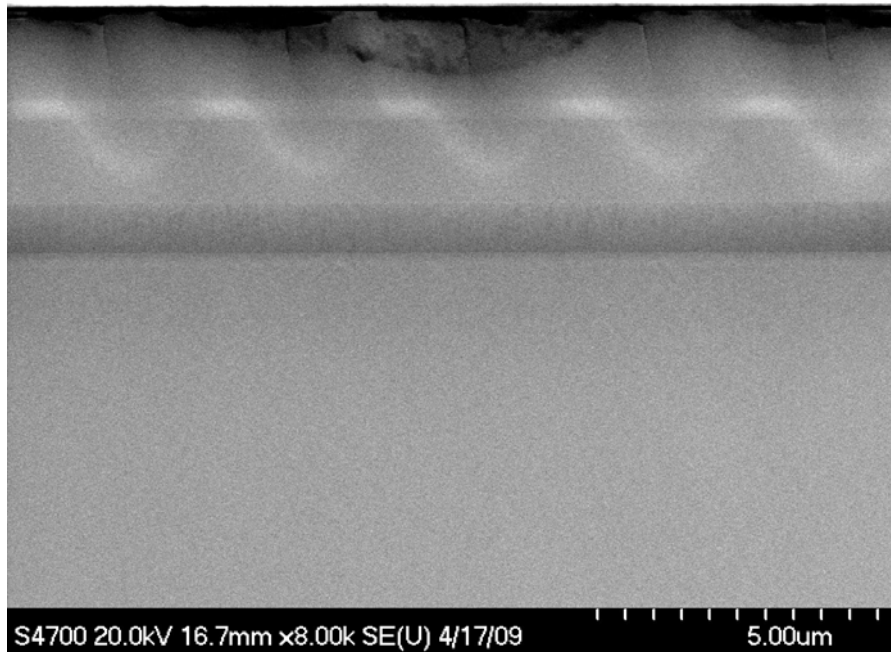


Cross-sectional SEM micrograph of a dose test for 15%15% PMMA

**1) 50: 50 (50 % Gold Mask: 50 % Exposed)**

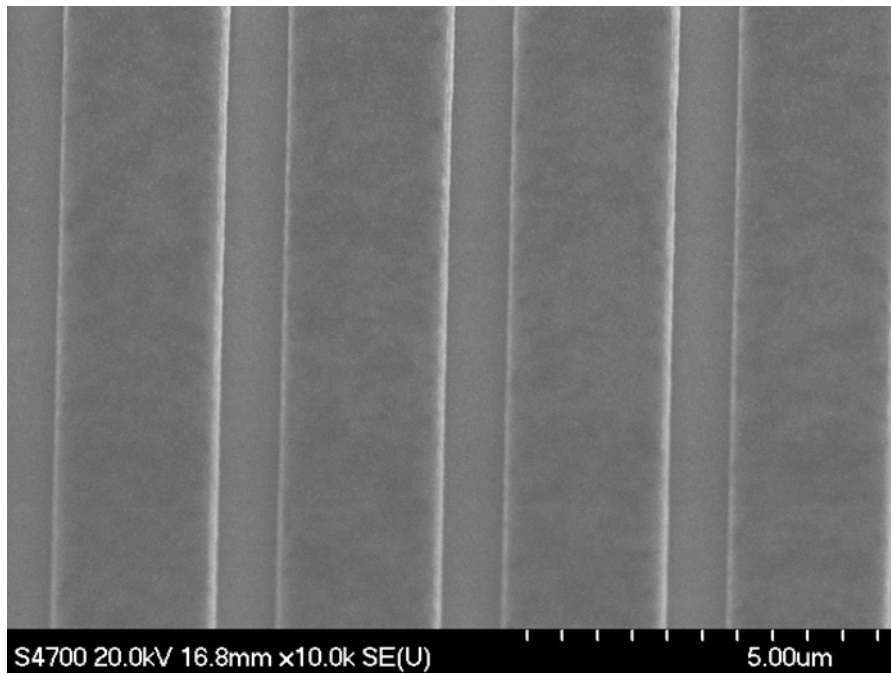


**Gold mask (top view)**

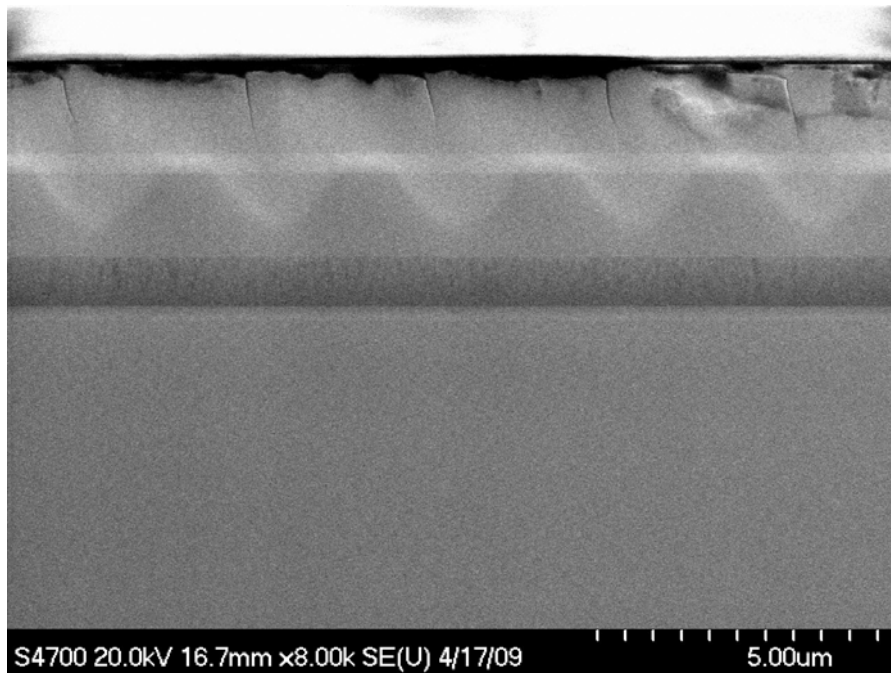


**Implanted sample (cross-sectional view)**

2) 55: 45 (55 % Gold Mask: 45 % Exposed)

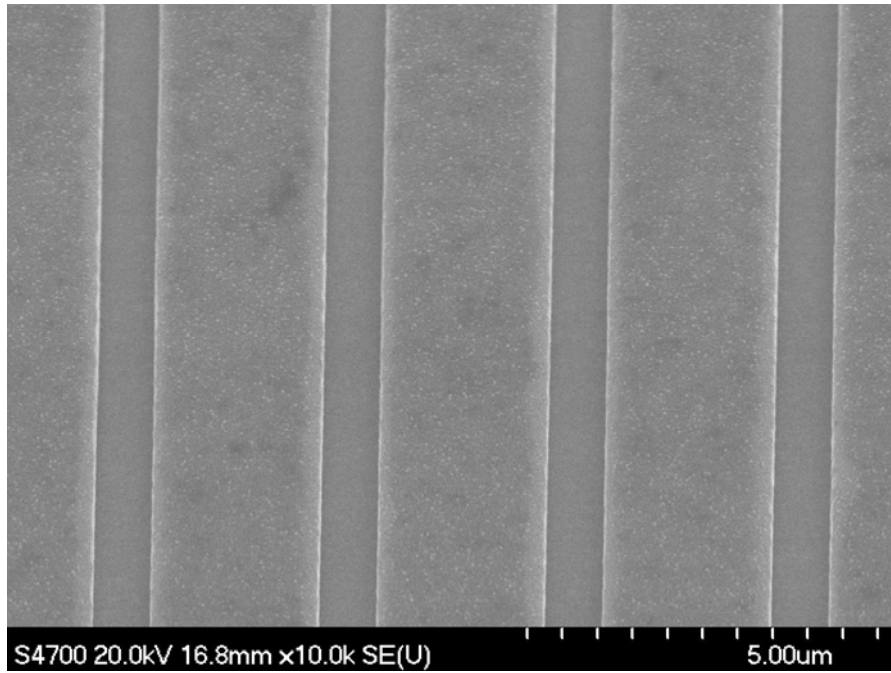


Gold mask (top view)

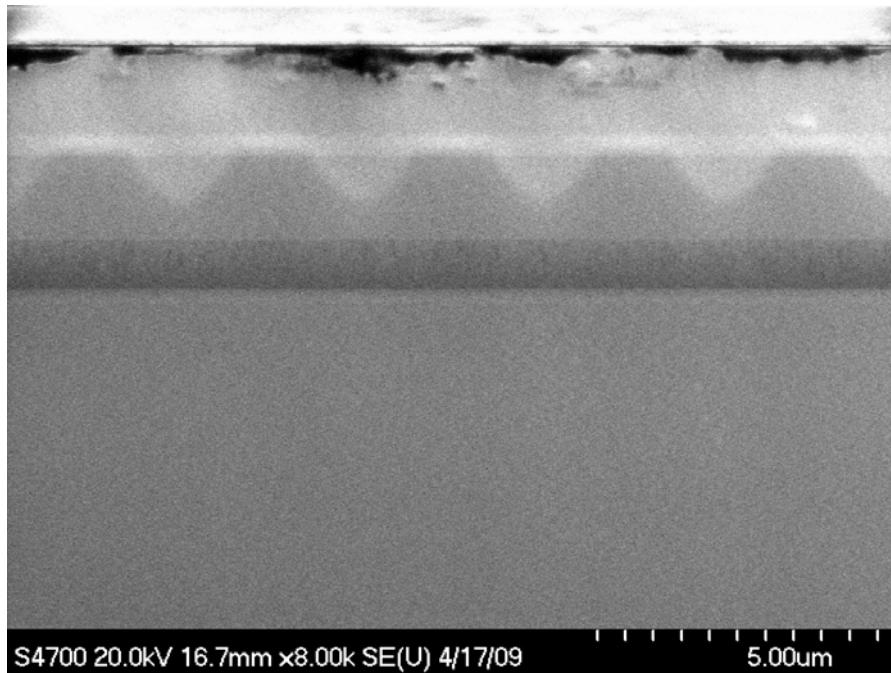


Implanted sample (cross-sectional view)

**3) 60: 40 (60 % Gold Mask: 40 % Exposed)**

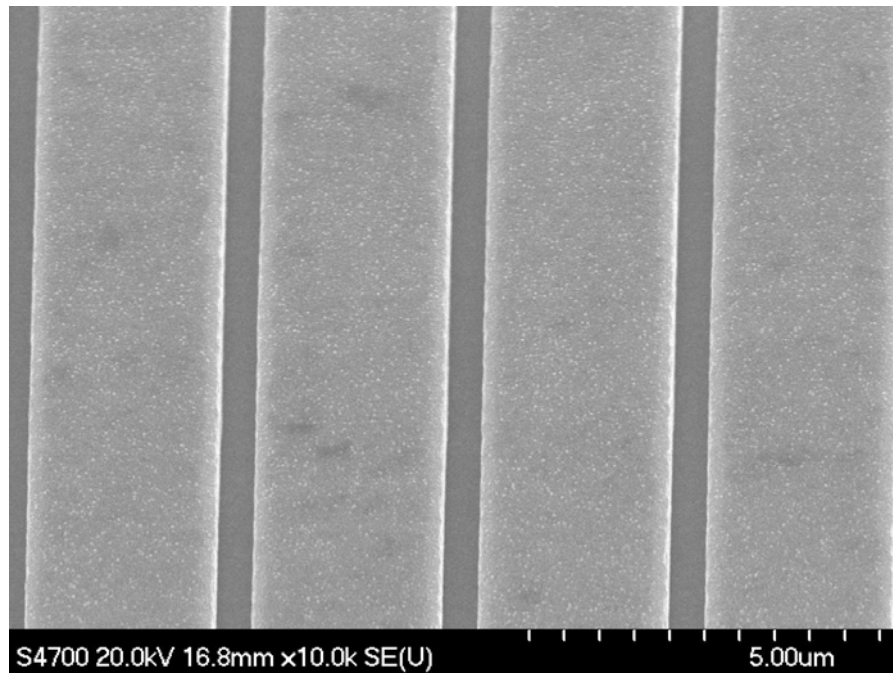


**Gold mask (top view)**

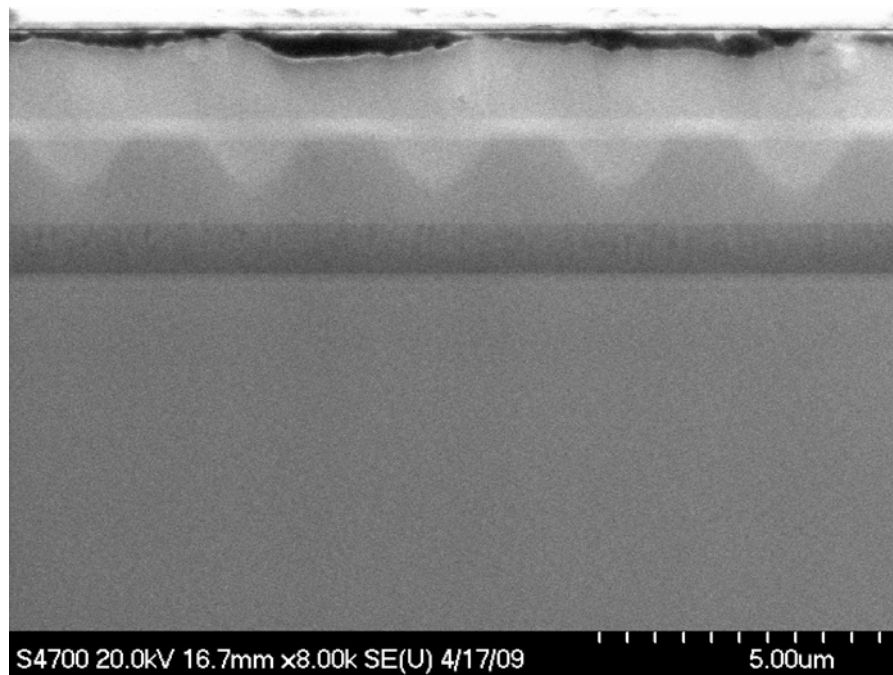


**Implanted sample (cross-sectional view)**

4) 65: 45 (65 % Gold Mask: 45 % Exposed)

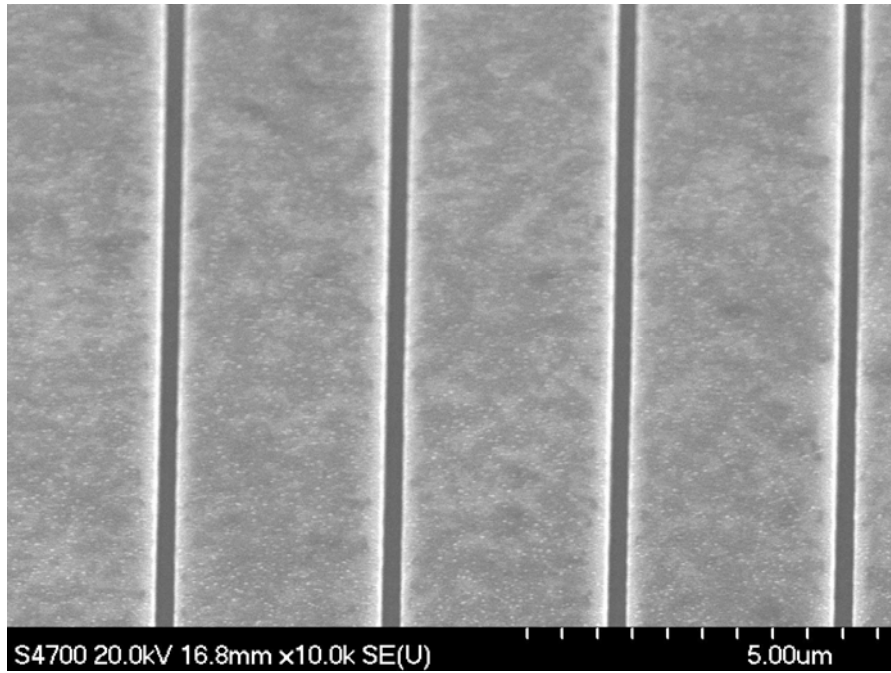


Gold mask (top view)

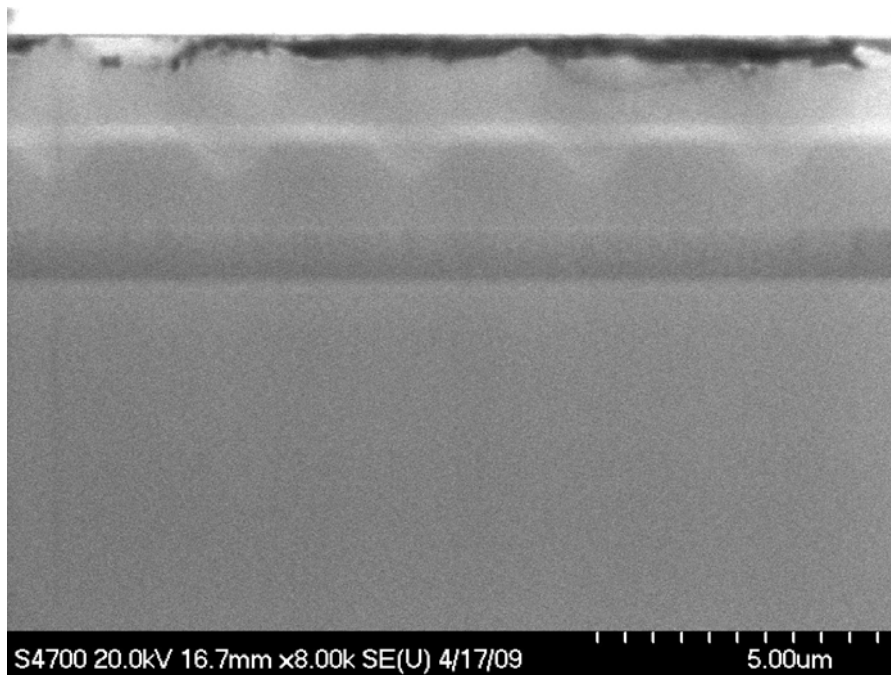


Implanted sample (cross-sectional view)

**5) 70: 30 (70% Gold Mask: 30 % Exposed)**



**Gold mask (top view)**



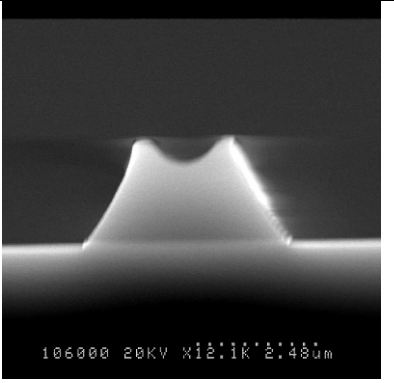
**Implanted sample (cross-sectional view)**

# APPENDIX III

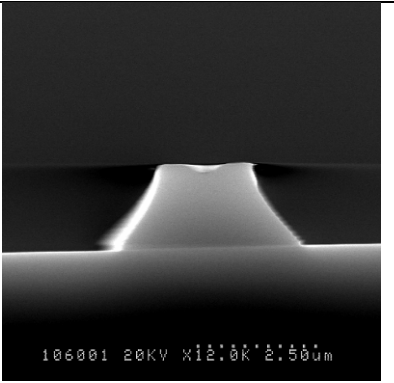
## S18 Photo-resists

- Motive was to achieve the best vertical sidewall profile with S18 resists
- Designed features were 3  $\mu\text{m}$  wide
- Optimum recipe used for S1818 (1.8  $\mu\text{m}$  thickness) is 90 °C oven baking for 30 min, 4 sec exposure and 75 sec development
- S18 manufacturer specification is 115 °C bake for 1 min at hotplate

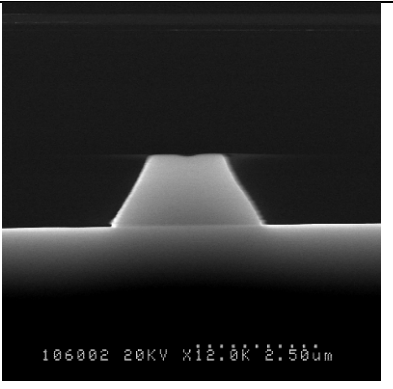
<b>R1</b>	Category	Spin Speed	Thickness	Bake
<b>Resist</b>	S1828	5000 RPM x 30 sec	2.5-2.6 $\mu\text{m}$	90 °C / 20 min (Hotplate)
<b>Exposure</b>	4.8 sec exposure (MA-6)			
<b>Development</b>	75 sec (1:1 Micro Dev:H <sub>2</sub> O)			



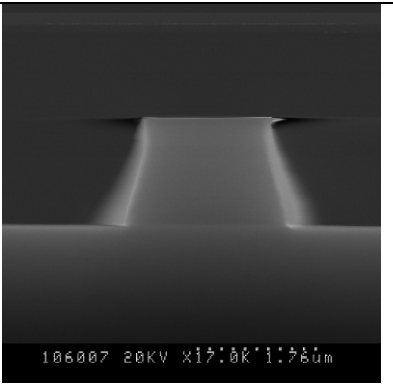
<b>R2</b>	Category	Spin Speed	Thickness	Bake
<b>Resist</b>	S1818	4000 RPM x 30 sec	1.8 $\mu\text{m}$	90 °C / 20 min (Hotplate)
<b>Exposure</b>	3.9 sec exposure (MA-6)			
<b>Development</b>	75 sec (1:1 Micro Dev:H <sub>2</sub> O)			



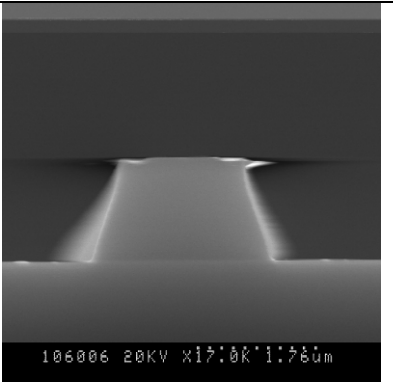
<b>R3</b>	Category	Spin Speed	Thickness	Bake
<b>Resist</b>	S1818	4000 RPM x 30 sec	1.8 $\mu\text{m}$	90 °C / 20 min (Hotplate)
<b>Exposure</b>	3.7 sec exposure (MA-6)			
<b>Development</b>	75 sec (1:1 Micro Dev:H <sub>2</sub> O)			



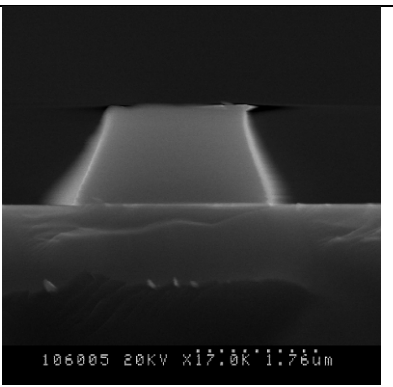
<b>R4</b>	Category	Spin Speed	Thickness	Bake
<b>Resist</b>	S1818	4000 RPM x 30 sec	1.8 $\mu\text{m}$	115 °C / 1 min (Hotplate)
<b>Exposure</b>	3.9 sec exposure (MA-6)			
<b>Development</b>	75 sec (1:1 Micro Dev:H <sub>2</sub> O)			



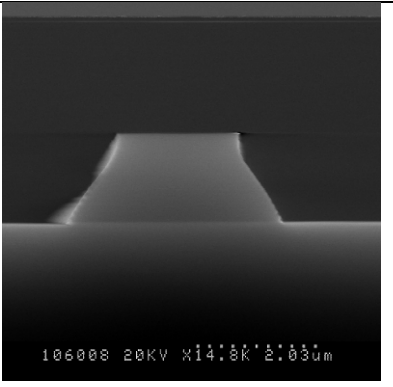
<b>R5</b>	Category	Spin Speed	Thickness	Bake
<b>Resist</b>	S1818	4000 RPM x 30 sec	1.8 $\mu\text{m}$	90 °C / 30 min (Oven bake)
<b>Exposure</b>	3.9 sec exposure (MA-6)			
<b>Development</b>	75 sec (1:1 Micro Dev:H <sub>2</sub> O)			



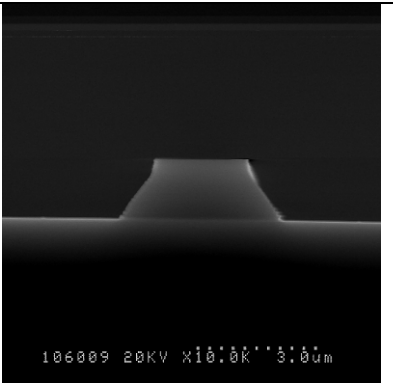
<b>R6</b>	Category	Spin Speed	Thickness	Bake
<b>Resist</b>	S1818	4000 RPM x 30 sec	1.8 $\mu\text{m}$	90 °C / 30 min (Oven bake)
<b>Exposure</b>	3.9 sec exposure (MA-6)			
<b>Development</b>	60 sec (1:1 Micro Dev:H <sub>2</sub> O)			



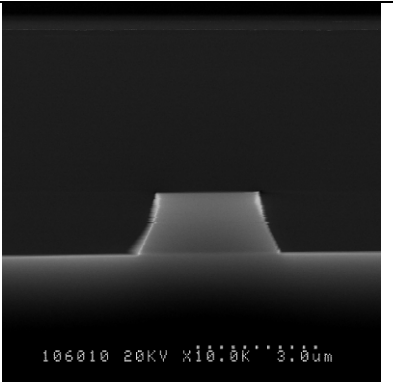
<b>R7</b>	Category	Spin Speed	Thickness	Bake
<b>Resist</b>	S1818	4000 RPM x 30 sec	1.8 μm	125 °C / 1 min (Hotplate)
<b>Exposure</b>	4 sec exposure (MA-6)			
<b>Development</b>	60 sec (1:1 Micro Dev:H <sub>2</sub> O)			



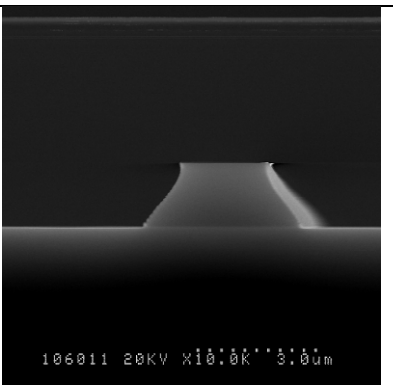
<b>R8</b>	Category	Spin Speed	Thickness	Bake
<b>Resist</b>	S1818	4000 RPM x 30 sec	1.8 μm	125 °C / 1 min (Hotplate)
<b>Exposure</b>	4 sec exposure (MA-6)			
<b>Development</b>	50 sec (1:1 Micro Dev:H <sub>2</sub> O)			



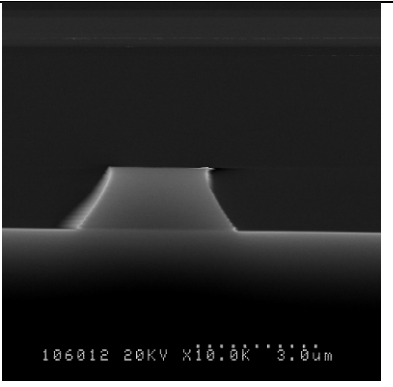
<b>R9</b>	Category	Spin Speed	Thickness	Bake
<b>Resist</b>	S1818	4000 RPM x 30 sec	1.8 μm	125 °C / 2 min (Hotplate)
<b>Exposure</b>	4 sec exposure (MA-6)			
<b>Development</b>	60 sec (1:1 Micro Dev:H <sub>2</sub> O)			



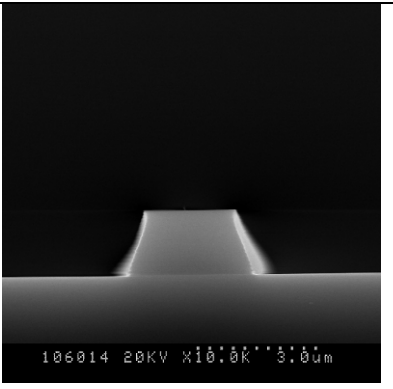
<b>R10</b>	Category	Spin Speed	Thickness	Bake
<b>Resist</b>	S1818	4000 RPM x 30 sec	1.8 μm	125 °C / 1 min (Hotplate)
<b>Exposure</b>	4.5 sec exposure (MA-6)			
<b>Development</b>	50 sec (1:1 Micro Dev:H <sub>2</sub> O)			



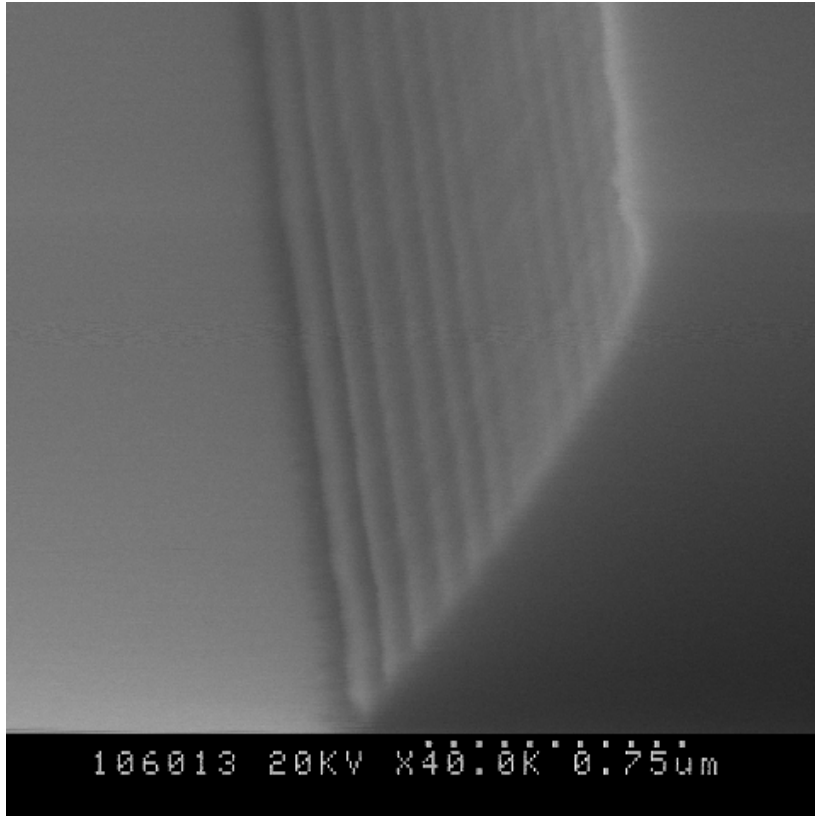
<b>R11</b>	Category	Spin Speed	Thickness	Bake
<b>Resist</b>	S1818	4000 RPM x 30 sec	1.8 $\mu\text{m}$	125 °C / 1 min (Hotplate)
<b>Exposure</b>	5 sec exposure (MA-6)			
<b>Development</b>	40 sec (1:1 Micro Dev:H <sub>2</sub> O)			



<b>R12</b>	Category	Spin Speed	Thickness	Bake
<b>Resist</b>	S1818	4000 RPM x 30 sec	1.8 $\mu\text{m}$	125 °C / 1 min (Hotplate)
<b>Exposure</b>	5.5 sec exposure (MA-6)			
<b>Development</b>	30 sec (1:1 Micro Dev:H <sub>2</sub> O)			



### Side wall S1818 photo-resist



- Recipe R9 was found to be the most appropriate.
- Exposure was also performed using HTG (level-6 Rankine building) to cross check MA-6 – again pyramids were found.

## REFERENCES

- [1] K. Fradkin, A. Arie, A. Skliar, and G. Rosenman, "Tunable midinfrared source by difference frequency generation in bulk periodically poled KTiOPO<sub>4</sub>," *Applied Physics Letters*, vol. 74, pp. 914-916, Feb. 15 1999.
- [2] D. J. M. Stothard, M. H. Dunn, and C. F. Rae, "Hyperspectral imaging of gases with a continuous-wave pump-enhanced optical parametric oscillator," *Optics Express*, vol. 12, pp. 947-955, Mar. 8 2004.
- [3] T. J. Kulp, S. E. Bisson, R. P. Bambha, T. A. Reichardt, U. B. Goers, K. W. Aniolek, D. A. V. Kliner, B. A. Richman, K. M. Armstrong, R. Sommers, R. Schmitt, P. E. Powers, O. Levi, T. Pinguet, M. Fejer, J. P. Koplow, L. Goldberg, and T. G. Mcrae, "The application of quasi-phase-matched parametric light sources to practical infrared chemical sensing systems," *Applied Physics B-Lasers and Optics*, vol. 75, pp. 317-327, Sep. 2002.
- [4] Y. Mine, N. Melander, D. Richter, D. G. Lancaster, K. P. Petrov, R. F. Curl, and F. K. Tittel, "Detection of formaldehyde using mid-infrared difference-frequency generation," *Applied Physics B-Lasers and Optics*, vol. 65, pp. 771-774, Dec. 1997.
- [5] M. Tacke, "New Developments and Application of Tunable Ir Lead Salt Lasers," *Infrared Physics & Technology*, vol. 36, pp. 447-463, Jan. 1995.
- [6] J. Faist, F. Capasso, D. L. Sivco, C. Sirtori, A. L. Hutchinson, and A. Y. Cho, "Quantum Cascade Laser," *Science*, vol. 264, pp. 553-556, Apr. 22 1994.
- [7] M. Beck, D. Hofstetter, T. Aellen, J. Faist, U. Oesterle, M. Ilegems, E. Gini, and H. Melchior, "Continuous wave operation of a mid-infrared semiconductor laser at room temperature," *Science*, vol. 295, pp. 301-305, Jan. 11 2002.
- [8] J. S. Yu, S. Slivken, S. R. Darvish, A. Evans, B. Gokden, and M. Razeghi, "High-power, room-temperature, and continuous-wave operation of distributed-feedback quantum-cascade lasers at  $\lambda \sim 4.8 \mu\text{m}$ ," *Applied Physics Letters*, vol. 87, p. 041104, Jul. 25 2005.
- [9] L. Diehl, D. Bour, S. Corzine, J. Zhu, G. Hofler, M. Loncar, M. Troccoli, and F. Capasso, "High-power quantum cascade lasers grown by low-pressure metal

- organic vapor-phase epitaxy operating in continuous wave above 400 K," *Applied Physics Letters*, vol. 88, p. 201115, May. 15 2006.
- [10] Y. Bai, S. Slivken, S. R. Darvish, and M. Razeghi, "Room temperature continuous wave operation of quantum cascade lasers with 12.5% wall plug efficiency," *Applied Physics Letters*, vol. 93, p. 021103, Jul. 14 2008.
- [11] A. Lyakh, C. Pflugl, L. Diehl, Q. J. Wang, F. Capasso, X. J. Wang, J. Y. Fan, T. Tanbun-Ek, R. Maulini, A. Tsekoun, R. Go, and C. K. N. Patel, "1.6 W high wall plug efficiency, continuous-wave room temperature quantum cascade laser emitting at 4.6  $\mu\text{m}$ ," *Applied Physics Letters*, vol. 92, p. 111110, Mar. 17 2008.
- [12] R. Maulini, I. Dunayevskiy, A. Lyakh, A. Tsekoun, C. K. N. Patel, L. Diehl, C. Pflugl, and F. Capasso, "Widely tunable high-power external cavity quantum cascade laser operating in continuous-wave at room temperature," *Electronics Letters*, vol. 45, pp. 107-U30, Jan. 15 2009.
- [13] G. Wysocki, R. Lewicki, R. F. Curl, F. K. Tittel, L. Diehl, F. Capasso, M. Troccoli, G. Hofler, D. Bour, S. Corzine, R. Maulini, M. Giovannini, and J. Faist, "Widely tunable mode-hop free external cavity quantum cascade lasers for high resolution spectroscopy and chemical sensing," *Applied Physics B-Lasers and Optics*, vol. 92, pp. 305-311, Sep. 2008.
- [14] B. G. Lee, M. A. Belkin, R. Audet, J. MacArthur, L. Diehl, C. Pflugl, and F. Capasso, "Widely tunable single-mode quantum cascade laser source for mid-infrared spectroscopy," *Applied Physics Letters*, vol. 91, p. 231101, Dec. 3 2007.
- [15] T. J. Edwards, G. A. Turnbull, M. H. Dunn, and M. Ebrahimzadeh, "Continuous-wave, singly-resonant, optical parametric oscillator based on periodically poled KTiOPO<sub>4</sub>," *Optics Express*, vol. 6, pp. 58-63, Jan. 31 2000.
- [16] D. J. M. Stothard, M. Ebrahimzadeh, and M. H. Dunn, "Low-pump-threshold continuous-wave singly resonant optical parametric oscillator," *Optics Letters*, vol. 23, pp. 1895-1897, Dec. 15 1998.
- [17] I. D. Lindsay, D. J. M. Stothard, C. F. Rae, and M. H. Dunn, "Continuous-wave, pump-enhanced optical parametric oscillator based on periodically-poled RbTiOAsO<sub>4</sub>," *Optics Express*, vol. 11, pp. 134-140, Jan. 27 2003.
- [18] T. J. Edwards, G. A. Turnbull, M. H. Dunn, M. Ebrahimzadeh, and F. G. Colville, "High-power, continuous-wave, singly resonant, intracavity optical

- parametric oscillator," *Applied Physics Letters*, vol. 72, pp. 1527-1529, Mar. 30 1998.
- [19] K. P. Petrov, A. T. Ryan, T. L. Patterson, L. Huang, S. J. Field, and D. J. Bamford, "Mid-infrared spectroscopic detection of trace gases using guided-wave difference-frequency generation," *Applied Physics B-Lasers and Optics*, vol. 67, pp. 357-361, Sep. 1998.
- [20] W. Schade, T. Blanke, U. Willer, and C. Rempel, "Compact tunable mid-infrared laser source by difference frequency generation of two diode-lasers," *Applied Physics B-Lasers and Optics*, vol. 63, pp. 99-102, Jul. 1996.
- [21] K. P. Petrov, A. T. Ryan, T. L. Patterson, L. Huang, S. J. Field, and D. I. Bamford, "Spectroscopic detection of methane by use of guided-wave diode-pumped difference-frequency generation," *Optics Letters*, vol. 23, pp. 1052-1054, Jul. 1 1998.
- [22] D. C. Hutchings, "Integrated self-pumped optical frequency conversion and generation in semiconductor waveguides," University of Glasgow, Jan. 26 2006.
- [23] D. J. M. Stothard, T. J. Edwards, D. Walsh, C. L. Thomson, C. F. Rae, M. H. Dunn, and P. G. Browne, "Line-narrowed, compact, and coherent source of widely tunable terahertz radiation," *Applied Physics Letters*, vol. 92, p. 141105, Apr. 7 2008.
- [24] K. L. Vodopyanov, "Optical THz-wave generation with periodically-inverted GaAs," *Laser & Photonics Review*, vol. 2, pp. 11-25, 2008.
- [25] M. A. Belkin, Q. J. Wang, C. Pflugl, A. Belyanin, S. P. Khanna, A. G. Davies, E. H. Linfield, and F. Capasso, "High-Temperature Operation of Terahertz Quantum Cascade Laser Sources," *IEEE Journal of Selected Topics in Quantum Electronics*, vol. 15, pp. 952-967, May-Jun. 2009.
- [26] P. Werle, F. Slemr, K. Maurer, R. Kormann, R. Mucke, and B. Janker, "Near- and mid-infrared laser-optical sensors for gas analysis," *Optics and Lasers in Engineering*, vol. 37, pp. 101-114, Feb-Mar. 2002.
- [27] K. Namjou, S. Cai, E. A. Whittaker, J. Faist, C. Gmachl, F. Capasso, D. L. Sivco, and A. Y. Cho, "Sensitive absorption spectroscopy with a room-temperature distributed-feedback quantum-cascade laser," *Optics Letters*, vol. 23, pp. 219-221, Feb 1 1998.

- [28] A. A. Kosterev, F. K. Tittel, C. Gmachl, F. Capasso, D. L. Sivco, J. N. Baillargeon, A. L. Hutchinson, and A. Y. Cho, "Trace-gas detection in ambient air with a thermoelectrically cooled, pulsed quantum-cascade distributed feedback laser," *Applied Optics*, vol. 39, pp. 6866-6872, Dec. 20 2000.
- [29] C. R. Webster, G. J. Flesch, D. C. Scott, J. E. Swanson, R. D. May, W. S. Woodward, C. Gmachl, F. Capasso, D. L. Sivco, J. N. Baillargeon, A. L. Hutchinson, and A. Y. Cho, "Quantum-cascade laser measurements of stratospheric methane and nitrous oxide," *Applied Optics*, vol. 40, pp. 321-326, Jan. 20 2001.
- [30] M. W. Todd, R. A. Provencal, T. G. Owano, B. A. Paldus, A. Kachanov, K. L. Vodopyanov, M. Hunter, S. L. Coy, J. I. Steinfeld, and J. T. Arnold, "Application of mid-infrared cavity-ringdown spectroscopy to trace explosives vapor detection using a broadly tunable (6-8  $\mu$  m) optical parametric oscillator," *Applied Physics B-Lasers and Optics*, vol. 75, pp. 367-376, Sep. 2002.
- [31] U. Younis, B. M. Holmes, D. C. Hutchings, and J. S. Roberts, "Towards Monolithic Integration of Nonlinear Optical Frequency Conversion," *IEEE Photonics Technology Letters*, vol. 22, pp. 1358-1360, Sep.15 2010.
- [32] G. A. Turnbull, T. J. Edwards, M. H. Dunn, and M. Ebrahimzadeh, "Continuous-wave singly-resonant intracavity optical parametric oscillator based on periodically-poled LiNbO<sub>3</sub>," *Electronics Letters*, vol. 33, pp. 1817-1818, Oct. 9 1997.
- [33] T. Skauli, K. L. Vodopyanov, T. J. Pinguet, A. Schober, O. Levi, L. A. Eyres, M. M. Fejer, J. S. Harris, B. Gerard, L. Becouarn, E. Lallier, and G. Arisholm, "Measurement of the nonlinear coefficient of orientation-patterned GaAs and demonstration of highly efficient second-harmonic generation," *Optics Letters*, vol. 27, pp. 628-630, Apr. 15 2002.
- [34] K. L. Vodopyanov, O. Levi, P. S. Kuo, T. J. Pinguet, J. S. Harris, M. M. Fejer, B. Gerard, L. Becouarn, and E. Lallier, "Optical parametric oscillation in quasi-phase-matched GaAs," *Optics Letters*, vol. 29, pp. 1912-1914, Aug. 15 2004.
- [35] U. Younis, B. M. Holmes, D. C. Hutchings, and J. S. Roberts, "Towards Monolithic Integration of Non-linear Optical Frequency Conversion," in *15th*

*European Conference On Integrated Optics (ECIO 2010)*, Cambridge, UK, 2010.

- [36] S. J. B. Yoo, R. Bhat, C. Caneau, and M. A. Koza, "Quasi-Phase-Matched 2nd-Harmonic Generation in AlGaAs Wave-Guides with Periodic Domain Inversion Achieved by Wafer-Bonding," *Applied Physics Letters*, vol. 66, pp. 3410-3412, Jun. 19 1995.
- [37] S. J. B. Yoo, C. Caneau, R. Bhat, M. A. Koza, A. Rajhel, and N. Antoniadis, "Wavelength conversion by difference frequency generation in AlGaAs waveguides with periodic domain inversion achieved by wafer bonding," *Applied Physics Letters*, vol. 68, pp. 2609-2611, May. 6 1996.
- [38] D. C. Hutchings, "Modulation of the second-order susceptibility in GaAs/AlAs superlattices," *Applied Physics Letters*, vol. 76, pp. 1362-1364, Mar. 13 2000.
- [39] Y. D. Galeuchet and P. Roentgen, "Selective Area Mowpe of Gainas/Inp Heterostructures on Masked and Nonplanar (100) and (111) Substrates," *Journal of Crystal Growth*, vol. 107, pp. 147-150, Jan. 1991.
- [40] F. Xia, V. M. Menon, and S. R. Forrest, "Photonic integration using asymmetric twin-waveguide (ATG) technology: Part I - Concepts and theory," *IEEE Journal of Selected Topics in Quantum Electronics*, vol. 11, pp. 17-29, Jan-Feb. 2005.
- [41] V. A. Menon, F. Xia, and S. R. Forrest, "Photonic integration using asymmetric twin-waveguide (ATG) technology: Part II - Devices," *IEEE Journal of Selected Topics in Quantum Electronics*, vol. 11, pp. 30-42, Jan-Feb. 2005.
- [42] P. A. Franken, G. Weinreich, C. W. Peters, and A. E. Hill, "Generation of Optical Harmonics," *Physical Review Letters*, vol. 7, pp. 118-119, 1961.
- [43] A. Ferguson, "Nonlinear Optics," University of Strathclyde,
- [44] D. C. Hutchings, "Applied Nonlinear Optics," University of Glasgow, 2004.
- [45] O. Bryngdahl, "Image formation using self-imaging techniques," *J. Opt. Soc. Am.*, vol. 63, pp. 416-419, 1973.
- [46] R. Ulrich, "Image formation by phase coincidences in optical waveguides," *Optics Communications*, vol. 13, pp. 259-264, 1975.
- [47] R. Ulrich and T. Kamiya, "Resolution of self-images in planar optical waveguides," *J. Opt. Soc. Am.*, vol. 68, pp. 583-592, 1978.
- [48] R. Ulrich and G. Ankele, "Self-imaging in homogeneous planar optical waveguides," *Applied Physics Letters*, vol. 27, pp. 337-339, 1975.

- [49] J. M. Heaton, R. M. Jenkins, D. R. Wight, J. T. Parker, J. C. H. Birbeck, and K. P. Hilton, "Novel 1-to-N way integrated optical beam splitters using symmetric mode mixing in GaAs/AlGaAs multimode waveguides," *Applied Physics Letters*, vol. 61, pp. 1754-1756, 1992.
- [50] R. M. Jenkins, J. M. Heaton, D. R. Wight, J. T. Parker, J. C. H. Birbeck, G. W. Smith, and K. P. Hilton, "Novel 1 x N and N x N integrated optical switches using self-imaging multimode GaAs/AlGaAs waveguides," *Applied Physics Letters*, vol. 64, pp. 684-686, 1994.
- [51] R. v. Roijen, E. C. M. Pennings, M. J. N. v. Stalen, T. v. Dongen, B. H. Verbeek, and J. M. M. v. d. Heijden, "Compact InP-based ring lasers employing multimode interference couplers and combiners," *Applied Physics Letters*, vol. 64, pp. 1753-1755, 1994.
- [52] T. Krauss, R. M. DeLaRue, I. Gontijo, P. J. R. Laybourn, and J. S. Roberts, "Strip-loaded semiconductor ring lasers employing multimode interference output couplers," *Applied Physics Letters*, vol. 64, pp. 2788-2790, 1994.
- [53] D. A. May-Arrijoja and et al., "A reconfigurable multimode interference splitter for sensing applications," *Measurement Science and Technology*, vol. 18, p. 3241, 2007.
- [54] L. B. Soldano and E. C. M. Pennings, "Optical Multimode Interference Devices Based on Self-Imaging - Principles and Applications," *Journal of Lightwave Technology*, vol. 13, pp. 615-627, Apr. 1995.
- [55] E. C. M. Pennings, R. J. Deri, A. Scherer, R. Bhat, T. R. Hayes, N. C. Andreadakis, M. K. Smit, L. B. Soldano, and R. J. Hawkins, "Ultracompact, low-loss directional couplers on InP based on self-imaging by multimode interference," *Applied Physics Letters*, vol. 59, pp. 1926-1928, 1991.
- [56] P. A. Besse, M. Bachmann, H. Melchior, L. B. Soldano, and M. K. Smit, "Optical Bandwidth and Fabrication Tolerances of Multimode Interference Couplers," *Journal of Lightwave Technology*, vol. 12, pp. 1004-1009, Jun. 1994.
- [57] F. B. Veerman, P. J. Schalkwijk, E. C. M. Pennings, M. K. Smit, and B. H. Verbeek, "An Optical Passive 3-dB TMI-Coupler with Reduced Fabrication Tolerance Sensitivity," *Journal of Lightwave Technology*, vol. 10, pp. 306-311, Mar. 1992.

- [58] L. H. Spiekman, Y. S. Oei, E. G. Metaal, F. H. Groen, I. Moerman, and M. K. Smit, "Extremely Small Multimode Interference Couplers and Ultrashort Bends on Inp by Deep-Etching," *IEEE Photonics Technology Letters*, vol. 6, pp. 1008-1010, Aug. 1994.
- [59] A. Ferreras, F. Rodriguez, E. Gomezsalas, J. L. Demiguel, and F. Hernandezgil, "Useful Formulas for Multimode Interference Power Splitter Combiner Design," *IEEE Photonics Technology Letters*, vol. 5, pp. 1224-1227, Oct. 1993.
- [60] T. H. Maiman, "Stimulated Optical Radiation in Ruby," *Nature*, vol. 187, pp. 493-494, 1960.
- [61] R. N. Hall, R. O. Carlson, T. J. Soltys, G. E. Fenner, and J. D. Kingsley, "Coherent Light Emission from Gaas Junctions," *Physical Review Letters*, vol. 9, pp. 366-368, 1962.
- [62] M. I. Nathan, W. P. Dumke, G. Burns, F. H. Dill, and G. Lasher, "Stimulated Emission of Radiation from Gaas P-N Junctions," *Applied Physics Letters*, vol. 1, pp. 62-64, 1962.
- [63] T. M. Quist, R. H. Rediker, R. J. Keyes, W. E. Krag, B. Lax, A. L. Mcwhorter, and H. J. Zeigler, "Semiconductor Maser of Gaas," *Applied Physics Letters*, vol. 1, pp. 91-92, 1962.
- [64] H. Kroemer, "A Proposed Class of Heterojunction Injection Lasers," *Proceedings of the IEEE*, vol. 51, pp. 1782-1783, 1963.
- [65] Z. I. Alferov, "Nobel Lecture: The double heterostructure concept and its applications in physics, electronics, and technology," *Reviews of Modern Physics*, vol. 73, pp. 767-782, Jul. 2001.
- [66] Z. I. Alferov, V. M. Andreev, V. I. Korolkov, E. L. Portnoi, and Tretyako.Dn, "Coherent Radiation of Epitaxial Heterojunction Structures in AlAs-GaAs System," *Soviet Physics Semiconductors-USSR*, vol. 2, p. 1289, 1969.
- [67] Z. I. Alferov, V. M. Andreev, E. L. Portnoi, and M. K. Trukan, "AlAs-GaAs Heterojunction Injection Lasers with a Low Room-Temperature Threshold," *Soviet Physics Semiconductors-USSR*, vol. 3, p. 1107, 1970.
- [68] Z. I. Alferov, V. M. Andreev, D. Z. Garbuzov, Y. V. Zhilyaev, E. P. Morozov, E. L. Portnoi, and V. G. Trofim, "Investigation of the Influence of the AlAs-GaAs Heterostructure Parameters on the Laser Threshold Current and

- Realization of Continuous Emission at Room Temperature," *Soviet Physics Semiconductors-USSR*, vol. 4, p. 1573, 1971.
- [69] I. Hayashi, "Heterostructure Lasers," *IEEE Transactions on Electron Devices*, vol. 31, pp. 1630-1642, 1984.
- [70] M. B. Panish, I. Hayashi, and S. Sumski, "Double-Heterostructure Injection Lasers with Room-Temperature Thresholds as Low as  $2300 \text{ A/cm}^2$ ," *Applied Physics Letters*, vol. 16, p. 326, 1970.
- [71] I. Hayashi, M. B. Panish, P. W. Foy, and S. Sumski, "Junction Lasers Which Operate Continuously at Room Temperature," *Applied Physics Letters*, vol. 17, p. 109, 1970.
- [72] I. Hayashi, M. B. Panish, and F. K. Reinhart, "GaAs-Al<sub>x</sub>Ga<sub>1-x</sub>As Double Heterostructure Injection Lasers," *Journal of Applied Physics*, vol. 42, pp. 1929-1941, 1971.
- [73] E. Pinkas, B. I. Miller, I. Hayashi, and P. W. Foy, "GaAs-Al<sub>x</sub>Ga<sub>1-x</sub>As Double Heterostructure Lasers---Effect of Doping on Lasing Characteristics of GaAs," *Journal of Applied Physics*, vol. 43, pp. 2827-2835, 1972.
- [74] J. R. Arthur, "Interaction of Ga and As<sub>2</sub> Molecular Beams with GaAs Surfaces," *Journal of Applied Physics*, vol. 39, p. 4032, 1968.
- [75] A. Y. Cho, "Film Deposition by Molecular-Beam Techniques," *Journal of Vacuum Science & Technology*, vol. 8, p. S31, 1971.
- [76] R. Dingle, W. Wiegmann, and C. H. Henry, "Quantum States of Confined Carriers in Very Thin Al<sub>x</sub>Ga<sub>1-x</sub>As-GaAs-Al<sub>x</sub>Ga<sub>1-x</sub>As Heterostructures," *Physical Review Letters*, vol. 33, pp. 827-830, 1974.
- [77] J. P. Vanderziel, R. Dingle, R. C. Miller, W. Wiegmann, and W. A. Nordland, "Laser Oscillation from Quantum States in Very Thin GaAs-Al<sub>0.2</sub>Ga<sub>0.8</sub>As Multilayer Structures," *Applied Physics Letters*, vol. 26, pp. 463-465, 1975.
- [78] R. D. Dupuis, P. D. Dapkus, J. Nick Holonyak, E. A. Rezek, and R. Chin, "Room-temperature laser operation of quantum-well Ga<sub>(1-x)</sub>Al<sub>x</sub>As-GaAs laser diodes grown by metalorganic chemical vapor deposition," *Applied Physics Letters*, vol. 32, pp. 295-297, 1978.
- [79] W. T. Tsang, "A graded-index waveguide separate-confinement laser with very low threshold and a narrow Gaussian beam," *Applied Physics Letters*, vol. 39, pp. 134-137, 1981.

- [80] W. T. Tsang, "Extremely Low Threshold (AlGa)as Graded-Index Waveguide Separate Confinement Heterostructure Lasers Grown by Molecular-Beam Epitaxy," *Applied Physics Letters*, vol. 40, pp. 217-219, 1982.
- [81] W. T. Tsang, "Device Characteristics of (AlGa)as Multi-Quantum-Well Heterostructure Lasers Grown by Molecular-Beam Epitaxy," *Applied Physics Letters*, vol. 38, pp. 204-207, 1981.
- [82] W. T. Tsang, "Extremely Low Threshold (AlGa) as Modified Multi-Quantum Well Heterostructure Lasers Grown by Molecular-Beam Epitaxy," *Applied Physics Letters*, vol. 39, pp. 786-788, 1981.
- [83] P. Blood, E. D. Fletcher, and K. Woodbridge, "Dependence of Threshold Current on the Number of Wells in AlGaas-Gaas Quantum Well Lasers," *Applied Physics Letters*, vol. 47, pp. 193-195, 1985.
- [84] P. W. A. McIlroy, A. Kurobe, and Y. Uematsu, "Analysis and Application of Theoretical Gain Curves to the Design of Multi-Quantum-Well Lasers," *IEEE Journal of Quantum Electronics*, vol. 21, pp. 1958-1963, Dec. 1985.
- [85] A. Kurobe, H. Furuyama, S. Naritsuka, N. Sugiyama, Y. Kokubun, and M. Nakamura, "Effects of Well Number, Cavity Length, and Facet Reflectivity on the Reduction of Threshold Current of Gaas/AlGaas Multi-Quantum Well Lasers," *IEEE Journal of Quantum Electronics*, vol. 24, pp. 635-639, Apr. 1988.
- [86] A. Kurobe, H. Furuyama, S. Naritsuka, Y. Kokubun, and M. Nakamura, "Submilliamper Lasing of Zn-Diffused Mesa Buried-Hetero Al<sub>x</sub>Ga<sub>1-x</sub>As/Gaas Multi-Quantum-Well Lasers at 77-K," *Electronics Letters*, vol. 22, pp. 1117-1118, Oct. 9 1986.
- [87] K. Woodbridge, P. Blood, E. D. Fletcher, and P. J. Hulyer, "Short Wavelength (Visible) Gaas Quantum Well Lasers Grown by Molecular-Beam Epitaxy," *Applied Physics Letters*, vol. 45, pp. 16-18, 1984.
- [88] L. Esaki, "A Birds-Eye-View on the Evolution of Semiconductor Superlattices and Quantum-Wells," *IEEE Journal of Quantum Electronics*, vol. 22, pp. 1611-1624, Sep. 1986.
- [89] L. Esaki, "Long Journey into Tunneling," *Reviews of Modern Physics*, vol. 46, pp. 237-244, 1974.

- [90] L. L. Chang, L. Esaki, W. E. Howard, and R. Ludeke, "The Growth of a GaAs-GaAlAs Superlattice," *Journal of Vacuum Science & Technology*, vol. 10, pp. 11-16, 1973.
- [91] L. L. Chang, L. Esaki, and R. Tsu, "Resonant tunneling in semiconductor double barriers," *Applied Physics Letters*, vol. 24, pp. 593-595, 1974.
- [92] L. Esaki and L. L. Chang, "New Transport Phenomenon in a Semiconductor "Superlattice"," *Physical Review Letters*, vol. 33, p. 495, 1974.
- [93] F. Capasso, K. Mohammed, and A. Y. Cho, "Sequential resonant tunneling through a multiquantum well superlattice," *Applied Physics Letters*, vol. 48, pp. 478-480, 1986.
- [94] P. D. Dapkus, J. J. Coleman, W. D. Laidig, N. Holonyak, B. A. Vojak, and K. Hess, "Continuous Room-Temperature Photopumped Laser Operation of Modulation-Doped Al<sub>x</sub>Ga<sub>1-x</sub>As-GaAs Super-Lattices," *Applied Physics Letters*, vol. 38, pp. 118-120, 1981.
- [95] J. J. Coleman, P. D. Dapkus, D. R. Clarke, M. D. Camras, and N. Holonyak, "Absorption and Stimulated-Emission in an Al<sub>x</sub>As-GaAs Super-Lattice," *Applied Physics Letters*, vol. 39, pp. 864-866, 1981.
- [96] M. J. Ludowise, W. T. Dietze, C. R. Lewis, M. D. Camras, J. N. Holonyak, B. K. Fuller, and M. A. Nixon, "Continuous 300-K laser operation of strained superlattices," *Applied Physics Letters*, vol. 42, pp. 487-489, 1983.
- [97] L. Esaki and R. Tsu, "Superlattice and Negative Differential Conductivity in Semiconductors," *IBM Journal of Research and Development*, vol. 14, p. 61, 1970.
- [98] S. M. SZE, *Semiconductor Devices*: New York: John Wiley & Sons, 1985.
- [99] D. C. Hutchings and T. C. Kleckner, "Quasi phase matching in semiconductor waveguides by intermixing: optimization considerations," *Journal of the Optical Society of America B-Optical Physics*, vol. 19, pp. 890-894, Apr. 2002.
- [100] K. Zeaiter, D. C. Hutchings, R. M. Gwilliam, K. Moutzouris, S. V. Rao, and M. Ebrahimzadeh, "Quasi-phase-matched second-harmonic generation in a GaAs/AlAs superlattice waveguide by ion-implantation-induced intermixing," *Optics Letters*, vol. 28, pp. 911-913, Jun. 1 2003.
- [101] J. P. Bouchard, M. Tetu, S. Janz, D. X. Xu, Z. R. Wasilewski, P. Piva, U. G. Akano, and I. V. Mitchell, "Quasi-phase matched second-harmonic generation in

- an AlxGa1-xAs asymmetric quantum-well waveguide using ion-implantation-enhanced intermixing," *Applied Physics Letters*, vol. 77, pp. 4247-4249, Dec. 25 2000.
- [102] S. Adachi, "Gaas, Alas, and Alxga1-Xas - Material Parameters for Use in Research and Device Applications," *Journal of Applied Physics*, vol. 58, pp. R1-R29, 1985.
- [103] S. Gehrsitz, F. K. Reinhart, C. Gourgon, N. Herres, A. Vonlanthen, and H. Sigg, "The refractive index of AlxGa1-xAs below the band gap: Accurate determination and empirical modeling," *Journal of Applied Physics*, vol. 87, pp. 7825-7837, Jun. 1 2000.
- [104] W. D. Laidig, N. Holonyak, M. D. Camras, K. Hess, J. J. Coleman, P. D. Dapkus, and J. Bardeen, "Disorder of an Alas-Gaas Super-Lattice by Impurity Diffusion," *Applied Physics Letters*, vol. 38, pp. 776-778, 1981.
- [105] J. H. Marsh, "Quantum-Well Intermixing," *Semiconductor Science and Technology*, vol. 8, pp. 1136-1155, Jun. 1993.
- [106] J. P. Reithmaier and A. Forchel, "Focused ion-beam implantation induced thermal quantum-well intermixing for monolithic optoelectronic device integration," *IEEE Journal of Selected Topics in Quantum Electronics*, vol. 4, pp. 595-605, Jul-Aug. 1998.
- [107] D. G. Deppe, L. J. Guido, N. Holonyak, K. C. Hsieh, R. D. Burnham, R. L. Thornton, and T. L. Paoli, "Stripe-Geometry Quantum-Well Heterostructure Alxga1-Xas-Gaas Lasers Defined by Defect Diffusion," *Applied Physics Letters*, vol. 49, pp. 510-512, Sep. 1 1986.
- [108] O. P. Kowalski, C. J. Hamilton, S. D. McDougall, J. H. Marsh, A. C. Bryce, R. M. De la Rue, B. Vogeles, C. R. Stanley, C. C. Button, and J. S. Roberts, "A universal damage induced technique for quantum well intermixing," *Applied Physics Letters*, vol. 72, pp. 581-583, Feb. 2 1998.
- [109] S. Charbonneau, P. J. Poole, P. G. Piva, G. C. Aers, E. S. Koteles, M. Fallahi, J. J. He, J. P. McCaffrey, M. Buchanan, M. Dion, R. D. Goldberg, and I. V. Mitchell, "Quantum-Well Intermixing for Optoelectronic Integration Using High-Energy Ion-Implantation," *Journal of Applied Physics*, vol. 78, pp. 3697-3705, Sep. 15 1995.

- [110] H. Leier, A. Forchel, G. Horcher, J. Hommel, S. Bayer, H. Rothfritz, G. Weimann, and W. Schlapp, "Mass and Dose Dependence of Ion-Implantation-Induced Intermixing of GaAs GaAs Quantum-Well Structures," *Journal of Applied Physics*, vol. 67, pp. 1805-1813, Feb. 15 1990.
- [111] S. I. Hansen, J. H. Marsh, J. S. Roberts, and R. Gwilliam, "Refractive-Index Changes in a GaAs Multiple Quantum-Well Structure Produced by Impurity-Induced Disorder Using Boron and Fluorine," *Applied Physics Letters*, vol. 58, pp. 1398-1400, Apr. 1 1991.
- [112] T. C. Kleckner, A. S. Helmy, K. Zeaiter, D. C. Hutchings, and J. S. Aitchison, "Dispersion and modulation of the linear optical properties of GaAs-AlAs superlattice waveguides using quantum-well intermixing," *IEEE Journal of Quantum Electronics*, vol. 42, pp. 280-286, Mar-Apr. 2006.
- [113] J. S. Aitchison, C. J. Hamilton, M. W. Street, N. D. Whitbread, D. C. Hutchings, J. H. Marsh, G. T. Kennedy, and W. Sibbett, "Control of the second- and third-order nonlinearities in GaAs-AlGaAs multiple quantum wells," *Pure and Applied Optics*, vol. 7, pp. 327-333, Mar. 1998.
- [114] S. Furst, "Monolithic Integration of Semiconductor Ring Lasers," *PhD Thesis, University of Glasgow*, 2008.
- [115] C. J. Hamilton, J. H. Marsh, D. C. Hutchings, J. S. Aitchison, G. T. Kennedy, and W. Sibbett, "Localized Kerr-type nonlinearities in GaAs/AlGaAs multiple quantum well structures at 1.55  $\mu$  m," *Applied Physics Letters*, vol. 68, pp. 3078-3080, May. 27 1996.
- [116] G. Tittelbach, B. Richter, and W. Karthe, "Comparison of three transmission methods for integrated optical waveguide propagation loss measurement," *Pure and Applied Optics: Journal of the European Optical Society Part A*, vol. 2, p. 683, 1993.
- [117] S. J. Wagner, B. M. Holmes, U. Younis, A. S. Helmy, D. C. Hutchings, and J. S. Aitchison, "Controlling Third-Order Nonlinearities by Ion-Implantation Quantum-Well Intermixing," *IEEE Photonics Technology Letters*, vol. 21, pp. 85-87, Jan-Feb. 2009.
- [118] S. D. McDougall, O. P. Kowalski, C. J. Hamilton, F. Camacho, B. C. Qiu, M. L. Ke, R. M. De La Rue, A. C. Bryce, and J. H. Marsh, "Monolithic integration via a universal damage enhanced quantum-well intermixing technique," *IEEE*

- Journal of Selected Topics in Quantum Electronics*, vol. 4, pp. 636-646, Jul-Aug. 1998.
- [119] S. McMaster, "Monolithically Integrated Mode-Locked Ring Lasers and Mach-Zehnder Interferometers in AlGaInAs," *PhD Thesis, University of Glasgow*, 2010.
- [120] S. J. Wagner, A. Al Muhairi, J. S. Aitchison, and A. S. Helmy, "Modeling and optimization of quasi-phase matching via domain-disordering," *IEEE Journal of Quantum Electronics*, vol. 44, pp. 424-429, May-Jun. 2008.
- [121] A. S. Helmy, D. C. Hutchings, T. C. Kleckner, J. H. Marsh, A. C. Bryce, J. M. Arnold, C. R. Stanley, J. S. Aitchison, C. T. A. Brown, K. Moutzouris, and M. Ebrahimzadeh, "Quasi phase matching in GaAs-AlAs superlattice waveguides through bandgap tuning by use of quantum-well intermixing," *Opt. Lett.*, vol. 25, pp. 1370-1372, 2000.
- [122] Jerphagn.J and S. K. Kurtz, "Optical Nonlinear Susceptibilities - Accurate Relative Values for Quartz, Ammonium Dihydrogen Phosphate, and Potassium Dihydrogen Phosphate," *Physical Review B*, vol. 1, p. 1739, 1970.
- [123] Jerphagn.J, "Optical Nonlinear Susceptibilities of Lithium Iodate," *Applied Physics Letters*, vol. 16, p. 298, 1970.
- [124] M. M. Choy and R. L. Byer, "Accurate 2nd-Order Susceptibility Measurements of Visible and Infrared Nonlinear Crystals," *Physical Review B*, vol. 14, pp. 1693-1706, 1976.
- [125] C. B. Ebert, L. A. Eyres, M. M. Fejer, and J. S. Harris, "MBE growth of antiphase GaAs films using GaAs/Ge/GaAs heteroepitaxy," *Journal of Crystal Growth*, vol. 202, pp. 187-193, May. 1999.
- [126] X. J. Yu, L. Scaccabarozzi, A. C. Lin, M. M. Fejer, and J. S. Harris, "Growth of GaAs with orientation-patterned structures for nonlinear optics," *Journal of Crystal Growth*, vol. 301, pp. 163-167, 2007.
- [127] X. Yu, L. Scaccabarozzi, J. S. Harris, P. S. Kuo, and M. M. Fejer, "Efficient continuous wave second harmonic generation pumped at 1.55  $\mu\text{m}$  in quasi-phase-matched AlGaAs waveguides," *Optics Express*, vol. 13, pp. 10742-10748, Dec. 22 2005.
- [128] S. Thoms, "Lecture notes on basic fabrication and electron-beam lithography course," James Watt Nanofabrication Centre, University of Glasgow, 2008.

- [129] S. L. Chin, *Fundamentals of Laser Optoelectronics*: Singapore: World Scientific Publishing, 1989.
- [130] S. J. Wagner, "Report on QPM-2," University of Toronto, Mar. 4 2008.
- [131] S. J. Wagner, B. M. Holmes, U. Younis, A. S. Helmy, J. S. Aitchison, and D. C. Hutchings, "Continuous wave second-harmonic generation using domain-disordered quasi-phase matching waveguides," *Applied Physics Letters*, vol. 94, p. 151107, 2009.
- [132] J. S. Aitchison, J. D. Valera, A. C. Walker, S. Ritchie, P. M. Rodgers, P. McIlroy, and G. I. Stegeman, "Whole-Sample and Localized Induced-Absorption Optical Bistability in GaAs Wave-Guides," *Applied Physics Letters*, vol. 51, pp. 561-563, Aug. 24 1987.
- [133] B. M. Holmes, U. Younis, D. C. Hutchings, S. J. Wagner, A. S. Helmy, and J. S. Aitchison, "Type-II quasi-phase-matched second-harmonic generation in domain-disordered semiconductor waveguides," in *Lasers and Electro-Optics, 2009 and 2009 Conference on Quantum electronics and Laser Science Conference. CLEO/QELS 2009. Conference on*, 2009, pp. 1-2.
- [134] David C. Hutchings, Sean J. Wagner, Barry M. Holmes, U. Younis, Amr S. Helmy, and J. S. Aitchison, "Type-II quasi phase matching in periodically intermixed semiconductor superlattice waveguides," *Opt. Lett.*, vol. 35, pp. 1299-1301, 2010.
- [135] S. J. Wagner, I. Sigal, A. S. Helmy, J. S. Aitchison, U. Younis, B. M. Holmes, and D. C. Hutchings, "Difference Frequency Generation in Domain-Disordered Quasi-Phase Matching Semiconductor Waveguides," in *Conference on Lasers and Electro-Optics, 2010 and 2010 Conference on Quantum electronics and Laser Science Conference. CLEO/QELS 2010.*, San Jose, California, 2010.
- [136] C. D. Farmer, "Recent work carried out to improve gold electroplating," University of Glasgow, Jul. 27 2009.
- [137] J. C. Moore, "Solvent removal of photoresist mask and gold impregnated residue and process," US 2007/0093061 A1, 2007.
- [138] T. C. Tisone and J. Drobek, "Diffusion in Thin-Film Ti-Au, Ti-Pd, and Ti-Pt Couples," *Journal of Vacuum Science & Technology*, vol. 9, pp. 271-275, 1972.
- [139] R. Pretorius, J. M. Harris, and M. A. Nicolet, "Reaction of Thin Metal-Films with SiO<sub>2</sub> Substrates," *Solid-State Electronics*, vol. 21, pp. 667-675, 1978.

- [140] X. S. Wu, L. A. Coldren, and J. L. Merz, "Selective Etching Characteristics of Hf for Al<sub>x</sub>Ga<sub>1-x</sub>As/GaAs," *Electronics Letters*, vol. 21, pp. 558-559, 1985.
- [141] C. D. Farmer, "HF-Free Titanium Etching Using H<sub>2</sub>O<sub>2</sub>-Based Solution," University of Glasgow, Nov. 20 2009.
- [142] E. J. Murphy, W. J. Minford, and T. C. Rice, "Integrated-Optics Processing - Uses of an Edta Etch Solution," *Electronics Letters*, vol. 20, pp. 760-761, 1984.
- [143] T. A. Cloud, M. R. Houston, P. A. Kohl, and S. A. Bidstrup, "Processing and Performance of Gold Mcms," *IEEE Transactions on Components Hybrids and Manufacturing Technology*, vol. 16, pp. 724-730, Nov. 1993.
- [144] S. Y. Lee, S. Darmawan, C. W. Lee, and M. K. Chin, "Transformation between directional couplers and multi-mode interferometers based on ridge waveguides," *Optics Express*, vol. 12, pp. 3079-3085, Jul. 12 2004.
- [145] E. C. M. Pennings, R. Vanroijen, M. J. N. Vanstralen, P. J. Dewaard, R. G. M. P. Koumans, and B. H. Verbeek, "Reflection Properties of Multimode Interference Devices," *IEEE Photonics Technology Letters*, vol. 6, pp. 715-718, Jun. 1994.
- [146] V. M. Donnelly, D. L. Flamm, C. W. Tu, and D. E. Ibbotson, "Temperature-Dependence of Inp and Gaas Etching in a Chlorine Plasma," *Journal of the Electrochemical Society*, vol. 129, pp. 2533-2537, 1982.
- [147] M. B. Stern and P. F. Liao, "Reactive Ion Etching of Gaas and Inp Using SiCl<sub>4</sub>," *Journal of Vacuum Science & Technology B*, vol. 1, pp. 1053-1055, 1983.
- [148] S. Salimian and C. B. Cooper, "Selective Dry Etching of Gaas over Algaas in Sf<sub>6</sub>/SiCl<sub>4</sub> Mixtures," *Journal of Vacuum Science & Technology B*, vol. 6, pp. 1641-1644, Nov-Dec. 1988.
- [149] H. Granier, J. Tasselli, A. Marty, and H. P. Hu, "A SiCl<sub>4</sub> reactive ion etching and laser reflectometry process for AlGaAs/GaAs HBT fabrication," *Vacuum*, vol. 47, pp. 1347-1351, Nov. 1996.
- [150] G. Smolinsky, R. P. Chang, and T. M. Mayer, "Plasma-Etching of III-V-Compound Semiconductor-Materials and Their Oxides," *Journal of Vacuum Science & Technology*, vol. 18, pp. 12-16, 1981.
- [151] S. N. M. Mestanza, J. A. Diniz, and N. C. Frateschi, "Laser reflectometry applied to the in-situ etching control in an electron cyclotron resonance plasma

- system," in *International Microwave and Optoelectronics Conference (IMOC)*, 1999, p. 616.
- [152] L. B. Soldano, F. B. Veerman, M. K. Smit, B. H. Verbeek, A. H. Dubost, and E. C. M. Pennings, "Planar Monomode Optical Couplers Based on Multimode Interference Effects," *Journal of Lightwave Technology*, vol. 10, pp. 1843-1850, Dec. 1992.
- [153] M. Sorel and D. C. Hutchings, "AlAs/GaAs Superlattice Lasers (private communication),"
- [154] E. F. Schubert and J. M. Shah "Specific resistance of ohmic contacts (tutorial),"
- [155] M. Hopkinson and B. M. Holmes, "Growth information BMH8 (private communication)," 2009.
- [156] L. M. L. Ltd, "Leica Vectorbeam Series - Vectorbeam Operator Manual," 2005.
- [157] H. C. Casey and M. B. Panish, *Heterostructure Lasers*, 1978 ed. New York: Academic, 1978.
- [158] F. Stern, "Gain-current relation for GaAs lasers with n-type and undoped active layers," *IEEE Journal of Quantum Electronics*, vol. 9, pp. 290-294, 1973.
- [159] F. Klopff, S. Deubert, J. P. Reithmaier, and A. Forchel, "Correlation between the gain profile and the temperature-induced shift in wavelength of quantum-dot lasers," *Applied Physics Letters*, vol. 81, pp. 217-219, Jul. 8 2002.
- [160] F. Klopff, J. P. Reithmaier, and A. Forchel, "Highly efficient GaInAs/(Al)GaAs quantum-dot lasers based on a single active layer versus 980 nm high-power quantum-well lasers," *Applied Physics Letters*, vol. 77, pp. 1419-1421, Sep. 4 2000.
- [161] U. Younis and J. S. Roberts, "Growth Information - BMH9 (private communication)," 16 Jan. 2010.
- [162] V. J. Goldman, D. C. Tsui, and J. E. Cunningham, "Observation of intrinsic bistability in resonant tunneling structures," *Physical Review Letters*, vol. 58, p. 1256, 1987.
- [163] F. W. Sheard and G. A. Toombs, "Space-charge buildup and bistability in resonant-tunneling double-barrier structures," *Applied Physics Letters*, vol. 52, pp. 1228-1230, 1988.
- [164] P. A. Postigo, F. Suarez, A. Sanz-Hervas, J. Sangrador, and C. G. Fonstad, "Growth of InP on GaAs (001) by hydrogen-assisted low-temperature solid-

source molecular beam epitaxy," *Journal of Applied Physics*, vol. 103, p. 013508, 2008.